THE USE OF TRANSFERRIN AND ULTRASOUND IN CANCER TREATMENT

by

Nour Majdi AlSawaftah

A Thesis Presented to the Faculty of the
American University of Sharjah
College of Engineering
in Partial Fulfillment
of the Requirements
for the Degree of

Master of Science in
Biomedical Engineering

Sharjah, United Arab Emirates

May 2019

Approval Signatures

We, the undersigned, approve the Master's Thesis of Nour Majdi AlSawaftah.

Thesis Title: The Use of Transferrin and Ultrasound in Cancer Treatment.

Signature	**Date of Signature** (dd/mm/yyyy)
_____	_____
Dr. Ghaleb Husseini Professor, Department of Chemical Engineering Thesis Advisor	
_____	_____
Dr. Rana Sabouni Assistant Professor, Department of Chemical Engineering Thesis Committee Member	
_____	_____
Dr. Nahid Awad Senior Research Associate, Biosciences and Bioengineering Research Institute (BBRI) Thesis Committee Member	
_____	_____
Dr. Hasan AlNashash Director, Biomedical Engineering Graduate Program	
_____	_____
Dr. Lotfi Romdhane Associate Dean for Graduate Affairs and Research College of Engineering	
_____	_____
Dr. Naif Darwish Acting Dean, College of Engineering	
_____	_____
Dr. Mohamed El-Tarhuni Vice Provost for Graduate Studies	

Acknowledgements

I would like to take this opportunity to express my deepest gratitude to my thesis advisor Dr. Ghaleb Husseini for his guidance, motivation and continuous support during my research process.

I would like to thank Dr. Nahid Awad, Mr. Vinod Paul, Dr. Rute Vitor and Dr. Mohammad Sayah for providing knowledge, guidance, support, and motivation throughout my research stages. I'm deeply grateful for their great assistance, worthy discussion and suggestions. And I sincerely thank my friends Paul Kawak, Afifa Farooq, Rand AbuSamra, Omnia Sarsar and Ahmed Ahmed for their support and motivation and for making my time with the drug delivery group an enjoyable and unforgettable journey.

I am also thankful for my thesis examiners, Dr. Nahid Awad and Dr. Rana Sabouni whose valued questions, comments and suggestions greatly helped me in achieving this stage of my research and in writing my thesis.

I would like to extend my deepest gratitude to the director of the biomedical engineering graduate program Dr. Hasan AlNashash for his guidance and support. Finally, I would like to thank the American University of Sharjah for providing me with this opportunity to pursue my goals in graduate studies through a teaching assistantship.

Abstract

Site-specific drug delivery represents an attractive approach in cancer treatment to reduce the undesirable side-effects of anticancer therapeutics and increase the accumulation of drugs at tumor sites. Surface modification of nanoparticles such as liposomes with targeting moieties specific to the receptors on the surface of tumor cells further improves the selectivity of liposomes, while external triggers such as ultrasound can be used to enhance the release of liposomal contents. In this study, the anticancer activity of PEGylated calcein-loaded liposomes targeted with transferrin (Tf) was evaluated. The sizes of liposomes were measured using dynamic light scattering; control liposomes were found to have an average diameter of 82.70±2.88 nm while transferrin liposomes had an average diameter of 87.54±4.81 nm. The presence of transferrin was established using the bicinchoninic acid (BCA) assay, and the total lipid content was quantified using the Stewart assay. Next, low-frequency ultrasound (LFUS) of 20 kHz at three power densities (7.46, 9.85, and 17.31 mW/cm^2) and high-frequency ultrasound (HFUS) at two frequencies (1.07MHz and 3MHz) were used to release the contents of 3 batches of control and transferrin liposomes. For LFUS, the release profiles showed an increase in calcein release with increased power density and that transferrin-conjugated liposomes have a significantly higher release when compared to non-targeted liposomes at all three power densities. In addition, nine drug release kinetics' models were utilized to model the LFUS release profiles. For both types of liposomes, the best fitting models were Korsmeyer-Peppas, Hixson-Crowell, Weibull and Hopfenberg. With regard to HFUS release; both types of liposomes showed a clear increase in release after each insonation; however, the release at 1.07 MHz was higher than that of 3 MHz even though the power density was higher at 3 MHz. Moreover, the release profile for transferrin liposomes showed a more linear increase with time, and the fraction release values tended to be higher than those obtained for control liposomes for both frequencies. Finally, the results of the *in-vitro* cell work indicated that Tf-modified liposomes coupled with US were able to enhance the intracellular uptake and cytotoxicity of the entrapped calcein by HeLa cells by around 80.09±30.08% compared to control liposomes.

Keywords: ***Drug delivery, Ultrasound, Liposomes, Transferrin, Kinetic Modeling.***

Table of Contents

List of Figures

List of Tables

List of Abbreviations

ACF	Autocorrelation Function
ANOVA	Analysis of Variance
CEA	Carcino-embryonic antigen
CLR	C-type lectin receptor
DC-SIGN	Dendritic Cell-specific Intercellular Adhesion Molecule-3-grabbing Non-integrin
DLS	Dynamic Light Scattering
DOX	Doxorubucin
DPPC	Dipalmitoylphosphatidylcholine
DT	Targeted Delivery
EDA	Exploratory Data Analysis
EGFR	Endothelial Growth Factor Receptor
EPR	Enhanced Permeability and Retention Effect
Fab	Antigen-binding Fragments
FBS	Fetal Bovine Serum
FDA	Food and Drug Administration
FR	Folate Receptor
Fv	Variable Fragment
GSH	Glutathione
HFUS	High-Frequency Ultrasound
LFUS	Low-Frequency Ultrasound

mAbs	Monoclonal Antibodies
MAL	Maleimide
MANOVA	Multivariate Analysis of Variance
MI	Mechanical Index
MLV	Multilamellar Vesicle
MMP	Matrix Metalloprotease
MPS	Mononuclear Phagocyte System
MR	Mannose Receptor
NIR	Near-Infrared
NP	Nanoparticle
ODN	Oligonucleotide
PBS	Phosphate Buffer Saline
PCS	Photon Correlation Spectroscopy
PEG	Poly-ethylene Glycol
PNIPAM	Poly(N-isopropylacrylamide)
PSD	Particle Size Distribution
QD	Quantum Dot
RES	Reticuloendothelial System
RFC	Reduced Folate Receptor
scFv	Single Chain Variable Fragments
SDDS	Smart Drug Delivery System
siRNA	Short Inhibitory RNA

SL	Stealth Liposome
SUV	Small Unilamellar Vesicle
Tf	Transferrin
TfR	Transferrin Receptor
ULV	Unilamellar Vesicle
US	Ultrasound
UV	Ultraviolet
VCAM	Vascular Cell-Adhesion Molecule
VEGFR	Vascular Endothelial Growth Factor Receptor

Chapter 1. Introduction

Cancer is a complex disease characterized by the uncontrolled division and spread of abnormal cells. The American Cancer Society estimated that around 1.6 million new cases of cancer were diagnosed in 2017 in the United States alone; accordingly the death rate was approximated at about 600,920 which translates to 1650 individuals per day [1].

The human body is made up of trillions of cells; under normal conditions cells follow an orderly path of growth, division and apoptosis (programmed cell death). Carcinogenesis is a multi-step process in which cells undergo extensive metabolic and behavioral changes that perturb the systematic life course of the cell. The aforementioned changes arise mainly due to alterations in the genetic programs controlling cell proliferation, relations with neighboring cells and detection by the immune system. The three main types of genes that are usually affected by such modifications are: proto-oncogenes, tumor suppressor genes and DNA repair genes. Proto-oncogenes are involved in regulating cell growth and division; they act as intermediaries between growth factor receptors on cell surfaces and the system that sends these growth signals to the cell nuclei. Mutant proto-oncogenes or simply oncogenes act disruptively permitting the cells to grow and divide beyond their natural limit. On the other hand, tumor suppressor genes act as inherent “emergency breaks” to avoid inappropriate cell division; hence mutations to these genes result in loss of functionality rendering them useless in stopping unwarranted cell divisions. Lastly, cells with alterations in their DNA repair genes (genes responsible for reparation of damaged DNA) may develop genetic and/or genomic instabilities which are hallmarks of cancer [2, 3].

Aberrant cell divisions usually lead to the formation of growths known as tumors. Generally, tumors are divided into three categories [4]:

- Benign: this type of tumors is not cancerous as it is localized meaning that it does not spread into other body locations.
- Premalignant: such tumors are not cancerous but appear to be acquiring cancerous properties.

- Malignant: also known as metastatic cancer, are cancerous tumors that cannot be confined. They tend to spread within the affected organ then into neighboring cells and organs. They can also enter the bloodstream or lymphatic vessels disseminating to distant body locations. Metastatic cancer is aided by angiogenesis, which is the ability of cancer cells to drive nearby normal cells to form blood vessels in order to vascularize the tumor and keep it supplied with oxygen and nutrients [2].

The last few decades have witnessed a rapid and continuous increase in the number of investigations into cancer therapy. Current technological advances have greatly aided the development of novel therapeutic modalities. Some of the most common treatment approaches include [5]:

- Surgery: surgery can be used as a diagnostic tool to determine if a certain mass is cancerous through a procedure called biopsy; the removal of suspect tissue is referred to as prophylactic or preventive surgery. Surgery can also be used to determine the extent of cancer which is known as cancer staging. Primary or curative surgery involves the removal of the cancerous mass and this procedure is usually performed when cancer is found in one part of the body only. Surgical interventions can also be used to treat problems caused by advanced cancer as well as in the reconstruction and restoration of body parts and functions.
- Chemotherapy: usually referred to as chemo involves the use of medicines or drugs to treat cancer by interfering with the cell cycle. The advantage that chemotherapy has over surgery is that it can work throughout the whole body targeting cancer cells that have metastasized beyond the primary tumor site.
- Radiation therapy: radiation is one of the most common methods used in cancer treatment. High-energy particles or waves, e.g., x-rays, gamma rays, irradiate the region to be treated and damage or destroy cancer cells by making small breaks in their DNA preventing them from growing and dividing.
- Targeted therapy: this is a particular type of chemotherapy in which the administered drugs target the cancer cell's inner workings (which is

distinguished from other healthy cells), for instance targeted drugs can block the growth signals delivered to cancer cells, change the proteins within the cancer cells or interfere with angiogenesis to cut-off their supply of oxygen and nutrients causing the cancer cells to die.

- Immunotherapy: (also known as biotherapy) is a treatment modality that uses the individual's immune system to fight diseases such as cancer. This can be done either by stimulating the patient's immune system or providing the patient with immune system components, such as man-made immune system proteins to help the body mount a smarter yet more aggressive attack against the disease.

Cancer patients are usually prescribed one or a combination of the above mentioned treatment modalities. Unfortunately, these treatments are often accompanied by adverse side effects that can greatly reduce the quality of life of cancer patients such as: dehydration, fatigue, hair loss, infections, pain, nausea and vomiting. Researchers and medical professionals are continuously searching for alternative methods to treat cancer with fewer or no side effects; such ventures include: stem cell transplants, hyperthermia, photodynamic therapy and smart drug delivery systems (SDDS). SDDS are nanoplatforms capable of delivering the active drug to the diseased area and release its contents in response to an endogenous or exogenous trigger such as temperature, pH, enzymes, light, mechanical waves or magnetic fields. Their unique nanoscale properties and specific bio-functions allow them to accumulate in target regions and release their payloads in a controlled fashion hence increasing drug targeting efficiency all while reducing side effects. A variety of SDDS have been developed such as stimuli-responsive polymeric nanoparticles, metals/metal oxides, micelles and liposomes [6, 7].

In this work transferrin (Tf)-poly-ethylene glycol (PEG)-liposomes were synthesized, and their contents were released using ultrasound (US). The details pertinent to liposomes, transferrin and ultrasound will be discussed in-depth in the following chapters.

Chapter 2. Objectives

The aim of this research is to develop an improved method for the delivery of anticancer therapeutic agents by using ligand conjugated liposomes and ultrasound as an external trigger. In order to achieve these aims the following objectives were set:

1. Synthesize non-targeted (i.e. moiety free) control liposomes.
2. Synthesize transferrin-conjugated stealth liposomes.
3. Perform characterization tests on both control and targeted liposomes to determine the size, phospholipid content and ligand attachment using dynamic light scattering, Stewart and BCA assays respectively.
4. Study the acoustic release of the model drug calcein from the aforementioned types of liposomes, using 20 kHz-LFUS at the following power densities: 7.46, 9.85, and 17.31 mW/cm^2.
5. Study the acoustic release of the model drug calcein from the aforementioned types of liposomes using HFUS at 1.07 MHz and 3 MHz.
6. Perform mathematical modeling for the drug release kinetics of the developed drug delivery system.
7. Conduct *in-vitro* studies to investigate the effects transferrin- targeted-liposomes have on cancer cells overexpressing transferrin receptors particularly the HeLa cell line (cervical cancer).

Chapter 3. Literature Review

3.1. Nanoparticles as Drug Delivery Systems

Smart drug delivery systems (SDDS) were previously defined as enhanced, stimulus-sensitive targeted drug delivery (DT) systems. The design rationale behind these smart dug delivery platforms mandates that they satisfy the following criteria [8, 9]:

- Release medications in appropriate dosages to targeted anatomical sites only.
- Improve the solubility and stability of the drug/payload.
- Reduce systemic side effects of the drug.
- Increase drug circulation time and prolong interaction with the diseased area.
- The system should be non-toxic and non-immunogenic.
- The carriers used should be easily bio-degradable and freely eliminated from the body without producing any adverse side effects.

Nanoparticles (NP) are best defined as objects ranging in size between 1 nm-30 μm. Due to their nanoscale properties and specific bio-functions nanoparticles have proven to be amongst the most promising SDDS, refer to Figure 1. NPs can be synthesized chemically or biologically; however due to the hazards associated with some of the chemicals used in the synthesis of NPs the biological route offers a safer, more eco-friendly alternative. A diversity of microorganisms, both eukaryotic and prokaryotic, can be used for the intracellular or extracellular synthesis of NPs. Table 1 presents some such biologically synthesized nanoparticles [10].

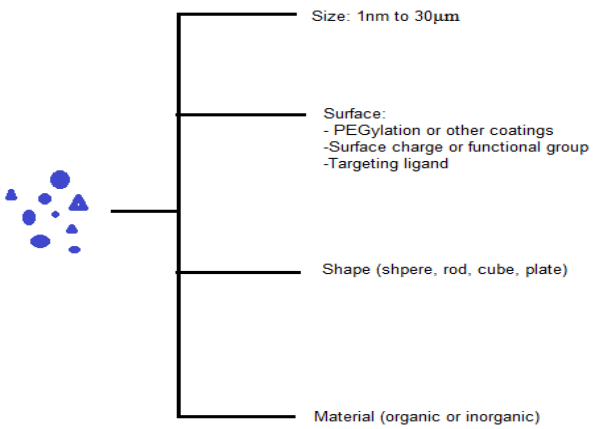

Figure 1: Biophysicochemical properties of nanoparticles.

Table 1: Synthesis of nanoparticles by different microorganisms [10].

Microorganism	Type	Location	Size (nm)
Phoma sp.	Ag	Extracellular	71-74
Fusarium oxysporum	Au	Extracellular	20-40
Verticillium sp.	Ag	Intracellular	25±12
Aspergillus fumigates	Ag	Extracellular	5-25
Trichoderma asperellum	Ag	Extracellular	13-18
Phaenerochaete chrysosporium	Ag	Extracellular	50-200

The properties of NPs can greatly influence their behavior *in-vivo*. Morphological properties such as size and shape are determinants of the duration of NPs' circulation and targeting within the body. Ideally, NPs should remain in circulation until they reach their target anatomical site. However, these particles will be directly eliminated from the body if recognized by the immune system. Studies have shown that particles with radii larger than 7μm are filtered mechanically by the lungs. Particles with diameters between 0.1–7μm are detected by the reticuloendothelial system (RES) in the liver or spleen, and are phagocytized by macrophages. However, if the particle's diameter is lower than 100 nm, it will remain within the fenestrae of the endothelial lining of blood vessels hence reducing the possibility of it being recognized and phagocytized. The smallest NPs, with diameters less than 6 nm undergo glomerular filtration in the kidneys. With regard to shape, studies have reported that spherically shaped particles are more free to move and less likely to line up with or drop into the bifurcations of vessels or filtering organs than irregularly shaped NPs. Additionally, it was noted that cylindrically or spherically shaped NPs are internalized more promptly than their irregularly shaped counterparts. Surface properties such as hydrophobicity and surface charge in addition to the presence/absence of surface ligands can also influence the NPs' behavior within the biological system and potentiate great changes in their performance [11].

As mentioned earlier, after administration it is desired that nanoparticles have the ability to target specific body locations in order to reduce side effects experienced by healthy tissues. To achieve this goal targeting approaches, either passive or active targeting, can be employed [11].

3.1.1. Passive targeting. As mentioned in the introductory section tumor cells can develop their own vasculature by inducing nearby normal cells to form

blood vessels (angiogenesis). The cancer cells become dependent on this neovasculature for their nutritional and oxygen supply. However, the capillary endothelium in tumor tissues is disorganized, imparting a defective and leaky architecture with wide fenestrations between cells. In addition, tumor tissue endothelia lack smooth muscle layers, proper innervation and lymphatic drainage. All of which are factors which contribute to abnormal molecular and fluid transport dynamics across tumors and allow the extravasation and accumulation of nanosized particles, circulating for targeted drug delivery purposes, within the tumor interstitium. This phenomenon is referred to as the Enhanced Permeability and Retention (EPR) effect. Passive targeting makes use of these unique pathophysiological characteristics of tumor vessels as well as the EPR effect to enable the accumulation of drug-carrier systems at tumor sites [9, 12].

3.1.2. Active targeting. The random nature of the passive targeting approach makes it subject to several limitations, for instance not all tumors exhibit the EPR effect and the permeability of blood vessels may vary throughout a single tumor meaning that drugs cannot diffuse uniformly throughout. Active targeting can overcome these limitations because it entails specific interactions between the targeted cells and the drug carrier, usually through receptor-ligand interactions. Specific receptors are highly expressed on tumor cells but not on normal cells; active targeting takes advantage of this trait. Nanocarriers will recognize and bind to the receptors on the cell surface through ligand-receptor interactions, and the formed complex is then internalized through receptor-mediated endocytosis thereby enhancing cellular uptake and facilitating drug release inside the cell [9, 13]. Figure 2 depicts the difference between active and passive targeting.

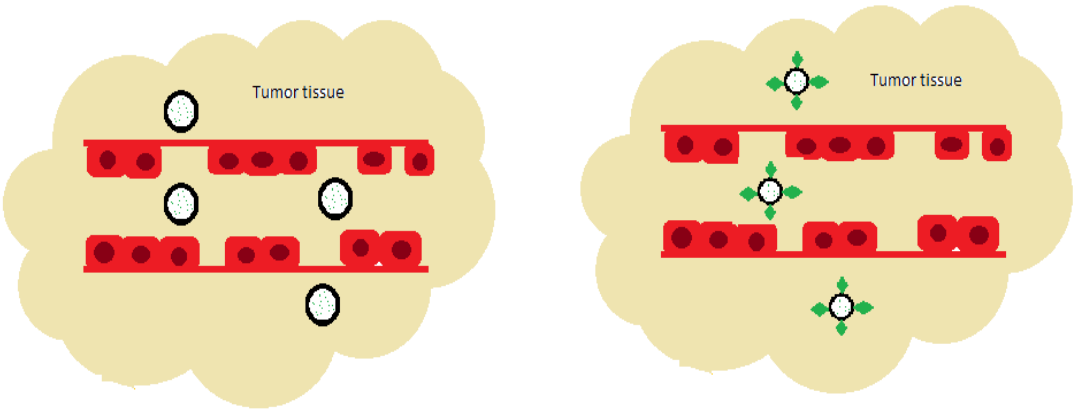

Figure 2: (left) passive targeting compared to (right) Active targeting.

3.2. Types of Nanoparticles

The majority of nanoparticles can be divided into two main groups: organic and inorganic nanoparticles.

3.2.1. Inorganic nanoparticles. The inorganic group includes gold nanoparticles, fullerenes, fluorescent quantum dots, magnetic and ceramic nanoparticles [11].

3.2.1.1. Gold nanoparticles. These nanoparticles are emerging as a promising delivery carrier for therapeutic drugs and in-vivo imaging because of their electrical and optical properties. Gold nanoparticles consist of a core of gold atoms that can be functionalized by the addition of a monolayer of ligands for active targeting applications. These nanoparticles were found to be non-toxic and potentially biodegradable in some human cell lines [14].

3.2.1.2. Fullerenes. Fullerenes are highly symmetric and stable structures made up of carbon molecules (carbon allotrope). The most well-known fullerene, buckminsterfullerene for short bucky balls is composed of 60 carbon atoms arranged in a shape known as truncated icosahedrons. Fullerenes have unique optical, electrical and magnetic properties making them powerful tools in imaging and diagnostic purposes. They are also being investigated for drug delivery applications of antiviral drugs, antibiotics and anticancer agents [11, 15].

3.2.1.3. Semiconductor fluorescent quantum dots. Quantum dots (QD) are light-emitting nanocrystals made from semiconductor materials. Atoms of elements from groups II to VI (e.g. Cd, Zn, Se, Te) or III to V (e.g. In, P, As) are used to form the QDs' inorganic semiconductor core as well as the outer aqueous organic shell. The most popular QD system comprises of a cadmium sulfide (CdS) or cadmium selenide (CdSe) core coated with zinc sulfide (ZnS). The unique optical properties of QDs, i.e., broad absorption range, narrow emission spectrum, bright fluorescence, high photostability and resistance to photobleaching originate from their small size and highly compact structure. Due to their singular physical and chemical properties, QDs have gained multiple applications in the medical field as diagnostic and therapeutic tools. Some of these applications include detection and analysis of biomolecules, DNA hybridization, time-graded fluorescence imaging of tissues,

magnetic resonance imaging (MRI), and transport vehicles for DNA, proteins or drugs. In addition, they can be coupled with biomolecules and used as highly sensitive probes or biosensors [11, 14, 15].

3.2.1.4. Ceramic nanoparticles. Chemically inert, non-metallic, inorganic nanoscale ceramics such as hydroxyapatite (HA), zirconia (ZrO_2), silica (SiO_2), titanium oxide (TiO_2), and alumina (Al_2O_3) have generated a great deal of interest in biomedical circles mostly because of their high natural abundance, low cost and ease of synthesis. Currently, the development of ceramic materials suited for biomedical applications is growing rapidly. New synthesis methods aimed at improving their physical and chemical properties are underway. Concurrently, ceramic nanostructures of varying size, shape, porosity and exterior surface coatings of different organic groups are being explored especially as targeted theranostics [14, 16].

3.2.1.5. Paramagnetic nanoparticles. Magnetic nanoparticles are nanostructures that can be targeted using a magnetic field. These particles are composed of magnetic elements such as cobalt, iron, nickel and their oxides such as magnetite, cobalt ferrite and chromium dioxide. The paramagnetic properties of these particles arise from the magnetic moment that they acquire when exposed to an external magnetic field, removing the magnetic field eliminates this paramagnetism. Paramagnetic NPs have greater magnetic susceptibility than conventional contrast agents making them attractive candidates for imaging applications, for instance, ligand-coupled paramagnetic NPs together with MRI technology have been used in the detection of tumors and protein identification. Moreover, ligand-coupled magnetic nanoprobes are used in targeted cancer therapy. The nanoparticles are directed to tumor cells where they accumulate and, using an externally applied alternating magnetic field, generate high levels of heat, a procedure that kills cancer cells selectively[15, 17].

3.2.2. Organic nanoparticles. The organic group includes dendrimers, polymeric nanoparticles, micelles and liposomes [11].

3.2.2.1. Dendrimers. Dendrimers are hyperbranched, nanosized molecules. The name comes from the Greek word (Dendron) which translates to “tree”. Synonymous terms for dendrimers include arborols and cascade molecules.

Dendrimers were discovered and heavily researched by Fritz Vogtle in 1978, by Donald Tomalia and co-workers in the early 1980s, and at the same time, but independently by George R. Newkome. The structure of dendrimers consists of a central atom or group of atoms labeled as the core. Branches of other atoms referred to as 'dendrons' project from the core through a variety of chemical reactions, the ends of these branches can be functionalized by modifying their physiochemical or biological properties. Given their unique architecture, the first proposed application of dendrimers was as container compounds, wherein small substances are enclosed within the internal voids of the dendrimer [18]. Figure 3 depicts the structure of a dendrimer.

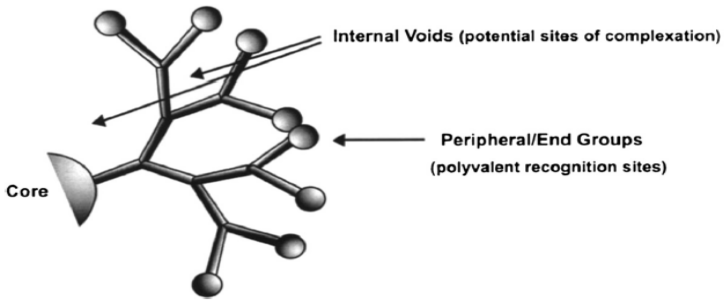

Figure 3: The main parts of dendrimers: the core, the end-groups and the subunits linking to the two molecules [18].

The ease with which other branched units and/or molecules can be attached to the peripheral ends of or be enclosed within the internal voids of dendrimers has garnered great attention as promising molecular containers to be used in targeted drug delivery. Various strategies have been proposed to incorporate drugs, genetic materials, targeting agents and dyes within the dendrimer structure through encapsulation, conjugation, or complexation. The research exploring the targeted drug delivery capabilities of dendrimers has shown some promising findings, as the drug-dendrimer complex demonstrated high solubility, reduced systemic toxicity and selective accumulation in solid tumors [18].

3.2.2.2. Polymeric nanoparticles. Polymers are macromolecules comprised of a large number of repeating subunits. Because of their broad range of properties, both synthetic and natural polymers play an essential role in everyday life. It is due to this wealth in composition, structure and properties that polymers are being used to

synthesize NPs suited for numerous biomedical applications, e.g., drug delivery, bioimaging and biosensing assays. With regard to drug delivery, a great deal of research has been focused on generating polymeric nanoparticles that are efficient, tissue-specific, and most importantly, nontoxic. The most widely used natural polymers in the synthesis of nanoparticles include chitosan, albumin and heparin. On the other hand, synthetic polymers used in the preparation of NPs may be in the form of preformed polymers, e.g., polyesters like polycaprolactone (PCL), poly lactic acid (PLA), or monomers that are polymerized *in situ*, e.g. polyalkyl cyanoacrylate. In these polymeric NPs, the therapeutic agent may either be entrapped within the structure or adsorbed onto the surface of the NP. In addition, the polymer coating of NPs facilitates their biofunctionalization and nanoparticle-cell interactions. The coatings also camouflage the NPs from the RES and phagocytic plasma proteins making them more efficient at targeted therapeutics [11, 15, 16].

3.2.2.3. Micelles. Micelles are biocompatible, core-shell structures varying in size from 50 to 200nm. They are made up of amphiphilic molecules such as lipids or polymers. When exposed to an aqueous environment, the component molecules of micellar systems arrange themselves in spheroidal structures with the hydrophobic cores hidden inside the structure while the hydrophilic groups would be directed outwards. Drugs can be loaded into micelles either through chemical covalent bonding or through physical encapsulation. Poorly water-soluble drugs tend to be loaded into the micelle's hydrophobic core, whereas hydrophilic drugs tend to align themselves near the hydrophilic components of the micellar structure. Micelles have proven to be remarkable SDDS due to their ease of preparation, high stability under physiological conditions, efficient and versatile loading capacity, controlled release kinetics and the possibility and ease of functionalization. Various cancer-related drugs such as paclitaxel, doxorubicin, 5-fluorouracil, cisplatin, triptorelin and xanthone have been successfully encapsulated into micelles [11, 14–16].

3.2.2.4. Liposomes. Liposomes are nanosized to microsized artificial vesicles composed of the same materials that make up the cell membrane, i.e., cholesterol, nontoxic surfactants and natural phospholipids. The name liposome is derived from the Greek words 'Lipos' meaning fat and 'Soma' meaning body. Liposomes were first discovered in 1961 by British hematologist Dr. Alec D. Bangham, while studying the

effects of phospholipids on blood clotting. Bangham noticed that phospholipids impulsively formed closed structures when hydrated in an aqueous medium. Ever since their discovery, liposomes have found numerous applications in many scientific disciplines [19].

Structurally, liposomes are concentric spheres of phospholipid bilayers separated by aqueous compartments. When amphipathic phospholipids are exposed to water they tend to reassemble themselves into tiny spheroidal structures that are either bilayered or monolayered. The monolayered structures are micelles which have been discussed earlier while the bilayer structures are liposomes (refer to Figure 4) [19]. Liposomes are bilayered structures because the phospholipids tend to adopt a conformation where their hydrophobic fatty acid tails are shielded from water. For this reason, liposomes are structured in such a way that both outer surfaces are comprised of the hydrophilic head groups, whereas the hydrophobic tails are directed opposite to each other forming the inner part of the structure [20, 21].

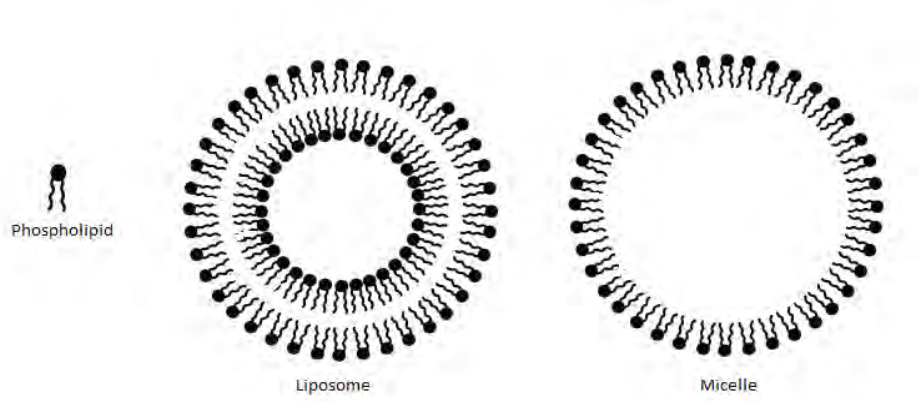

Figure 4: Structure of liposome and micelle.

3.2.2.4.1. Classification of liposomes. Liposomes can be classified on the basis of structure, the method of preparation and composition. With respect to structural parameters liposomes can be categorized as unilamellar, small unilamellar, medium unilamellar, large unilamellar, giant unilamellar, oligolamellar, multilamellar, and multi-vesicular vesicles. Figure 6 below details the size range of each category of liposomes [19, 22].

On the basis of composition liposomes can be classified into: conventional, fusogenic, pH-sensitive, cationic, long circulatory, and immune-liposomes. The next

section presents a more detailed discussion of the grouping of liposomes according to the method of preparation.

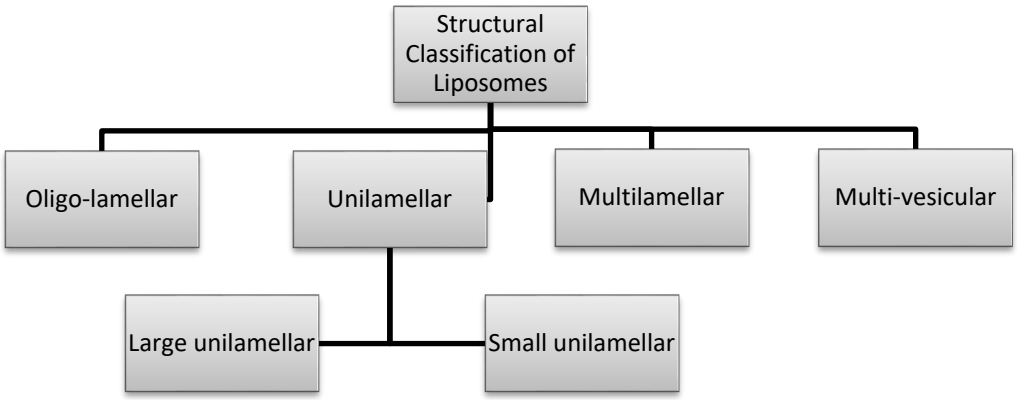

Figure 5: Structural categorization of liposomes.

3.2.2.4.2. Methods of liposomal preparation. The choice of liposomal preparation method relies on several factors such as the physicochemical properties of the liposomal ingredients and the material to be encapsulated, the nature of the medium in which the lipids will be dispersed, as well as the concentration of the entrapped substance and its potential toxicity. All methods of preparing liposomes involve the four following steps [23]:

1. Drying down the lipids from an organic solvent.
2. Dispersing the lipids in an aqueous medium.
3. Purifying the resultant liposomes.
4. Analyzing the final product.

The entrapped agents can be loaded into the liposomes either before or during the formulation process (passive loading); certain compounds, which display both water and lipid solubility, can be introduced into the liposomes after the formation of the vesicles (remote or active loading). Consequently, the techniques for preparing liposomes are divided into passive and active loading methods (refer to Figure 6).

3.2.2.4.3. Liposome surface functionalization. Liposomes with long-circulating properties have garnered considerable attention in biomedical fields particularly in applications such as blood pool imaging and targeted drug delivery. Applications necessitating increased circulation-time primarily require liposomes to evade detection by the reticuloendothelial system (RES) and clearance by the organs

of the mononuclear phagocyte system (MPS). This desired invisibility can be constituted onto liposomes by decorating their surfaces with stealth-imparting polymeric substances that suppress ‘tagging’ by plasma proteins (opsonization) and subsequent uptake by macrophages. Such liposomes are referred to as stealth liposomes [24]. Surface enrichment of liposomes with polymeric substances can be performed in one of three ways [25]:

1. Physical adsorption of the polymer onto the surface of the liposomes.
2. Incorporation during liposome preparation.
3. Covalent attachment of the reactive groups onto the surface of pre-formed liposomes.

Other than developing macrophage-resistant properties, grafting liposomes with polymeric substances enhances their surface stability. The presence of such surfactants greatly reduces the attractive Van der Waals forces between approaching particles. Elastic and osmotic factors play a role in increasing the repulsive barrier between the liposomes. The elastic contribution results from a loss of conformational freedom of the polymer chains, as the available volume for each polymer group is reduced the particles are forcedly separated. On the other hand, the osmotic pressure contribution arises from an increase in polymer density on the liposomal surface necessitating an influx of water to the region, forcing the particles apart [26].

Several natural and synthetic materials have been investigated to be used in developing stealth liposomes; dextrans, pullulan and gangliosides were amongst such materials. Of these, gangliosides garnered the most attention. Gangliosides are sialic acid-containing glycosphingolipids which are present and concentrated on cell surfaces. The role played by gangliosides in prolonged circulation of erythrocytes led to the application of their derivatives in the modification of liposomes. Monosialotetrahexosylganglioside, GM1 for short, is one such derivative of the ganglioside series that has been used as a surface modifier to increase the circulation time of liposomes. Research into GM1 modified liposomes has shown that the bulky, neutral hydrophilic sugar moiety of GM1 can conceal liposomes by creating a steric surface barrier that reduces charge-based interactions with opsonizing proteins. Despite its early successes, the high cost of sialic acid instigated investigations into other materials [24, 27].

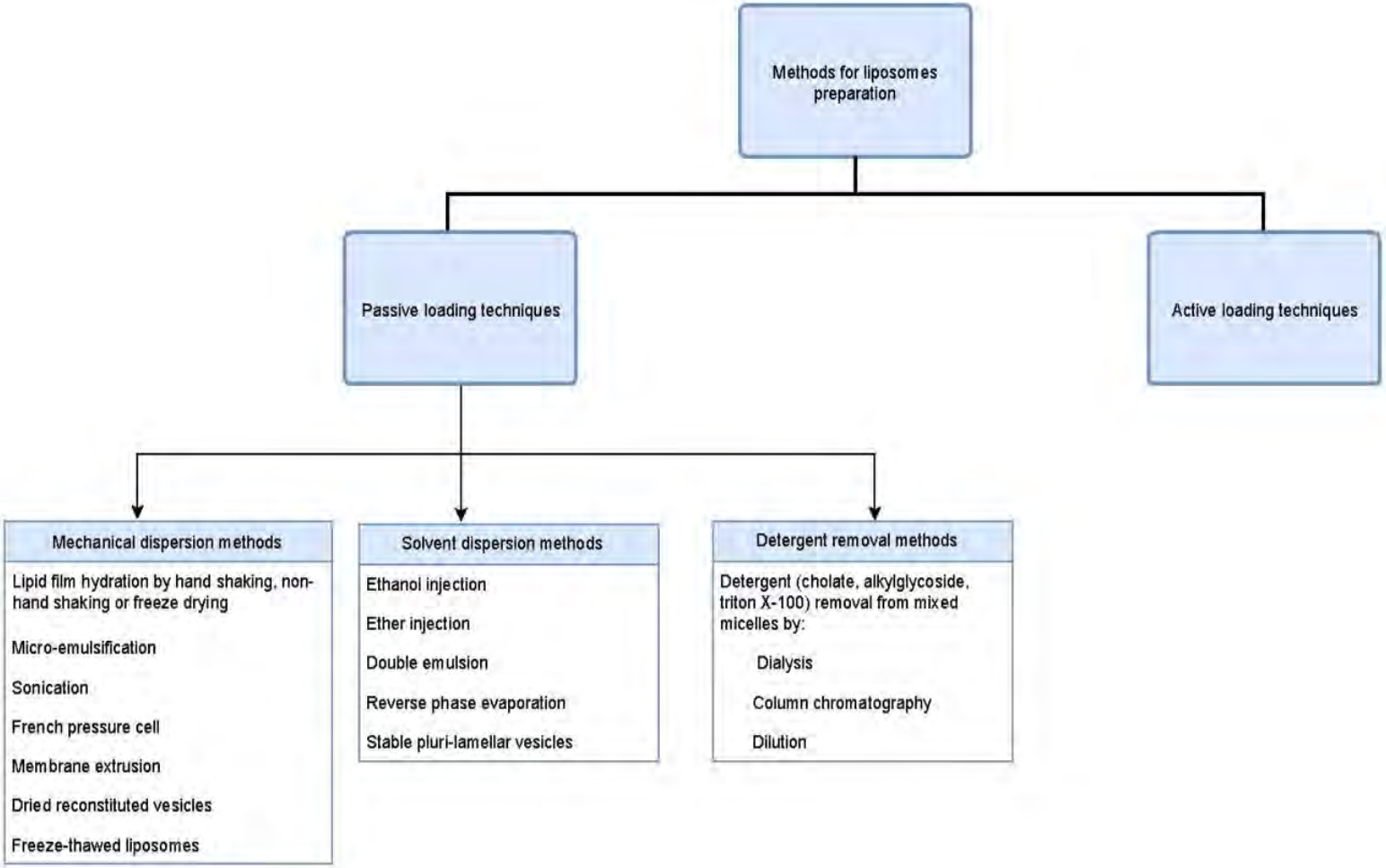

Figure 6: Different methods for liposomes preparation.

3.2.2.4.4. Poly-Ethylene Glycol (PEG)-Linked-Liposomes. PEGylated lipopolymers have brought about the most significant breakthrough in the development of stealth technologies. The presence of PEG on the surface on nanocarriers extends their blood circulation time while reducing their uptake by the RES, improving the distribution of the carriers in perfused tissues. The presence of PEG also helps reduce vesicle aggregation, thus enhancing the stability of the formulations[27]. PEG is a synthetic, linear polyether diol that exhibits high biocompatibility, low immunogenicity, ease of synthesis, high flexibility and aqueous/organic solubility. The fact that PEG is soluble in organic media facilitates the synthesis of PEGylated lipids and the formulation of stealth liposomes as the components need to be solubilized in an organic solvent. The PEG segment may be synthesized with molecular weights varying between 400 to 50,000 Da [28]. The molecular weight, along with the grafting density is essential in determining the conformation of PEG and the steric suppression of opsonization. Brush-like PEG conformations dominate at high PEG grafting density, whereas the mushroom conformation is more common at low grafting densities. Figure 7 depicts both PEG configurations.

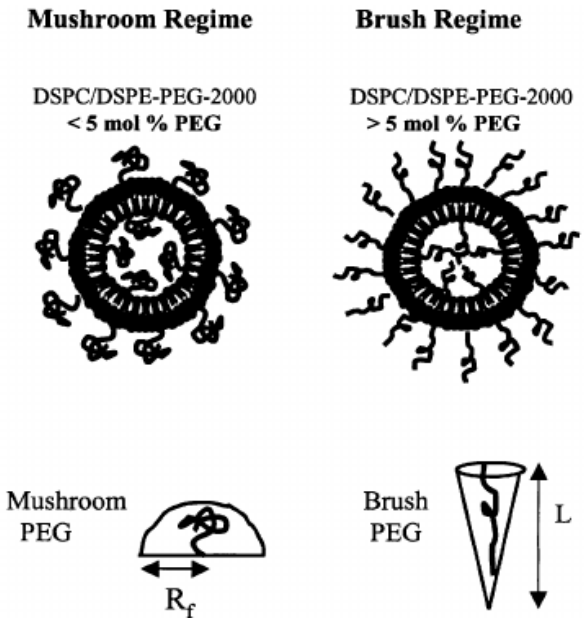

Figure 7: PEGylated liposomes [28].

PEG-based lipopolymers consist of a PEG segment of variable length or configuration attached to the lipid (acyl) moiety through a linker, e.g. phosphate ester,

carboxylate ester, amide or another linkage. The acyl group is a determining factor of the physical state of the lipid assemblies, that is lamellar or micellar and controls the extent of PEG lipopolymers' inclusion into the liposomal membrane. In addition, the choice of linker groups directly influences the behavior of the modified liposomes, for instance ester linkages are highly susceptible to decomposition in biological media whereas phosphate linkers may incite opsonization [24, 29].

3.2.2.4.5. Functionalization of liposomal surface using targeting ligands. Earlier on, active targeting was introduced as the direct targeting of payloads at requisite sites via ligand-receptor interactions. In this connection, liposomes can be engineered to enhance cellular uptake and drug accumulation at the intended site through suitable surface functionalization. Actively targeted liposomal systems are generated by grafting moieties such as monoclonal antibodies and their engineered fragments, peptides, aptamers or small ligand molecules onto the surface of the liposomes. The ligand can be either incorporated directly to the lipids or attached to the distal end of the polymeric coating, i.e. PEG, based on three types of reactions: (1) formation of an amide bond between the carboxyl and amino groups (2) the formation of a disulfide bond through the reaction of pyridylithiols and thiol groups (3) or through thioester bonds formed due to the reaction of maleimide (MAL) and thiol groups. To ensure efficient targeting, it is necessary to optimize the ligand density on the liposomal surface, issues such as aggregation may occur if the optimal amount of linked moieties is exceeded. The choice of targeting ligand depends on several parameters, the most important of which include: binding affinity, size, immunogenicity, clinical application and cost. The ligand should be exclusive to the target cell and be characterized by high binding affinity and low immunogenicity. Table 2 presents some common moieties used as targeting ligands with respect to the aforementioned parameters [30–33].

3.2.2.4.6. Targeting of over-expressed cancer cell surface receptors. Specific cell surface receptors are over-expressed in cancer cells as compared to healthy cells. Ligand-coupled liposomes will recognize and subsequently bind to the cell surface receptors through ligand-receptor interactions. The formed ligand-liposome-receptor complex is then internalized through receptor-mediated endocytosis, hence facilitating site-specific drug delivery. Active targeting via cell surface receptors has been widely

investigated in cancer therapy. Some of the most popular cell surface tumor-specific receptors studied in this regard include: epidermal growth factor receptors (EGFR), fibroblast growth factor receptors (FGFR), folate receptors (FR) and transferrin receptors (TfR) [30, 32].

3.2.2.4.6.1. Targeting of folate receptors (FR). Folates are low molecular-weight vitamins needed by eukaryotic cells for one-carbon metabolism and *de novo* nucleotide synthesis. There are two mechanisms by which cellular uptake of folic acid (FA) can take place: reduced folate carrier (RFC) and folate receptor (FR). RFC involves a membrane carrier protein that transports folate across the plasma membrane and into the cytosol. RFC is ubiquitously distributed and aids the uptake of dietary folate, whereas FR is upregulated mainly on activated macrophages and cancer cells, including a wide range of solid and hematological malignancies, e.g., ovarian, lung, renal and breast cancers. The overexpression of FR on macrophages can be used to treat inflammatory disorders such as psoriasis, rheumatoid arthritis and atherosclerosis [30, 33, 34]. Delivery of imaging, diagnostic and therapeutic agents using folate-linked liposomes has proven to be superior to non-targeted liposomes, however, research has shown that the direct attachment of folate to the lipid does not allow for efficient binding to cells expressing FR. By contrast, liposomes with folate attached to their surface using a PEG spacer arm are taken up by cancer cells efficiently [31].

Several folate-conjugated liposomal systems have been reported for the delivery of therapeutic agents to tumor cells overexpressing FR. The experiments conducted by Gabizon *et al*. showed that folate-conjugated liposomes bind to the FR of J6456 lymphoma cells *in-vivo* and play a vital role in liposome biodistribution in solid tumors [33]. In addition, Low *et al*. explored the activity of doxorubicin-loaded PEGylated liposomes by testing their toxicity against tumor cells overexpressing FR. The targeted liposomes demonstrated 45-times higher uptake than non-targeted liposomes. Doxorubicin-mediated cytotoxicity was 85-times higher in targeted liposomes compared with conventional liposomes [31].

3.2.2.4.6.2. Targeting of transferrin receptors (TfR). Transferrin (Tf), the moiety of choice in this research, is a double-lobed serum glycoprotein, with a molecular weight of approximately 80 kDa, secreted by the liver. The main function

of Tf is to regulate the cellular uptake, transport and utilization of iron from ingested food [31]. Iron is necessary for a number of highly complex processes in the body including: the conversion of blood sugar to metabolic energy, production of enzymes, hematopoiesis (production of blood cells), in addition to oxygen transport to body cells and tissues as iron is a component of hemoglobin (a metalloprotein in red blood cells responsible for oxygen transport) [35]. Our bodies do not produce iron; therefore the iron needed to maintain bodily functions is obtained through diet. As mentioned earlier, it is the responsibility of Tf to translocate iron into cells via Tf/Tf receptor (TfR)-mediated endocytosis. Iron free or apo-Tf can bind to two iron molecules forming diferric or holo-Tf. The resultant holo-Tf binds to TfRs with greater affinity than apo-Tf. Next, the Tf-TfR complex is endocytosed into the endosome, where the acidic environment (pH~5.5) prompts conformational changes of the Tf-TfR complex and the ensuing release of Tf. Finally, the Tf-TfR complex is recycled to the cell surface where the return to physiological pH (pH~7.4) will dissociate the complex and release Tf for re-use (refer to Figure 8) [36]. Table 2 presents a summary of some moieties commonly used as targeting ligands.

A defining characteristic of cancer cells is their rapid rate of proliferation. This phenomenon entails that cancer cells have a higher iron demand than their healthy counterparts (for DNA synthesis and iron-mediated regulation of molecules that control cell cycle progression). The high intrinsic demand for iron is in turn linked with the overexpression of TfR on cancer cells. The Transferrin receptor family includes TfR1 (also known as CD71) and TfR2 (also known as CD77); analyses of malignant cells from various tissue origins revealed that TfRs are overexpressed in hematopoietic malignancies and several solid tumors such as: breast, liver, ovarian and prostate cancers [52–54]. The overexpression of the Tf receptor on malignant cells, its ability to internalize, and the necessity of iron for cancer cell proliferation all make transferrin receptors a highly appealing route for the delivery of drugs into malignant cells and thus, an attractive target for cancer therapy. Targeting of TfR can occur through a variety of methods that utilize either its natural ligand Tf, monoclonal antibodies or their fragments. Short peptides have also been used as targeting moieties.

Table 2: Summary of moieties used as targeting ligands.

Ligand	Target Cell-line	Size kDa	Immunogenicity	Clinical Status	References
Antibody fragments					
Fab	e.g. NCA-90 (granolucyte), CEA (apical surface of gastrointestinal epithelium, lung tissues, breast, and colorectal cancer), VEGF (breast, colon, lung, gastric, renal, and oropharyngeal cancers), HER2 (breast, ovarian, stomach cancer)	50	Lower than mAb	Approved by FDA	[34–38]
scFv	e.g. CEA, HER2	30	Lower than mAb	Preclinical trials	
Monoclonal antibodies (mAb)					
Rituximab	CD20 (pre-B and B-cell)	145	Low	In clinical use	[37, 39-42]
Trastuzumab	HER2	145	Very Low		
Bevacizumab	VEGF	145	Very Low		

Ligand	Target Cell-line	Size (kDa)	Immunogenicity	Clinical Status	References
Proteins and peptides RGD	Integrins $\alpha_v\beta_3$ and $\alpha_v\beta_5$ (overexpressed on tumor endothelium)	1-5	High	Clinical trials	[43, 44]
Other targeting molecules Folates	Folate receptors: RFC (all cells) and FR (ovarian, brain, head and neck, renal, and breast cancers).	0.44	Low	Yes	[45–49]
Transferrin	CD71	80	Low	Not in clinical use	

Abbreviations: Av, average; CEA, carcino-embryonic antigen; CLR, C-type lectin receptor; DC-SIGN, dendritic cell-specific intercellular adhesion molecule-3-grabbing non-integrin; FR, folate receptor; Fab, antigen-binding fragments; RFC, reduced folic carrier; mAbs, monoclonal antibodies; scFV, single chain variable fragments; VEGF, vascular endothelial growth factor.

Tf conjugates are capable of interacting with both TfR1 and TfR2 (which are highly expressed in the liver) therefore they may be particularly toxic in certain cases to liver cells [38]. Of the three methods available for targeting of TfR this research focuses on the approach that uses the natural Tf ligand.

The literature on the use of TfR as a target for the delivery of diagnostic and therapeutic agents to malignant cells continues to grow. A broad repertoire of therapeutic agents have been explored for TfR-targeted cancer therapy, this includes chemotherapeutic drugs, bacterial toxins, plant toxins, DNA, oligonucleotides (ODN), short inhibitory RNA (siRNA), and enzymes [38, 55]. For instance, Li *et al*. used TfR-targeted stealth liposomes loaded with doxorubicin to demonstrate that TfR-targeted dox-liposomes enhanced intracellular uptake of doxorubicin and led to improved therapeutic efficacy against liver cancer. The work of Zhai *et al*. showed that Tf-coupled liposomes were an efficient delivery system for the chemotherapeutic agent docetaxel (commonly used in the treatment of breast, colon, ovarian, head, neck and lung cancer). *In-vitro* studies indicated a 3.6-fold increase in the cytotoxicity of TfR-targeted liposomes when compared to conventional liposomes loaded with docetaxel [31].

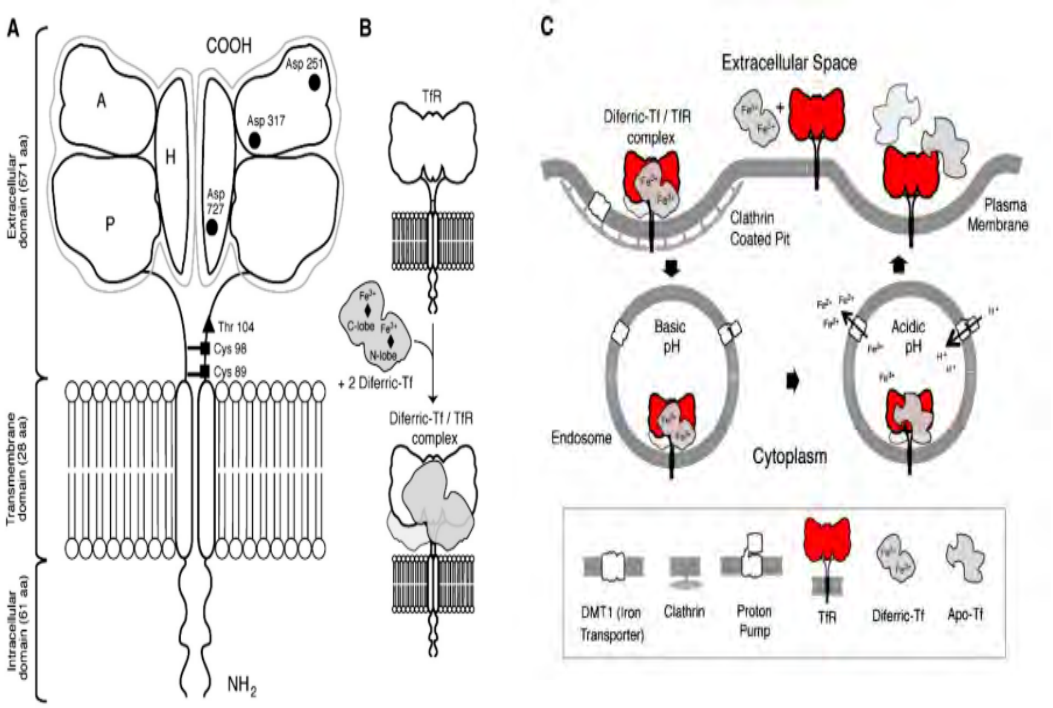

Figure 8: (A) Schematic diagram of Tf and (B) binding of iron to Tf whereas (C) displays Tf/Tf receptor-mediated endocytosis [38].

3.2.2.4.7. Targeting of tumor microenvironment. Another approach to diminish cancer cell growth is to target overexpressed receptors in the tumor microenvironment. It was mentioned earlier that tumors are able to drive neighboring healthy cells into angiogenesis (formation of new blood vessels). Targeting the tumor microenvironment/vasculature would cut off the oxygen and nutrient supply to the tumor which in turn would diminish or inhibit the growth and metastasis of the tumor, the added advantage of this method is that tumor vasculature is not specific for any type of cancer. Similar to cancer cells, the tumor microenvironment overexpresses a number of receptors that can be used for site-requisite delivery of anticancer agents. Examples of such targets include vascular endothelial growth factor receptors (VEGFR), vascular cell-adhesion molecule (VCAM), matrix-metalloproteases (MMPs) and integrins [30, 31].

3.3. Stimuli-responsive Liposomes

The use of pathological changes in the tumor microenvironment has been extensively researched as an approach to enhance liposomal release kinetics at targeted anatomical sites. The tumor microenvironment has certain defining characteristics that can be exploited in the concept of stimuli-responsive liposomes, including lower pH, higher temperature and upregulation of certain proteolytic enzymes. These stimuli-sensitive liposomes are designed in such a way that they retain their structure and physical properties while circulating through the body, but upon exposure to a particular stimulus, they destabilize and release the entrapped material. The stimulus could be endogenous, such as a drop in pH, change in temperature or presence of certain enzymes, or it could be an exogenous [30, 31]. The following are the main stimuli being investigated for enhanced delivery of anticancer agents at targeted sites using liposomes.

3.3.1. Temperature responsive liposomes. Inflamed pathological sites and tumors are characterized by higher temperatures compared to normal tissues. The difference in temperature between the tumor site and normal tissues can act as an internal trigger for functionalized drug carriers. Another temperature-responsive strategy utilizes the fact that hyperthermia is associated with increased tumor permeability to enhance drug uptake. In this technique, the temperature of the tumor site is manipulated externally in such a way to incite increased blood flow and

vascular pore size in the area, which in turn results in improved internalization of the drug-loaded liposomes. In general, thermo-sensitive nanocarriers are designed to retain their payloads around the physiological temperature of 37°C, and release their payloads rapidly when the temperature is increased above 40-45°C. Temperature-sensitive liposomes are usually prepared using thermo-sensitive lipids or polymers with a low critical solution temperature (the temperature below which the components of a mixture are miscible for all compositions). The most commonly used thermo-sensitive lipid is dipalmitoylphosphatidylcholine (DPPC), and its polymeric equivalent poly N-isopropylacrylamide (PNIPAM). The commercial anticancer liposomal formulation Thermodox® (Celsion, Lawrenceville, NJ, USA) is an example of temperature-sensitive liposomes. This formulation is in Phase III clinical trials for the treatment of hepatocellular carcinoma and Phase II trials for breast cancer and colorectal liver metastases [6, 30, 31, 56].

3.3.2. pH responsive liposomes. It is well known that different anatomical sites in the body have different pH values, e.g., the stomach has a pH≈2 while the lungs have a pH≈7.3. Similarly, a significant pH gradient exists between healthy and cancerous body tissues. The standard extracellular physiological pH in healthy body tissues and blood is around 7.4, however, in tumors the extracellular pH values are usually below 7 [6, 56]. This phenomenon can be explained by the Warburg effect. This widely accepted theory states that cancer cells favor the anaerobic glycolytic pathway, even in the presence of sufficient oxygen, rather than oxidative phosphorylation for cellular energy generation. A side effect of opting for the glycolytic path is the generation of lactic acid, ergo the acidic nature of tumor microenvironments [57]. This pH difference between neoplastic and normal tissues has stimulated researchers to develop pH-responsive liposomes for anticancer therapeutics. These liposomes are stable at physiological pH but the alteration of pH at tumor sites causes an instability in the lipid bilayer resulting in the liposomes releasing their contents [30, 31].

3.3.3. Redox responsive liposomes. Redox responsive liposomes have gained great attention in cancer and gene therapy research. In biological systems different redox conditions exist between intracellular and extracellular compartments. Redox-responsive polymers contain reducible disulfide bonds which remain intact

while the drug carrier is circulating in the oxidizing extracellular environment but are readily cleaved when the carrier is introduced into the intracellular reducing environment, triggering the cytosolic release of the drugs [58]. This reducibility of disulfide bonds can be exploited to design redox sensitive liposomes for intracellular delivery of drugs or functional genes in targeted tumors and other tissues. A good example of such a system are liposomes responsive to the levels of Glutathione (GSH), GSH is a reducing agent abundant in cells particularly the cytosol and the nucleus. The intracellular levels of GSH are tremendously higher than those in the extracellular environment. Similarly, the concentration of GSH in tumor tissues and the cytosol of tumor cells is at least four times higher than that in normal tissues, making tumors a reducing environment. This high redox potential difference can break the reducible disulfide bonds, destabilize the liposomal system and release its payload [31, 56].

3.3.4. Light-responsive liposomes. The use of light irradiation for the activation/deactivation of biochemical processes has long been recognized as the most valuable tool in the biomedical field. Light irradiation has been used extensively in biomedical research because it is non-invasive and its parameters, e.g., intensity, wavelength and exposure duration, can be readily manipulated. Visible light, ultraviolet (UV) and near- infrared (NIR) light have the most clinical applications, however light in the NIR region is the most desirable form of light for tumor targeting since it penetrates deep into the tissues and is less damaging to the biological system than UV light. For the above mentioned reasons photodynamic therapy has become a well-established treatment tool of superficial tumors where photosensitizing agents, such as chlorins, which generate radical oxygen species are used to eradicate malignant tumors. Various light-sensitive lipids/polymers are being used in drug delivery applications. Whether the liposomes are made out of lipids or polymeric materials, to be light-responsive they must contain a chromophore in their architecture. Chromophores are moieties which undergo structural and conformational changes, e.g., photoisomerization, photodimerization or photocleavage, upon exposure to light, with subsequent disruption of the liposome and release of the drug [31, 56, 58].

3.3.5. Ultrasound responsive liposomes. Ultrasonics is a branch of acoustics that focuses on vibratory waves of frequencies higher than the audible range, i.e., greater than 20 kHz. Ultrasonics became an independent field of study during World War I when technologies using ultrasound waves were being developed to detect enemy vessels. Ultrasound (US) waves are mechanical sound waves requiring a medium to transfer their energy from one location to another. In fact within a single phase, be it gas, liquid or solid, the sound wave velocity *c* is dependent upon the medium's elasticity *K* and density ρ, as is shown by equation (1) below [59].

$$\boldsymbol{c} = \sqrt{\frac{\boldsymbol{\kappa}}{\boldsymbol{\rho}}} \tag{1}$$

In most applications, US waves are generated by a transducer containing a piezoelectric crystal. Piezoelectric crystals convert electrical energy (electric current) to mechanical energy (sound waves) and vice versa. When an electrical pulse is applied to the crystal it vibrates, and as it vibrates it pushes and pulls the air surrounding it, producing an ultrasound wave. In turn, when ultrasound waves strike an object and are reflected back to the transducer as echoes, the crystal converts this mechanical pulse to an electrical signal. Alternatively, US waves can be generated using magnetism instead of electricity a phenomenon known as magnetostriction. In this case, a magnetostrictive crystal changes its dimensions in response to magnetism thereby producing ultrasonic waves. Moreover, US may be produced using a whistle or siren-type generator. In this method, gas or liquid streams are passed through a resonant cavity causing ultrasonic vibrations characteristic of the particular gas or liquid [60, 61].

US in medical applications can be divided into either low-or high-intensity. Low intensity US is generally used in diagnostic applications meant to obtain information about the state of tissues and organs, e.g., imaging. The US energy deposition, in this case, is intended to be minimal as not to produce any biological effects. On the other hand, high-intensity US is aimed at manipulating matter and therefore finds more usage in therapeutic purposes where the deposited energy is intended to create a biological effect, be it mild such as healing in physical therapy or more extreme and destructive, such as ablation of tumors [59, 62].

In therapeutic applications, the biological effects of US on tissues and cells can be either thermal or mechanical. The three primary mechanisms by which US waves induce these bio-effects are: thermal, cavitational and acoustic streaming. Krasovitski *et al*. [55] proposed an additional, non-thermal, non-cavitational interaction mode called the bilayer sonophore effect.

3.3.5.1. Thermal effect. The thermal effect of US is primarily an increase in the medium's temperature due to the absorption of energy from US waves. The rate of heat generated by US waves is directly proportional to the frequency of the waves and exposure time, and is inversely proportional to the specific absorption coefficient of the targeted tissue. Consequently, the higher is the medium's absorption coefficient, the more signigicant the increase in temperature and in turn the thermal effect experienced by the tissue [55, 62].

3.3.5.2. Cavitational effect. Acoustic cavitation can be best defined as the formation, growth, oscillation and collapse of gas-filled cavities, i.e., bubbles, in a fluid medium due to induced pressure changes. The sources of the gas bubbles or cavitation nuclei are usually pre-existing bubbles that were present in the fluid, or bubbles that were formed when the pressure was reduced below the vapor pressure of the liquid. The pressure change caused by the passage of an ultrasound wave through the insonated medium leads to the formation of such bubbles, an event termed as the cavitational effect. There are two main types of acoustic cavitation: stable and inertial (transient) cavitation. In stable cavitation, the bubble's radius varies about an equilibrium value. In contrast, inertial cavitation bubbles grow rapidly, expanding to twofold or threefold their resonant size (limiting value), and then collapse violently (refer to Figure 9) [63]. The growth of cavitating bubbles in an ultrasound field is aided by a process called rectified diffusion, where the net amount of gas diffusing into a bubble during its expansion is greater than that diffusing out of it during its contractile stage. During inertial cavitation, the collapse of bubbles produces momentary surges in local temperature and pressure. The vicinity of these cavitation spots has been shown to reach temperatures of 5000 K and pressures of 1000 atm. In addition, the bubble collapse creates shock waves that propagate and cause structural shifts in the surrounding tissues by micro-jets. Although it has been proposed that stable cavitation bubbles can stimulate damage to biological tissues, it is widely

accepted that the primary mechanism for structural alteration of cells is transient cavitation [59, 62, 64].

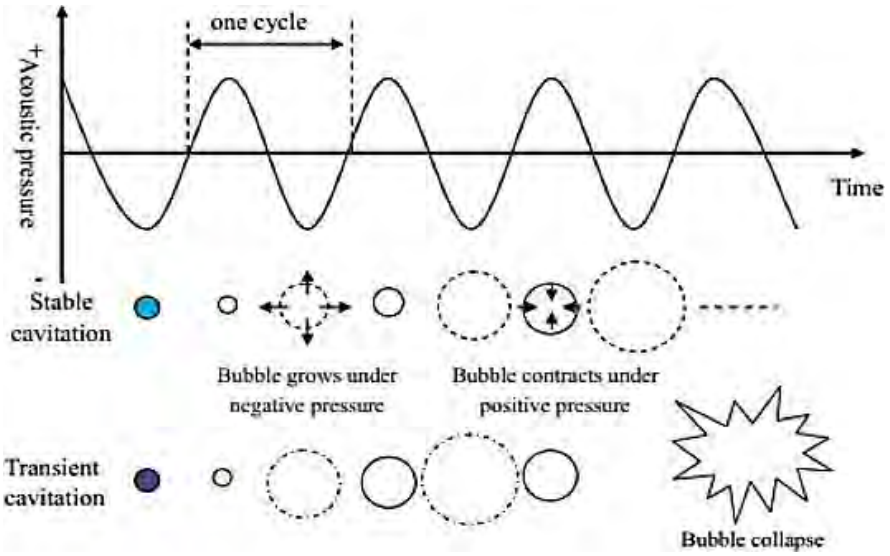

Figure 9: Stable and transient cavitation [48].

The most critical factors that determine whether cavitation will occur or not are [55, 59, 62]:

- Ultrasound intensity: cavitation does not happen at all intensities; for a particular bubble size there is a threshold intensity beyond which transient cavitation occurs. The threshold intensity tends to increase with increasing US frequency, ambient pressure, medium viscosity and ion concentration. In contrast, the threshold intensity decreases with elevated medium temperatures and gas content. Therefore, transient cavitation is more frequent at low frequencies. Apfel and Holland introduced a Mechanical Index (MI) that can act as an indicator of the possibility of occurrence of transient cavitation in an insonated medium. The MI is mathematically defined according to equation (2) [59]:

$$\boldsymbol{MI} = \frac{\boldsymbol{P_{neg}}}{\boldsymbol{f^{0.5}}} \qquad (2)$$

Where P_{neg} is the maximal negative pressure, in MPa, and f is the frequency in MHz. When MI > 0.7 there is a high possibility that transient cavitation will occur. Apfel and Holland also showed that for ultrasonic frequencies below 1 MHz an acoustic pressure threshold of around 0.2 MPa is sufficient to initiate transient cavitation in aqueous solutions and in blood.

- The number and availability of cavitation nuclei: the likelihood of cavitation occurrence tends to increase with an increased number of nuclei available, which are common in non-degassed water, but are rare in animal tissues.
- The availability of physical space for bubbles to form and grow. Intact cells and extra-cellular matrices do not have the dimensions and preexisting nuclei to support cavitation. On the other hand, blood vessels possess both the dimensions and cavitation nuclei needed for initiation of cavitation when a high enough ultrasound pressure fields exists.

3.3.5.3. Acoustic streaming effects. When US waves with high amplitudes are used to insonate a medium, a transfer of momentum from the US wave to the medium may lead to the generation of unidirectional flow currents in the fluid, this phenomenon is known as acoustic streaming. The velocity of the stream is directly proportional to the attenuation coefficient of the medium, the ultrasound intensity, and the surface area of the transducer and is inversely proportional to the speed of sound in the medium in question and the bulk viscosity. The main cause of acoustic streaming is US reflection and other distortions that take place during wave propagation. So far, the clinical value of acoustic streaming has only been minimally explored [55, 59, 62].

3.3.5.4. Bilayer sonophore effect. This model is based on the direct effect US waves have on bilayer membranes. The ultrasonic pressure wave fluctuates between positive (compression) and negative (rarefaction) values. At the negative pressure stage, the space between the membrane bilayers tends to increase while at the positive pressure phase the spacing decreases. As a result, the continuity of the membrane is briefly interrupted, and fenestrations through which substances can be transported across the plasma membrane are created. The authors of this theory intended for the bilayer sonophore effect to be an explanation of the non-thermal effects of US at intensities below the threshold intensity [55].

Ultrasound-guided drug delivery is a promising approach to treat certain types of cancer because the technology is noninvasive, readily available, relatively inexpensive and permits spatially confined delivery of drugs to targeted areas with a high degree of precision while minimizing adverse effects. The ultrasound-responsive liposomal system can be designed to respond to the thermal, mechanical or a

combination of both effects of US [65]. Before detailing the uses of US as an external trigger for drug release, it is worthy of mentioning the role US plays in the processes involved in the formation of liposomes that will act as drug delivery vehicles. In the early 1960s Saunders *et al.* [45] discovered that exposing aqueous lecithin dispersions to US resulted in the formation of what was then believed to be "lecithin micelles". At that time the discovery had not been made yet that these micellar structures were in fact, unilamellar vesicles with an aqueous inner core. Later on, Papahadjopoulos *et al.* [45] showed that phospholipid suspensions exposed to low-frequency ultrasound (LFUS) also led to the formation of such small unilamellar vesicles (SUVs). However, it was Huang and coworkers [45] who first studied these SUVs carefully. All of these studies provided fundamental information regarding the liposomal structure and behavior, for instance, it was discovered that different phospholipid formulations exposed to similar LFUS conditions resulted in differently sized liposomes; and that for a given phospholipid formulation the longer the exposure to US irradiation and/or the higher the power density the smaller and more homogeneous the liposomes [59]. Another application of US in liposome formation is the disruption of multilamellar vesicles (MLV) to produce unilamellar vesicles (ULV). Lipid vesicles form spontaneously when phospholipids are dispersed in an aqueous solution. In the early stages of vesicle formation, the hydrated lipid sheets detach by agitation and close to form large MLVs. This formation prevents contact between water and the hydrophobic core of the bilayer. Once MLVs have formed any reduction of size requires energy. A number of methods can be employed for this step, one of which involves the disruption of MLVs using ultrasound. These approaches produce almost exclusively SUVs, and the most common instruments for the preparation of vesicles using ultrasound are bath and probe sonicators [66].

With respect to controlled drug release from liposomes using ultrasound, the disruption of the liposomal structure in this case and the subsequent release of the payload can be in response to either the elevation in temperature or mechanical effects produced by US. Conventionally, liposomes are stable in the physiological temperature range, as they are usually made up of lipids with phase transition temperatures in the range of 40-45^{o}C. When an ultrasonic beam is focused on a particular area of the body, the temperature in that region may rise beyond the transition temperatures of the lipids, interrupting the orderly packing of the lipid

bilayer and introducing free volumes into the structure which allow the drug to move freely from the liposomal core to the extra-liposomal medium [59, 62].

The mechanical effect of US-mediated drug release manifests in the form of sonoporation, where sound energy is used to enhance the permeability of plasma membranes through the creation of pores (refer to Figure 10). Both stable and transient cavitation can bring about the process of sonoporation. Stable cavitation can create pores by altering vascular permeability hence improving the delivery of the whole tissue. In contrast, inertial cavitation affects the permeability of individual cells for improved delivery of payloads at that level. Studies have found that transient cavitation can increase drug release in a more substantial manner because it induces additional mechanical effects, i.e., shockwaves and micro-jets that further enhance the effects of sonoporation. Sonoporation was first described by Fechheimer *et al*. [48], who exposed cell suspensions of live slime mold amoebae to ultrasound in the presence of fluorescein-labeled dextrans, which are normally impermeable to cells due to their size. The exposed cell samples were found to have around 40% uptake of the fluorophore, and the process was subsequently reproduced in mammalian cells for delivering DNA. Ultrasound-mediated drug delivery is considered a safe route which allows for the delivery of therapeutics without compromising the body's physiological barriers, since the cell membrane permeabilization is reversible with the membranes usually returning to their original configurations within a short period of time [56, 59, 62, 65].

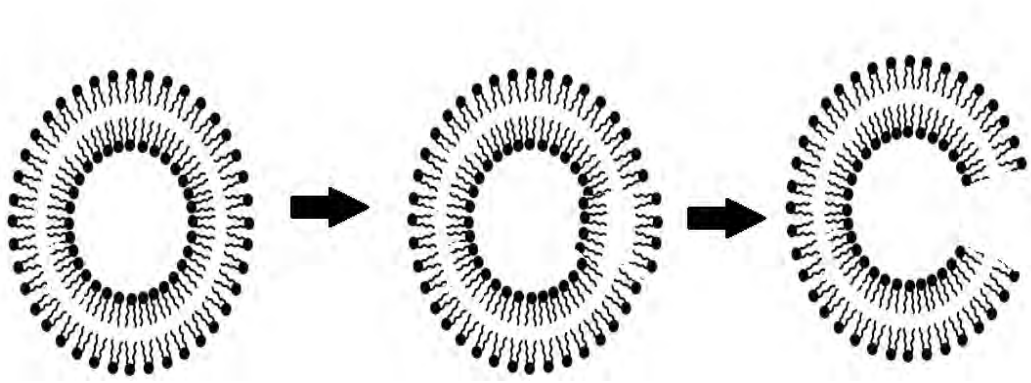

Figure 10: A schematic representation of the formation of transient pores in the liposome membrane by ultrasound.

3.4. Relevant *in-vitro* Studies

A number of different liposomal formulations encapsulating different anticancer agents have been shown to deliver the drug at the site of solid tumors with minimum toxicity when compared to the free drug. This section presents some *in-vitro* studies relevant to this research. Low and Lee [67] inspected the delivery of the anticancer drug Doxorubicin using PEGylated folate-coupled liposomes. By measuring the change in DOX fluorescence, the uptake of folate-PEG-liposomal DOX by KB human oral carcinoma cell line was found to be 1.6 times higher than free DOX and 45-times higher than that of non-targeted liposomes. Moreover, the cytotoxicity of DOX was found to be 86 times greater when delivered through the liposomal route.

Another research study by Li *et al.* [68] investigated the site-specific delivery of anti-cancer drugs and therapeutics using doxorubicin-loaded- transferrin-conjugated stealth liposomes (Tf-SL-DOX). The *in-vitro* anticancer effects of the drug-loaded liposomes (cytotoxicity) were evaluated using human hepatoma cell line HepG2. The cells were sequentially exposed to concentrations of Free DOX, SL-DOX and Tf-SL-DOX, and flow cytometry was used to quantify the cellular uptake of DOX. The flow cytometry results revealed that the cellular DOX level for Tf-SL-DOX in HepG2 cells was higher than that of SL-DOX.

With regard to the effect of US on liposomal drug delivery, Schroeder *et al.* [69] used low-frequency (20 kHz) ultrasound to trigger the release of three different encapsulated drugs: methylprednisolone hemisuccinate, doxorubicin and cisplatin. Ultrasound exposure periods up to 180 seconds demonstrated release of approximately ~80% of drug from liposomes, independent of the drug or method of drug loading.

3.5. Relevant *in-vivo* Studies

In-vivo is a term associated with biological processes that are studied in a living organism. *In-vivo* research usually employs rats and mice and other such small mammals. Several research studies have investigated the effectiveness of anticancer drug delivery using liposomes. Other experiments evaluated the effect of coupling liposomal delivery with ultrasound. In a study conducted by Li *et al.* [68] the therapeutic effects of doxorubicin-loaded-stealth-liposomes (Tf-SL-DOX) were

investigated in tumor-bearing mice. Male ICR mice were injected with human hepatoma cells, the animals were then divided into three groups, one receiving treatment in the form of free DOX, another receiving SL-DOX while the last group received Tf-SL-DOX. The anti-tumor effects of DOX from each treatment formulation were determined by the changes in tumor volume and weight at selected time intervals. The therapeutic effects were then evaluated by measuring the suppression of tumor growth in weight. This test confirmed that the highest efficiency of drug delivery was achieved by Tf-SL-DOX liposomes as the average weight of excised tumors in mice treated with Tf-SL-DOX liposomes was 0.33 g compared to tumors weighing around 1.38 and 1.17 g excised from groups treated with free doxorubicin and SL-DOX liposomes respectively.

Mercy and Afadzi [70] performed an *in-vivo* experiment to investigate the effects of low (300kHz) and medium (1MHz) frequency ultrasound on the release of liposomal doxorubicin in tumor bearing mice. The data obtained from the *in-vivo* studies showed increased levels of released doxorubicin when the liposomal delivery was coupled with US (for both frequencies).

Presently, there are many products in the market and under clinical development for use as anti-cancer drug delivery vehicles. Doxil® or Caelyx® as it is referred to outside the United States, a PEGylated liposomal formulation encapsulating the anthracycline doxorubicin and commercialized by Johnson & Johnson, was the first liposomal product to be approved by the FDA for the treatment of Kaposi's sarcoma in AIDS patients. Recently Doxil was approved by the FDA for the treatment of breast cancer in the USA for the treatment of multiple myeloma in combination with Velcade in Europe and Canada [71]. Table 3 presents some liposomal products that are in the market or still in clinical development [72].

Table 3: Liposomal products being marketed or under clinical development

Product	Drug	Indications	Year Approved	References
Approved Products				
Doxil/Caelyx (Johnsons & Johnson)	Doxorubicin	Ovarian cancer, breast cancer	2000	[71, 73]
Myocet (Cephalon)	Doxorubicin	Breast cancer	1995 (Europe), 2007 (Canada)	
Marqibo (Talon)	Vincristine	Acute lymphoblastic leukemia	2012 (USA)	

Chapter 4. Experimental Procedures

4.1. Chemicals and Reagents

The chemical reagents used to synthesize the liposomes included: 1,2-dipalmitoyl-sn-glycero-3-phosphocholine (DPPC) and 1,2-distearoyl-*sn*-glycero-3-phosphoethanolamine-N-[amino(polyethylene glycol)-2000] (ammonium salt) (DSPE-PEG(200)-NH2) which were obtained from Avanti Polar Lipids Inc. (Alabaster, AL, USA, supplied by Labco LLC. Dubai, UAE).The cholesterol, holo-Transferrin human, and calcein disodium salt were obtained from Sigma-Aldrich Chemie GmbH (supplied by Labco LLC. Dubai, UAE). In addition, the bicinchoninic acid (BCA) kit was also obtained from Sigma-Aldrich Chemie GmbH (supplied through Labco LLC. Dubai, UAE).

As for the cell work, the HeLa cell line was obtained from the European Collection of Authenticated Cell Cultures (ECACC general cell collection, UK). The RPMI-1640 medium, Dulbecco's Phosphate Buffered Saline (DPBS), fetal bovine serum and the trypan blue solution were all obtained from Sigma-Aldrich Chemie GmbH (supplied by Labco LLC. Dubai, UAE).

4.2. Methodology

The following sections present the procedures adopted in synthesizing both control and Tf-conjugated liposomes.

4.2.1. Preparation of DSPE-PEG control liposomes. The control liposomes were prepared using: 1,2-dipalmitoyl-sn-glycero-3-phosphocholine (DPPC), 1,2-distearoyl-*sn*-glycero-3-phosphoethanolamine-N-[amino(polyethyleneglycol)-2000] (ammonium salt) (DSPE-PEG(200)-NH2) and cholesterol. The chemical structures of the aforementioned lipids are depicted in Figure 11 [64, 74].

The liposomes were prepared using a modification of Torchilin and Weissig's thin film hydration method [75] where DPPC, DSPE-PEG(2000) amine and cholesterol were taken at a molar ratio of 13:1:6 respectively and dissolved in 4 mL of chloroform in a round bottom flask. The thin lipid film was formed on the walls of the flask by slow evaporation of the organic solvent under vacuum using a rotary evaporator. During this process the rotary evaporator was maintained at a temperature

of 50°C. The formed dried lipid film was then hydrated with 2 mL of 50 mM calcein disodium salt solution whose pH was pre-adjusted to physiological pH (pH~7.4). This step was undertaken in a rotary evaporator (without vacuum) pre-heated to 60°C [76–78]. Next, the liposomal suspension was downsized using sonication and extrusion to obtain small, unilamellar vesicles. The sonication was performed for 2 minutes in a sonication bath pre-heated to 60°C; while the extrusion was performed using the Avanti ® mini-extruder assembly (Avanti Polar Lipids, Inc., Alabaster, AL, USA, supplied by Labco LLC. Dubai, UAE). The extruder stand/heating block along with the gas-tight syringes containing the liposomes were heated to around 60°C using a heating plate. The liposomes were extruded a total of 30 passes through the 0.2 µm polycarbonate membrane. Finally, any external, unencapsulated materials were removed using size exclusion chromatography. The gel filtration chromatography was performed using a single stage Sephadex ® G-100 column (Sigma Aldrich, Supplied by Labco LLC. Dubai, UAE) previously equilibrated with PBS pH 7.4 (0.5 g of G-100 in 10 mL of PBS). The turbid liposome fractions were collected in Eppendorf tubes and stored at 4°C until use. Figure 12 presents the aforementioned steps of the thin film hydration method [64, 79].

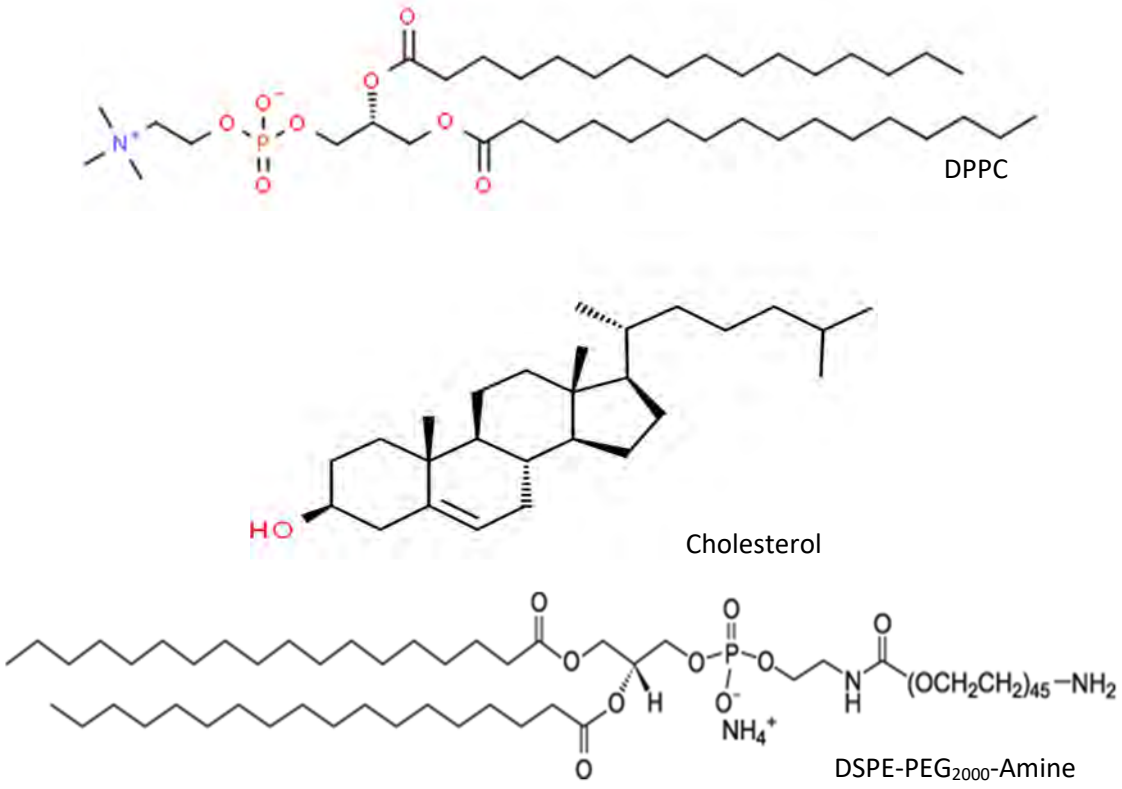

Figure 11: Chemical structures of liposomal components.

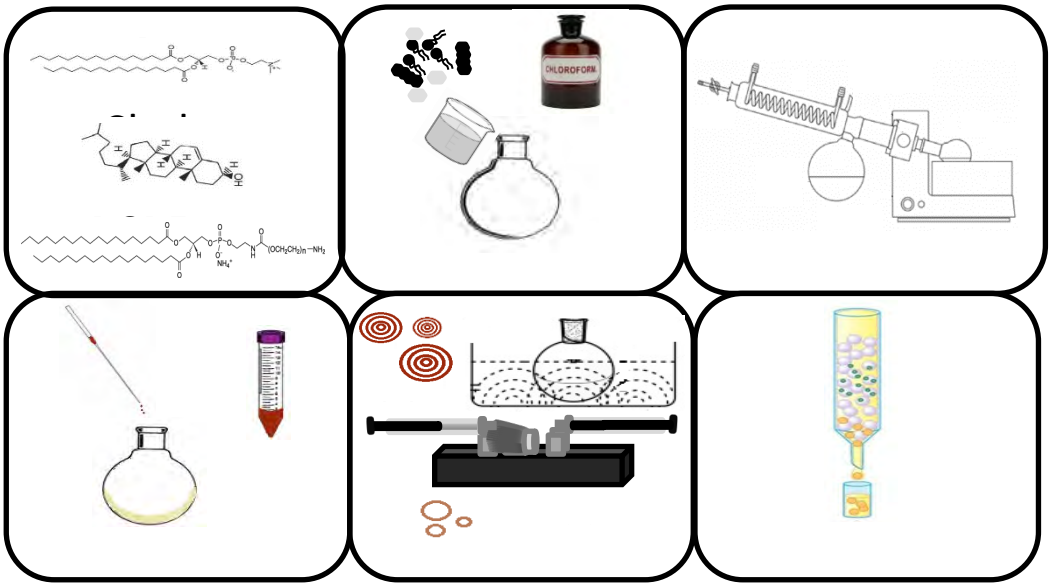

Figure 12: Preparation of liposomes using the thin film hydration method.

4.2.2. Preparation of transferrin Tf-DSPE-PEG liposomes. The liposomes to which transferrin would be conjugated were prepared according to the procedure described in the previous section, the sole difference is that in the preparation of Tf-liposomes the Sephadex for the gel filtration column is hydrated using borate buffer (pH~8.5) rather than PBS as a basic environment is required for the reaction involving cyanuric chloride to proceed. The PEGylated liposomes were then coupled to holo-transferrin human (Sigma-Aldrich Chemie GmbH (supplied through LABCO LLC. Dubai, UAE) via PEG terminus modified with cyanuric chloride. Protein-PEG conjugates are prepared by synthesizing an activated PEG with a reactive functional group that can be readily coupled with some functional group on the protein. Cyanuric chloride is a common agent that can be used to activate PEG (refer to Figure 13) [80, 81].

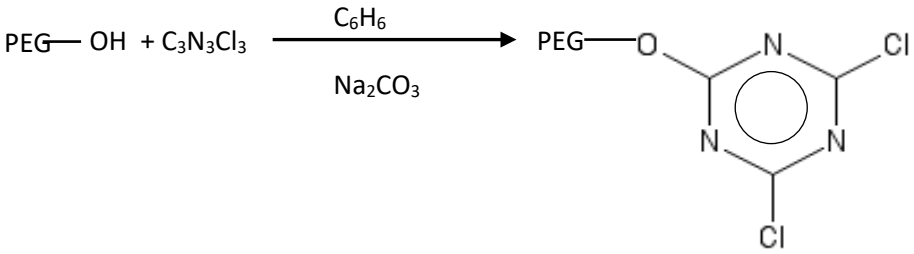

Figure 13: Cyanuric chloride activated PEG.

As for the protein, the availability of a number of accessible primary amino groups on the surface of proteins makes conjugation through this functional group quite an attractive and extensively used route, with lysine, ornithine and N-terminal amino groups being the most commonly exploited. The cyanuric chloride activated PEG is then reacted with the protein to form the desired conjugation, which in this case is that of transferrin with DSPE-PEG liposomes (refer to Figure 14) [80, 81].

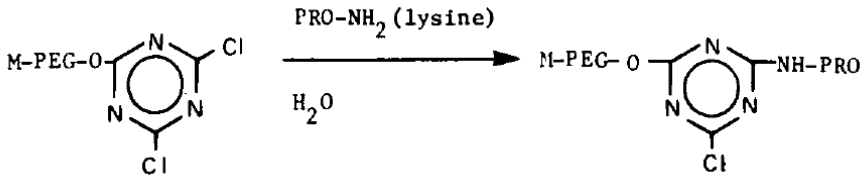

Figure 14: Preparation of PEG protein derivative [64].

In this research, to prepare the Tf-coupled liposomes, 10 mg of cyanuric chloride were dissolved in a mixture of 2.5 mL of deionized water and 500 μL of pure acetone. 55 μL of this solution were added to the liposomes which had been transferred to a glass vial containing a magnetic stirrer to ensure the uniform mixing of the solution. The vial and its contents are placed in a bath of ice where the reaction is left to take place for 3 to 4 hours. Next, 0.125 mL of a solution made out of 2 mg of transferrin dissolved in 1 mL of borate buffer was pipetted and added to the liposomes in the vial. The liposomal solution is then left to stir for 24 hours in order for the attachment to take place. After the protein attachment is performed, the Tf-conjugated liposomes are passed through a two stage G-100 PBS column (1 g of G100 Sephadex in 20 mL of PBS) to remove any free proteins and change the medium in which the liposomes are suspended.

4.2.3. Determination of liposomes size by dynamic light scattering. The size distribution of liposomal drug carriers is of key interest because size affects both the liposome's *in-vitro* and *in-vivo* characteristics. The *in-vitro* properties affected by liposomal size include encapsulation capacity, aggregation and sedimentation behavior. While the *in-vivo* behaviors affected, include circulation time in the blood-stream, biodistribution especially when targeting solid tumors and uptake by the mononuclear phagocytic system (MPS) [82]. Dynamic light scattering (DLS) also known as photon correlation spectroscopy (PCS) or quasi-elastic light scattering, is a

technique used to measure the size of particles in the sub-micron range [83]. This technique is based on the concept of Brownian motion or pedesis which states that the movement of particles suspended in a fluid, i.e., liquid or gas is random because the particles are continuously colliding with the fast moving molecules of the suspending medium. In most DLS systems a laser of known wavelength is focused through a dilute sample, and the intensity of scattered light is collected by a detector, and an algorithm-based process is then applied to resolve the instrumental data to its constituents and simplify it to determine the particle size distribution of the sample (refer to Figure 15) [84, 85].

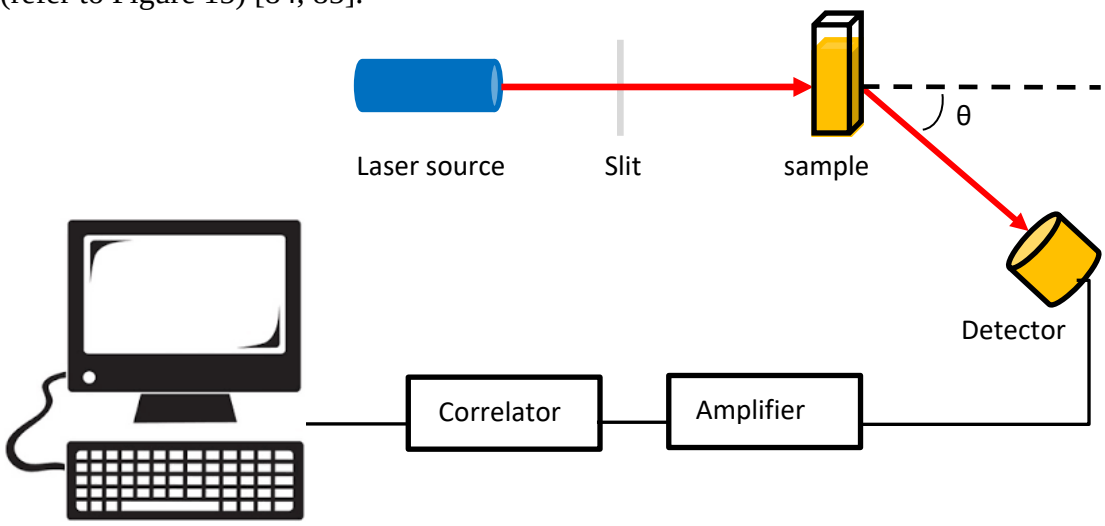

Figure 15: Block diagram for DLS arrangement.

To determine the numerical size of the particles, represented by the hydrodynamic radius D_h, it is necessary to correlate intensity to the diffusion coefficient of the particles. This is done using an autocorrelation function or ACF. This ACF examines the changes in scattered intensity over a period of time for a given volume of particles. In the case of a simple monodisperse particle size distribution (PSD), the ACF is a single decaying exponential function as shown in Figure 16 and equation (3) [86]. Here τ indicates the delay, that is, the amount that a duplicate intensity trace is shifted from the original before the averaging is performed and β is the correlation function amplitude at zero delay. A series of calculations yield the decay constant γ that is inversely proportional to the diffusivity of the particle. In equation (4), q, is a constant called the "scattering wave vector", this constant translates the time scale of the diffusion process into the distance scale set by the laser wavelength. In equations (5) and (6), θ represents the scattering angle while the index

of refraction of the solvent is given by η, the thermodynamic temperature is symbolized by T, λ represents the wavelength of the laser's light while the Boltzmann's constant is given by k_B. Once the coefficient of diffusion D_t had been determined the hydrodynamic radius can be evaluated using the Stokes-Einstein equation [84].

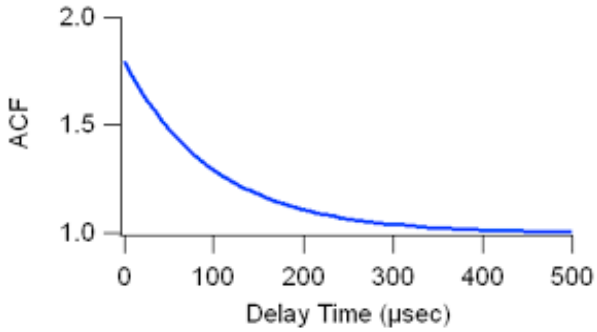

Figure 16: Exponential decay function for monodispersed size distribution [70].

$$\boldsymbol{C(\tau) = 1 + \beta e^{-2\gamma\tau}} \quad (3)$$

$$\boldsymbol{\gamma = D_t q^2} \quad (4)$$

$$\boldsymbol{q = \frac{4\pi\eta}{\lambda} \sin\left(\frac{\theta}{2}\right)} \quad (5)$$

$$\boldsymbol{D_h = \frac{k_B T}{3\pi\eta(T) D_t}} \quad (6)$$

The mean size of the liposomes was determined using the DynaPro® NanoStar™ (Wyatt Technology Corp., Santa Barbara, CA, USA). The sample to be measured was prepared by diluting15 µL of liposomes in 1 mL of Phosphate Buffered Saline (PBS).

4.2.4. Protein quantitation using bicinchoninic acid (BCA) assay. The BCA Protein Assay was introduced by Smith, *et al.*, in 1985. Since then it has become the most popular method for colorimetric detection and protein quantitation because of its ease of use, high sensitivity and tolerance of interfering species [87, 88]. This assay is based on two reactions; the first is the reduction of cupric ions Cu^{+2}, to cuprous ions Cu^{+1} by proteins in an alkaline medium, a reaction known as the biuret reaction (refer to Figure 17). The second step involves the chelation of one Cu^{+1} with two BCA reagent molecules, a highly sensitive and selective colorimetric detection reagent, forming an intense purple complex, which has a peak absorbance at 562 nm [88, 89].

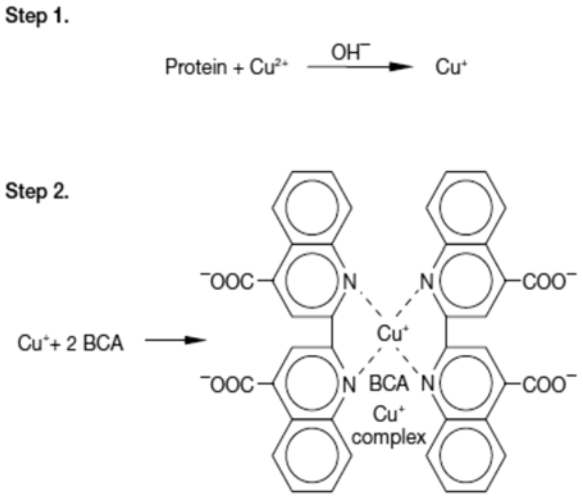

Figure 17: Reaction schematic for the BCA protein assay [73].

The procedure involved in conducting the BCA assay is as follows: first, 14 mL of the working reagent was prepared by mixing 7mL QuantiPro ™ buffer QA with 7 mL of QuantiPro ™ buffer QB as well as 0.28 mL $CuSO_4$ solution (Sigma-Aldrich Chemie GmbH (supplied through LABCO LLC. Dubai, UAE). Next, 8 samples in total were prepared including:

- 2 blank samples, consisting of PBS and the working reagent only,
- 3 samples of control liposomes with the working reagent and PBS as well as;
- 3 samples containing Tf-coupled liposomes, working reagent and PBS.

Table 4 details the volumes used to prepare the samples. It is important to note that the quantities used to conduct the BCA assay may vary according to the volume of the prepared liposomes. However, the BCA tests conducted in this research mostly followed the values indicated in Table 4. Following the preparation of the samples the microtubes containing the samples are heated in a water bath set to 60°C for 60 minutes. Following this incubation period the samples are removed from the bath and left to cool down to room temperature. Finally, the samples are transferred to cuvettes and the absorbance is measured against the blank as a reference at 562 nm using the Evolution™ 60S Ultraviolet-visible (UV-VIS) spectrophotometer (Thermo Fisher Scientific, Waltham, MA, USA).

Table 4: BCA assay sample preparation

Sample	Liposomes(µL)	PBS(µL)	BCA reagent(µL)
Blank 1	-	1000	1000
Blank 2	-	1000	1000
NH_2 1	800	200	1000
NH_2 2	400	600	1000
NH_2 3	200	800	1000
Tf 1	800	200	1000
Tf 2	400	600	1000
Tf 3	200	800	1000

4.2.5. Estimation of phospholipid content using stewart assay. The phospholipid content of liposomes can be determined calorimetrically, without the need for acid digestion or color development procedures. This is achievable using the Stewart assay which relies on the formation of a complex with ammonium ferrothiocyanate. The red inorganic compound ammonium ferrothiocyanate is insoluble in chloroform, but forms a complex with phospholipids which is soluble in chloroform. The mixing of a phospholipid containing chloroform solution with ammonium ferrothiocyanate at room temperature yields a colored complex that partitions in the chloroform phase whose maximal absorbance (A_{max}=472 nm) [90]. The procedure adopted to perform the Stewart assay is as follows: the first step requires breaking the liposomes up. Therefore the liposomes were transferred to a round bottom flask and placed in the rotary evaporator under vacuum in order to dry up the medium in which the liposomes are suspended. Next, 1 mL of chloroform was added to the flask, and this mixture was sonicated until no more particles were visible in the solution. Varying volumes of liposomes were pipetted out of the flask and transferred to centrifuge tubes. Chloroform was added to these tubes in such a way that the volume of liposomes in addition to the volume of chloroform would add up to 2 mL. Next, 2 mL of ammonium ferrothiocyanate was added to the tubes. Five such samples were created one of which is a blank containing only chloroform and the Fe solution to act as a reference, while the remaining four samples contained liposomes, chloroform and the Fe solution. The solutions in the tubes are mixed vigorously for around 20 seconds to initiate the reaction between the lipids and the Fe solution; then the samples are centrifuged for 10 minutes at 1000 rpm. A biphasic system will result after the centrifugation step; the top dark layer was removed and discarded while the

bottom clear chloroform layer was removed using a syringe and transferred to quartz cuvettes. Then, the optical density of this chloroform phase was measured using ultraviolet-visible spectroscopy at A_{max}=485 nm against chloroform as a blank. The procedure was repeated for transferrin coupled liposomes.

4.2.6. Low-Frequency ultrasound release studies (Online Experiments). The release of calcein from liposomes was triggered using 20-kHz low-frequency ultrasound (LFUS) and monitored by fluorescence changes using a QuantaMaster QM 30 Phosphorescence Spectrofluorometer (Photon Technology International, Edison NJ, USA). Calcein is a fluorescent molecule with excitation and emission wavelengths of 495-515nm respectively [91]. The sample to be tested was prepared by diluting 75 µL of liposomes in 3 mL of PBS in a fluorescence cuvette. There are 4 slits to the sample compartment which were set to 1.25 mm. The cuvette was then inserted into the designated spectrofluorometer chamber, and the 20 kHz ultrasonic probe (model VC130PB, Sonics & Materials Inc., Newtown, CT) was inserted around 2 mm into the cuvette through a specified opening. For the first 50 seconds, the initial fluorescence was recorded without sonication to generate the baseline. Then, pulsed sonication was initiated with 20 seconds *on*, 10 seconds *off* cycles for a total of 8 min. Three different machine power settings were examined at 20%, 25%, 30% which are equivalent to power densities of 7.46, 9.85, and 17.31 mW/cm^2 respectively [92]. The 20s *on* ,10s *off* cycle mentioned earlier was continued until a plateau was reached, at which point 50µL of Triton X-100 (Tx100) was added to the sample cuvette to lyse liposomes and release all the encapsulated calcein. The detailed procedure is depicted in Figure 18.

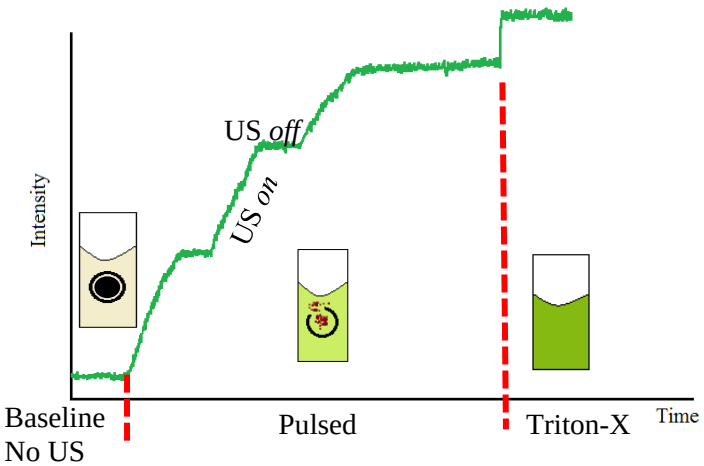

Figure 18: LFUS pulsed release.

4.2.7. High-Frequency ultrasound release studies (Offline Experiments). High-frequency release experiments (HFUS) were performed at two frequencies 1.07 MHz and 3 MHz and similar to the LFUS experiments the release of calcein from liposomes was tracked by monitoring fluorescence changes using a QuantaMaster QM 30 Phosphorescence Spectrofluorometer (Photon Technology International, Edison NJ, USA). The US waves were supplied using an ultrasonic probe immersed in a water bath and connected to an AC amplifier (High Voltage Amplifier WMA-300, Falco Systems, Amsterdam, Netherlands). The arrangement of the devices used and the positioning of the sample is depicted in Figure 19. The preparation of the sample follows that of LFUS studies detailed in section 4.2.6; the sample to be tested was prepared by diluting 75 µL of liposomes in 3 mL of PBS in a fluorescence cuvette. The cuvette was placed in the spectrofluorometer chamber to read the initial fluorescence intensity (baseline) for 30 seconds. The sample was then transferred to a conical bottom centrifuge tube whose opening was sealed using parafilm. This tube is then flipped and placed in a way such that the parafilm now holding the sample is barely touching the surface of the water in the bath and at a certain distance from the submerged probe. This arrangement was adopted to achieve better contact between the sample and the applied US waves and to prevent any scattering of the waves that might be caused by a glass beaker.

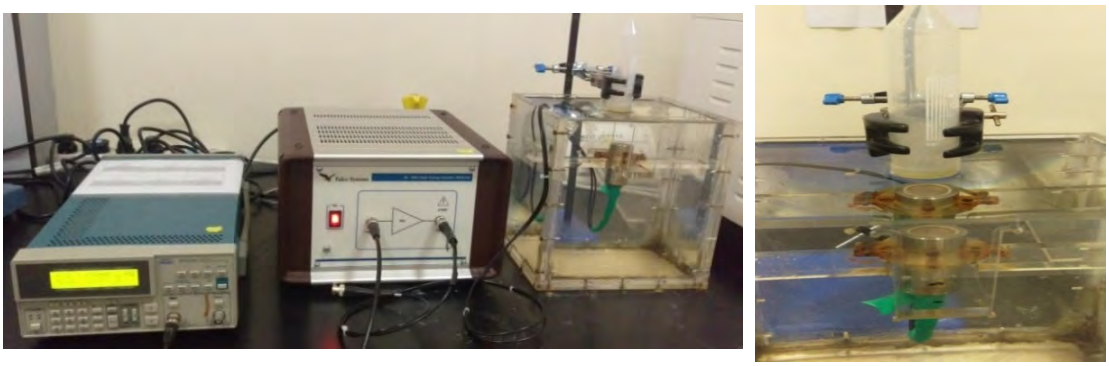

Figure 19: HFUS apparatus (left) and placement of sample (right).

The sample was sonicated in a continuous fashion (in contrast to the pulsed mode in LFUS release experiments), at a given frequency and voltage (2.4 V for 1 MHz and 7 V for the 3 MHz experiments), for 10 minutes after which the sample was

transferred to the fluorescence cuvette to record its fluorescence intensity for 30 seconds. The process was repeated every 10 minutes, for a total sonication time of 200 minutes. Finally, the detergent Tx100 was added to lyse the remaining liposomes and to record the maximum intensity of fluorescence corresponding to the final release. In this work, the release was studied at 1.07 MHz with a power density of 22.59 W/cm^2), and at 3 MHz, at a power density of approximately 158 W/cm^2.

4.3. Kinetic Modeling of Drug Release

Over the past few years significant advancements have been made in the field of mathematical modeling of drug delivery. Analogous to other scientific and engineering disciplines that rely extensively on mathematical modeling and programming, computer simulations are expected to become an integral part of the development of pharmaceutical technologies. Incorporating mathematical models and simulations into the pharmaceutical products' design process offers numerous advantages such as: better estimates of the required compositions, dimensions and geometry of the delivery systems, taking into account the desired administration route, drug dose and release profile. All of which are factors that would significantly reduce the amount of experimentation required during product development, hence saving both time and capital. Moreover, quantitative analyses of the chemical, physical and biological phenomena involved in drug release permit a better understanding of the mechanisms underlying drug release which in turn would help improve the safety of the developed products.

Ever since Professor Takeru Higuchi, known as the "father of physical pharmacy" developed his famous equation quantifying drug release from thin ointment films, the quantitative approach towards drug release has been in a constant state of growth. Numerous models, varying in accuracy and complexity, have been proposed including *empirical/semi-empirical* as well as *mechanistic-realistic* ones. The difference between the two is that in the former the mathematical treatment is purely descriptive; it is not based on physical, chemical or biological phenomena. Consequently, the predictive power of such models is very low. The *mechanistic-realistic* models, however, are based on well-established scientific phenomena such as diffusion, dissolution, swelling and precipitation. The conclusions drawn from such models permit the determination of system-specific parameters as well as the effects

these parameters have on the resulting drug release kinetics. Therefore during product development, the required composition, size, shape and preparation procedure of a novel treatment with desired properties becomes theoretically predictable [93, 94]. When developing and/or using mathematical models that quantify drug release the following considerations need to be taken into account [94]:

1. The accuracy of the model generally increases with increased complexity. That is, the more physical, chemical or biological phenomena taken into account the more complex, but at the same time, realistic the model becomes. However, if too many processes are considered, the model becomes too cumbersome to use; thus to achieve a balance between accuracy and usability only the dominant processes must be accounted for, e.g., If several mass transport steps take place sequentially and if one of these processes is much slower than all others, only this step needs to be considered in the model (as the rate limiting step).
2. Theoretical calculations should always be compared to experimental results. This can be achieved in one of two ways: the theory could either be fitted to experimental data, or theoretical predictions can be compared with independent experimental results. In the first case, good agreement between the theory and experimentation is achieved through the optimization of one or more model parameters. The second approach is a much more reliable indicator of the validity of the mathematical theory for a specific type of drug delivery system. This is because system-specific parameters can be determined via fittings to different sets of experimental results. Once all required model parameters are known, the effects of different formulations and/or processing parameters on the systems' properties can be predicted. Then, the respective formulations/devices are prepared in reality and the predicted systems' properties experimentally measured.
3. There is no universal mathematical theory that can be applied to all types of drug delivery systems. Some models are applicable to only a very limited number of drug delivery systems, whereas others have a broader scope of application.

Depending on the type of drug(s), incorporated drug dose(s), preparation technique, environmental conditions during drug release as well as geometry and dimensions of the drug delivery system, one or more of the following phenomena might be involved in the control of drug release from a delivery system: wetting of the system's surface, water penetration into the device, creation of pores, dissolution and/or precipitation, pore closure due to swelling, changes in system geometry and/or dimensions, etc… the specification of the phenomena involved allows mathematical models to be developed in different ways for each type of system. It is important to note that presently most models treat the overly complex human body as one or two well stirred liquid compartments. Biological processes such as enzymatic degradation, intra-cellular drug transport, interactions with compounds in the extra- and intracellular space, drainage into the lymphatic system, transport across the Blood Brain Barrier and other such complications are not taken into account. In the future, it will be of major importance to account for these events to achieve more holistic and realistic mathematical theories [94, 95].

With respect to the phenomenon of dissolution, the study of the kinetics of drug release is governed by three theories: the diffusion layer model (film theory), Danckwert's model (surface renewal theory) and double barrier theory. The diffusion layer model consists of two steps the first being the dissolution of the solid to form a stagnant film which is saturated with the drug, the second step involves the diffusion of the solubilized drug from the stagnant film into the bulk of the solution; this being the rate determining step of the process [96]. Equations (7) and (8) constitute the mathematical representation of the diffusion layer model [93, 97, 98]:

1. Noyes-Whitney equation: developed in the early 20th century, this equation is used to describe the process of solid dissolution. The equation is based on Fick's second law of diffusion and entails the following assumptions: (1) the particle/system is spherical in shape, (2) the drug dissolves uniformly from all surfaces of the particle, (3) the thickness of the diffusion boundary is constant and (4) the thickness of the diffusion boundary is independent of the particle size. Accordingly, the mathematical representation of the Noyes-Whitney rule is as follows [99]:

$$\frac{dm}{dt} = kS(C_s - C) \quad (7)$$

Here *m* represents the mass transferred per unit time *t*, by dissolution from a solid particle of instantaneous surface *S* and *k* is a constant. The concentration gradient constitutes the driving force for this dissolution process and is represented in the above equation by $(C_s\text{-}C_t)$, where C_t is the concentration at time *t*, and C_s is the equilibrium solubility of the solute. The rate of dissolution *dm/dt* is the amount dissolved per unit area per unit time, and for most solids the conventional unit is g/cm^2 s. If C_t is less than 15% of the saturated solubility C_s, C_t is considered to have a negligible influence on the dissolution rate of the solid. In such a case, the dissolution of the solid is said to be occurring under sink conditions. Moreover, the surface area, *S* is not considered constant except when the quantity of material present exceeds the saturation solubility, or initially, when only small quantities of the drug have dissolved.

2. Nersnt-Brunner equation: this equation is a modification of the Noyes-Whitney equation in which Nersnt and Brunner used Fick's first law of diffusion to establish a relationship between the constant *k* seen in Equation 7 and the diffusion coefficient of the solute producing the following equation [93]:

$$k = \frac{D\,S}{h\,\gamma} \quad (8)$$

Where *D* is the diffusion coefficient, *S* is the area of dissolving surface or area of the diffusion layer, γ is the solution volume and *h* is the diffusion layer thickness. In formulating this equation, Nernst and Brunner made the assumption that the process at the surface proceeds much faster than the transport process and that a linear concentration gradient is confined to the layer of solution adhering to solid surface.

Danckwert's model adds to the diffusion layer model by accounting for the packets that are present in an agitated fluid. These packets or eddies absorb the solute at the solid-liquid interface and carry it into the bulk of the solution. On the other hand, the double barrier theory proposes the concept that an intermediate concentration exists at the solid-liquid interface due to solvation that is a function of solubility rather than diffusion [96].

Next, the methods to investigate the kinetics of drug release from controlled release dosage formulations can be classified into three categories: (1) statistical methods, (2) model dependent methods and (3) model independent methods [93].

4.3.1. Statistical methods. Statistical methods are mathematical formulas, models, and techniques used in statistical analyses of raw research data. Statistical methods are employed in the extraction of information from research data and provide different ways to assess the robustness of research outputs [100]. Statistical methods are usually employed to compare dissolution profiles (concentration versus time plots of the release of a drug from a dosage form).

4.3.2. Model dependent methods. Model-dependent methods are based on different mathematical functions which describe the dissolution profile. Once a suitable function has been selected, the model parameters are used to evaluate the dissolution profile. Deciding on a suitable function is usually carried out using non-linear regression analyses. Non-linear regression is a form of statistical analysis in which observational data are modeled by a function which is a non-linear combination of the model parameters and depends on one or more independent variables [93, 100]. Model-dependent methods include:

4.3.2.1. Zero order kinetics. The zero order model is usually used to describe dosage forms which do not disaggregate and release the drug slowly. The equation representing zero order kinetics is as follows [93]:

$$\boldsymbol{Q_0 - Q_t = k_0 t} \quad (9)$$

Where Q_t is the amount of drug dissolved in time t, Q_0 is the initial amount of drug in the solution (most times, $Q_0 = 0$) and k_0 is the zero order release constant expressed in units of concentration/time. Pharmaceutical dosage forms following this profile release the same amount of drug per unit of time and are therefore ideal for achieving prolonged pharmacological action [86]. The study of the release kinetics of systems obeying zero order kinetics involves plotting the cumulative amount of drug released versus time. This relationship can be used to describe the dissolution of several types of modified dosage forms as well as transdermal systems, matrix tablets with low solubility drugs and osmotic systems [93].

4.3.2.2. First order kinetics. The application of this model to drug dissolution was first proposed by Gibaldi and Feldman in 1967 and later by Wagner in 1969. This model can also be extended to describe the absorption and/or elimination of some drugs; however this mechanism is somewhat difficult to conceptualize theoretically [94]. The release of the drug which followed first order kinetics can be expressed by the equation [93]:

$$\frac{dC}{dt} = -kC \tag{10}$$

Here *k* is first order rate constant expressed in units of time^{-1}. The data obtained are plotted as cumulative log percentage of the drug remaining versus time which would yield a straight line with a slope of –k/2.303.

Since a semi-logarithmic plot is used to describe first order models it is more convenient to re-arrange equation (10) in the following form:

$$\log(C) = \log(C_0) - \frac{kt}{2.303} \tag{11}$$

Where C_0 is the initial concentration of the drug, *k* is the first order rate constant, and *t* is the time.

4.3.2.3. Higuchi model. The Higuchi equation was previously introduced as the earliest mathematical quantifier of drug release. The famous square root of time relationship (refer to equation (11)) published by Professor Higuchi was initially developed for the simple geometry of thin films, however the model was modified to encompass other geometries and porous systems [93].

The main advantage of this equation is its simplicity; however, when applying it to controlled drug delivery systems, the assumptions Higuchi based this equation on must be fulfilled [94]:

- The initial drug concentration in the system must be much higher than drug solubility.
- Diffusivity occurs only in one dimension (negligible edge effects).
- The size of the drug particles is much smaller than the thickness of the film.
- The carrier material does not swell or dissolve.
- The diffusivity of the drug is constant (not dependent on time or position).
- Perfect sink conditions are maintained throughout the experiment.

$$\boldsymbol{Q = A\sqrt{D(2C - C_s)C_s t}} \quad (12)$$

Where Q is the amount of drug released per unit time t per unit area A, C is the initial drug concentration, C_s is the drug solubility in the matrix media and D is the diffusion coefficient.

The above equation can be altered to quantify drug release in systems where the initial concentration is lower than the solubility and release, in this case, occurs through pores in the system, the adjusted equation becomes of the form [93]:

$$\boldsymbol{Q = \sqrt{\frac{D\delta}{\tau}(2C - \delta C_s)C_s t}} \quad (13)$$

Where D is the diffusion coefficient,δ is the porosity of the matrix, τ is the tortuosity of the porous system and Q, A, C_s and t have the same definitions as above.

4.3.2.4. Hixon-Crowell model. This was developed to describe release from systems where the surface area and diameter are not assumed to be constant. Hixson and Crowell recognized that the shrinking particles' area is proportional to the cubic root of its volume. Therefore their derived equation expressed the rate of dissolution based on the cubic root of the weight of particles [93, 94]:

$$\boldsymbol{W_0^{1/3} - W_t^{\frac{1}{3}} = \kappa t} \quad (14)$$

W_0 is the initial amount of drug in the pharmaceutical dosage form, W_t is the remaining amount of drug in the pharmaceutical dosage form at time t and κ is a constant incorporating the surface-volume relation.

4.3.2.5. Korsmeyer-Peppas model. A frequently used and relatively easy-to-apply model to describe drug release from polymeric systems is the Korsmeyer-Peppas equation also known as the power law [93, 94].

$$\boldsymbol{\frac{M_t}{M_\infty} = kt^n} \quad (15)$$

Here, M_t and M_∞ are the absolute cumulative amount of drug released at time t and infinite time, respectively; k is a constant incorporating structural and geometric characteristics of the system, and n is the release exponent, which is indicative of the mechanism of drug release as seen in Table 5.

Table 5: Diffusional drug release from polymeric systems [78].

Release exponent (n)			**Drug transport mechanism**	**Rate as a function of time**
Cylinder	Sphere	Thin film		
0.5	0.43	0.5	Fickian diffusion	$t^{-0.5}$
0.45<n<0.89	0.43<n<0.85	0.5<n<1	Anomalous transport	t^{n-1}
0.89	0.85	1	Polymer swelling	zero order release

4.3.2.6. Baker-Lonsdale model. This model is a variation of the Higuchi model which can be used to describe drug release from spherical matrices according to the equation [101]:

$$\boldsymbol{f_1 = \frac{3}{2}\left[1 - \left(1 - \frac{M_t}{M_\infty}\right)^{\frac{2}{3}}\right] - \frac{M_t}{M_\infty} = \frac{3D_m C_{ms}}{r_0^2 C_0} - t} \quad (16)$$

Where M_t is the drug released amount at time t and M_∞ is the amount of drug released at an infinite time, D_m is the diffusion coefficient; C_{ms} is the drug solubility in the matrix, r_0 is the radius of the spherical matrix and C_0 is the initial concentration of drug in the matrix.

If the matrix is nonhomogeneous and contains some fractures or capillaries that may contribute to drug release the equation becomes [98]:

$$\boldsymbol{f_1 = \frac{3}{2}\left[1 - (1 - \frac{M_t}{M_\infty})^{2/3}\right] - \frac{M_t}{M_\infty} = \frac{3D_f C_{fs} \varepsilon}{r_0^2 C_0 \tau} - t} \quad (17)$$

Where D_f is the diffusion coefficient, C_{fs} is the drug solubility in the liquid surrounding the matrix, τ is the tortuosity factor of the capillary system, and ε is the porosity of the matrix. The matrix porosity can be described by ($\varepsilon = \varepsilon_0 + KC_0$) where ε_0 is the initial porosity, and K is the drug-specific volume. If ε_0 is small enough equation (17) can be re-written as [98]:

$$\boldsymbol{f_1 = \frac{3}{2}\left[1 - (1 - \frac{M_t}{M_\infty})^{2/3}\right] - \frac{M_t}{M_\infty} = \frac{3D_f C_{fs} K}{r_0^2 \tau} - t = kt} \quad (18)$$

Here, k is release constant and corresponds to the slope.

4.3.2.7. Weibull model. The Weibull model is an empirical equation which defines the cumulative fractional drug release expression as a function of time as follows [95]:

$$\frac{M_t}{M_\infty} = 1 - exp\left[\frac{-(t-t_{lag})^b}{t_{scale}}\right] \quad (19)$$

In this equation, t_{lag} is the lag time before the drug release takes place, t_{scale} is the time scale of the release process, and b characterizes the shape of the release curve. The case of b=1 gives an exponential curve, b>1 gives a sigmoid (S-shaped) curve, and b<1 gives a parabolic curve with high initial slope followed by an exponential decay.

4.3.2.8. Hopfenberg model. The Hopfenberg model is a semi-empirical equation developed to describe drug release from degradable drug release systems by assuming that the overall release behaves as a zero order process confined to the surface area of the system. This zero order process could be a single or a combination of physical and/or chemical phenomena occurring at the surface. Therefore, this empirical equation is suitable for the quantification of drug release from surface-eroding particles since it assumes that the release rate is controlled by the dissolution process occurring at the surface [93–95].

$$\frac{M_t}{M_\infty} = 1 - \left[1 - \frac{k_0 t}{C_L a}\right]^n \quad (20)$$

k_0 is the zero order rate constant describing the surface erosion process, C_L is the initial drug loading throughout the system, a is the system's half thickness (i.e. the radius for a sphere or cylinder), and n is an exponent that varies with geometry n = 1, 2 and 3 for flat, cylindrical and spherical geometries, respectively.

4.3.2.9. Gompertz model. The Gompertz model is useful for comparing release profiles of drugs with good solubility and intermediate release rates. In this model, the dissolution profile is represented by a somewhat simple exponential model [93].

$$X(t) = X_{max} exp\left[-\alpha e^{\beta \log(t)}\right] \quad (21)$$

In the above equation $X(t)$ stands for the percentage of dissolved solid at time t; X_{max} denotes the maximum dissolution; α determines the undissolved proportion at time $t=1$described as a location parameter, while β is the dissolution rate per unit of time described as a shape parameter.

4.3.2.10. Regression models. Regression analysis is a mathematical technique used to answer the questions: which variables affect the system at hand, which factors

matter most, how do these factors interact with each other and which ones can be ignored. In regressional analyses there are two types of factors or variables: (1) the main factor under question, which is referred to as the dependent variable, in addition to (2) one or more independent variables suspect of having an influence on the dependent variable [102]. Several types of regression analysis are used to optimize the formulation from *in-vitro* release studies.

1. Linear regression models: these methods model the relationship between the dependent and independent variable(s) using linear equations of the form [93]:

$$\boldsymbol{Y = \beta_0 + \beta_1 X_1 + \beta_2 X_2 + \cdots + \beta_k X_k} \quad (22)$$

Where *Y* denotes the independent variable, *X* is the dependent variable and β is called the partial regression coefficient (it measures the change in *Y* per unit change in *X*). Interaction terms (when two variables act simultaneously) may be added to the first order model generating more complex models such as [93]:

$$\boldsymbol{Y = \beta_0 + \beta_1 X_1 + \beta_2 X_2 + \beta_{12} X_1} \quad (23)$$

2. Quadratic or second order regression models are of the form [93]:

$$\boldsymbol{Y = \beta_0 + \beta_1 X_1 + \beta_2 X_2 + \beta_{11} {X_1}^2 + \beta_{12} {X_2}^2} \quad (24)$$

Any quadratic regression equation can be reduced to a linear one as long as the partial regression coefficient is linear in form.

3. Nonlinear regression models: in nonlinear regression, the relationship between the dependent and independent variables is expressed using a nonlinear equation. A number of nonlinear regression techniques may be used to obtain a more accurate regression. A common application of nonlinear regression in drug release modeling is the determination of the most suitable dissolution medium. A large number of dissolution media exist for solid dosage forms (the choice of medium is critical for testing solid dosage forms), using regression models helps in the evaluation of the alternatives hence simplifying the choice process [93].

4.3.3. Model-Independent methods. Model-independent methods provide a simple approach to compare drug release profiles. Moore and Flanner proposed a method which quantifies the differences and similarities between curves using two factors, the difference factor f_1 and the similarity factor f_2. The difference factor is a

measurement of the relative error between two curves; it is obtained by calculating the percentage difference between two curves at every point and is expressed mathematically as follows [93]:

$$\boldsymbol{f_1 = \left[\frac{\sum_{t=1}^{n}(R_t - T_t)}{\sum_{t=1}^{n} R_t}\right] \times 100} \quad (25)$$

The similarity factor, on the other hand, is a logarithmic reciprocal square root transformation of the sum of the squared error, the mathematical expression for which is [93,105]:

$$\boldsymbol{f_2 = 50\ log\left\{\left[1 + \left(\frac{1}{n}\right)\sum_{t=1}^{n}(R_t - T_t)^2\right]^{-0.5} \times 100\right\}} \quad (26)$$

In both equations above n denotes the number of time points, R is the dissolution value of the reference batch at time t, and T_t is the dissolution value of the test batch at time t.

In dissolution profile comparisons, the regulatory focus is on determining how similar two curves are to each other, especially when the comparison is performed to assure similarity in product performances. For this reason, the similarity factor comparison has garnered more attention than its difference counterpart in FDA guidelines. When two profiles are identical the value of f_2 is 100; however, an average difference of 10% across all measured time points results in an f_2 value of 50. The FDA has set the public standard f_2 value between 50 and 100 to indicate similarity between two dissolution profiles. Other guidelines for applying this method for dissolution profile comparisons include [103]:

- At least 12 units should be used for each profile determination.
- The f_2 factor can be determined using mean dissolution values.
- The dissolution measurements of the two products (test and reference) should be made under the same test conditions.
- Given that f_2 values are sensitive to the number of dissolution time points, only one measurement should be considered after 85% dissolution of the product.
- For rapidly-dissolving products, i.e., more than 85% in 15 minutes or less, a profile comparison is not necessary.
- f_2 values between 50 and 100 ensure sameness between the two curves which in turn ensures the sameness in the performance of the two tested products.

4.4. *In-Vitro* Cell Work

The use of tissue cultures is an invaluable tool in studies of clinical relevance, particularly those related to diseases, screening, and studies of cell toxicity mechanisms. *In-vitro* cell culturing dates as far back as the 16th century, when Sir William Harvey observed that a piece of myocardium kept in the palm of his hand covered in his own saliva would continue to contract for a considerable period of time. Several important developments in cell culture techniques evolved from these early observations; for instance in the late 19th century Roux showed that embryonic chick cells can be maintained alive in a saline solution outside the animal body.

Nevertheless, the fact that these cultured cells had a time limit was established early on. The notion of *in-vitro* immortalization was first discovered in 1910 by Rous, who successfully induced a tumor by using a filtered extract of chicken tumor cells. This remarkable discovery prompted the concept of enhanced tissue survival in culture, and therefore, the possibility of producing cell models. By the middle of the 20th century, Earle and colleagues were able to isolate single cells from the L cell line and showed that these cells were able to clone themselves in tissue culture. Later, Gey and colleagues established probably the most well-known continuous line of cells derived from human cervical carcinoma, which later became the famed HeLa cell line. However, concerns began to arise regarding loss of function with such immortalization processes. Hence, researchers were faced with the challenge of preserving the functionality of these cell lines using externally applied stimuli such as media supplementation and physical agents. In 1945, Rita Levi-Montalcini observed that the nerve growth factor stimulates the growth of axons in tissue cultures, these observations were what brought attention to the importance of the surrounding environment in maintaining the viability of cultured cells. Later, Eagle made the first systematic investigation of the essential nutritional requirements of cultured cells and found that animal cells proliferate in a defined mixture of small molecules supplemented with serum proteins. The first immortalized cell line to retain differentiated traits was a mouse neuroblastoma (nerve cell tumor) adapted for tissue culture by Augusti-Tocco and Sato in 1968 [99].

The HeLa cell line, introduced briefly in the above discussion, is of particular importance for this research and merits further discussion. This cell line was first discovered in 1951, when Henrietta Lacks was diagnosed and treated for cervical

cancer (adenocarcinoma of the cervix). The physician treating Lacks, Dr. George Gey, had been collecting cancerous tissue samples from patients in an attempt to develop a cure for cancer by first creating an immortalized cell line on which he could experiment therapies and medicines. All of Dr. Gey's attempts at cultivating human cells *in-vitro* were met with failure until Henrietta's tumor sample. The cervical adenocarcinoma cells Dr. Gey collected from Lacks constituted the first successful attempt at immortalizing human-derived cells *in-vitro*; ergo the name HeLa which was derived from the first two letters of Henrietta and Lacks. Researchers found that HeLa cells possess certain characteristics which might have been the reason why they could be immortalized as a cultured cell line. Firstly, HeLa cells grow unusually fast, even in comparison to other types of cancer. In fact, HeLa cells grow so fast that they could contaminate and overtake other cell cultures. This was attributed to the fact that Lacks suffered from syphilis which weakened her immune system and resulted in a more aggressive form of cancer. Secondly, HeLa cells possess overactive tolemerase enzymes which rebuild telomeres after each cell division, preventing cellular aging and allowing perpetual divisions of the cells [104].

In this research *in-vitro* studies were conducted to examine the interactions between ultrasound triggered transferrin-conjugated liposomes and cancer cells overexpressing transferrin receptors. HeLa cells, belonging to a human cervical carcinoma cell line, were obtained from the European Collection of Authenticated Cell Cultures (ECACC). The procedure adopted for the cell work experiments in this research is as follows:

1. The cells are first plated in 6 well plates; each well is expected to have a cell concentration of $2x10^5$ cells/mL. The plating process involves first, washing with Dulbecco's phosphate-buffered saline (DPBS added to the T-flask containing the cell line) to ensure that any remaining medium is removed as it interferes with the action of the digestive enzyme trypsin. After discarding the added DPBS, 3 mL of trypsin are added and the trypsinized flask is incubated for around 3 minutes to ensure that the cell line has completely detached from the walls of the flask (the conditions in the incubator are maintained at $37^{\circ}C$ and 5% CO_2). Following the incubation period, 3 mL of RPMI-1640 medium (a mixture of fetal bovine serum (FBS), L-glutamine and the antibiotics

penicillin and streptomycin) were added to the flask to neutralize the effects of trypsin. The contents of the flask are then passed through a cell strainer fixed on a centrifuge tube; the strainer is used to ensure the cells do not clump together. In order to determine the cell concentration in the cell stock at hand, the volume of medium needed to achieve the desired cell density a cell count was calculated using the trypan blue exclusion method. Therefore, 50 µL of the cell stock is transferred to an eppendorf tube and mixed thoroughly with 50 µL of trypan blue. A small amount of this solution is pipetted and transferred onto a hematocytometer, the slide is then placed under a microscope and the cell count is performed as shown in Figure 20 [105].

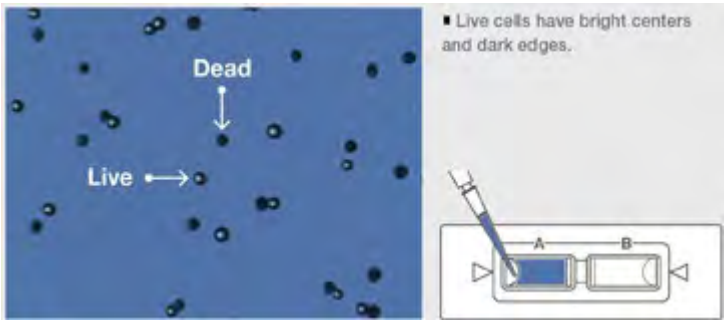

Figure 20: Cell count [91].

The cell concentration, volume of the medium needed and volume to be added to cell stock are determined using the following equations [106]:

$$\boldsymbol{viability} = \frac{\boldsymbol{live\ cell\ count}}{\boldsymbol{total\ cell\ count}} \tag{27}$$

$$\textbf{Cell concentration} = \frac{\textbf{viable cell count}}{\textbf{quadrant counted}} \times \textbf{dilution factor} \times \textbf{hemocytometer factor} \times \textbf{current volume} \tag{28}$$

$$\boldsymbol{Total\ volume\ needed(mL)} = \frac{\boldsymbol{cell\ concentration}}{\boldsymbol{desired\ cell\ density}\ (\frac{\boldsymbol{10^6 cells}}{\boldsymbol{mL}})} \tag{29}$$

$$\boldsymbol{Volume\ to\ add\ to\ stock = total\ volume\ needed - current\ volume} \quad \boldsymbol{(all\ in\ mL)} \tag{30}$$

After performing the detailed calculations, the determined volume of medium is added to the centrifuge tube, 3 mL of the solution are transferred to each well ($2x10^5$ cells/mL translates to 600,000 cells per well, meaning that each well must

contain 3 mL of the cell stock to achieve the desired density). The plates are then incubated under 37°C and 5% CO_2 overnight.

2. After the 24 hours incubation period, the medium in the plates is changed, and depending on the quantity of liposomes available and the number of plates prepared, equal quantities of control and transferrin liposomes are added to the wells as depicted by the figure below (Figure 21 depicts a general arrangement, the actual distribution varies depending on the number of plates and quantities of liposomes available) and the plates are then incubated for 60 minutes.
3. One plate is not exposed to ultrasound to serve as a reference while the other plate(s) are sonicated using a sonicating bath. The sonicated plates are then incubated for around 1 hour.

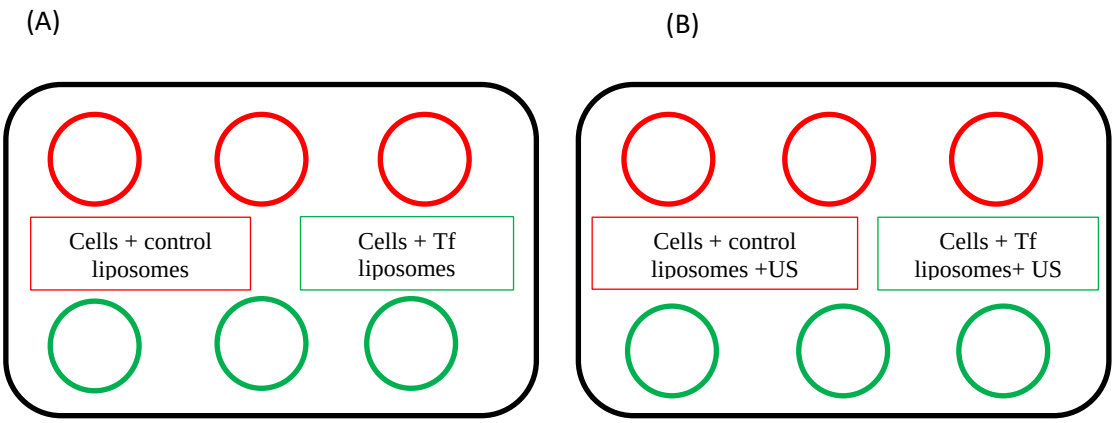

Figure 21: Effects of liposomes and ultrasound on cancer cells (A) is the control plate while (B) is the insonated plate.

4. Following the incubation period transfer the medium from the wells to centrifuge tubes, add 1 mL of DPBS to each well then pipette the contents of the wells into the centrifuge tubes. Next, add 500 µL of trypsin to each well, incubate for 3 to 4 minutes then collect and transfer the detached cells to the tube.
5. Take 50 µL out of the remaining solution to determine cell viability using the trypan blue exclusion method.
6. Centrifuge for 7 minutes to force the cells to settle at the bottom of the tube then discard of the PBS.

7. Add 1mL of DPBS to the tubes and mix thoroughly to re-suspend the cells (cell washing).
8. Again centrifuge for 7 minutes to force the cells to settle at the bottom of the tube then discard of the DPBS.
9. Finally, transfer these suspensions into the tubes allocated for flow cytometry.

Flow cytometry is a laser based technology used to analyze the characteristics of cells and particles. The modern flow cytometer measures multiple parameters (fluorescence intensity, as well as, light scattering) for each particle and discriminates cell or particle populations based on size, morphology, and other properties. Based on light scattering, a cell suspension is run through the cytometer and the stream of sheath fluid takes the cells through the laser light one cell at a time. As the cells or particles pass through the laser beam they cause some scattering of this light beam. The scattered light is sensed by a set of conveniently positioned detectors, where the detector in front of the light beam measures forward scatter (FS) while side detectors measure side scatter (SS) [107]. In fluorescence-based flow cytometry, detectors measure the fluorescence emitted from positively stained cells or particles. This research relies on fluorescence-based cytometry in order to determine and compare the efficiency of cellular uptake of control, targeted and US complemented liposomes. The concept behind this approach is that cells take-in any free calcein outside the cell as well as the liposomes through endocytosis and sonoporation (caused by ultrasound). After internalization, the cell breaks up the liposomes, releasing the encapsulated calcein. Given that calcein is fluorescent, the cells that have internalized and lysed the phagocytosed liposomes will be giving higher fluorescence readings. Therefore, the efficiency of the administered liposomal treatment is evaluated based on the difference in fluorescence values between the cells to which we added liposomes and those that were not subjected to the liposomal treatment. Similarly, targeted and US released liposomes are expected to have an even higher fluorescence difference when compared to the control cell line, as active targeting and US are supposed to further enhance the permeability and cellular uptake of liposomes which will be observed as a greater shift in fluorescence intensity.

Chapter 5. Results

5.1. Estimation of Total Lipid Concentration by Stewart Assay

In this research the liposomes were prepared using DPPC as the major lipid constituent, the previous chapter detailed the procedure involved in Stewart assay to determine the phospholipid content in liposomes. The procedure mentioned above was used to develop a calibration curve (refer to Figure 22). A least squares regression analysis of the plot was performed, and the equation of the line yielded an intercept (-0.0131), slope (6.0252) and correlation coefficient (R^2=0.9997). The high value of the regression coefficient and the minor value of the intercept confirm the linearity of the calibration plot.

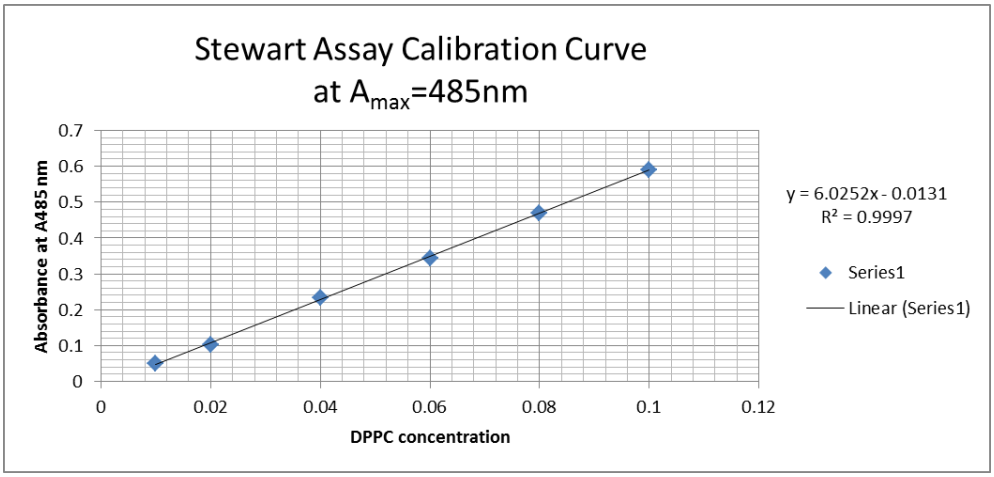

Figure 22: Calibration curve of phospholipid mixture in chloroform at A_{max} of 485nm.

5.2. Estimation of Protein Content Using BCA Assay

The presence of transferrin was tested for using the BCA assay, the detailed procedure of which was presented in section 4.2.4. As with the Stewart assay, a calibration curve (refer to Figure 23) was generated, and a linear regression analysis was performed. From the equation of the line, the intercept was found to be (-0.2968), slope (0.2936) and correlation coefficient (R^2=1). Again the unity value of the regression coefficient and the minor value of the intercept all confirm the linearity of the calibration plot. In addition, the transferrin coupled liposomes were found to have a protein content of 0.0646 μg/mL while the control (NH_2) liposomes had a protein concentration of 0.0198 μg/mL, meaning that the transferrin liposomes have

almost a 3 folds higher protein concentration which agrees with the expected behavior.

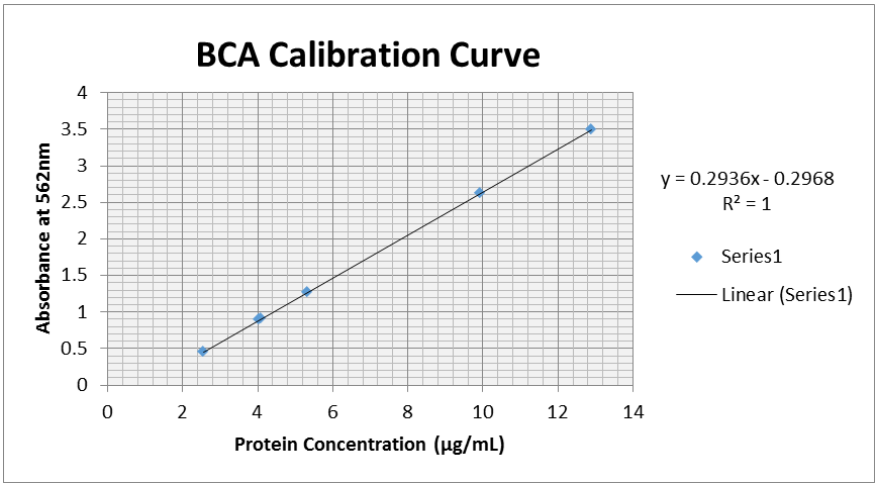

Figure 23: BCA calibration curve at 562 nm.

5.3. Liposome Size

After the phospholipid content was determined and the attachment of the protein was established, the sizes of 3 batches of control and transferrin coupled liposomes were measured using DLS. The average diameters for each batch of liposomes were then calculated; the average diameter for control liposomes was found to be 82.70±2.88 nm with a percent polydispersity index (%Pd) value of 14.44±1.72. The Tf-liposomes were found to be slightly larger particles with an average diameter of 87.54±4.81 nm and a %Pd of 14.39±2.42. A statistical two-tailed t-test was conducted to compare the sizes of both types of liposomes, and it was found that the differences in size were not statistically significant (p-value=0.246). These findings agreed with the size expectations and confirmed that both types of synthesized liposomes are small unilamellar vesicles (SUV) and if used in *in-vivo* studies are expected to be efficient for drug delivery as they can make use of the enhanced permeability and retention (EPR) effect.

5.4. Online Low-Frequency Induced Release

Low-frequency US release was performed on three batches of control and transferrin- conjugated liposomes (three replicates per batch) using a 20 kHz probe at three different power densities (7.46 mW/cm^2, 9.85 mW/cm^2 and 17.31 mW/cm^2). The fluorescence level of the sample is first measured prior to sonication, and the

obtained readings are defined as the baseline intensity I_0. This baseline intensity has the lowest value amongst the fluorescence readings because at this point calcein is encapsulated in a self-quenched state inside the liposomes. Once sonication is initiated the intensity increases due to calcein release. This intensity is measured continuously with time and is represented as I_t. The 20 seconds *on* 10 seconds *off* sonication cycle mentioned in the previous chapter was applied for 5 minutes, with a total sonication time of 3.83 minutes. The pulsed sonication was continued until a plateau was reached indicating maximum calcein release. Next Triton X-100 was added to the sample to lyse the liposomes, and the fluorescence level increased slightly above the plateau indicating that the liposomes have released all their remaining contents. The highest value of intensity recorded during the release experiment is denoted by I_∞. The aforementioned power intensities are then used to calculate the cumulative fraction release (CFR) given by equation (31).

$$\boldsymbol{CFR = \frac{I_t - I_0}{I_\infty - I_0}} \tag{31}$$

5.4.1. LFUS online release studies with NH_2 Liposomes. LFUS release of NH_2 liposomes was studied by exposing three batches of NH_2 liposomes to 20 kHz pulsed US at three different power densities. The obtained release profiles are depicted in Figure 24.

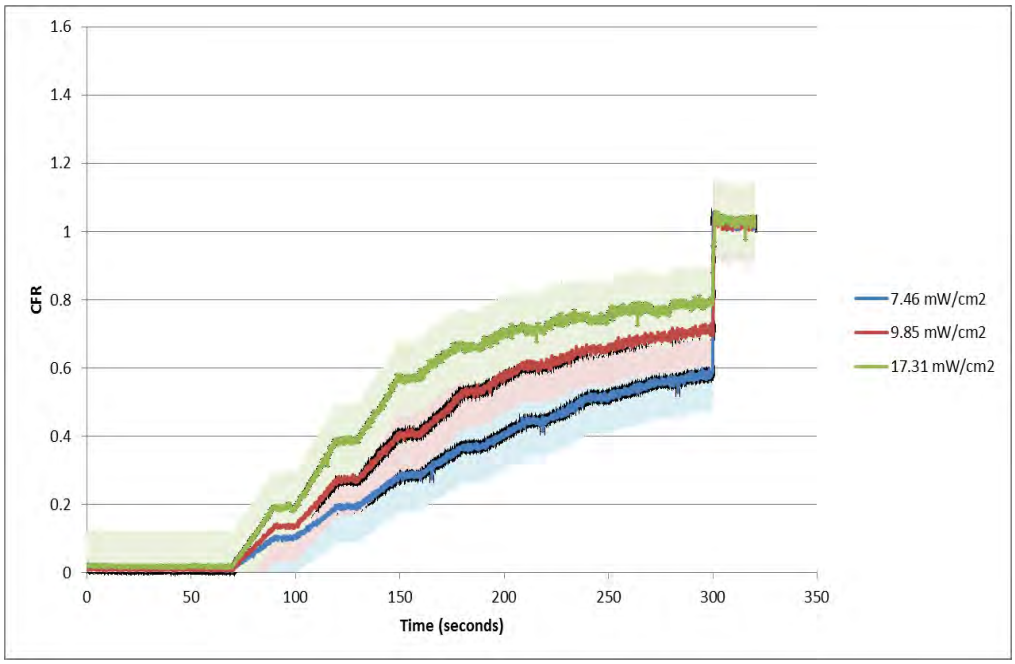

Figure 24: Normalized release profiles of NH_2 liposomes. Results are depicted as average± standard deviation of 3 batches of liposomes.

The release profiles of the NH_2 liposomes used in this research, as seen in Figure 24, followed the expected trend of increased release of encapsulated contents with increased power density.

A comparison between the first four pulses at each power density was performed, the findings of this comparison, are represented by Figures 25 and 26. In terms of intensity, it can be observed that the intensity values increase with increased power density for each pulse at the 7.46 mW/cm^2 and 9.85 mW/cm^2 power densities; however at the 17.31 mW/cm^2 power density the third pulse has the highest fluorescence intensity value, this could be a result of the thermal effects of US acting simultaneously with the cavitational effects and it can also be explained by micellar release, that is the sonoporation effect has disrupted the bilayer causing some of the phospholipids to form micelles which then add to the release when the US is in the *on* cycle. With respect to CFR, the values for these pulses are shown to increase with increased power density. Both observations further prove the conclusion that the release of liposomal contents increases with increased power density.

The statistical analysis of the results (refer to Table 6) showed that the percentage of release after the first pulse increases significantly ($p<0.05$) with increased power density. The percentage release at 7.46 mW/cm^2, which is the lowest power density used, was significantly lower than the release obtained at 9.85 mW/cm^2 with a p-value of $1.75x10^{-8}$ in terms of CFR and 0.000914 in terms of intensity, similarly when the release at 9.85mW/cm^2 was compared to that obtained at the highest power density of 17.31 mW/cm^2 a significant difference was observed (CFR p-value of $9.74x10^{-14}$ and 0.007568 in terms of intensity). Comparable results were obtained when the percentage release values were compared after the second, third and fourth US pulses ($p<0.05$), these findings further support the conclusion that the release increases significantly with increasing power density.

As for the final release, the statistical analysis of the results revealed that there was no significant difference between 7.46 mW/cm^2 and 9.85 mW/cm^2 (CFR p-value=0.180). Similarly, there no significant difference was obtained when comparing the final release at 9.85mW/cm^2 with that at 17.31 mW/cm^2 (CFR p-value=0.967).

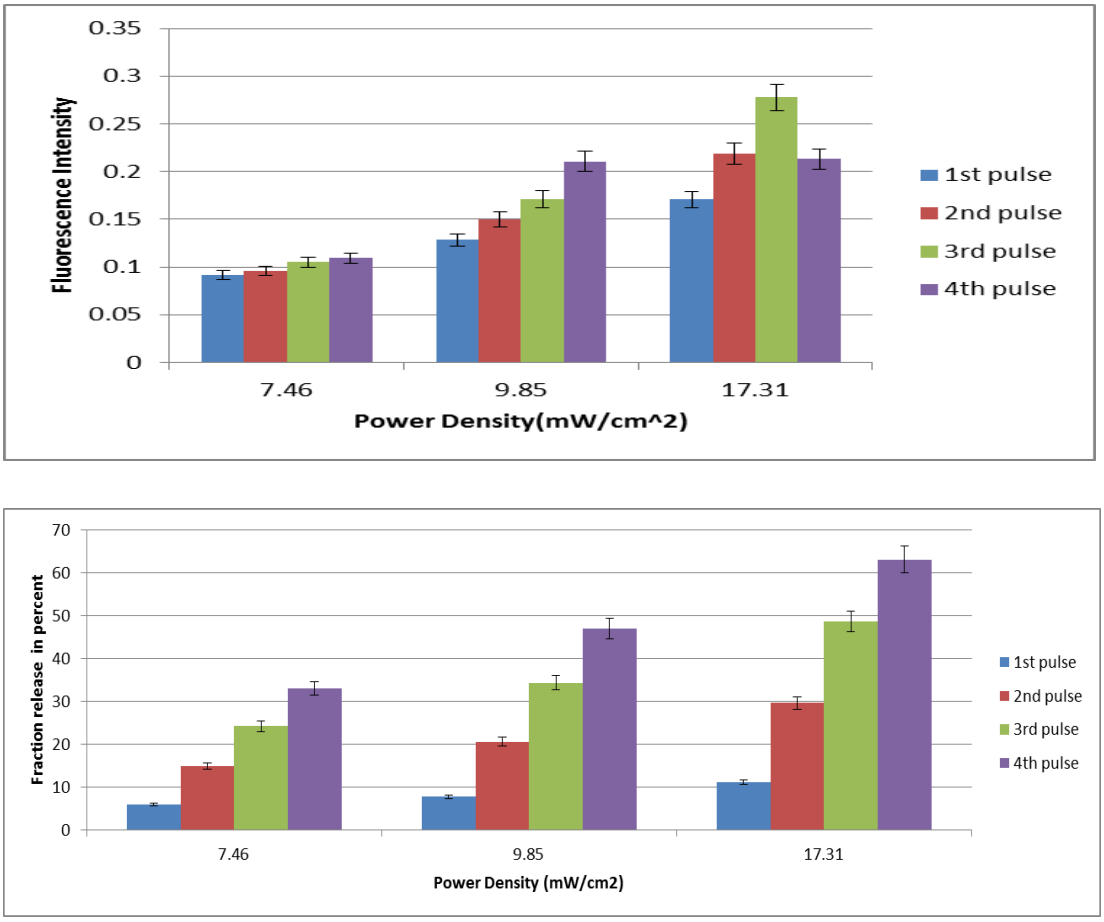

Figure 25: Comparison of the four pulses between each of the three power densities in terms of fluorescence intensity (top) and CFR (bottom).

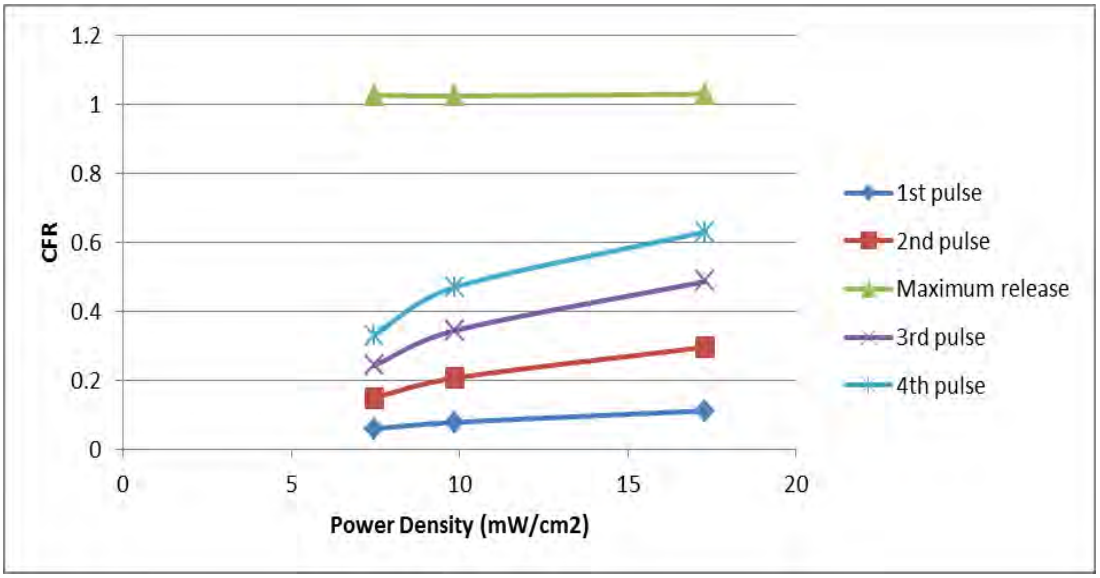

Figure 26: Normalized release profiles for four pulses in addition to final release for NH_2 liposomes at three different power densities.

Table 6: Statistical comparison of fraction release values and fluorescence intensity values at different power densities across four pulses.

Intensity			CFR		
Pulse	**Power Density (mW/cm^2)**	**NH_2 p-value**	**Pulse**	**Power Density (mW/cm^2)**	**NH_2 p-value**
1st	*7.46 vs. 9.85*	0.0009136	**1st**	*7.46 vs. 9.85*	$1.752x10^{-8}$
	9.85 vs. 17.31	0.007567		*9.85 vs. 17.31*	$9.742x10^{-14}$
2nd	*7.46 vs. 9.85*	$9.438x10^{-5}$	**2nd**	*7.46 vs. 9.85*	$2.1960x10^{-48}$
	9.85 vs. 17.31	0.001321		*9.85 vs. 17.31*	$1.668x10^{-53}$
3rd	*7.46 vs. 9.85*	$5.435x10^{-5}$	**3rd**	*7.46 vs. 9.85*	$2.801x10^{-107}$
	9.85 vs. 17.31	0.0004911		*9.85 vs. 17.31*	$1.743x10^{-108}$
4th	*7.46 vs. 9.85*	0.0001498	**4th**	*7.46 vs. 9.85*	$6.709x10^{-168}$
	9.85 vs. 17.31	0.9649		*9.85 vs. 17.31*	$2.489x10^{-186}$
Maximum release	*7.46 vs. 9.85*	-	**Maximum release**	*7.46 vs. 9.85*	0.1797
	9.85 vs. 17.31	-		*9.85 vs. 17.31*	0.9670

$p \geq 0.05$	$0.04 \leq p < 0.05$	$0.03 \leq p < 0.04$	$0.02 \leq p < 0.03$	$0.01 \leq p < 0.02$	$p < 0.01$

5.4.2. LFUS release studies with transferrin liposomes. LFUS release of transferrin liposomes was studies by exposing three batches of transferrin liposomes to 20 kHz pulsed US at three different power densities. The obtained release profiles are depicted in Figure 27.

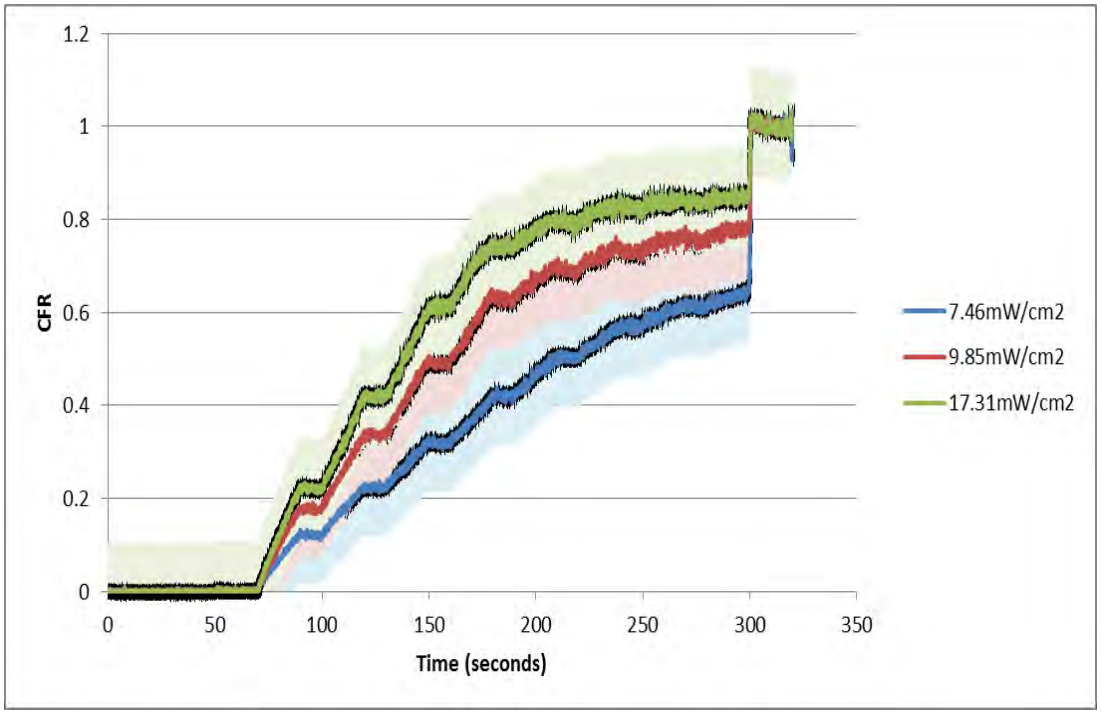

Figure 27: Normalized release profiles of transferrin liposomes. Results are depicted as average± standard deviation of 3 batches of liposomes

As was observed with NH_2 liposomes, the release profiles of the transferrin liposomes used in this research, depicted in Figure 27, showed an increased release of encapsulated contents with increased power density. Moreover, the comparison between the pulses at each power density (refer to Figures 28 and 29) in terms of fluorescence intensity shows that for 7.46mW/cm^2 the 1st pulse is slightly higher than the 2nd and 3rd pulses which could be attributed to thermal US effects. Similar to what was seen in the control liposomes' release the third pulse of the 17.31 mW/cm^2 gave the highest intensity value which again can be attributed to thermal effects or additional micellar release. In terms of CFR the release of Tf-liposomes was found to be in agreement with that obtained for the NH_2 liposomes as it shows that the CFR value for all pulses increases with increased power density.

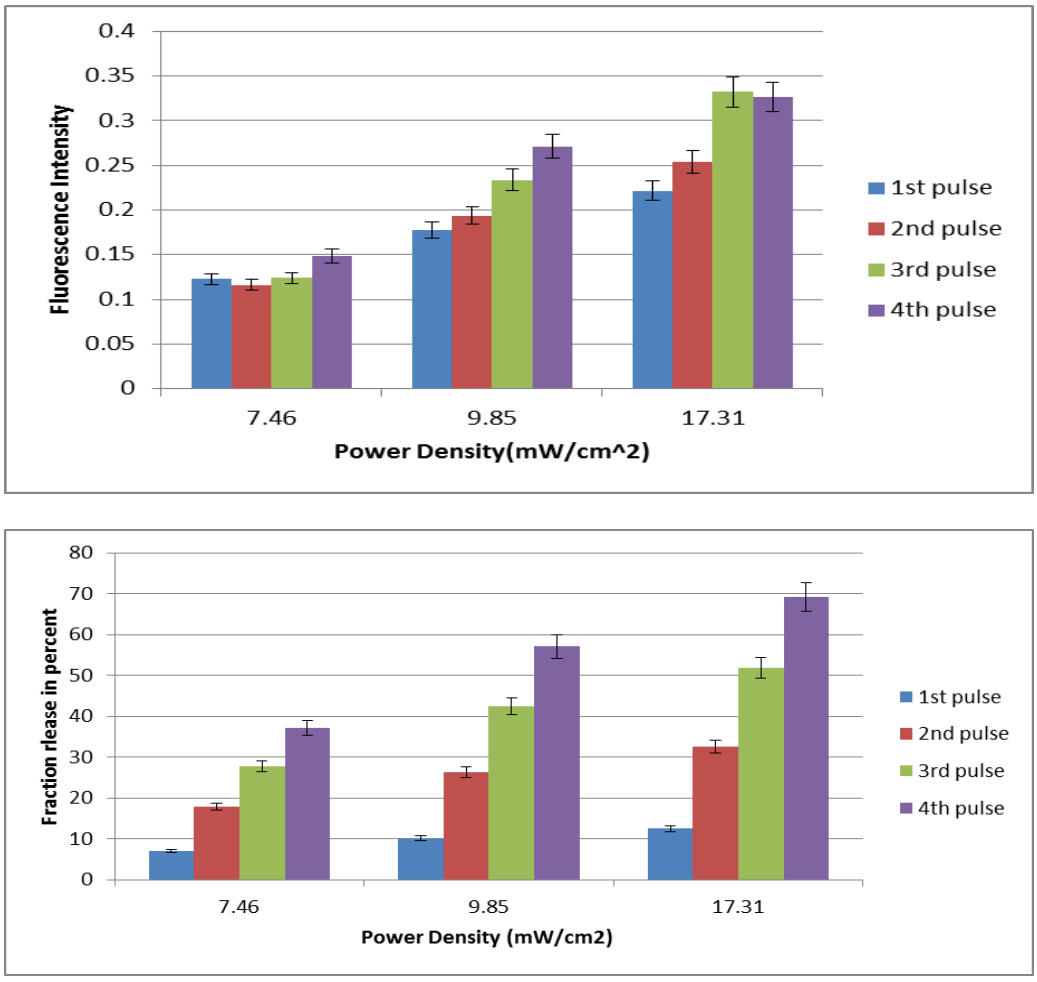

Figure 28: Comparison of four pulses between each of the three power densities in terms of fluorescence intensity (top) and CFR (bottom).

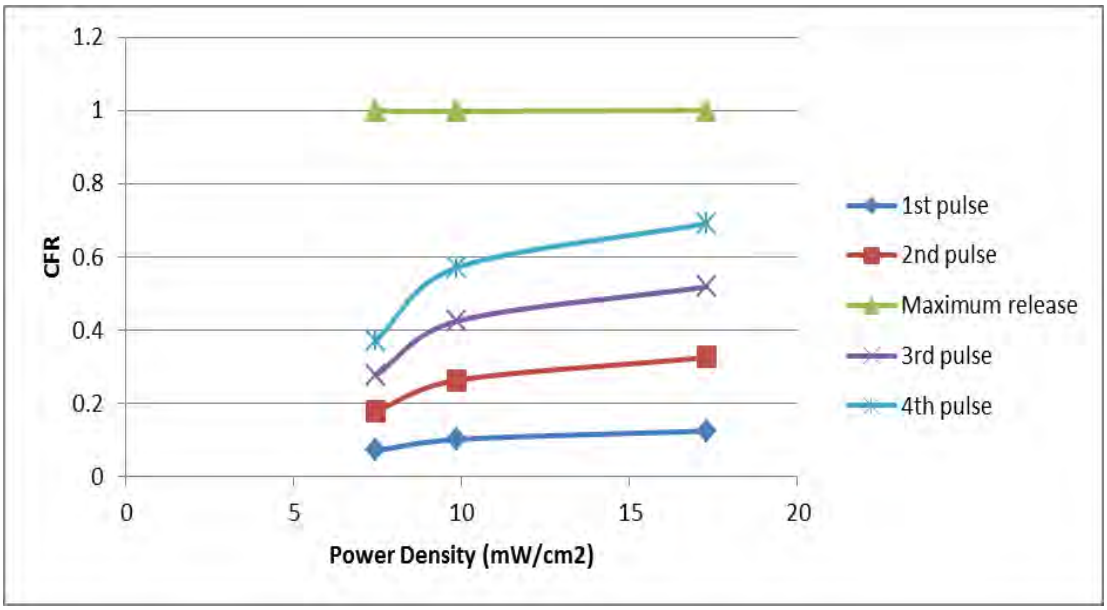

Figure 29: Normalized release profiles for four pulses in addition to final release for transferrin liposomes at three different power densities.

The statistical analysis of the results obtained for transferrin liposomes (refer to Table 7) yielded results similar to those obtained for NH_2 liposomes. The percentage of release after the first pulse was found to increase significantly ($p<0.05$) with increased power density. The percentage release at 7.46 mW/cm^2, which is the lowest power density used, was significantly lower than the release obtained at 9.85 mW/cm^2 (with a p-value of $1.95x10^{-11}$ in terms of CFR and 0.000464 in terms of intensity). The release at 9.85 mW/cm^2 was compared to that obtained at the highest power density of 17.31 mW/cm^2 a significant difference between the two was observed (CFR p-value of $7.53x10^{-5}$ and p-value=0.009106 for intensity). Comparable results were obtained when the percentage release values were compared after the second, third and fourth US pulses ($p<0.05$), these findings further support the conclusion that the release increases significantly with increasing power density.

As for the final release, the statistical analysis of the results revealed that there was no significant difference between 7.46 mW/cm^2 and 9.85 mW/cm^2 (CFR p-value=0.742) and 7.46 mW/cm^2 when compared with 17.31 mW/cm^2 (CFR p-value=0.421). Similarly, there no significant difference was obtained when comparing the final release at 9.85 mW/cm^2 with that at 17.31mW/cm^2 (CFR p-value=0.129).

Table 7: Statistical comparison of fraction release values and fluorescence intensity values at different power densities across four pulses.

Intensity			CFR		
Pulse	**Power Density (mW/cm^2)**	**Tf p-value**	**Pulse**	**Power Density (mW/cm^2)**	**Tf p-value**
1st	*7.46 vs. 9.85*	4.641×10^{-4}	**1st**	*7.46 vs. 9.85*	1.946×10^{-11}
	9.85 vs. 17.31	0.009105		*9.85 vs. 17.31*	7.526×10^{-5}
2nd	*7.46 vs. 9.85*	3.660×10^{-5}	**2nd**	*7.46 vs. 9.85*	4.459×10^{-70}
	9.85 vs. 17.31	0.01943		*9.85 vs. 17.31*	9.612×10^{-28}
3rd	*7.46 vs. 9.85*	1.449×10^{-4}	**3rd**	*7.46 vs. 9.85*	3.489×10^{-136}
	9.85 vs. 17.31	0.08341		*9.85 vs. 17.31*	1.986×10^{-54}
4th	*7.46 vs. 9.85*	0.08973	**4th**	*7.46 vs. 9.85*	6.750×10^{-190}
	9.85 vs. 17.31	0.4458		*9.85 vs. 17.31*	1.652×10^{-102}
Maximum release	*7.46 vs. 9.85*	-	**Maximum release**	*7.46 vs. 9.85*	0.7421
	9.85 vs. 17.31	-		*9.85 vs. 17.31*	0.1286

$p \geq 0.05$	$0.04 \leq p < 0.05$	$0.03 \leq p < 0.04$	$0.02 \leq p < 0.03$	$0.01 \leq p < 0.02$	$p < 0.01$

5.4.3. Comparison between NH_2 and transferrin liposomes. This section presents a comparison between the LFUS release behavior of NH_2 and transferrin conjugated liposomes after four pulses at three different power densities. Figure 30 presents the normalized release profiles for both control and transferrin liposomes while the histograms shown in Figure 31 compare the release between both types of liposomes for four pulses. As can be observed from Figure 31 across all four pulses the CFR for both types of liposomes increases with increasing power density, moreover, transferrin liposomes tend to have a higher fraction release than control liposomes. A similar trend was observed when comparing the fluorescence intensity of both types of liposomes; this slight difference in release could be indicative that the attachment of transferrin to the surface of liposomes has rendered them more sono-sensitive than control liposomes (the presence of the protein in a way slightly destabilizes the membrane making the liposomes more susceptible to acoustic mechanical waves). The findings of the statistical analysis results were as follows, in terms of intensity the transferrin-conjugated liposomes showed significantly higher release ($p<0.05$) when compared to non-targeted liposomes at all three power

densities or the first pulse only. However, in terms of CFR the Tf-liposomes showed significantly higher release when compared to control liposomes at all three power densities after all four pulses. Table 8 presents the p-values comparing the release between control and Tf-conjugated liposomes at a particular pulse between the different applied power densities.

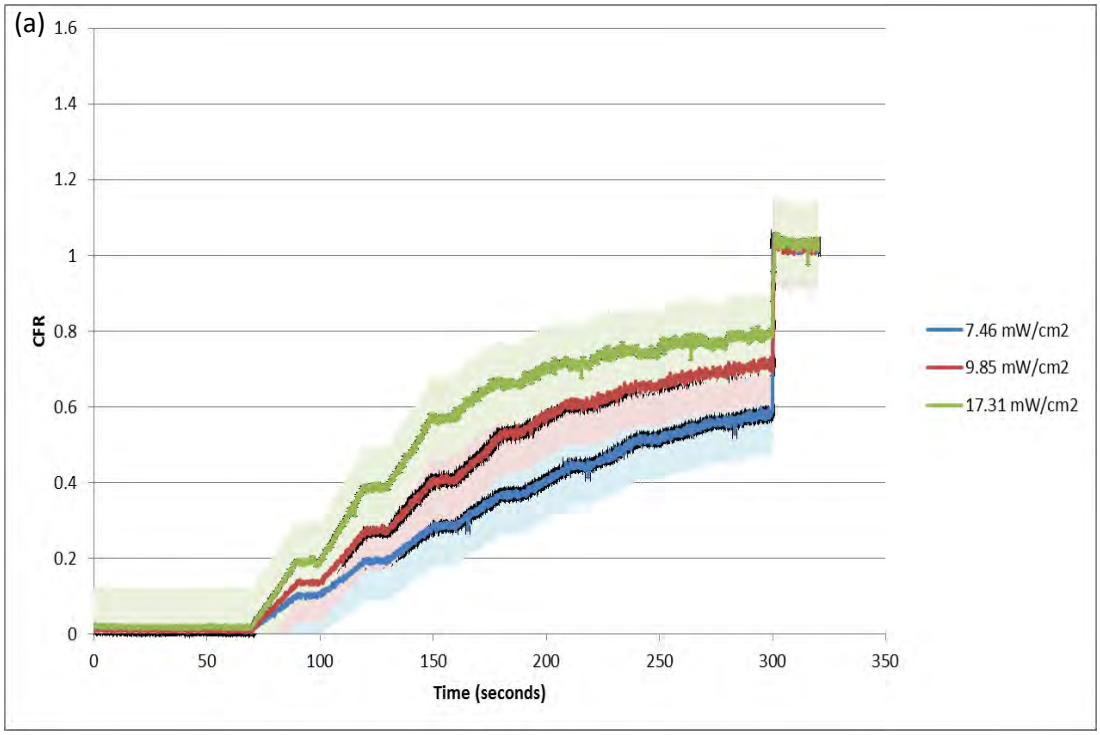

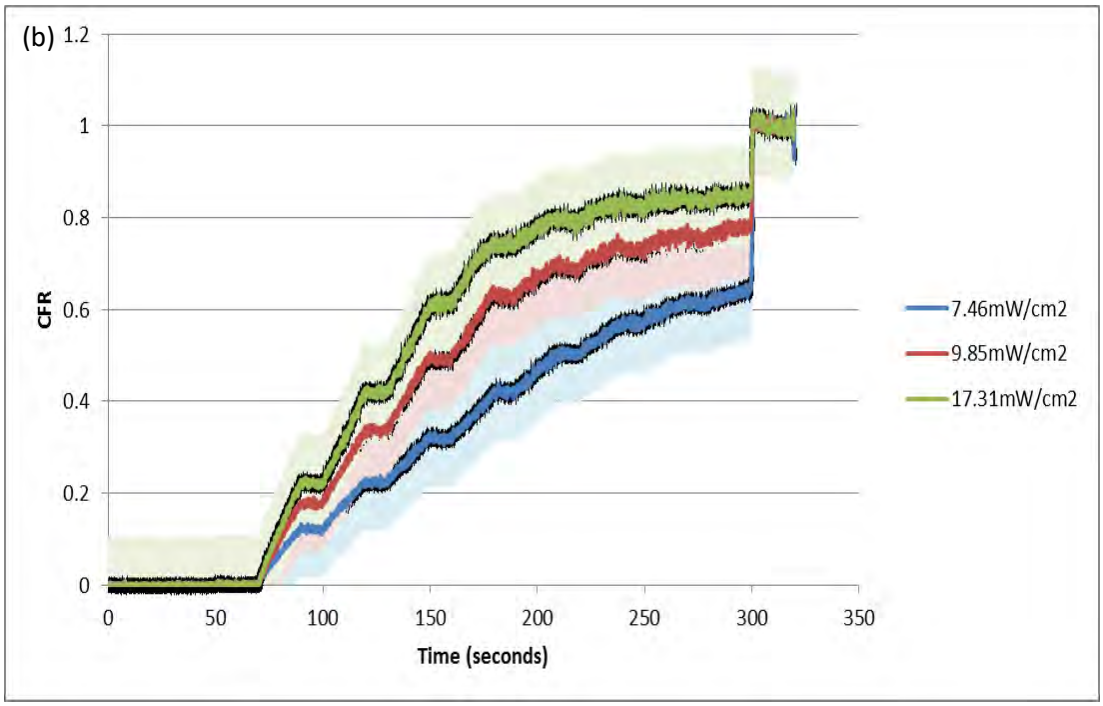

Figure 30: Normalized release profile of (a) NH_2 and (b) transferrin liposomes.

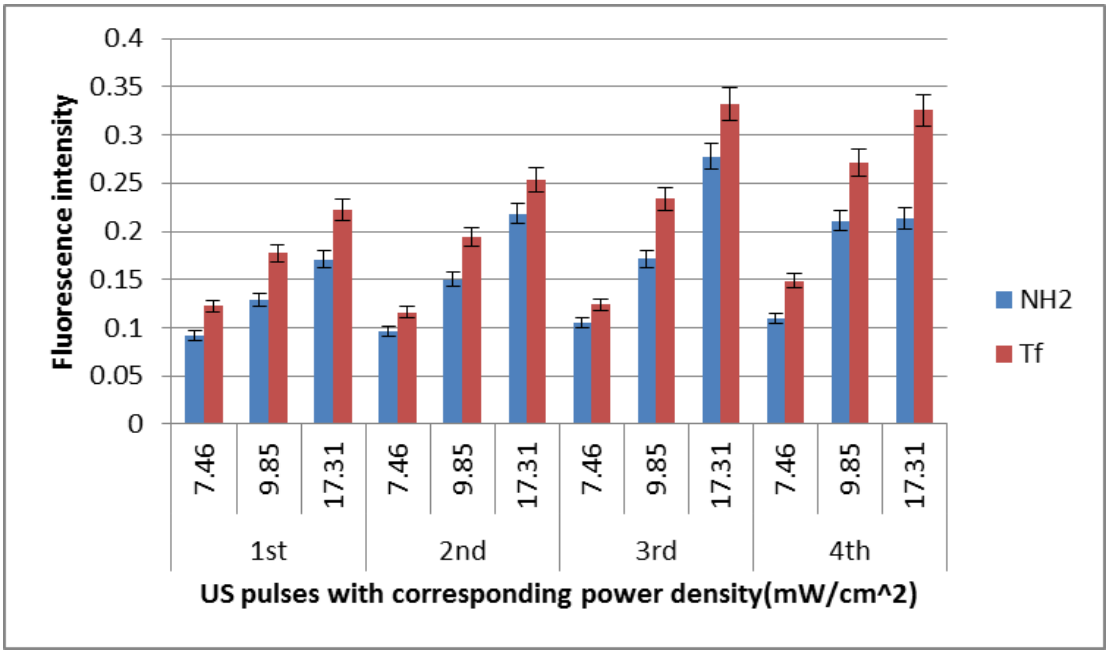

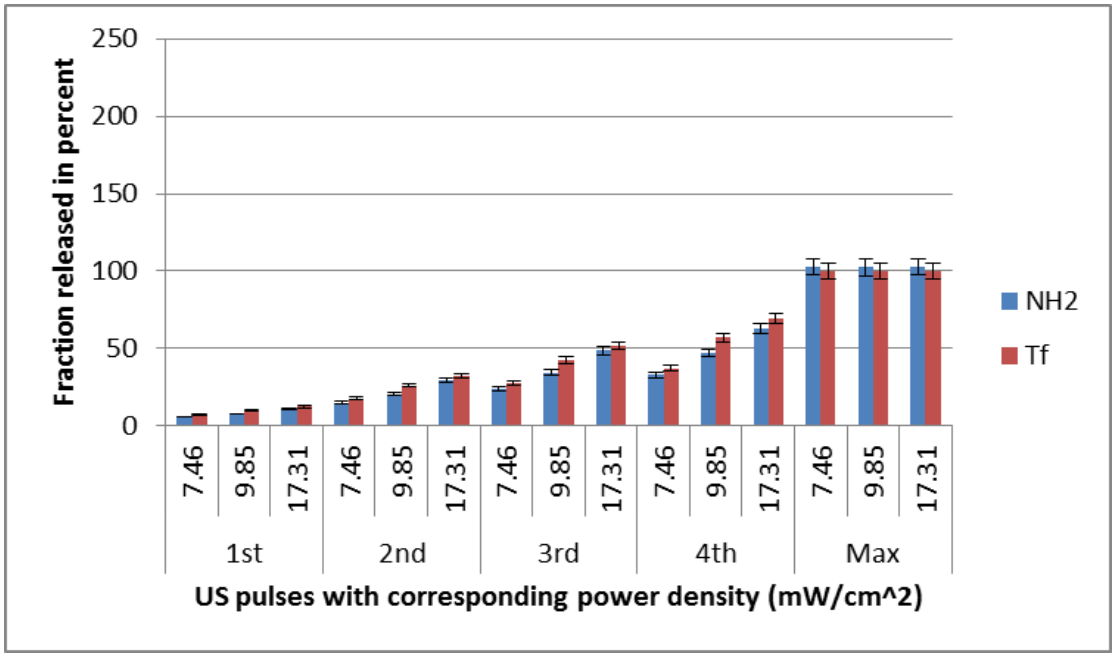

Figure 31: Comparison of LFUS calcein release from NH_2 liposomes and transferrin liposomes for four pulses in terms of fluorescence intensity (top) and CFR (bottom)

Table 8: Statistical comparison of LFUS release between NH_2 and transferrin liposomes for four pulses at different power densities

Intensity			CFR		
Pulse	**Power Density (mW/cm^2)**	**NH_2 vs. Tf p-value**	**Pulse**	**Power Density (mW/cm^2)**	**NH_2 vs. Tf p-value**
1st	*7.46*	0.03385	**1st**	*7.46*	0.0002688
	9.85	0.002905		*9.85*	$2.063x10^{-7}$
	17.31	0.01224		*17.31*	0.02601
2nd	*7.46*	0.06814	**2nd**	*7.46*	$4.641x10^{-23}$
	9.85	0.01391		*9.85*	$4.892x10^{-33}$
	17.31	0.1488		*17.31*	$1.054x10^{-6}$
3rd	*7.46*	0.1319	**3rd**	*7.46*	$2.095x10^{-31}$
	9.85	0.02098		*9.85*	$1.311x10^{-56}$
	17.31	0.5549		*17.31*	$1.087x10^{-8}$
4th	*7.46*	0.02439	**4th**	*7.46*	$1.525x10^{-43}$
	9.85	0.5683		*9.85*	$2.526x10^{-88}$
	17.31	0.1216		*17.31*	$5.329x10^{-55}$
Maximum release	*7.46*	-	**Maximum release**	*7.46*	$1.092x10^{-23}$
	9.85	-		*9.85*	$7.806x10^{-12}$
	17.31	-		*17.31*	0.0001037
$p \geq 0.05$	$0.04 \leq p < 0.05$	$0.03 \leq p < 0.04$	$0.02 \leq p < 0.03$	$0.01 \leq p < 0.02$	$p < 0.01$

5.4.4. Calculation of mechanical index. The mechanical index (MI) was introduced in section 3.3.5.2 as a parameter used to indicate the possibility of the occurrence of cavitation and is mathematically represented by equation (32).

$$MI = \frac{P_{neg}}{f^{0.5}} \tag{32}$$

The negative pressure (expressed in units of MPa) in the above equation is dependent upon the acoustic impedance of water *Z* (for human soft tissues the values of *Z* are comparable to those of water), and the intensity of the low-frequency ultrasound *I*. Mathematically, negative pressure is denoted by equation (33) below [108].

$$P_{neg} = \sqrt{2\,I\,Z} \tag{33}$$

For water, the acoustic impedance has a value of 1.48 MPasec/m [108, 109], and for the LFUS power densities used in this research, 7.46, 9.85, and 17.31 mW/cm^2 , the calculated MI values are 0.11, 0.12, and 0.16, respectively. According to literature, the threshold of collapse cavitation is expected to occur at around MI=0.3, biological effects are observed at MI>0.7, and tissue damage is expected to

occur at MI>1 [110–113]. Therefore, the obtained values are well below the collapse cavitation threshold of 0.3 indicating the occurrence of stable cavitation.

5.5. Offline High-Frequency Induced Release

As with low-frequency release, high frequency US release was performed on three batches of control and transferrin-conjugated liposomes (three replicates per batch) using an immersed probe at two different frequencies (1.07 MHz and 3 MHz) with corresponding power densities of (22.59 W/cm^2 and 158 W/cm^2 respectively). Again, the fluorescence level of the sample is first measured prior to sonication, and the obtained readings define the baseline intensity I_0. The increase in intensity associated with sonication is measured continuously with time and is represented as I_t. As mentioned in section 4.7.2, the US pulse is applied for 10 minutes, for a total of 200 minutes of sonication (the point at which there was no more observable increase in intensity). Next Triton X-100 was added to the sample to lyse the liposomes, and the fluorescence level increased slightly above the plateau indicating that the liposomes have released all their remaining contents. The highest value of intensity recorded during the release experiment is denoted by I_∞. The intensities were then used to determine the cumulative fraction release (CFR) given by equation (31).

5.5.1. HFUS offline release studies with NH_2 liposomes. This section describes the HFUS-triggered release of calcein from 3 batches of control liposomes (3 replicates each) at two frequencies 1.07 MHz and 3 MHz. Figure 32 depicts the release profiles at both frequencies.

As can be seen from Figure 32, release is indeed induced and increases as the time of sonication increases. Although the release profile at the higher frequency of 3 MHz showed a more sustained linear increase with time; the calcein release after each 10-minute insonation is quite lower than that achieved using the lower frequency of 1.07 MHz. The final release achieved after 200 minutes for 1.07 MHz was 45.27% while that of the 3 MHz was 18.85% (the percent release values at each time point are summarized in Table 9). The reason behind this behavior could be attributed to the fact that the cavitation threshold increases with increased frequency; in other words, collapse cavitation is less likely to occur because the bubbles are not given enough time to grow and collapse.

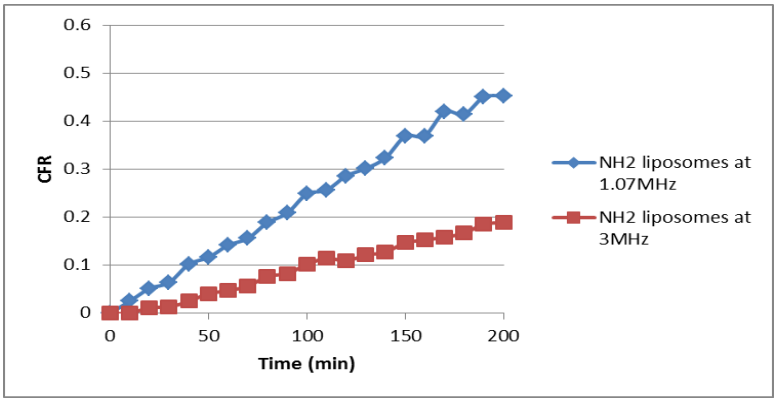

Figure 32: Normalized HFUS release profiles for control liposomes at 1.07MHz and 3MHz.

Table 9: Percent release obtained at 10 minute intervals for control liposomes at both 1.07 MHz and 3 MHZ.

Time (min)	**Calcein release (% normalized)**	
	1.07MHz	3MHz
10	2.496	0.0056
20	5.150	1.158
30	6.386	1.314
40	10.19	2.481
50	11.62	4.065
60	14.15	4.700
70	15.56	5.623
80	18.88	7.667
90	20.82	8.253
100	24.81	10.14
110	25.62	11.44
120	28.57	10.93
130	30.13	12.10
140	32.33	12.72
150	36.82	14.65
160	36.96	15.24
170	41.90	15.84
180	41.42	16.65
190	45.00	18.54
200	45.27	18.85

5.5.2. HFUS offline release studies with Tf liposomes. Similar to the analysis conducted in section 5.5.1 3 batches of transferrin conjugated liposomes (3 replicates each) were tested for release at the same two frequencies (1.07 MHz and 3 MHz) and corresponding power densities (22.59 and 158 W/cm^2). The release profile is depicted by Figure 33. The trend obtained was similar to that of the control

liposomes where a clear increase in release is observed after each insonation, and the release for 1.07 MHz is higher than that of 3 MHz. The final percent release values for the 1.07 MHz was 54.76% while that of the 3 MHz was 40.39%. Table 10 outlines the CFR values at each time point.

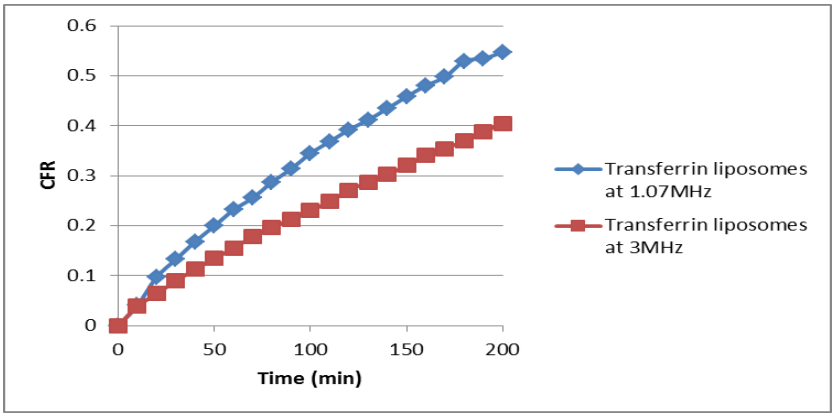

Figure 33: Normalized HFUS release profiles for Tf liposomes at 1.07MHz and 3MHz.

Table 10: Percent release obtained at each 10 minute interval for Tf liposomes at both 1.07MHz and 3MHZ.

Time (min)	**Calcein release (% normalized)**	
	1.07MHz	3MHz
10	4.020	3.879
20	9.701	6.367
30	13.25	8.966
40	16.83	11.26
50	19.94	13.40
60	23.17	15.52
70	25.57	17.83
80	28.73	19.67
90	31.38	21.34
100	34.48	23.01
110	36.81	24.81
120	39.20	27.09
130	41.17	28.74
140	43.45	30.26
150	45.84	32.01
160	48.04	34.01
170	49.77	35.39
180	52.93	36.99
190	53.46	38.82
200	54.75	40.39

5.5.3. Comparison between NH_2 and transferrin liposomes. This section presents a comparison between control and targeted liposomes at each of the frequencies (1.07 MHz and 3 MHz) used in the HFUS experiments. As can be observed from Figure 34, the release profile for transferrin liposomes shows a more linear increase with time, and the fraction release values tend to be higher than those obtained for control liposomes for both 1.07 MHz and 3 MHz frequencies. This slight difference in release could be indicative that the attachment of transferrin to the surface of liposomes has rendered them less stable and more sensitive to the mechanical effects of US waves than control liposomes. The above findings were further corroborated by the statistical analysis results, as transferrin-conjugated liposomes showed significantly higher release ($p<0.05$) when compared to non-targeted liposomes at both frequencies and power densities studied.

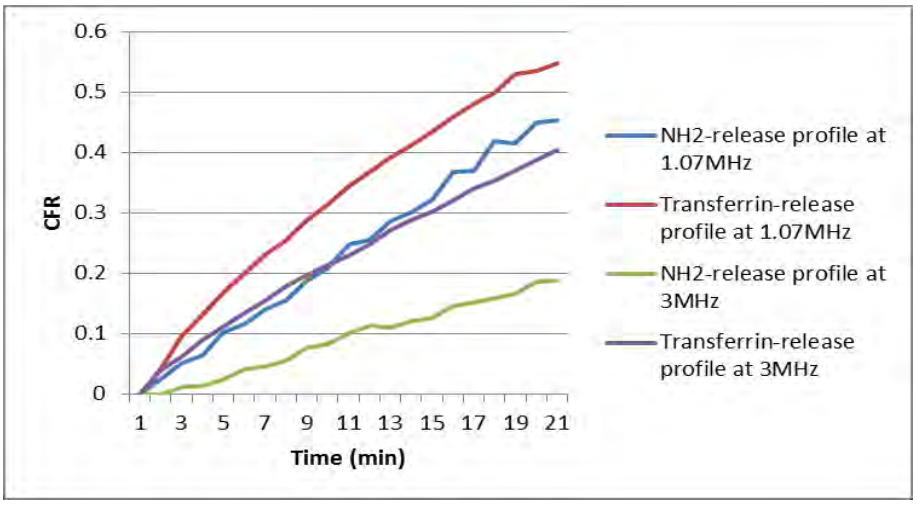

Figure 34: Comparison of HFUS release profiles for both types of liposomes at 1.07MHz and 3MHz.

5.5.4. Calculation of mechanical index. The mechanical indices MI were calculated using equation (32) detailed in section 5.4.4. For 1.07 MHz the obtained MI was 0.791, while at 3 MHz the MI was found to be 1.249. According to literature, collapse cavitation is expected to occur at MI>0.7. Given the MI values obtained for both frequencies, it is reasonable to deduce that the release in HFUS was induced by collapse cavitation. From the previous discussions it was noted that the release at 22.59 W/cm^2 was higher than that achieved at 158 W/cm^2; since a higher frequency was used for the latter power density the observation is consistent with the fact that

attenuation of US waves increases as frequency increases [112]. Thus, to achieve a higher release at 3 MHz, the power density should be increased to compensate for the energy lost in the form of heat. Finally, based on literature, release is expected to be higher at LFUS than HFUS because cavitation events are easier to be induced at LFUS conditions. This behavior can be attributed to the fact that cavitation is more likely to occur when bubbles are given enough time to grow and collapse, which is achieved at LFUS because the time interval for the negative peak pressure is sufficient for nucleation [113].

5.6. Kinetic Modeling of Drug Release

The significance of mathematical modeling in drug delivery applications along with the various types of models that can be used to simulate drug release kinetics were discussed in section 4.3.2. This section presents the derivations of some of the aforementioned models as well as their application to the results obtained from LFUS release studies in an attempt to find the best fitting model for the release kinetics of this research [101, 114–117]:

5.6.1. Zero order model. The zero order model assumes that the drug dosage form does not disaggregate and that the release of the drug is very slow, i.e. the amount of drug dissolved per unit time is a constant value. If the function *Q(t)*is assumed to represent the amount of the drug that is in solution at any time *t* then according to the zero order assumptions the behavior of the drug in solution is represented by:

$$\frac{dQ(t)}{dt} = K_0 \tag{34}$$

Where K_0 is a zero-order release constant which has units of concentration per unit time. Applying definite integration (integration by parts) with respect to time over the interval [0,t].

$$\int_{Q_0}^{Q_t} dQ(t) = \int_0^t K_0 dt \tag{35}$$

Where Q_t is the amount of drug released at time *t*. Q_0 is the initial amount of the drug in solution and is usually very small or assumed to be zero.

$$Q_t - Q_0 = K_0(t - 0) \tag{36}$$

$$Q_t = Q_0 + K_0 t \tag{37}$$

In order to re-define the model in terms of the variables used in this research, first the Cumulative Fraction Released (CFR) is given by the following equation:

$$\boldsymbol{CFR} = \frac{\boldsymbol{Drug\ released\ at\ any\ time,t - Initial\ Amount}}{\boldsymbol{Total\ amount\ of\ drug\ present}} = \frac{\boldsymbol{Q_t - Q_0}}{\boldsymbol{Q_T}} \quad (38)$$

Dividing equation (37) by Q_T, the total amount of the drug released/present gives:

$$\boldsymbol{CFR} = \frac{\boldsymbol{K_0}}{\boldsymbol{Q_T}}\boldsymbol{t} \quad (39)$$

Recalling the assumption that Q_0 is very small, and can be assumed to be 0. Introducing a constant k_0:

$$\boldsymbol{k_0} = \frac{\boldsymbol{K_0}}{\boldsymbol{Q_T}} \quad (40)$$

$$\boldsymbol{CFR} = \boldsymbol{k_0 t} \quad (41)$$

The plot of CFR vs. time should give a straight line with a slope of k_0 passing through the origin.

5.6.2. First order model. This model can be used to describe drug dissolution of dosage forms such as water-soluble drugs encapsulated in porous matrices as well as the modeling of the absorption and elimination of certain drugs. Contrary to the zero order model, the first order model assumes that the change in the concentration of the drug in solution is not constant but is a function of the instantaneous concentration. This can be represented mathematically as follows:

$$\frac{\boldsymbol{dC(t)}}{\boldsymbol{dt}} = -\boldsymbol{KC(t)} \quad (42)$$

Here $C(t)$ is the concentration of the drug at any time t, and K is the first-order release constant expressed-per unit time. Integrating both sides of the equation,

$$\int_{\boldsymbol{C_0}}^{\boldsymbol{C_t}} \frac{\boldsymbol{dC(t)}}{\boldsymbol{C(t)}} = \int_{\boldsymbol{0}}^{\boldsymbol{t}} -\boldsymbol{Kdt} \quad (43)$$

Where C_0 is the initial concentration of the drug in solution, and C_t is the concentration at any time t.

$$\boldsymbol{\ln\left(\frac{C_t}{C_0}\right) = -K(t - 0)} \quad (44)$$

Taking the exponential of both sides of the equation,

$$\frac{C_t}{C_0} = e^{-Kt} \tag{45}$$

Then simplifying the expression by multiplying both sides by C_0,

$$C_t = C_0 e^{-Kt} \tag{46}$$

Subtracting C_0 from both sides,

$$C_t - C_0 = C_0(e^{-Kt} - 1) \tag{47}$$

As with the zero order model, we desire to express the model in terms of the variables used in the research, therefore the definition of CFR is re-introduced:

$$CFR = \frac{Drug\ released\ at\ any\ time,t - Initial\ Amount}{Total\ amount\ of\ drug\ present} = \frac{C_t - C_0}{C_T} \tag{48}$$

Where C_T is the total amount of drug dissolved in the solution. Substituting the denominator in equation (48) by the expression generated in equation (47) and dividing both sides by C_T yields:

$$CFR = \frac{C_t - C_0}{C_T} = \frac{C_0}{C_T}(e^{-Kt} - 1) \tag{49}$$

Plot CFR vs. time at this point generates an exponential graph. In order to linearize this relationship first add $\frac{C_0}{C_T}$ to both sides of the equation, yielding

$$CFR + \frac{C_0}{C_T} = \frac{C_0}{C_T} e^{-Kt} \tag{50}$$

Taking the natural logarithm of both sides of the equation,

$$\ln\left(CFR + \frac{C_0}{C_T}\right) = \ln\left(\frac{C_0}{C_T}\right) - Kt \tag{51}$$

Thus, plotting $\ln\left(CFR + \frac{C_0}{C_T}\right)$ versus time would give a straight line graph with a slope of -K and non-zero y-intercept of $\ln\left(\frac{C_0}{C_T}\right)$. Assuming that the initial concentration of the drug in solution, C_0, is very low, the left-hand-side expression reduces to ln(CFR), consequently plotting ln(CFR) versus time would give a straight-line graph with the characteristics mentioned above.

5.6.3. Higuchi model. The Higuchi model was the first mathematical model formulated to describe drug release from a matrix system. This model was first conceived to describe release from planar systems; however it was modified to

account for other geometries and for porous systems. As mentioned in section 4.3.2.3 the equation describing the Higuchi model is based on the following assumptions [94, 103]:

- The initial drug concentration in the system must be much higher than drug solubility.
- Diffusivity occurs only in one dimension (negligible edge effects).
- The size of the drug particles is much smaller than the thickness of the film.
- The carrier material does not swell or dissolve.
- The diffusivity of the drug is constant (not dependent on time or position).
- Perfect sink conditions are maintained throughout the experiment.

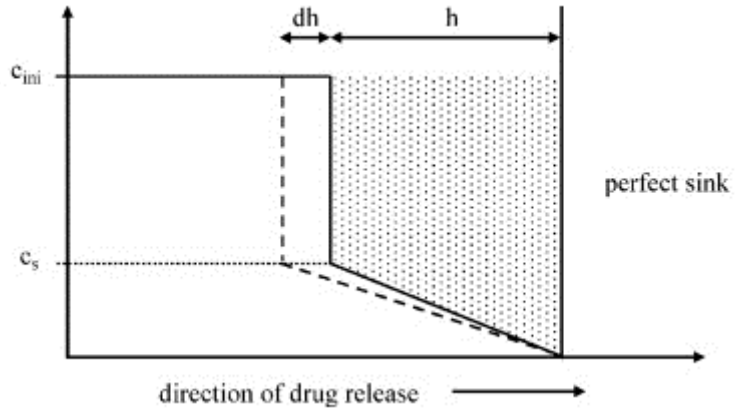

Figure 35: Representation of drug concentration profile according to Higuchi model assumptions [87].

For the system shown in Figure 35, the mass/mole flux of the drug can be defined as:

$$\frac{Q(t)}{A} = h\left(c_{lip} - \frac{c_s}{2}\right) \quad (52)$$

Where $Q(t)$ is the amount of drug released after time t, A is the surface area of the DDS in contact with the medium, c_{lip} is the concentration of the drug within the liposome (or any other DDS being used), and c_s is the solubility of the drug in the sink. To use this equation, however, the value of h, the distance from the DDS surface, must be known. The drug-concentration-distance profile, h, in equation (52) can be determined by taking infinitesimal time intervals of dt:

$$\frac{dQ}{A} = dh\left(c_{lip} - \frac{c_s}{2}\right) \tag{53}$$

The amount of the drug released after a time interval *dt*, is determined using Fick's 1st law of diffusion given by equation (54). Here *D* is the diffusion coefficient, *dc* is the differential of concentration, and *dx* is the differential of distance,

$$J = -D\frac{dc}{dx} = -D\left(\frac{-c_s}{h}\right) = \frac{1}{A}\frac{dQ}{dt} \tag{54}$$

This can be algebraically manipulated to yield:

$$\frac{dQ}{A} = -D\left(\frac{-c_s}{h}\right)dt \tag{55}$$

Equating the right-hand-side of equation (55) to the expression given by equation (53),

$$-D\left(\frac{-c_s}{h}\right)dt = dh\left(c_{lip} - \frac{c_s}{2}\right) \tag{56}$$

Using separation of variables, and integrating within the limits [0,t] for time and distance from the surface, 0 to a distance *h*,

$$\int_0^t \frac{2Dc_s}{2c_{lip}-c_s}\,dt = \int_0^h h\,dh \tag{57}$$

$$\frac{2Dc_s}{2c_{lip}-c_s}\,t = \frac{h^2}{2} \tag{58}$$

$$h = 2\sqrt{\frac{Dc_s t}{2c_{lip}-c_s}} \tag{59}$$

Manipulating equation (52) to generate an expression for *h*,

$$h = \frac{Q}{A\left(c_{lip}-\frac{c_s}{2}\right)} \tag{60}$$

Equating equations (52) and (59) and with some algebraic manipulation,

$$2\sqrt{\frac{Dc_s t}{2c_{lip}-c_s}} = \frac{2Q}{A(2c_{lip}-c_s)} \tag{61}$$

$$Q = A\sqrt{Dc_s t}\,\frac{(2c_{lip}-c_s)}{\sqrt{(2c_{lip}-c_s)}} \tag{62}$$

$$Q = A\sqrt{Dc_s(2c_{lip}-c_s)t} \tag{63}$$

In the classical Higuchi equation, the Higuchi constant, k_h, is taken to be

$$k_h = A\sqrt{Dc_s(2c_{lip} - c_s)} \tag{64}$$

Substituting the expression for the Higuchi constant in equation (63) yields:

$$Q = k_h\sqrt{t} \tag{65}$$

In order to find the relation between CFR and time, as with the previous models, the following manipulations were performed:

$$CFR = \frac{Q-Q_0}{Q_T} = \frac{k_h\sqrt{t}}{Q_T} - \frac{Q_0}{Q_T} \tag{66}$$

Finally, plotting CFR versus the square root of time provides a linear graph with a slope of $\frac{k_h}{Q_T}$ and a y-intercept of $-\frac{Q_0}{Q_T}$. If the value of Q_0 is very small in comparison to that of Q_T, which is generally the case, the y-intercept will be very close to 0.

5.6.4. Hixson-Crowell. In this model, the following assumptions are made:

- Dissolution occurs normal to the surface of the solute particles.
- Agitation is uniform over the exposed surface.
- The particles are spherical.

Using a special form of Fick's law known as the Noyes-Whitney equation to describe the dissolution of the drug,

$$\frac{dW}{dT} = \frac{kA(C_s - C_\infty)}{l} \tag{67}$$

Where dW/dT represents the rate of dissolution, k is the Noyes-Whitney constant and contains the diffusion constant D, A is the surface area, C_s is the solute concentration, C_o is the concentration of the bulk solution, which in this case is assumed to be zero, and L is the diffusion layer. Simplifying the previous equation gives:

$$dW = kA\frac{(C_s)}{l}dt \tag{68}$$

The mass is represented as follows and is taken as negative because we are dealing with drug loss,

$$dW = -\rho dV \tag{69}$$

Since liposomes are considered to be spherical in shape (*N* represents the number of spheres),

$$\boldsymbol{V = \frac{4}{3}\pi r^3 N} \tag{70}$$

$$\boldsymbol{\frac{dV}{dr} = 4\pi N r^2} \tag{71}$$

Next, combining equations (68) and equations (69) and substituting for *dV* and *A*, we get the following:

$$\boldsymbol{dW = -\rho 4\pi N r^2 dr = \frac{k4\pi N r^2 C_s dt}{l}} \tag{72}$$

Eliminating similar terms and integrating on both sides,

$$\boldsymbol{\int_{r_o}^{r_t} -\rho dr = \frac{kC_s}{l}\int_0^t dt} \tag{73}$$

$$\boldsymbol{-(r - r_o) = \frac{kC_S T}{\rho l}} \tag{74}$$

$$\boldsymbol{r_t = -\frac{kC_S T}{\rho l} + r_o} \tag{75}$$

Given that we require the results in terms of CFR, the weight of dissolution *W* is used instead of the volume, equation (70) should be used to determine the volume for *N* spheres. Then the weight of each sphere can be expressed as:

$$\boldsymbol{W = \rho\frac{4}{3}\pi r^3 N} \tag{76}$$

Raising all variables to the cubic root and re-arranging for *r* yields:

$$\boldsymbol{r = \frac{W^{\frac{1}{3}}}{\left(\rho\frac{4}{3}\pi N\right)^{\frac{1}{3}}}} \tag{77}$$

Equating equation (74) and equation (75) while also expressing r_o in the form provided by equation (77) gives:

$$\boldsymbol{\frac{W_t^{\frac{1}{3}}}{\left(\rho\frac{4}{3}\pi N\right)^{\frac{1}{3}}} = -\frac{kC_S T}{\rho l} + \frac{W_o^{\frac{1}{3}}}{\left(\rho\frac{4}{3}\pi N\right)^{\frac{1}{3}}}} \tag{78}$$

Simplifying the above equation into the Hixson-Crowell form,

$$\boldsymbol{W_t^{\frac{1}{3}} = -\frac{kC_S T}{\rho l}\left(\rho\frac{4}{3}\pi N\right)^{\frac{1}{3}} + W_o^{\frac{1}{3}}} \tag{79}$$

Let *K'* represent the constant related to the surface, the shape and the density of the particle,

$$W_0^{\frac{1}{3}} - W_t^{\frac{1}{3}} = \frac{kK'C_S T}{l}(N)^{\frac{1}{3}} \quad (80)$$

Re-defining the model in terms of CFR to make compatible with the variables used in this research,

$$CFR = \frac{Drug\ released\ at\ any\ time, t - Initial\ Amount}{Total\ amount\ of\ drug\ present} = \frac{C_t - C_0}{C_T} = \frac{W_t - W_0}{W_0} \quad (81)$$

Simplifying and linearizing the above equation yields:

$$[(1 - CFR)]^{\frac{1}{3}} = K_{HC}t \quad (82)$$

Here K_{HC} represents the release constant and according to equation 81 a plot of $[(1\text{-}CFR)]^{1/3}$ versus time would yield a straight line with a slope of K_{HC}.

5.6.5. Korsmeyer-Peppas (power law) model. The Korsmeyer-Peppas model has the simple form:

$$CFR \approx k_{kp}t^n \quad (83)$$

Where k_{kp} is a constant that accounts for the structural and geometrical characteristics of the DDS, and *n* is the release exponent which characterizes the drug release mechanism. Starting with Fick's second law in three-dimensional space,

$$\frac{\partial C}{\partial t} = D\left(\frac{\partial^2 C}{\partial x^2} + \frac{\partial^2 C}{\partial y^2} + \frac{\partial^2 C}{\partial z^2}\right) \quad (84)$$

Here *C* represents concentration, *D* is the diffusion coefficient and *x*, *y* and *z* represent the direction of diffusion. Assuming diffusion of the drug only in the x-direction the expression reduces to:

$$\frac{\partial C}{\partial t} = D\frac{\partial^2 C}{\partial x^2} \quad (85)$$

This second order differential equation can be solved using the error function, and numerical methods, an approach that was initially described and derived by John Crank in 1975 [118]. The general solution for the above differential equation for a non-steady state general boundary conditions problem where the surface concentrations are constant and the initial distribution within the DDS is given by a function of position *f(x)* can be expressed by the following trigonometric series:

$$t \geq 0, \qquad x = 0, \qquad C = C_1$$

$$t \geq 0, \qquad x = l, \qquad C = C_2$$

$$t = 0, \qquad 0 < x < l, \qquad C = f(x)$$

$$\boldsymbol{C = C_1 + (C_2 - C_1)\frac{x}{l} + \frac{2}{\pi}\sum_1^\infty \frac{C_2\cos(n\pi) - C_1}{n}\, sin\frac{n\pi x}{l}\, e^{\frac{-Dn^2\pi^2 t}{l^2}} + \frac{2}{l}\sum_1^\infty \sin\left(\frac{n\pi x}{\pi}\right) e^{\frac{-Dn^2\pi^2 t}{l^2}} \int_0^1 f(x')\sin\left(\frac{n\pi x'}{l}\right) dx'} \qquad (86)$$

Assuming uniform initial distribution and equal surface concentrations, the boundary conditions are:

$$t = 0, \qquad -\frac{l}{2} < x < \frac{l}{2}, \qquad C = C_0$$

$$t > 0, \qquad x = \pm\frac{l}{2}, \qquad C = C_1$$

The physical meaning of these conditions is that initially, within the drug carrier, the concentration is uniformly the initial concentration of the drug, C_0. Then at any time, t, the concentration of the drug at the boundary between the DDS and the solution is equal and constant at C_1. These conditions may be interpreted as perfect sink conditions, where the drug has an endless sink to dissolve into, and the DDS is separated from the solution by a membrane. Now, the earlier solution can be simplified to be:

$$\boldsymbol{\frac{C - C_0}{C_1 - C_0} = 1 - \frac{4}{\pi}\sum_{n=0}^\infty \frac{8}{(2n+1)^2\pi^2}\, e^{\frac{-D(2n+1)^2\pi^2 t}{4l^2}} \cos\left(\frac{(2n+1)\pi x}{2l}\right)} \qquad (87)$$

By rearranging and integrating the equation to yield M_t the total amount of the drug diffused into the solution, and M_∞ the total amount of the drug diffused after infinite time,

$$\boldsymbol{\frac{M_t}{M_\infty} = 1 - \sum_{n=0}^\infty \frac{8}{(2n+1)^2\pi^2}\, e^{\frac{-D(2n+1)^2\pi^2 t}{4l^2}}} \qquad (88)$$

Using the error function to derive a more simplified form of the above equation that is useful for small intervals of time,

$$\boldsymbol{\frac{M_t}{M_\infty} = 2\left(\frac{Dt}{l^2}\right)^{\frac{1}{2}}(\pi^{-\frac{1}{2}} + 2\sum_{n=1}^\infty (-1)^n\, ierfc\left(\frac{nl}{\sqrt{Dt}}\right)} \qquad (89)$$

Where,

$$\boldsymbol{erfc(z) = 1 - \mathrm{erf}(z) = \frac{2}{\sqrt{\pi}} \int_z^{\infty} e^{-t^2} dt} \quad (90)$$

And subsequently,

$$\boldsymbol{ierfc(x) = \int_x^{\infty} erfc(z) dz = \frac{1}{\pi^{\frac{1}{2}}} e^{-x^2} - x\, erfc(x)} \quad (91)$$

In the above equation as the argument of the i_{erfc} function increases toward infinity, its value decreases to a value close to 0. Thus, the smaller the time intervals the argument for the i_{erfc} function becomes infinitely large, yielding a small contribution from the i_{erfc} term. Consequently, the second term from the derived equation tends to 0 and can be removed from the expression when dealing with small intervals of time, giving:

$$\boldsymbol{\frac{M_t}{M_\infty} = 2\left(\frac{Dt}{\pi l^2}\right)^{\frac{1}{2}}} \quad (92)$$

Taking the Korsmeyer-Peppas constant as:

$$\boldsymbol{k_{kp} = 2\left(\frac{D}{\pi l^2}\right)^{\frac{1}{2}}} \quad (93)$$

Again to express the equation in terms of the variables used in this research the value for $\frac{M_t}{M_\infty}$ is taken to be equal to CFR (assuming the initial amount of the diffused drug is minute enough to assume it to be 0), and introducing the constant from equation 92, then the above relation can be denoted as:

$$\boldsymbol{CFR = \frac{M_t}{M_\infty} = k_{kp} t^{\frac{1}{2}}} \quad (94)$$

The above expression is similar to the Korsmeyer-Peppas model introduced at the beginning of the section. Thus, if CFR is plotted against the square root of time, a straight-line graph will be observed, with a slope of $2(D/\pi l^2)^{1/2}$. This is the case where Fick's Law holds true. In most cases, the release mechanism deviates from Fick's Law, as there is usually more than one release mechanism in use. This leads to a more generic equation that explains a range of release mechanisms:

$$\boldsymbol{CFR = \frac{M_t}{M_\infty} = at^n} \quad (95)$$

As mentioned earlier, *n* characterizes the different release mechanisms. Taking the logarithms of both sides of the equation,

$$\log(\boldsymbol{CFR}) = \log(\boldsymbol{a}) + \boldsymbol{n}\log(\boldsymbol{t}) \quad (96)$$

Thus, if *log(CFR)* is plotted against the logarithm of time, a straight-line graph can be obtained with a y-intercept at *log(a)*, where *a*, in this case, is k_{kp}, and the slope is *n*.

5.6.6. Weibull model. The Weibull model is a more empirical model that has an extended exponential form and applies to most drug dissolution cases. It is well established that the geometry of the dosage form has an impact on the dissolution properties; the dissolution rates from Euclidean spaces has been described abundantly in literature, however, an interesting problem arises when the geometry of the release device is irregular, e.g. a fractal. Bunde *et al.* [119] were amongst the first to study the dissolution rates of dosage forms with fractal geometries. Their work reported that the release rate could be described using the power law. However, more recent studies have found that the power law, or Korsemeyer-Peppas model, is representative of the drug dissolution only at the initial stages of release, while at later stages of the release the Weibull model was found to be better at predicting the release behavior, thus giving a broader and more generalized view of the release profile [116]. This model is based on the assumptions are that there exist a number of drug particles in the system, *N*, that are homogeneously distributed in the percolation cluster (refer Figure 36).

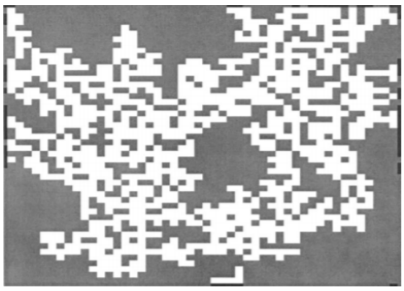

Figure 36: Example of a Percolation Fractal Embedded on a 2-dimensional Square Lattice [103].

In order for these particles to be released into the solution they must reach an exit and escape from the cluster. The rate at which the particles (drug particles, in our case) escape is expected to be proportional to the fraction of particles, f_r, that are able to reach an exit in a time interval, *dt*. After the particles start escaping, depletion zones are generated resulting in the de-homogenization of the system, and segregation

effects begin to have a significant impact on release. To describe these effects, f_r is taken to be a function of time $f_r(t)$ [103, 116, 118].

The drug release process is modeled by the fractal kinetics for the reaction:

$$A + B \rightarrow B$$

Where *A* represents the particles diffusing (the drug particles), and *B* are the sites or static particles (the solution) which is constant. Thus, the differential equation obtained is:

$$\frac{dN}{dt} = -k' fr(t) N \tag{97}$$

Where *k'* is a proportionality constant accounting for the constant concentration of *B*, and *fr(t)*. *N* denotes the number of particles that are able to reach an exit in a time interval *dt*, and the negative sign denotes that the value of *N*, i.e. the particles in the DDS, are decreasing with time. The major assumption in fractal kinetics is that $f_r(t)$ has the form of

$$fr(t) \approx t^{-m} \tag{98}$$

Therefore equation (97) can be expressed as:

$$\frac{dN}{dt} = -k' \frac{N}{t^m} \tag{99}$$

Using separation of variables, and integrating between the time interval 0 to *t*, and N_0 to *N* respectively; where N_0 is the initial amount of the drug within the DDS, and *N* denotes the final release of the drug into the solution,

$$\int_{N_0}^{N} \frac{dN}{N} = \int_0^t -k' t^{-m} dt \tag{100}$$

$$\ln\left(\frac{N}{N_0}\right) = -k' t^{1-m} \tag{101}$$

$$N = N_0 e^{-k' t^{1-m}} \tag{102}$$

If *N* and N_0 are replaced by the amounts of the drug, or M_d and M_0 , respectively and a constant b which is defined as $b = 1 - m$, the more familiar version of the Weibull equation is obtained:

$$M_d = M_0 e^{-k' t^b} \tag{103}$$

Given that M_d is the amount of drug remaining in the DDS, the amount of drug in solution at any time, *M*, is written as:

$$\boldsymbol{M = M_0 - M_d = M_0\left(1 - e^{-k't^b}\right)} \quad (104)$$

Assuming that the initial concentration of the drug in solution is negligible, expressing the equation in terms of CFR, $CFR = \frac{M}{M_0}$, and rearranging the expression after having taken the natural logarithm of both sides of the equation gives:

$$\boldsymbol{\ln(1 - CFR) = -k't^b} \quad (105)$$

Next, taking the logarithm of both sides of the equation (depending on if the values attained in the release experiment allow it),

$$\boldsymbol{\log(-\ln(1 - CFR)) = -\log(k') + b\,log(t)} \quad (106)$$

Where the log-log plot of *(-ln(1-CFR))* versus time would be a straight-line graph with a y-intercept value of *log(-k')* and a slope of *b*.

5.6.7. Baker-Lonsdale model. The Baker-Lonsdale model is a modification of the Higuchi model used to describe drug release from spherical matrices and is based on the assumption that the matrix is homogenous and has no fractures that will cause unintended release. Mathematically the model is represented by:

$$\boldsymbol{\frac{3}{2}\left[1 - \left(1 - \frac{M_t}{M_\infty}\right)^{\frac{2}{3}}\right] - \frac{M_t}{M_\infty} = \frac{3D_mC_{ms}}{r_0^2C_0}t} \quad (107)$$

Where M_t is the amount of drug released at time t, M_∞ is the amount of drug released at infinite time, D_m is the diffusion coefficient, C_{ms} is the drug solubility in the matrix, r_0 is the of the spherical matrix and C_0 is the initial concentration of the drug in the matrix. Assuming that the initial release of the drug is negligible and re-defining the equation in terms of CFR:

$$\boldsymbol{\frac{M_t}{M_\infty} = CFR} \quad (108)$$

Equation (107) becomes:

$$\boldsymbol{\frac{3}{2}\left[1 - (1 - CFR)^{\frac{2}{3}}\right] - CFR = k_{BL}t} \quad (109)$$

Where;

$$\boldsymbol{k_{BL} = \frac{3D_m C_{ms}}{r_0^2 C_0}} \quad (110)$$

Thus, if $\frac{3}{2}\left[1-(1-CFR)^{\frac{2}{3}}\right]-CFR$ was plotted against time, t, a straight line with slope k_{BL} can be obtained.

5.6.8. Hopfenberg model. This model was developed to describe the drug release kinetics from slabs, spheres, infinite cylinders undergoing heterogeneous erosion. The equation representing is model is given by:

$$\boldsymbol{\frac{M_t}{M_\infty} = 1 - \left[1 - \frac{k_0 t}{C_0 a_0}\right]^n} \quad (111)$$

Where M_t is the amount of drug dissolved at time t, M_∞ is the amount of drug dissolved when the pharmaceutical dosage form has been fully exhausted, k_0 is the erosion rate constant, C_0 is the initial concentration of drug in the matrix, a_0 is the initial radius of the sphere/cylinder or half the thickness of the slab and n has the values 1, 2 and 3 for a slab, cylinder, and sphere, respectively. Assuming that there is no initial amount of drug dissolved:

$$\boldsymbol{\frac{M_t}{M_\infty} = CFR} \quad (112)$$

Equation (111) can be expressed in terms of CFR as:

$$\boldsymbol{1-(1-CFR)^{\frac{1}{n}} = k_{Hf} t} \quad (113)$$

Where;

$$\boldsymbol{k_{Hf} = \frac{k_0}{C_0 a_0}} \quad (114)$$

Since liposomes have a spherical shape *n* here is equal to 3; thus, equation 108 can be written as:

$$\boldsymbol{1-(1-CFR)^{\frac{1}{3}} = k_{Hf} t} \quad (115)$$

By plotting $1-(1-CFR)^{\frac{1}{3}}$ against t a straight line with slope k_{Hf} can be obtained.

5.6.9. Gompertz model. The Gompertz model was developed to describe the release from drugs possessing good stability and intermediate release rate.

Mathematically, the model is expressed by a simple exponential relation describing the dissolution profile [117].

$$\boldsymbol{X(t) = X_{max}\exp\left[-\alpha e^{\beta\, log(t)}\right]} \quad (116)$$

Where $X(t)$ is the fraction of drug dissolved at time t, X_{max} is the maximum dissolution fraction, α stands for the scale parameter which is equivalent to the undissolved drug proportion while β is a shape parameter equivalent to the dissolution rate per unit time. After the linearization and re-definition of the model to make it compatible with the variables used in this study, the model becomes:

$$\boldsymbol{\ln(-\ln(CFR)) = k_G \log(t) + \ln(\alpha)} \quad (117)$$

Here k_G is the Gompertz release constant which was earlier introduced as β. According to equation 116, a plot of ln(-ln(CFR)) versus time would yield k_G as the slope.

5.6.10. Model accuracy for NH_2 liposomes. In this section, the data collected from LFUS release in this research was fitted to the linearized form of each of the previously discussed models. The concentration or amount of drug released from the liposomes was represented by the Cumulative Fraction Release (CFR) (defined by equation (30)), and the fit of each model equation was assessed in terms of the value of the coefficient of determination, R^2, which was obtained from the linear trend line equations. The plots for the first batch of NH_2 liposomes at 7.46 mW/cm^2 for each model are presented by Figures 37 through 45 below while the remaining plots are provided in the appendices.

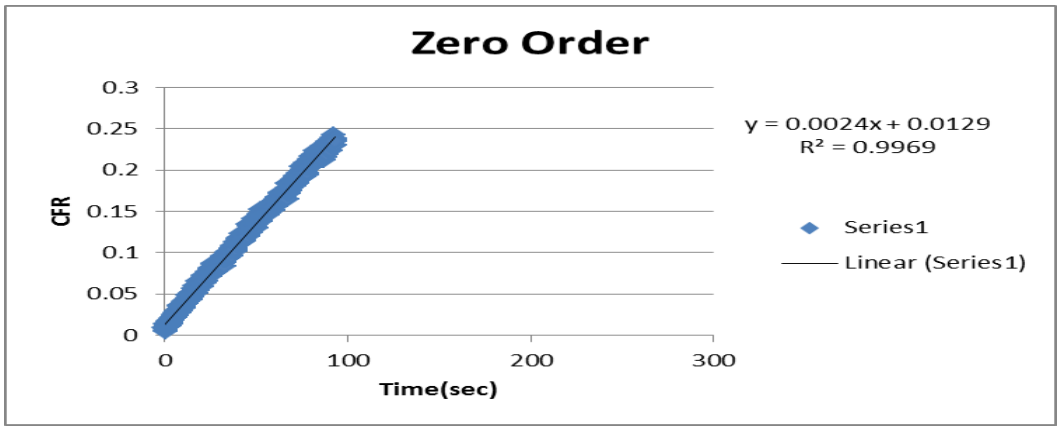

Figure 37: Zero Order Model plot for the first batch of NH_2 liposomes at a power density of 7.46mW/cm^2.

Figure 38: First Order Model plot for the first batch of NH_2 liposomes at a power density of 7.46mW/cm^2.

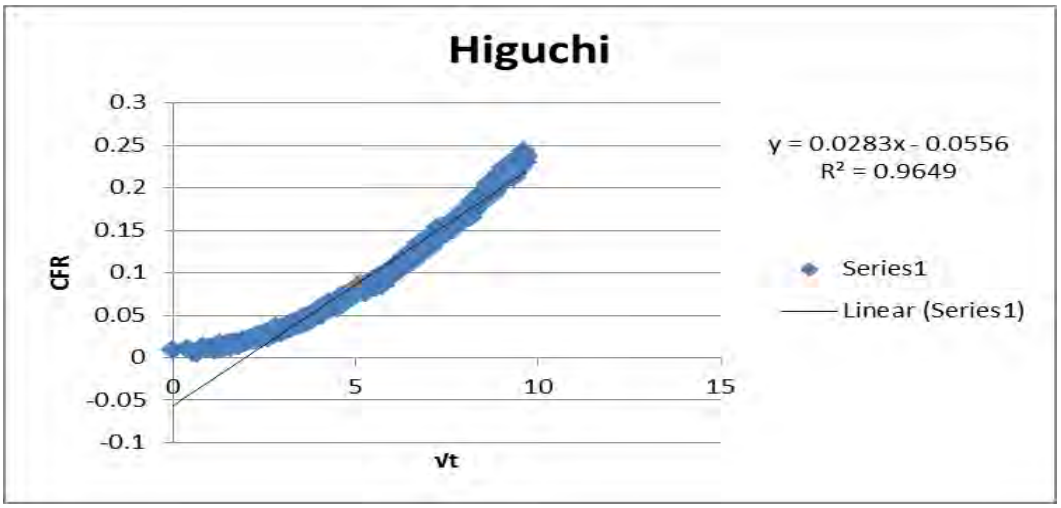

Figure 39: Higuchi Model plot for the first batch of NH_2 liposomes at a power density of 7.46mW/cm^2.

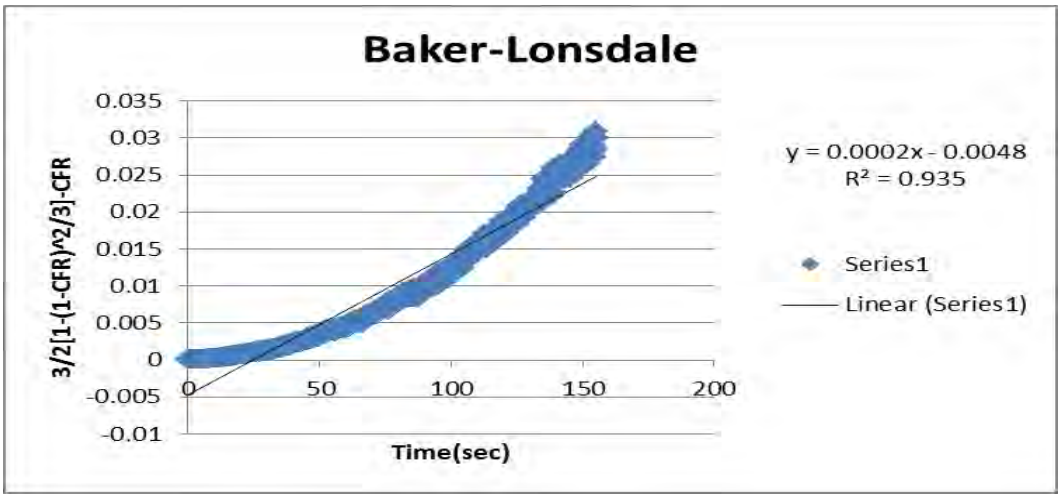

Figure 40: Baker-Lonsdale Model plot for the first batch of NH_2 liposomes at a power density of 7.46mW/cm^2.

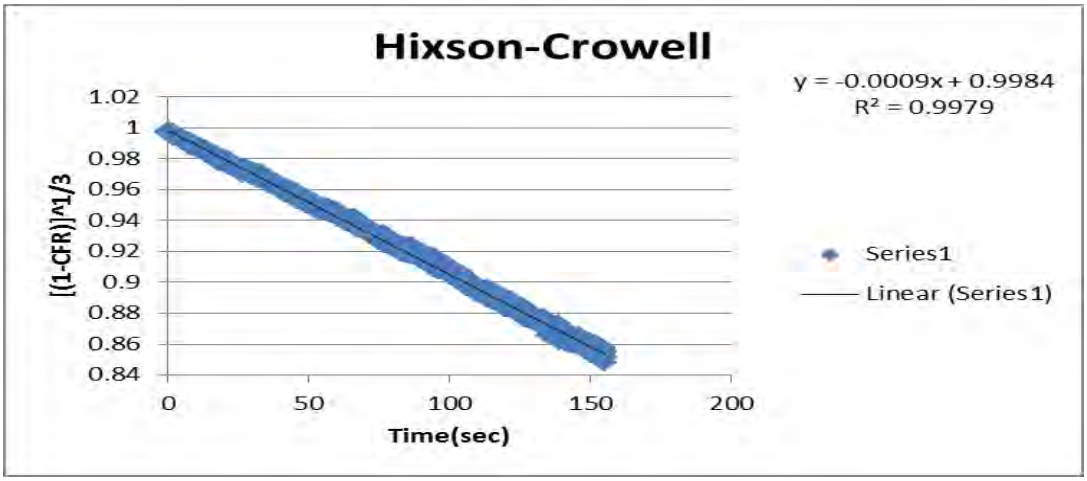

Figure 41: Hixson-Crowell Model plot for the first batch of NH_2 liposomes at a power density of 7.46mW/cm^2.

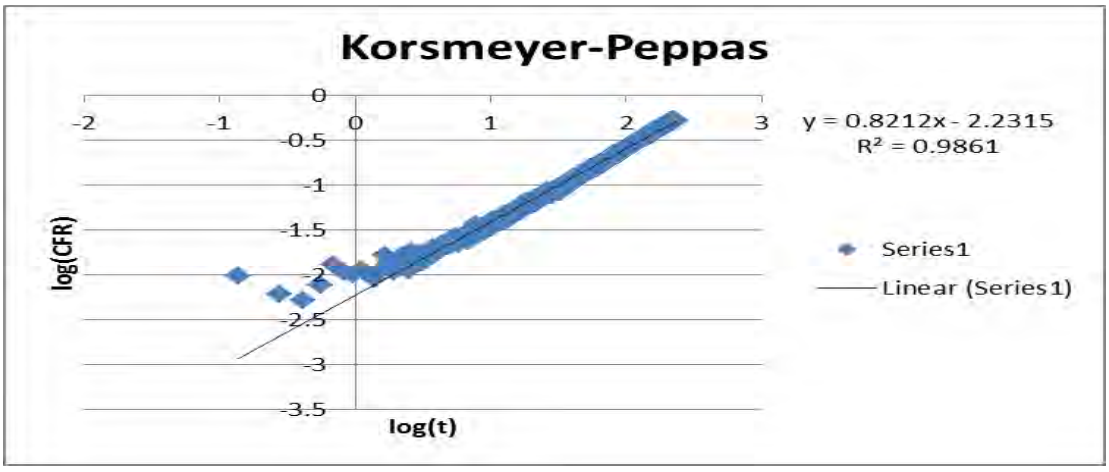

Figure 42: Korsmeyer-Peppas Model plot for the first batch of NH_2 liposomes at a power density of 7.46mW/cm^2.

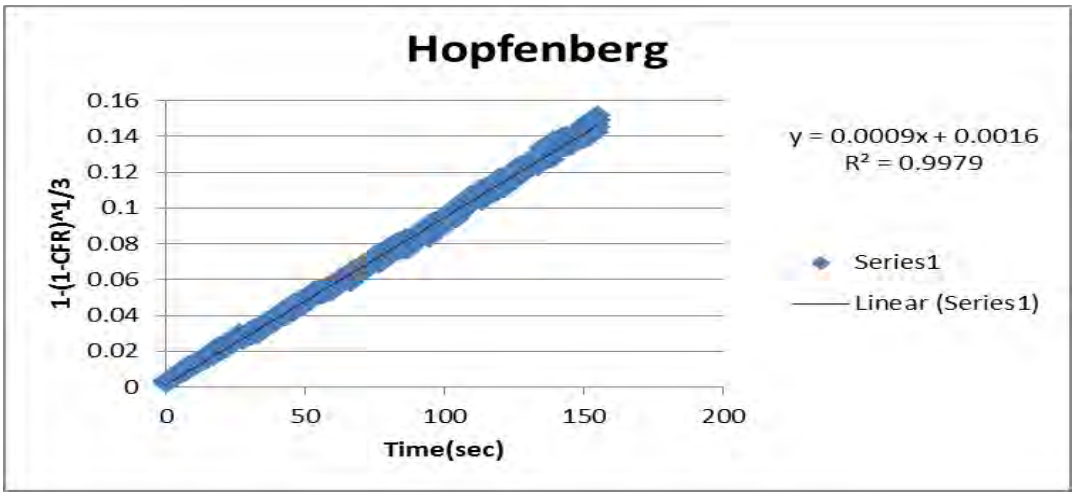

Figure 43: Hopfenberg Model plot for the first batch of NH_2 liposomes at a power density of 7.46mW/cm^2.

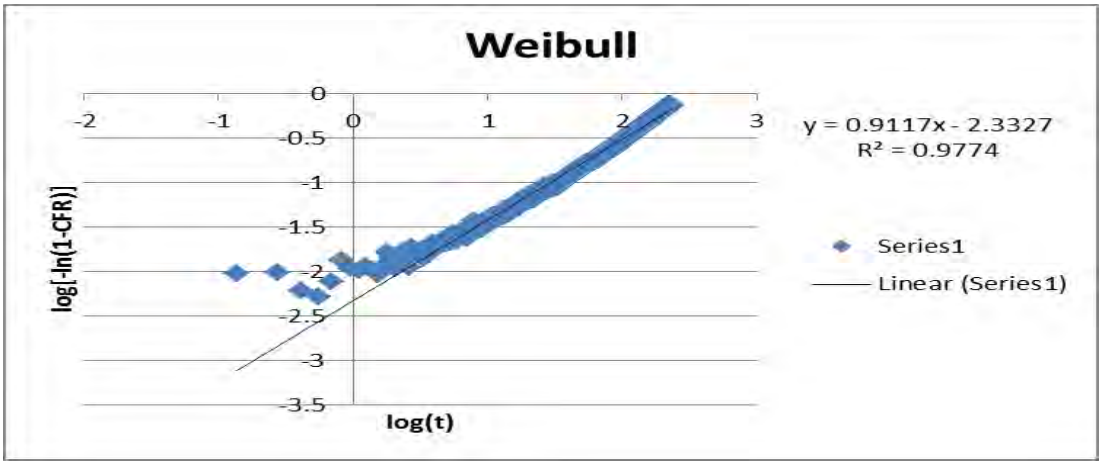

Figure 44: Weibull Model plot for the first batch of NH_2 liposomes at a power density of 7.46mW/cm^2.

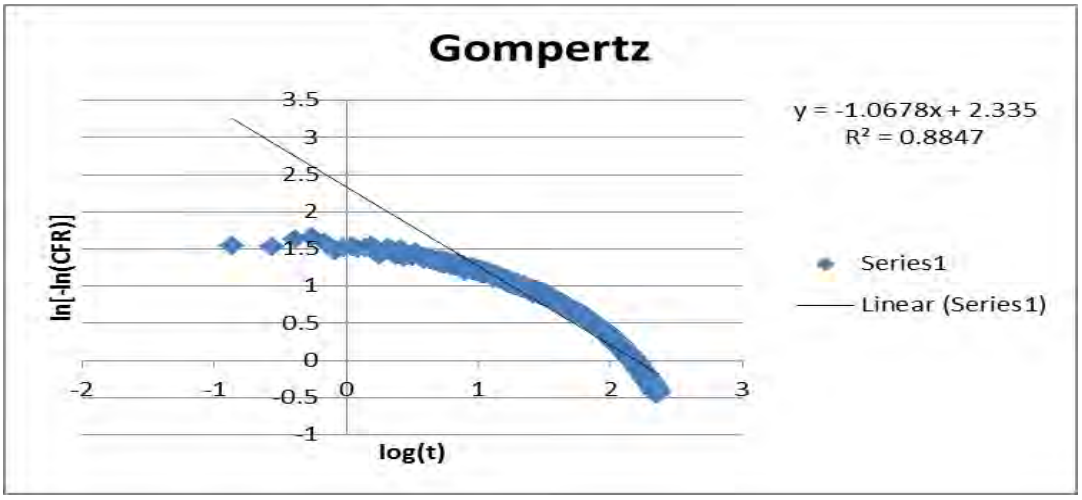

Figure 45: Gompertz Model plot for the first batch of NH_2 liposomes at a power density of 7.46mW/cm^2.

As mentioned earlier, the coefficient of determination R^2 values, obtained from the linear trend line equations of the generated plots, were used to determine the best fitting model(s). A summary of the R^2 values for each model is presented in Table 11. According to the obtained values, the collected data displayed excellent adherence to all models, particularly the Korsmeyer-Peppas, Hixson-Crowell, Weibull and Hopfenberg models. However, the R^2 values were slightly lower for the first order and Gompertz models for all of the tested NH_2 liposome batches.

Table 11: R^2 values for NH_2 liposomes for each model at three power densities (7.46, 9.85 and 17.31 mW/cm^2).

Model	NH_2 1st batch			NH_2 2nd batch			NH_2 3rd batch		
	7.46m W/cm^2	9.85m W/cm^2	17.31m W/cm^2	7.46m W/cm^2	9.85m W/cm^2	17.31m W/cm^2	7.46m W/cm^2	9.85m W/cm^2	17.31m W/cm^2
Zero Order	0.9969	0.9835	0.9442	0.9904	0.9464	0.8523	0.9841	0.9438	0.8671
First Order	0.8338	0.7568	0.7406	0.7827	0.7367	0.6298	0.7544	0.7285	0.6471
Higuchi	0.9649	0.9825	0.9769	0.9788	0.9796	0.9481	0.9821	0.98	0.9542
Korsmeyer-Peppas	0.9861	0.9923	0.9806	0.991	0.9853	0.9646	0.9923	0.9817	0.9643
Hixson-Crowell	0.9979	0.9964	0.9753	0.9969	0.9809	0.9253	0.9946	0.9739	0.9244
Baker-Lonsdale	0.935	0.9648	0.9764	0.9515	0.9761	0.9642	0.9668	0.9803	0.9636
Weibull	0.9774	0.9872	0.9752	0.982	0.978	0.9779	0.9897	0.9797	0.974
Hopfenberg	0.9979	0.9964	0.9753	0.9969	0.9809	0.9253	0.9946	0.9739	0.9244
Gompertz	0.8847	0.8850	0.8810	0.8735	0.8673	0.9119	0.9066	0.8975	0.9157

5.6.11. Model accuracy for transferrin liposomes. As with NH_2 liposomes, the data collected from LFUS release of transferrin liposomes was fitted to the linearized form of each of the previously discussed mathematical models. Similarly, the concentration or amount of drug released from the liposomes was given by the Cumulative Fraction Release (CFR) (defined by equation (30)) and the fit of each model equation was assessed in terms of the value of the coefficient of determination, R^2, which was obtained from the linear trend line equations. The plots for the first batch of transferrin liposomes at 7.46 mW/cm^2 (Figures 46-54) with the R^2 values for each model are presented below while the remaining plots are provided in the appendix. Table 12 presents the R^2 values obtained for transferrin liposomes and based on these values the transferrin liposomes seem to follow the behavior of NH_2 liposomes as they showed excellent adherence to all models, specifically the Korsmeyer-Peppas, Hixson-Crowell, Weibull and Hopfenberg models. However, once again the first order and Gompertz models had relatively lower R^2 values.

Figure 46: Zero Order Model plot for the first batch of Tf liposomes at a power density of 7.46mW/cm^2.

Figure 47: First Order Model plot for the first batch of Tf liposomes at a power density of 7.46mW/cm^2.

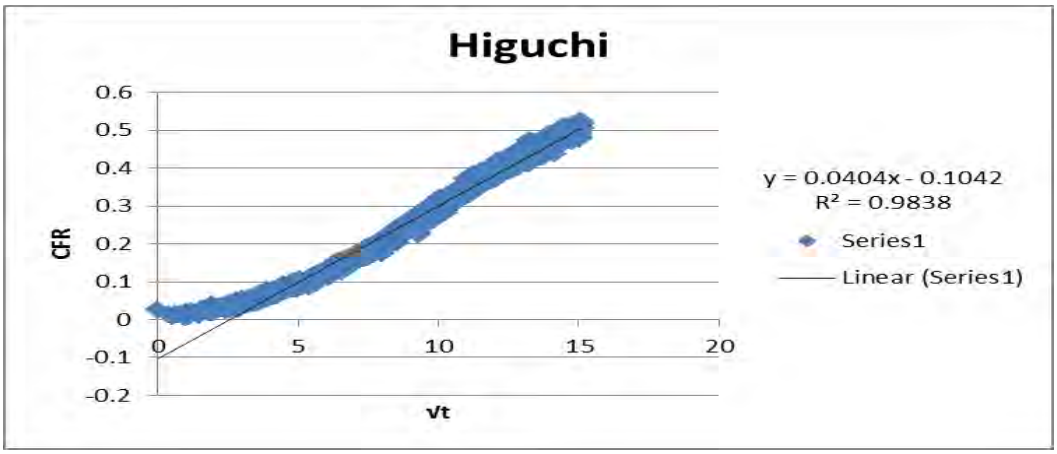

Figure 48: Higuchi Model plot for the first batch of Tf liposomes at a power density of 7.46mW/cm^2.

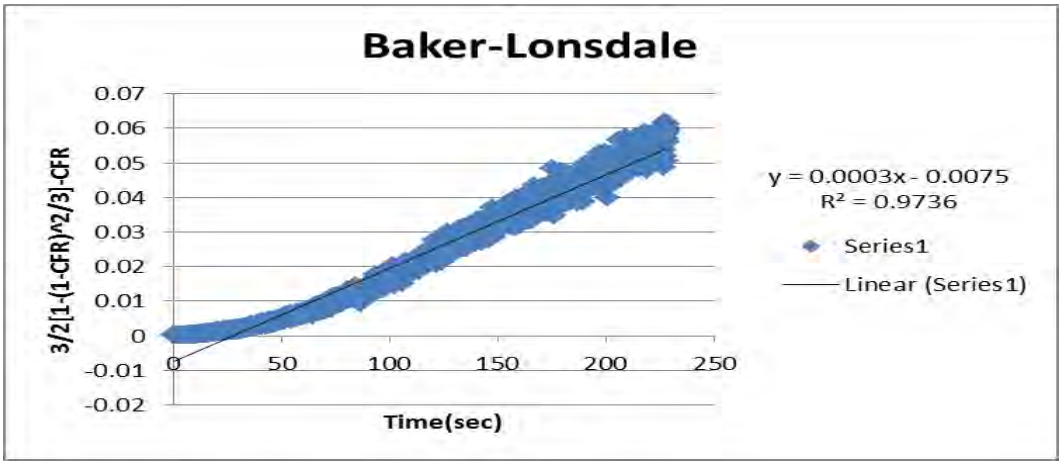

Figure 49: Baker-Lonsdale Model plot for the first batch of Tf liposomes at a power density of 7.46mW/cm^2.

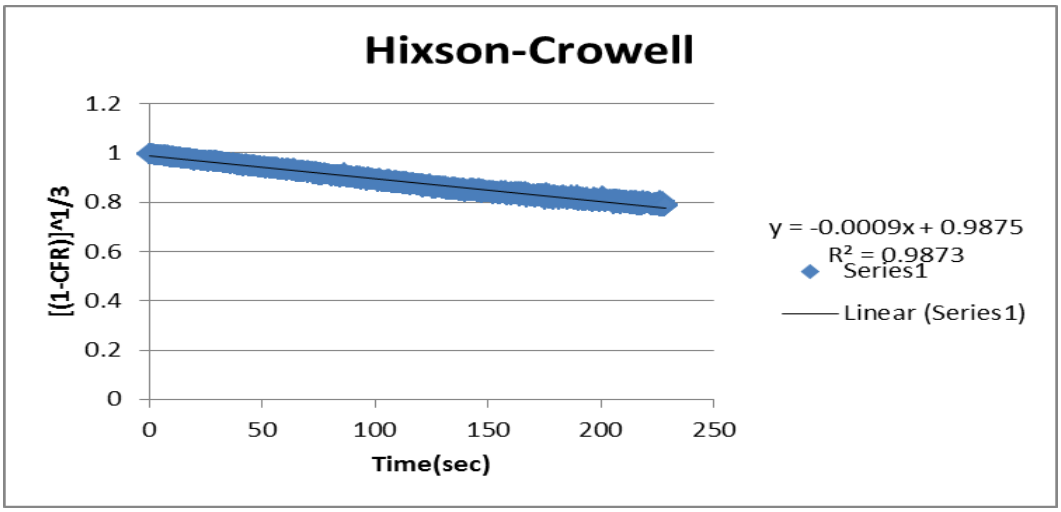

Figure 50: Hixson-Crowell Model plot for the first batch of Tf liposomes at a power density of 7.46mW/cm^2.

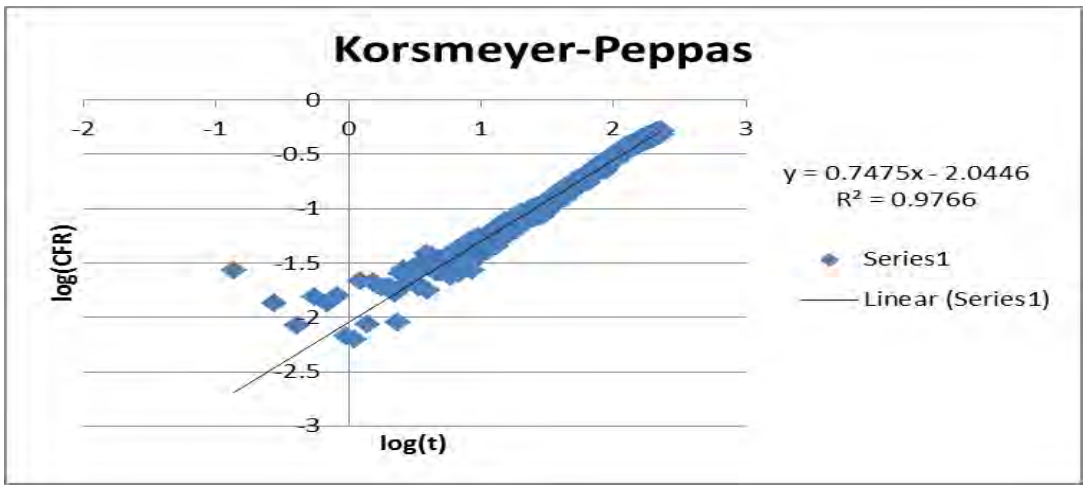

Figure 51: Korsemeyer-Peppas Model plot for the first batch of Tf liposomes at a power density of 7.46mW/cm^2.

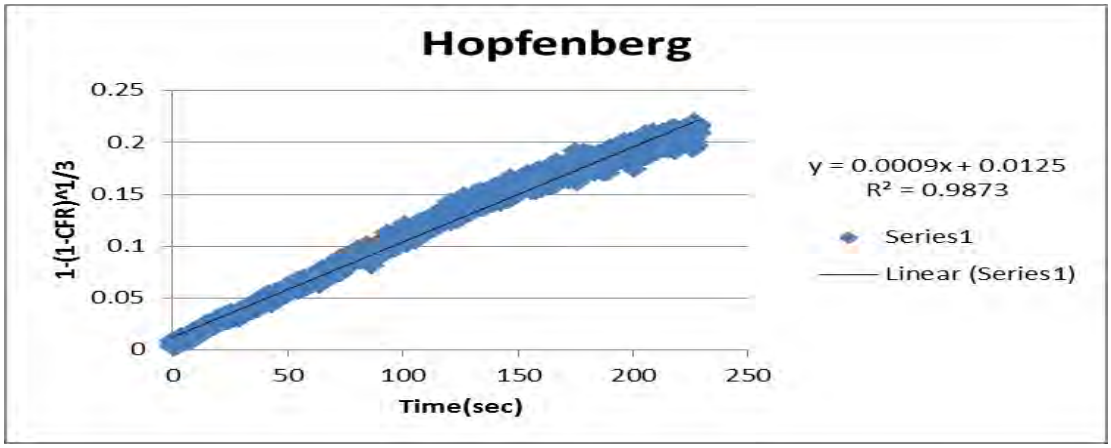

Figure 52: Hopfenberg Model plot for the first batch of Tf liposomes at a power density of 7.46mW/cm^2.

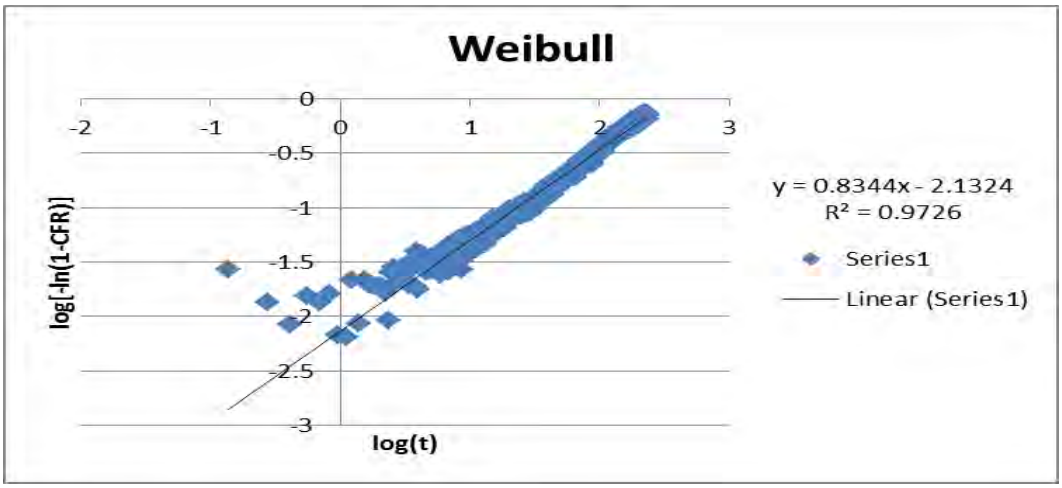

Figure 53: Weibull Model plot for the first batch of Tf liposomes at a power density of 7.46mW/cm^2.

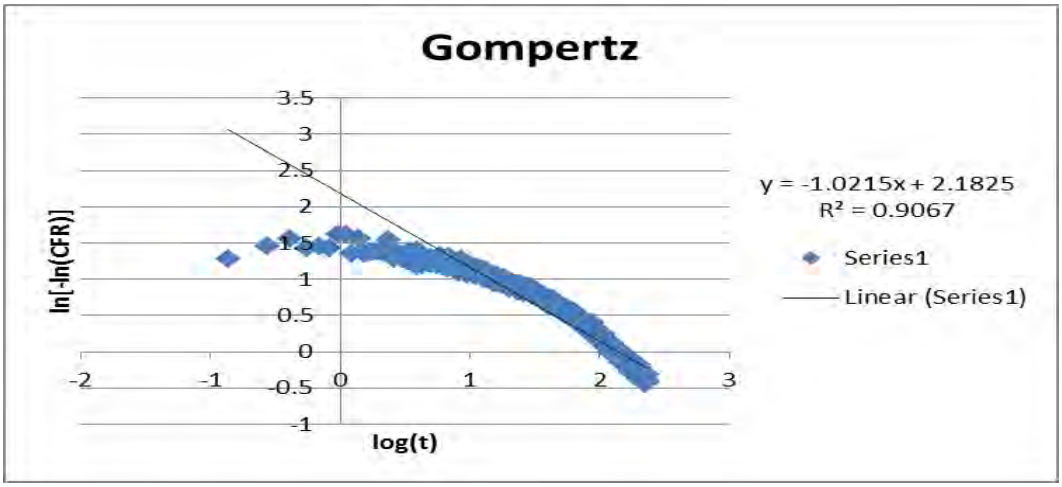

Figure 54: Gompertz Model plot for the first batch of Tf liposomes at a power density of 7.46mW/cm^2.

Table 12: R^2 values for Transferrin liposomes for each model at three power densities

Model	Tf 1st batch			Tf 2nd batch			Tf 3rd batch		
	7.46m W/cm^2	9.85m W/cm^2	17.31m W/cm^2	7.46m W/cm^2	9.85m W/cm^2	17.31m W/cm^2	7.46m W/cm^2	9.85m W/cm^2	17.31m W/cm^2
Zero Order	0.9759	0.9474	0.9244	0.9463	0.8829	0.8096	0.9833	0.8922	0.8286
First Order	0.7793	0.7219	0.7183	0.7602	0.6575	0.5808	0.7971	0.7055	0.6435
Higuchi	0.9838	0.9876	0.9794	0.9749	0.9617	0.9271	0.9800	0.9570	0.9237
Korsmeyer-Peppas	0.9766	0.9819	0.9760	0.9750	0.9680	0.9526	0.9870	0.9763	0.9665
Hixson-Crowell	0.9873	0.9759	0.9646	0.9652	0.9331	0.8909	0.9928	0.9446	0.8907
Baker-Lonsdale	0.9736	0.9838	0.9777	0.9682	0.9682	0.9365	0.9532	0.9480	0.8957
Weibull	0.9726	0.9823	0.9745	0.9695	0.9761	0.9761	0.9699	0.9655	0.9621
Hopfenberg	0.9873	0.9759	0.9646	0.9652	0.9331	0.8909	0.9928	0.9446	0.8907
Gompertz	0.9067	0.9140	0.8953	0.8965	0.9178	0.9245	0.8434	0.8448	0.8369

5.6.12. Comparison of data fitting between NH_2 and transferrin liposomes. The previous sections provided an analysis of the data fitting for control and Tf-targeted liposomes individually. The coefficient of determination, R^2, was used to assess which of the nine previously discussed models constituted the best fit for simulating the drug dissolution/release phenomena in this research. For both types of liposomes, the best fitting models were found to be the Korsmeyer-Peppas, Hixson-Crowell, Weibull and Hopfenberg models. Another aspect of comparison that can be drawn from the data fitting of both types of liposomes is the release mechanism. The drug release mechanism can be estimated using the exponential value *n* of the Korsmeyer-Peppas equation. Accordingly, the average values of the power *n* for the Korsmeyer-Peppas model was n = 0.8135 for NH_2 liposomes and n = 0.7207 for Transferrin liposomes. Based on the range of *n* values detailed in Table 5 in section 4.3.2, the diffusional release mechanism governing both control and transferrin liposomes is anomalous transport, i.e. the diffusion process has a non-linear relationship with time.

As mentioned above the models that best fit the release data in this research were Korsmeyer-Peppas, Hixson-Crowell, Weibull and Hopfenberg. Section 5.6 presented the linearization of each model equation and the plot parameters needed to

generate a graph representative of these linearizations. These plots provided the values of the release constant *k*; the following is a comparison between the release constants of control and Tf-targeted liposomes for the aforementioned models. The release constant values were compared using a two-way analysis of variance (ANOVA). This statistical analysis method was selected because it allows the comparison between the means of data sets that have been split on two independent variables (called factors). The primary purpose of a two-way ANOVA is to understand if there is an interaction between the two independent variables and the dependent variable. In this analysis, the first independent variable (referred to as sample) is the type of liposomes (control or targeted), the second independent variable is the US power density (referred to as columns), while the dependent variable is the release constant value. The two-way ANOVA test requires the formulation of three null hypotheses which in this case are as follows:

1. There is no difference in the release constant value for control and Tf-targeted liposomes.
2. There is no difference in the release constant value for different US power densities.
3. There is no interaction between the independent variables, i.e. type of liposomes and US power density.

The confidence level for this test was set at 95% with the p-value< 0.05 being statistically significant. Tables 13 and 14 present the k-values for the Korsmeyer-Peppas model. With regard to the first null hypothesis (comparing NH_2 and Tf liposomes), it can be seen that the F-value is much higher than the critical F-value, and the p-value is much lower than alpha (standard $\alpha = 0.05$). This suggests that there is enough evidence to reject the null hypothesis; meaning that the k-values are affected by the type of the carrier. Similarly, for the second null hypothesis (comparing different power densities), the F-value is also higher than the critical F-value, and the p-value is also much lower than 0.05. Thus, changes in the power density have significant effects on k-values. The cause behind these results is believed to be the effect the attached moieties have on the stability of liposomes, which significantly affects the release kinetics (causing the rate constants to increase with increased power density). Finally, the interaction p-value is greater than 0.05 meaning

that there is no interaction between the two independent factors. Although the prediction of the release constant values by this model was not very accurate, its applicability still holds due to the perfect fitting (high R^2-values) demonstrated earlier.

Table 13: Release Constant values for the Korsmeyer-Peppas model at different power densities.

Liposomes	**Power Density (mW/cm^2)**		
	7.46	**9.85**	**17.31**
NH_2-batch 1	5.868×10^{-3}	6.49×10^{-3}	9.77×10^{-3}
batch 2	7.257×10^{-3}	1.25×10^{-2}	2.05×10^{-2}
batch 3	5.054×10^{-3}	9.46×10^{-3}	1.60×10^{-2}
Average	6.06×10^{-3}	9.48×10^{-3}	1.54×10^{-2}
Standard Dev	9.10×10^{-4}	2.45×10^{-3}	4.39×10^{-3}
Tf-batch 1	9.024×10^{-3}	1.36×10^{-2}	1.93×10^{-2}
batch 2	1.142×10^{-2}	1.71×10^{-2}	3.04×10^{-2}
batch 3	1.282×10^{-2}	2.13×10^{-2}	2.43×10^{-2}
Average	1.109×10^{-2}	1.73×10^{-2}	2.46×10^{-2}
Standard Deviation	1.570×10^{-3}	3.15×10^{-3}	4.55×10^{-3}

Table 14: Two-way ANOVA test for release constant values of Korsmeyer-Peppas model.

ANOVA						
Source of Variation	**SS**	**df**	**MS**	**F**	**P-value**	**F-crit**
Sample	2.440×10^{-4}	1	0.000244	16.48	1.58×10^{-3}	4.747
Columns	3.97×10^{-4}	2	0.000199	13.42	8.69×10^{-4}	3.885
Interaction	1.36×10^{-5}	2	6.81×10^{-6}	0.4603	0.6417	3.885
Within	1.780×10^{-4}	12	1.48×10^{-5}			
Total	8.330×10^{-4}	17				

Contrastingly, the ANOVA analysis for the remaining three models, Hixson-Crowell, Hopfenberg and Weibull, yielded F-values that are lower than the critical F-value as well as p-values that are much higher than the statistically significant value

of 0.05 (refer to Table 15 through 20). This suggests that all three null hypotheses cannot be rejected. In release kinetics' terms this means that the k-values are not affected neither by the type of the carrier nor by changes in the power density. Accordingly, the Hixson-Crowell, Hopfenberg and Weibull models appear to be better than the Korsmeyer-Peppas model at predicting release k-values.

Table 15: Release Constant values for the Hixson-Crowell model at different power densities.

Liposome Type	**Power Density (mW/cm^2)**		
	7.46	**9.85**	**17.31**
NH2-batch 1	$-430x10^{-2}$	$-6.6x10^{-3}$	$-8.0x10^{-3}$
batch 2	$-6.4x10^{-3}$	$-9.1x10^{-3}$	$-9.2x10^{-3}$
batch 3	$-5.2x10^{-3}$	$-7.1x10^{-3}$	$-8.1x10^{-3}$
Average	$-1.82x10^{-2}$	$-7.6x10^{-3}$	$-8.4x10^{-3}$
Standard Deviation	$1.754x10^{-2}$	$1.08x10^{-3}$	$5.44x10^{-4}$
Tf- batch 1	$-4.3x10^{-3}$	$-6.1x10^{-3}$	$-7.7x10^{-3}$
batch 2	$-5.5x10^{-3}$	$-7.3\ x10^{-3}$	$-8.7x10^{-3}$
batch 3	$-7.9x10^{-3}$	$-1.15\ x10^{-2}$	$-1.3x10^{-2}$
Average	$-5.9x10^{-3}$	$-8.3x10^{-3}$	$-9.8x10^{-3}$
Standard Deviation	$1.497x10^{-3}$	$2.315\ x10^{-3}$	$2.299x10^{-3}$

Table 16: Two-way ANOVA test for release constant values of Hixson-Crowell model.

ANOVA						
Source of Variation	***SS***	***df***	***MS***	***F***	***P-value***	***F crit***
Sample	$5.24x10^{-5}$	1	$5.24x10^{-5}$	0.6502	0.4357	4.747
Columns	$5.36x10^{-5}$	2	$2.68x10^{-5}$	0.3325	0.7235	3.885
Interaction	$1.780x10^{-4}$	2	$8.91x10^{-5}$	1.105	0.3624	3.885
Within	$9.660x10^{-4}$	12	$8.05x10^{-5}$			
Total	$1.250x10^{-3}$	17				

Table 17: Release Constant values for the Hopfenberg model at different power densities.

Liposome Type	Power Density (mW/cm^2)		
	7.46	**9.85**	**17.31**
NH2-batch 1	$9.0x10^{-4}$	$1.4x10^{-3}$	$1.7x10^{-3}$
batch 2	$1.4x10^{-3}$	$2.0x10^{-3}$	$2.0x10^{-3}$
batch 3	$1.0x10^{-3}$	$1.5x10^{-3}$	$1.70x10^{-3}$
Average	$1.1x10^{-3}$	$1.633x10^{-3}$	$1.80x10^{-3}$
Standard Deviation	$2.1x10^{-4}$	$2.62\ x10^{-4}$	$1.410\ x10^{-4}$
Tf-batch 1	$9.0x10^{-4}$	$1.3x10^{-3}$	$1.70x10^{-3}$
batch 2	$1.2x10^{-3}$	$1.6x10^{-3}$	$1.90x10^{-3}$
batch 3	$1.7x10^{-3}$	$2.5x10^{-3}$	$2.80x10^{-3}$
Average	$1.267x10^{-3}$	$1.8x10^{-3}$	$2.133x10^{-3}$
Standard Deviation	$3.3x10^{-4}$	$5.1x10^{-4}$	$4.780x10^{-4}$

Table 18: Two-way ANOVA test for release constant values of Hopfenberg model.

ANOVA						
Source of Variation	**SS**	**df**	**MS**	**F**	**P-value**	**F crit**
Sample	$2.22x10^{-7}$	1	$2.22x10^{-7}$	1.212	0.2925	4.7472
Columns	$1.92x10^{-6}$	2	$9.61x10^{-7}$	5.239	0.02314	3.8852
Interaction	$2.78x10^{-8}$	2	$1.39x10^{-8}$	0.07575	0.9274	3.8852
Within	$2.2x10^{-6}$	12	$1.83x10^{-7}$			
Total	$4.37x10^{-6}$	17				

Table 19: Release Constant values for the Weibull model at different power densities.

Liposome Type	Power Density (mW/cm^2)		
	7.46	**9.85**	**17.31**
NH2-batch 1	$-4.65x10^{-3}$	$-4.62x10^{-3}$	$-6.42x10^{-3}$
batch 2	$-5.26x10^{-3}$	$-7.69x10^{-3}$	$-1.258x10^{-2}$
batch 3	$-3.90x10^{-3}$	$-6.54x10^{-3}$	1.9783
Average	$-4.60x10^{-3}$	$-6.28x10^{-3}$	0.653101
Standard Deviation	$5.58x10^{-4}$	$1.267x10^{-3}$	0.93706
Tf-batch 1	$-7.37x10^{-3}$	$-1.011x10^{-2}$	$-1.306x10^{-2}$
batch 2	$-8.73x10^{-3}$	$-1.18x10^{-2}$	$-1.948x10^{-2}$
batch 3	$-8.56x10^{-3}$	$-1.124x10^{-2}$	$-1.137x10^{-2}$
Average	$-8.22x10^{-3}$	$-1.105x10^{-2}$	$-1.464x10^{-2}$
Standard Deviation	$6.04x10^{-4}$	$7.03x10^{-4}$	$3.496x10^{-3}$

Table 20: Two-way ANOVA test for release constant values of Weibull model.

ANOVA						
Source of Variation	**SS**	**df**	**MS**	**F**	**P-value**	**F crit**
Sample	0.2285	1	0.2285	1.041	0.3276	4.747
Columns	0.4271	2	0.2135	0.9728	0.4059	3.885
Interaction	0.4402	2	0.2201	1.002	0.3956	3.885
Within	2.634	12	0.2195			
Total	3.730	17				

5.7. *In-Vitro* Experiments

The procedure adopted in conducting *in-vitro* cell work was described in detail in section 4.4. The cellular uptake of calcein and the *in-vitro* anticancer effects of drug-loaded liposomes (cell viability) were evaluated using the Trypan blue exclusion method and flow cytometry. As explained earlier, the concept behind flow cytometry is that the fluorescent nature of the model drug calcein taken in by cancer cells will make them emit higher fluorescence readings than cancer cells that have not internalized the drug and continue to proliferate. The use of liposomes modified with targeting moieties and triggering release using US is expected to enhance the cellular uptake and release of calcein. Therefore, combining targeted liposomes (in this case Tf-targeted liposomes) and US is supposed to give higher fluorescence intensity readings (signifying greater cell death) when compared to control liposomes alone and control liposomes with US. Figures 55 to 57 show the fluorescence distribution profile for the different combinations of HeLa cells with liposomes and US used in the *in-vitro* experiments, and since the distributions are not perfectly bell-shaped the best parameter to describe the distribution and permit a comparison to be conducted is the geometric mean. Tables 21 and 22 provide a summary of the geometric means, percent difference values of the different combinations, as well as the p-values associated with the t-test that was conducted to establish whether the observed differences were statistically significant (taking p-value <0.05 to be statistically significant). First, the values of NH_2 liposomes are compared against transferrin liposomes, as this comparison indicates whether internalization of the liposomes has occurred or not. Based on the values in Table 20 there is a significant shift (p-vlaue=$1.3x10^{-5}$) indicating that the liposomes have indeed been internalized by the cancer cells. Second, the combinations of NH_2 liposomes versus NH_2 liposomes

coupled with US and transferrin liposomes versus transferrin liposomes with US are inspected to determine if the application of US has had the desired effect (inducing cavitation). Looking at the fluorescence distributions, the percent differences in mean values and p-values it is evident that an increase has occurred through the coupling of both types liposomes and US. Finally, control liposomes are compared to transferrin coupled liposomes with US to study the combined effects of active targeting and US. Again by inspecting the plots and the obtained percent difference and p-values it is clear that the use of targeting moieties and US has achieved the desired effect, as the mean difference between control and Tf-coupled liposomes is 34.89±12.58% and with the addition of US this difference further increases to 80.09±30.08%.

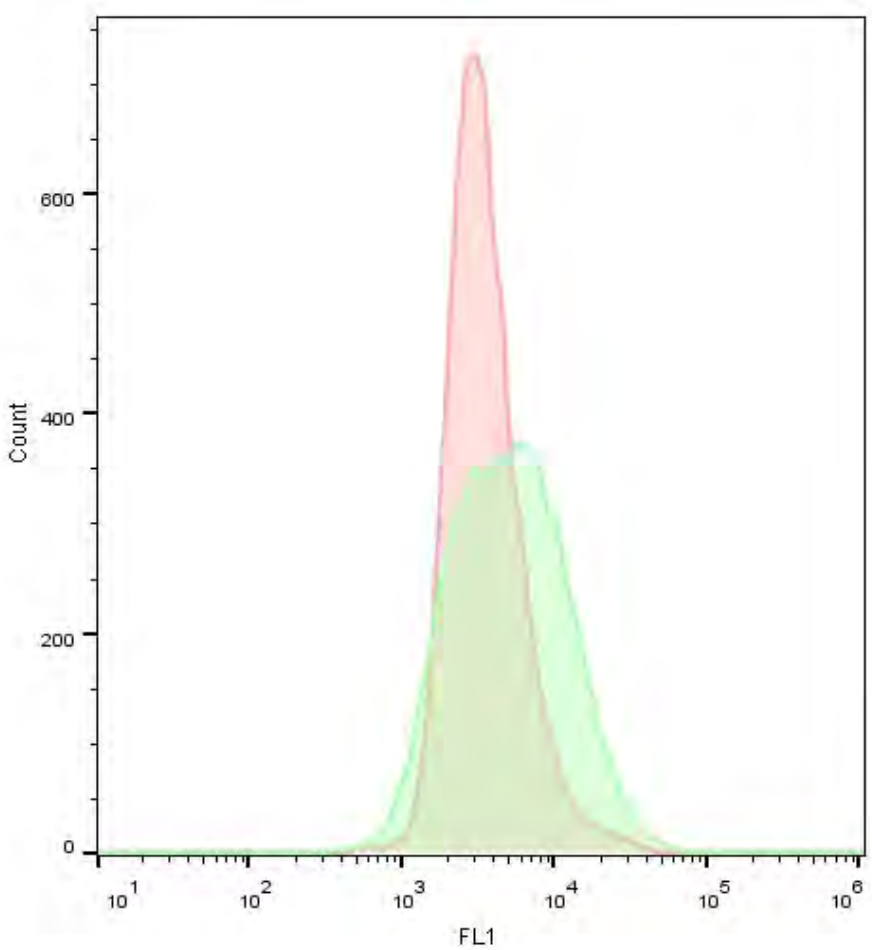

	Sample Name	Count	Geometric Mean : FL1
	1.4 HELA+ TF.LMD	20000	5058
	1.1 HELA+ NH2.LMD	20000	3521

Figure 55: Results of flow cytometric analysis of HeLa cells treated with control liposomes and HeLa cells treated with transferrin liposomes.

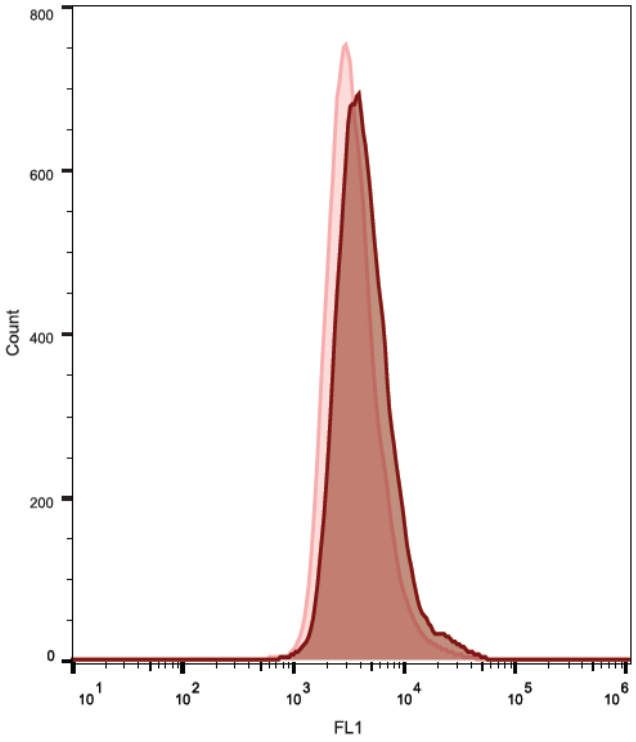

	Sample Name	Count	Geometric Mean : FL1
	2.2 HELA+ NH2+US.LMD	20000	4398
	1.3 HELA+ NH2.LMD	20000	3448

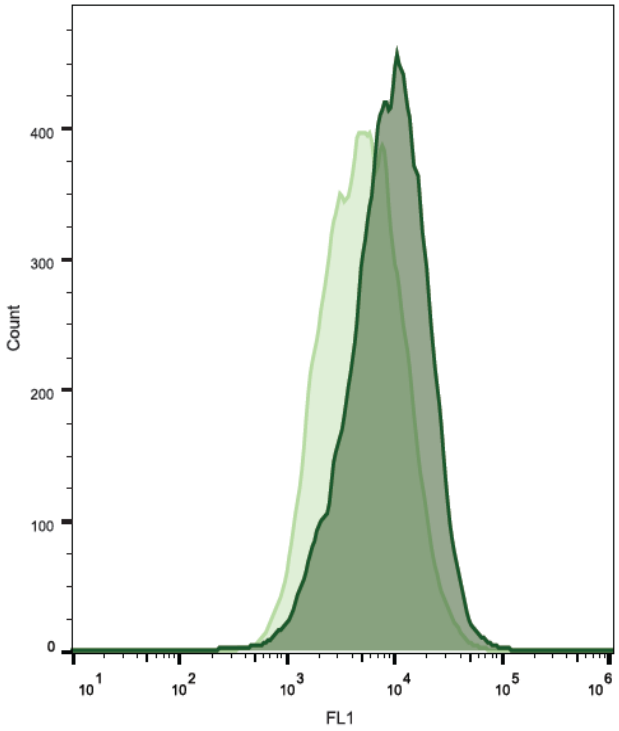

	Sample Name	Count	Geometric Mean : FL1
	2.5 HELA+ TF+US.LMD	20000	8297
	1.6 HELA+ TF.LMD	20000	4956

Figure 56: Results of flow cytometric analysis of HeLa cells treated with (top) control liposomes and US and with transferrin liposomes coupled with US (bottom)

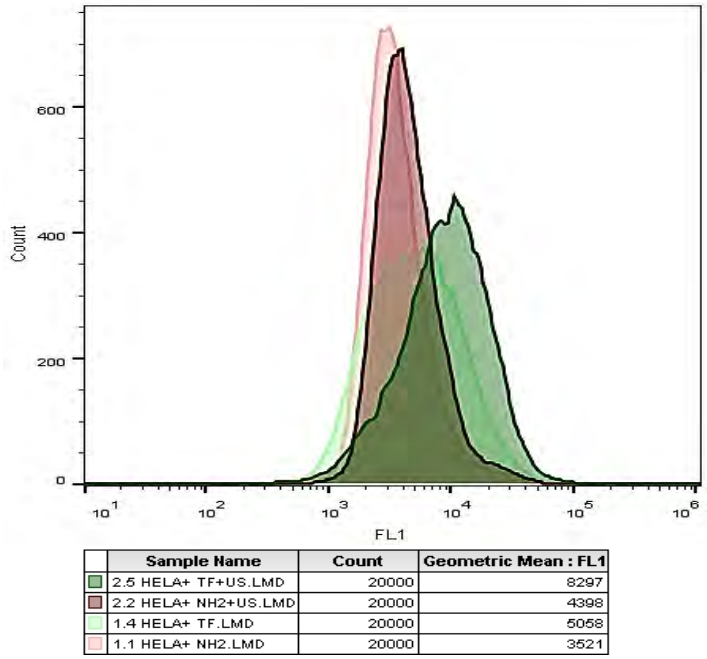

	Sample Name	Count	Geometric Mean : FL1
	2.5 HELA+ TF+US.LMD	20000	8297
	2.2 HELA+ NH2+US.LMD	20000	4398
	1.4 HELA+ TF.LMD	20000	5058
	1.1 HELA+ NH2.LMD	20000	3521

Figure 57: Results of flow cytometric analysis for the combined effect of liposomes and US

Table 21: Summary of geometric means of flow cytometry fluorescence distributions for all tested combinations

Trial no.	NH_2	Transferrin	NH_2 + US	Transferrin + US
1	3188	4132	3802	4824
	3002	4358	4069	5179
	3234	3755	4157	5411
2	3091	4365	3315	4040
	3131	3901	3386	4411
	3321	3971	3448	4321
3	3499	4927	4238	7905
	3434	5240	4387	8456
	3434	4922	4309	8281
Average	3259.3	4396.7	3901.2	5869.7

Table 22: Summary of percentage difference in geometric mean and p-values for all tested combinations.

	NH_2 vs. Tf	NH_2 vs. (NH_2 +US)	Tf vs. (Tf + US)	(NH_2+US) vs. (Tf+US)
Percent Difference (%)	34.89	19.69	33.50	80.09
p-value	$1.3x10^{-5}$	$6.625x10^{-4}$	$3.244x10^{-2}$	$5.510x10^{-4}$

Chapter 6. Conclusion and Recommendations

Liposomes are nano-sized particles capable of providing site-specific delivery in anticancer treatments. The selectivity of liposomal delivery systems can be further improved by the attachment of receptor-specific ligands to the surface of the liposomes. This work focused on the synthesis of transferrin (TF)-poly-ethylene glycol (PEG)-liposomes encapsulating the model drug calcein and studying the effects of low-frequency and high-frequency ultrasound on calcein release. Control (moiety free) and transferrin-modified liposomes were synthesized using the thin film hydration method, and the synthesized liposomes were characterized for size, lipid content and protein attachment. The determination of the sizes of 3 batches of liposomes using DLS gave diameter values of 82.70±2.88 nm for the control liposomes whereas the transferrin liposomes had an average diameter of 87.54±4.81 nm. Next, calcein release triggered by LFUS was carried out for three batches of liposomes at three power densities (7.46, 9.85 and 17.31 mW/cm^2); the normalized release profiles were in agreement with the expected pattern of behavior showing an increase in release with increased power density and higher release values achieved by Tf-coupled liposomes. LFUS release was also modeled using nine kinetic models and based on R^2 values the best fitting models for both types of liposomes were: Korsmeyer-Peppas, Hixson-Crowell, Weibull and Hopfenberg. With respect to high frequency ultrasound, the release was inspected at two frequencies of 1.07 MHz and 3 MHz (22.59 and 158 W/cm^2 respectively). The generated plots showed an increased release with each insonation; however, the release at 1.07MHz was higher than that obtained at 3 MHz for both types of liposomes. In addition, transferrin liposomes showed a more linear increase and yielded higher cumulative fraction release values at both frequencies. Finally, *in-vitro* cell experiments were conducted and the cytotoxicity of Tf-PEG-liposomal calcein coupled with US by HeLa cells was 80.09±30.08% higher than that of non-targeted liposomes. To extend this thesis further in the future, the investigation of Tf-coupled-Dox liposomes will further improve the utility of this drug delivery system. In addition, *in-vitro* release experiments with other cell lines and with Tf-positive cell lines would provide even greater insight into the effects of liposomes and US on cancer cells.

References

[1] American Cancer Society, “Cancer Facts & Figures 2017,” 2017. [Online]. Available: https://www.cancer.org/content/dam/cancer-org/research/cancer-facts-and-statistics/annual-cancer-facts-and-figures/2017/cancer-facts-and-figures-2017.pdf.[Accessed: 13-Nov-2018].

[2] National Cancer Institute, “What Is Cancer ? Differences between Cancer Cells and Normal Cells,” *National Cancer Institute*, 2015. [Online]. Available: https://www.cancer.gov/about-cancer/understanding/what-is-cancer. [Accessed: 20-Jan-2019].

[3] P. Boyle and B. Levin, “Mechanisms of Carcinogenesis 3,” *World Cancer Rep. 2008*, pp. 190–260, 2008.

[4] C. Nordqvist, “Tumors: Benign, premalignant, and malignant,” 2017. [Online]. Available: https://www.medicalnewstoday.com/articles/249141.php. [Accessed: 20-Jan-2019].

[5] American Cancer Society, “Treatment Types.” [Online]. Available: https://www.cancer.org/treatment/treatments-and-side-effects/treatment-types.html. [Accessed: 20-Jan-2019].

[6] D. Liu, F. Yang, F. Xiong, and N. Gu, “The smart drug delivery system and its clinical potential,” *Theranostics*, vol. 6, no. 9, pp. 1306–1323, 2016.

[7] The Institute of Biomedical Engineering, “Triggered Drug Release,” 2016. [Online]. Available: http://www.ibme.ox.ac.uk/research/non-invasive-therapy-drug-delivery/triggered-drug-release. [Accessed: 20-Jan-2019].

[8] K. U. Maheswari, “Stimuli responsive ‘smart’ nanosystems.”[Online]. Available: https://nptel.ac.in/courses/118106019/Module 8/Lecture 1/Lecture 1.pdf. [Accessed: 20-Jan-2019].

[9] S. Dhanasekaran and S. Chopra, “Getting a Handle on Smart Drug Delivery Systems – A Comprehensive View of Therapeutic Targeting Strategies,” in *Smart Drug Delivery System*, INTECH, 2016, pp. 31–62.

[10] S. Hasan, “A Review on Nanoparticles : Their Synthesis and Types,” *Res. J. Recent Sci. Res . J . Recent . Sci .*, vol. 4, no. 2, pp. 1–3, 2014.

[11] A. Cartaxo, “Nanoparticles types and properties – understanding these promising devices in the biomedical area,” M.S. thesis, Dept. Biomed. Eng., University of Minho., Braga, Portugal, 2010.

[12] K. Greish, “Enhanced permeability and retention effect for selective targeting of anticancer nanomedicine: Are we there yet?,” *Drug Discov. Today Technol.*, vol. 9, no. 2, pp. 161–166, 2012.

[13] S. Bamrungsap *et al.*, “Nanotechnology in therapeutics: a focus on nanoparticles as a drug delivery system,” *Nanomedicine*, vol. 7, no. 8, pp. 1253–1271, 2012.

[14] M. E. Grigore, “Organic and Inorganic Nano-Systems Used in Cancer Treatment,” *J. Med. Res. Heal. Educ.*, vol. 1, no. 1, pp. 1–8, 2017.

[15] S. Bhatia, “Nanoparticles Types, Classifi cation, Characterization, Fabrication Methods and Drug Delivery Applications,” in *Natural Polymer Drug Delivery Systems: Nanoparticles, Plants, and Algae*, vol.5, no. 2, pp. 1–225, 2016.

[16] A. I. Moreno-Vega, T. Gómez-Quintero, R. E. Nuñez-Anita, L. S. Acosta-Torres, and V. Castaño, “Polymeric and ceramic nanoparticles in biomedical applications,” *J. Nanotechnol.*, vol. 10, no. 2, pp. 1-6, 2012.

[17] H.C. Huang, S. Barua, G. Sharma, S. K. Dey, and K. Rege, “Inorganic nanoparticles for cancer imaging and therapy,” *J. Control. Release*, vol. 155, no. 3, pp. 344–357, 2011.
[18] E. Abbasi *et al.*, “Dendrimers: Synthesis, applications, and properties,” *Nanoscale Res. Lett.*, vol. 9, no. 1, pp. 1–10, 2014.
[19] M. Karthikeyan, T. Balasubramanian, M. I. Khaleel, M. Sahl, and P. Rashifa, “Liposomes: Preparations and Applications,” *Int. J. Drug Dev.*, vol. 4, no. 4, pp. 108–115, 2012.
[20] N. van Rooijen, “Liposomes,” *Encycl. Immunol.*, pp. 1588–1592, Jan. 1998.
[21] PHILPOT EDUCATION, “The origin of cells.” [Online]. Available: https://www.philpoteducation.com/mod/book/view.php?id=777&chapterid=1121#/. [Accessed: 21-Jan-2019].
[22] Y. Y. Khan and V. Suvarna, “Liposomes containing phytochemicals for cancer treatment-an update,” *Int. J. Curr. Pharm. Rev. Res.*, vol. 9, no. 1, pp. 20–24, 2017.
[23] A. Akbarzadeh, R. Rezaei-sadabady, S. Davaran, S. W. Joo, and N. Zarghami, “Liposome: classification, preparation, and applications,” *Nanoscale. Res. Lett.*, vol. 8, no. 1, pp. 1–9, 2013.
[24] O. K. Nag and V. Awasthi, “Surface engineering of liposomes for stealth behavior,” *Pharmaceutics*, vol. 5, no. 4, pp. 542–569, 2013.
[25] S. Drabu, S. Khanna, R. Bajaj, and B. Khurana, “Clinical pharmacokinetic aspects of stealth liposomes: A review,” *Int. J. Drug Dev. Res.*, vol. 2, no. 4, pp. 871–878, 2010.
[26] S. M. Moghimi and J. Szebeni, “Stealth liposomes and long circulating nanoparticles: Critical issues in pharmacokinetics, opsonization and protein-binding properties,” *Prog. Lipid Res.*, vol. 42, no. 6, pp. 463–478, 2003.
[27] M. L. Immordino, F. Dosio, and L. Cattel, “Stealth liposomes: review of the basic science, rationale, and clinical applications, existing and potential,” *Int. J. Nanomedicine*, vol. 1, no. 3, pp. 297–315, 2006.
[28] C. Allen *et al.*, “Controlling the physical behavior and biological performance of liposome formulations through use of surface grafted poly(ethylene glycol).,” *Biosci. Rep.*, vol. 22, no. 2, pp. 225–50, Apr. 2002.
[29] S. M. Moghimi, A. C. Hunter, and J. C. Murray, “Long-Circulating and Target-Specific Nanoparticles: Theory to Practice,” *Pharmacol. Rev.*, vol. 53, no. 2, pp. 283–318, 2001.
[30] M. K. Riaz *et al.*, “Surface functionalization and targeting strategies of liposomes in solid tumor therapy: A review,” *Int. J. Mol. Sci.*, vol. 19, no. 1, 2018.
[31] P. P. Deshpande, S. Biswas, and V. P. Torchilin, “Current trends in the use of liposomes for tumor targeting,” *Nanomedicine*, vol. 8, no. 9, pp. 1509–1528, 2013.
[32] T. Wilcox and A. Hirshkowitz, “Challenges in design and characterization of ligand-targeted drug delivery systems,” vol. 85, no. 0 1, pp. 1–27, 2015.
[33] A. F. Sikorski, M. Toporkiewicz, J. Meissner, L. Matusewicz, and A. Czogalla, “Toward a magic or imaginary bullet? Ligands for drug targeting to cancer cells: principles, hopes, and challenges,” *Int. J. Nanomedicine*, pp. 1316–1399, 2015.
[34] A. Gabizon, H. Shmeeda, A. T. Horowitz, and S. Zalipsky, “Tumor cell targeting of liposome-entrapped drugs with phospholipid-anchored folic acid-

PEG conjugates," *Adv. Drug Deliv. Rev.*, vol. 56, no. 8, pp. 1177–1192, 2004.
[35] University of California SanFrancisco, "Hemoglobin and Functions of Iron." [Online].Available:https://www.ucsfhealth.org/education/ hemoglobin_and_fun ctions_of_iron/.
[36] D. Zhang, "Characterization of transferrin receptor mediated endocytosis and cellular iron delivery of recombinant human serum transferrin from rice (Oryza sativa L .)", *BMC Biotechnology*, vol. 19 no. 92 August 2012, pp. 1–18, 2016.
[37] R. Luria-Pérez, G. Helguera, and J. A. Rodríguez, "Antibody-mediated targeting of the transferrin receptor in cancer cells" *Bol. Med. Hosp. Infant. Mex.*, vol. 73, no. 6, pp. 372–379, 2016.
[38] T. R. Daniels *et al.*, "The transferrin receptor and the targeted delivery of therapeutic agents against cancer," *Biochim. Biophys. Acta - Gen. Subj.*, vol. 1820, no. 3, pp. 291–317, 2012.
[39] Y. Shen, X. Li, D. Dong, B. Zhang, Y. Xue, and P. Shang, "Transferrin receptor 1 in cancer: a new sight for cancer therapy.," *Am. J. Cancer Res.*, vol. 8, no. 6, pp. 916–931, 2018.
[40] P. Holliger and P. J. Hudson, "Engineered antibody fragments and the rise of single domains," *Nat. Biotechnol.*, vol. 23, no. 9, pp. 1126–1136, Sep. 2005.
[41] V. Quintero-Hernández, V. R. Juárez-González, M. Ortíz-León, R. Sánchez, L. D. Possani, and B. Becerril, "The change of the scFv into the Fab format improves the stability and in vivo toxin neutralization capacity of recombinant antibodies," *Mol. Immunol.*, vol. 44, no. 6, pp. 1307–1315, Feb. 2007.
[42] Z. A. Ahmad, S. K. Yeap, A. M. Ali, W. Y. Ho, N. B. M. Alitheen, and M. Hamid, "scFv Antibody: Principles and Clinical Application," *Clin. Dev. Immunol.*, vol. 2012, pp. 1–15, 2012.
[43] T. Padró *et al.*, "Overexpression of vascular endothelial growth factor (VEGF) and its cellular receptor KDR (VEGFR-2) in the bone marrow of patients with acute myeloid leukemia," *Leukemia*, vol. 16, no. 7, pp. 1302–1310, Jul. 2002.
[44] N. Kokkonen *et al.*, "Hypoxia upregulates carcinoembryonic antigen expression in cancer cells," *Int. J. Cancer*, vol. 121, no. 11, pp. 2443–2450, Dec. 2007.
[45] J. Baselga and J. Albanell, "Mechanism of action of anti-HER2 monoclonal antibodies.," *Ann. Oncol. Off. J. Eur. Soc. Med. Oncol.*, vol. 12, pp. 35-41, 2001.
[46] A. F. Shaughnessy, "Monoclonal antibodies: magic bullets with a hefty price tag," *BMJ*, vol. 345, no.12 1, pp. 8346–8346, Dec. 2012.
[47] B. Kelley, "Industrialization of mAb production technology: the bioprocessing industry at a crossroads.," *MAbs*, vol. 1, no. 5, pp. 443–52.
[48] M. Li, X. Xiao, W. Zhang, L. Liu, N. Xi, and Y. Wang, "Nanoscale distribution of CD20 on B-cell lymphoma tumour cells and its potential role in the clinical efficacy of rituximab.," *J. Microsc.*, vol. 254, no. 1, pp. 19–30, Apr. 2014.
[49] A. Yano, A. Onozuka, K. Matin, S. Imai, N. Hanada, and T. Nisizawa, "RGD motif enhances immunogenicity and adjuvanicity of peptide antigens following intranasal immunization.," *Vaccine*, vol. 22, no. 2, pp. 237–43, Dec. 2003.
[50] M. T. Stumpp, H. K. Binz, and P. Amstutz, "DARPins: A new generation of protein therapeutics," *Drug Discov. Today*, vol. 13, no. 15–16, pp. 695–701, Aug. 2008.
[51] C. Chen *et al.*, "Structural basis for molecular recognition of folic acid by

folate receptors," *Nature*, vol. 500, no. 7463, pp. 486–489, Aug. 2013.
[52] C. P. Leamon and P. S. Low, "Delivery of macromolecules into living cells: a method that exploits folate receptor endocytosis.," *Proc. Natl. Acad. Sci. U. S. A.*, vol. 88, no. 13, pp. 5572–6, Jul. 1991.
[53] A. G. Barrientos *et al.*, "Modulating glycosidase degradation and lectin recognition of gold glyconanoparticles.," *Carbohydr. Res.*, vol. 344, no. 12, pp. 1474–8, Aug. 2009.
[54] F. Bou-Abdallah and T. R. Terpstra, "The thermodynamic and binding properties of the transferrins as studied by isothermal titration calorimetry.," *Biochim. Biophys. Acta*, vol. 1820, no. 3, pp. 318–25, Mar. 2012.
[55] A. Azagury, L. Khoury, G. Enden, and J. Kost, "Ultrasound mediated transdermal drug delivery: Mechanisms and Applications," *Adv. Drug Deliv. Rev.*, vol. 72, pp. 127–143, 2014.
[56] M. Karimi *et al.*, "Smart micro/nanoparticles in stimulus-responsive drug/gene delivery systems," *HHS Public Access*, vol. 45, no. 5, pp. 1457–1501, 2017.
[57] Y. Kato *et al.*, "Acidic extracellular microenvironment and cancer," *Cancer Cell Int.*, vol. 13, no. 1, p. 1, 2013.
[58] L. L. Tayo, "Stimuli-responsive nanocarriers for intracellular delivery," *Biophys. Rev.*, vol. 9, no. 6, pp. 931–940, 2017.
[59] A. Schroeder, J. Kost, and Y. Barenholz, "Ultrasound, liposomes, and drug delivery: principles for using ultrasound to control the release of drugs from liposomes," *Chem. Phys. Lipids*, vol. 162, no. 1, pp. 1–16, 2009.
[60] P. K. Sahu, "Ultrasonics - How Ultrasonic Waves Are Generated," , 2018.[Online]. Available: https://science.jrank.org/pages/7075/Ultrasonics-How-ultrasonic-waves-are-generated.html. [Accessed: 03-May-2018].
[61] C. Woodford, "Ultrasound," 2018. [Online]. Available: https://www.explainthatstuff.com/ultrasound.html. [Accessed: 03-May-2018].
[62] V. Frenkel, "Ultrasound mediated delivery of drugs and genes to solid tumors," *Adv. Drug Deliv. Rev.*, vol. 60, no. 10, pp. 1193–1208, 2008.
[63] X. Cheng, M. Zhang, B. Xu, B. Adhikari, and J. Sun, "The principles of ultrasound and its application in freezing related processes of food materials: A review," *Ultrason. Sonochem.*, vol. 27, pp. 576–585, 2015.
[64] E. Baykal-Caglar, E. Hassan-Zadeh, B. Saremi, and J. Huang, "Preparation of giant unilamellar vesicles from damp lipid film for better lipid compositional uniformity," *Biochim. Biophys. Acta - Biomembr.*, vol. 1818, no. 11, pp. 2598–2604, Nov. 2012.
[65] S. Mullick Chowdhury, T. Lee, and J. K. Willmann, "Ultrasound-guided drug delivery in cancer," *Ultrasonography*, vol. 36, no. 3, pp. 171–184, 2017.
[66] R. Tejera-Garcia, S. Ranjan, V. Zamotin, R. Sood, and P. K. J. Kinnunen, "Making unilamellar liposomes using focused ultrasound," *Langmuir*, vol. 27, no. 16, pp. 10088–10097, 2011.
[67] R. J. Lee and P. S. Low, "Folate-mediated tumor cell targeting of liposome-entrapped doxorubicin in vitro," *BBA - Biomembr.*, vol. 1233, no. 2, pp. 134–144, 1995.
[68] X. M. Li, L. Y. Ding, Y. Xu, Y. Wang, and Q. N. Ping, "Targeted delivery of doxorubicin using stealth liposomes modified with transferrin," *Int. J. Pharm.*, vol. 373, no. 1, pp. 116–123, 2009.
[69] A. Schroeder *et al.*, "Controlling Liposomal Drug Release with Low Frequency Ultrasound: Mechanism and Feasibility," *Langmuir*, vol. 23, no. 7, pp. 4019–

4025, Mar. 2007.
[70] M. Afadzi, “Delivery of Encapsulated Drugs to Cancer Cells and Tissue: The impact of Ultrasound,” Ph.D. dissertation, Dept. Sci. Technol., Norges teknisk-naturvitenskapelige Univ., Trondheim, 2012.
[71] H. Pandey, R. Rani, and V. Agarwal, “Liposome and Their Applications in Cancer Therapy Human & Animal Health,” *Arch. Biol. Technol. v. Arch. Biol. Technol. v*, vol. 5959, no. 59, pp. 16150477–16150477, 2016.
[72] P. R. Cullis and T. M. Allen, “Liposomal drug delivery systems: From concept to clinical applications,” *Adv. Drug Deliv. Rev.*, vol. 65, pp. 36–48, 2012.
[73] U. Bulbake, S. Doppalapudi, N. Kommineni, and W. Khan, “Liposomal formulations in clinical use: An updated review,” *Pharmaceutics*, vol. 9, no. 2, pp. 1–33, 2017.
[74] M. J. Kang, S. H. Park, M. H. Kang, M. J. Park, and Y. W. Choi, “Folic acid-tethered pep-1 peptide-conjugated liposomal nanocarrier for enhanced intracellular drug delivery to cancer cells: Conformational characterization and in vitro cellular uptake evaluation,” *Int. J. Nanomedicine*, vol. 8, pp. 1155–1165, 2013.
[75] V. P. Torchilin and V. Weissig, *Liposomes : a practical approach.* Oxford University Press, 2003.
[76] H. Zhang, “Thin-Film Hydration Followed by Extrusion Method for Liposome Preparation.,” in *Liposomes: Methods and Protocols*, 2017.
[77] L. Al-Zubaidi and M. Al-Rubaie, “Multi Lamellar Vesicles (Mlvs) Liposomes Preparation by Thin Film Hydration Technique,” *J. Eng. Tech.*, vol. 32, no. 3, pp.550-560. 2014.
[78] A. Shahiwala and A. Misra, “Nasal delivery of levonorgestrel for contraception: an experimental study in rats,” *Fertil. Steril.*, vol. 81, pp. 893–898, Mar. 2004.
[79] D. Yadav, K. Sandeep, D. Pandey, and R. K. Dutta, “Liposomes for Drug Delivery,” *J. Biotechnol Biomater*, vol. 7, no. 4, pp. 1–8, 2017.
[80] J. M. Harris, “Laboratory Synthesis of Polyethylene Glycol Derivatives,” *J. Macromol. Sci.*, vol. 25, no. 3, pp. 325–373, 1985.
[81] C. Fee and V. B. Damodaran, “Protein PEGylation: An overview of chemistry and process considerations,” *Eur. Pharm. Rev.*, vol. 3, no. 1, pp. 1–23, 2010.
[82] S. Hupfeld, A. M. Holsæter, M. Skar, C. B. Frantzen, and M. Brandl, “Liposome Size Analysis by Dynamic/Static Light Scattering upon Size Exclusion-/Field Flow-Fractionation,” *J. Nanosci. Nanotechnol.*, vol. 6, no. 9, pp. 3025–3031, 2006.
[83] D. Fields, “Using Dynamic Light Scattering (DLS) for Liposome Size Analysis.” [Online]. Available: https://www.news-medical.net/life sciences/Using-Dynamic-light-scattering-(DLS)-for-liposome-size-analysis.aspx. [Accessed: 19-Feb-2019].
[84] Entegris, “Light Scattering – Particle Sizing Systems.” [Online]. Available: http://pssnicomp.com/glossary/light-scattering/. [Accessed: 28-Jan-2019].
[85] D. Kumar, “Co-Functionalised Gold Nanoparticles for Drug Delivery Applications Co-Functionalised Gold Nanoparticles for Drug Delivery Applications," Ph.D. dissertation, Dept. Nano. Bio. Techol. University of Ulster., Coleraine, Ireland, 2017.
[86] J. Bodycomb, “Interpreting and Understanding Dynamic Light Scattering Data,” [Online]. Available:

http://www.horiba.com/fileadmin/uploads/Scientific/Documents/PSA/Webinar_Slides/TR012.pdf. 2012. [Accessed: 20-Oct-2018].
[87] Thermo Fisher Scientific, “Chemistry of Protein Assays.” [Online]. Available: *www.Piercenet.Com*. 2013.[Accessed: 20-Oct-2018].
[88] T. Huang, M. Long, and B. Huo, “Competitive Binding to Cuprous Ions of Protein and BCA in the Bicinchoninic Acid Protein Assay.,” *Open Biomed. Eng. J.*, vol. 4, pp. 271–8, 2010.
[89] Thermo Fisher Scientific, “Protein Assay Technical Handbook,” pp. 1–40, 2017.
[90] A. S. Manjappa, “Design and characterization of immunoliposomes for site specific delivery of selected anticancer drug,” M.S. thesis, Dept. Pharm., Baroda Univ., Gujarat, India, 2012.
[91] S. J. Soenen, M. De Cuyper, S. C. De Smedt, and K. Braeckmans, “Investigating the Toxic Effects of Iron Oxide Nanoparticles,” *Methods in enzymology*, vol. 509, 2012, pp. 195–224.
[92] N. Mohammad, “Acoustically Activated Release of Estrone-targeted Liposomes Used for Breast Cancer Treatment,” M.S. thesis, Dept. Chem. Eng. American Univ., Sharjah, UAE, 2016.
[93] S. Dash, P. N. Murthy, L. Nath, and P. Chowdhury, “Kinetic modeling on drug release from controlled drug delivery systems.,” *Acta Pol. Pharm.*, vol. 67, no. 3, pp. 217–23, 2014.
[94] J. Siepmann and F. Siepmann, “Mathematical modeling of drug delivery,” *Int. J. Pharm.*, vol. 364, no. 2, pp. 328–343, 2008.
[95] D. Y. Arifin, L. Y. Lee, and C. H. Wang, “Mathematical modeling and simulation of drug release from microspheres: Implications to drug delivery systems,” *Adv. Drug Deliv. Rev.*, vol. 58, no. 12–13, pp. 1274–1325, 2006.
[96] A. Deore Prashant, “Theories of Dissolution.” Dept. Pharm., R.C. Patel Res. Inst., Shirpur, India, 2014.
[97] Y. Shi, A. Wan, Y. Shi, Y. Zhang, and Y. Chen, “Experimental and mathematical studies on the drug release properties of aspirin loaded chitosan nanoparticles,” *Biomed Res. Int.*, vol. 2014, 2014.
[98] N. Shahrin, “Solubility and Dissolution of Drug Product: A Review,” *Int. J. Pharm. Life Sci.*, vol. 2, no. 1, pp. 33–39, 2013.
[99] D. D. Allen, R. Caviedes, A. M. Cárdenas, T. Shimahara, J. Segura-Aguilar, and P. A. Caviedes, “Cell lines as in vitro models for drug screening and toxicity studies,” *Drug Dev. Ind. Pharm.*, vol. 31, no. 8, pp. 757–768, 2005.
[100] nature.com, “Statistical methods,” 2018. [Online]. Available: https://www.nature.com/subjects/statistical-methods. [Accessed: 04-Sep-2018].
[101] V. S. Thatipamula, A. Azmeer, and M. Nour, “Drug Release Models: Derivations and Linearization of Plots,”Dept. Chem. Eng., American Univ., Sharjah, UAE, Sci. Rep., 2018.
[102] A. Gallo, “A Refresher on Regression Analysis,” *Harvard Business Piblishing*, 2015. [Online]. Available: https://hbr.org/2015/11/a-refresher-on-regression-analysis. [Accessed: 30-Jan-2019].
[103] V. P. Shah, Y. Tsong, P. Sathe, and R. L. Williams, “Dissolution profile comparison using similarity factor, f2,” *Dissolution Technol.*, vol. 6, no. 3, pp. 1–2, 1999.
[104] P. F. Ambros and H. I. Karlic, “HeLa cells: Origin of this important cell line in life science research,” *Hum. Genet.*, vol. 77, no. 3, pp. 251–254, 1987.

[105] Science Services, "EVE^{TM} Automatic Cell Counter." [Online]. Available: https://scienceservices.de/en/evetm-automatic-cell-counter.html. [Accessed: 30-Jan-2019].
[106] Lonza, "Cell Assays and Analysis," 2010. [Online]. Available: https://bioscience.lonza.com/lonza_bs/CH/en/primary-hepatocytes-admetox-information-quote-request?utm_campaign=C-00003405. [Accessed: 30-Jan-2019].
[107] J. V. Watson, *Introduction to flow cytometry*. Cambridge: Cambridge University Press, 1991.
[108] University of New South Wales, "Acoustic impedance, intensity and power." [Online]. Available: http://www.animations.physics.unsw.edu.au/jw/sound-impedance-intensity.htm. [Accessed: 30-Jan-2019].
[109] G. A. Husseini, M. A. Diaz de la Rosa, E. S. Richardson, D. A. Christensen, and W. G. Pitt, "The role of cavitation in acoustically activated drug delivery," *J. Control. Release*, vol. 107, no. 2, pp. 253–261, Oct. 2005.
[110] S. B. Stringham *et al.*, "Over-pressure suppresses ultrasonic-induced drug uptake.," *Ultrasound Med. Biol.*, vol. 35, no. 3, pp. 409–15, Mar. 2009.
[111] B. J. Staples, B. L. Roeder, G. A. Husseini, O. Badamjav, G. B. Schaalje, and W. G. Pitt, "Role of frequency and mechanical index in ultrasonic-enhanced chemotherapy in rats," *Cancer Chemother. Pharmacol.*, vol. 64, no. 3, pp. 593–600, Jul. 2009.
[112] H. Azhari, *Basics of Biomedical Ultrasound for Engineers*. Hoboken, NJ, USA: John Wiley & Sons, Inc., 2010.
[113] R. E. Apfel and C. K. Holland, "Gauging the likelihood of cavitation from short-pulse, low-duty cycle diagnostic ultrasound," *Ultrasound Med. Biol.*, vol. 17, no. 2, pp. 179–185, Jan. 1991.
[114] P. Costa and J. M. Sousa Lobo, "Modeling and comparison of dissolution profiles," *Eur. J. Pharm. Sci.*, vol. 13, no. 2, pp. 123–133, May 2001.
[115] M. Mahmoud, "The Effect of Ultrasound on the Drug Delivery of RGD-targeted Liposomes," M.S. thesis, Dept. Chem. Eng. American Univ., Sharjah, UAE, 2018.
[116] K. Kosmidis, P. Argyrakis, and P. Macheras, "Fractal kinetics in drug release from finite fractal matrices," *J. Chem. Phys.*, vol. 119, no. 12, pp. 6373–6377, Sep. 2003.
[117] M. P. Paarakh, P. A. N. I. Jose, C. M. Setty, and G. V Peter, "Release Kinetics – Concepts and Applications," *Int. J. Pharm. Res. Technol.*, vol. 10, no. 1, pp. 1–9, 2018.
[118] J. Crank, *The Mathematics of Diffusion*, 2nd ed. London: Oxford University Press, 1973.
[119] A. Bunde, S. Havlin, R. Nossal, H. E. Stanley, and G. H. Weiss, "On controlled diffusion-limited drug release from a leaky matrix," *J. Chem. Phys.*, vol. 83, no. 11, pp. 5909–5913, Dec. 1985.

Appendix A: Plots of Kinetic Models for 2nd Batch of NH2 Liposomes at 7.46mW/cm^2

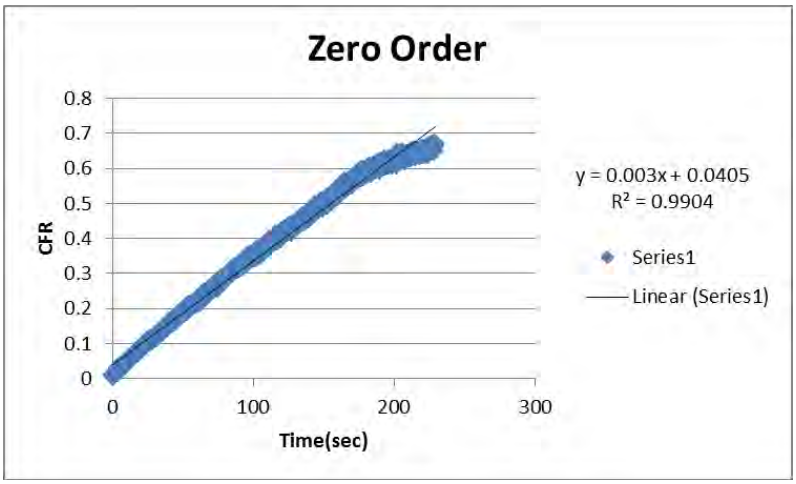

Figure 58: Zero-order plot for control liposomes, batch #2, at 7.46mW/cm^2

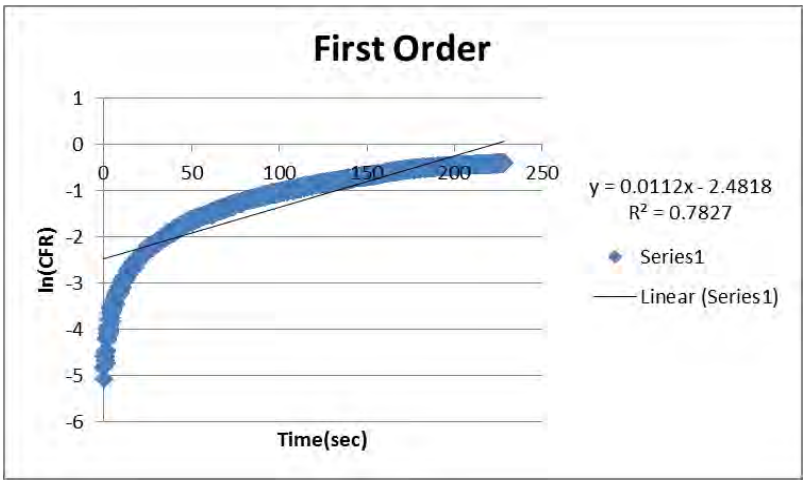

Figure 59: First-order plot for control liposomes, batch #2, at 7.46mW/cm^2

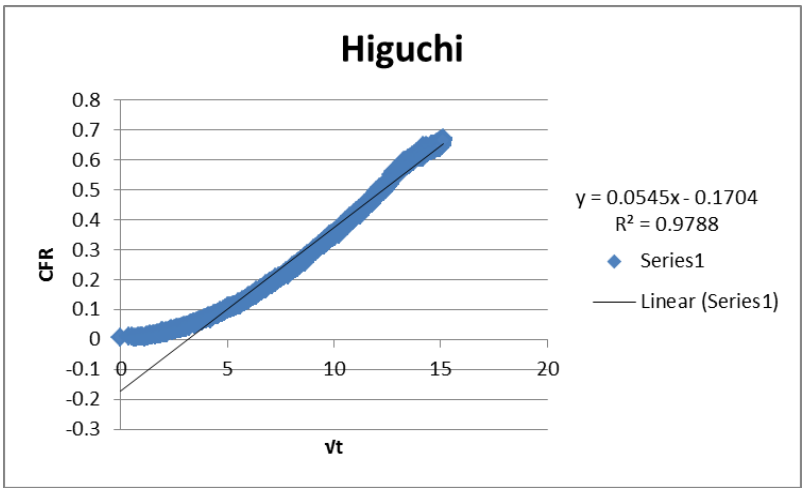

Figure 60: Higuchi model plot for control liposomes, batch #2, at 7.46mW/cm^2

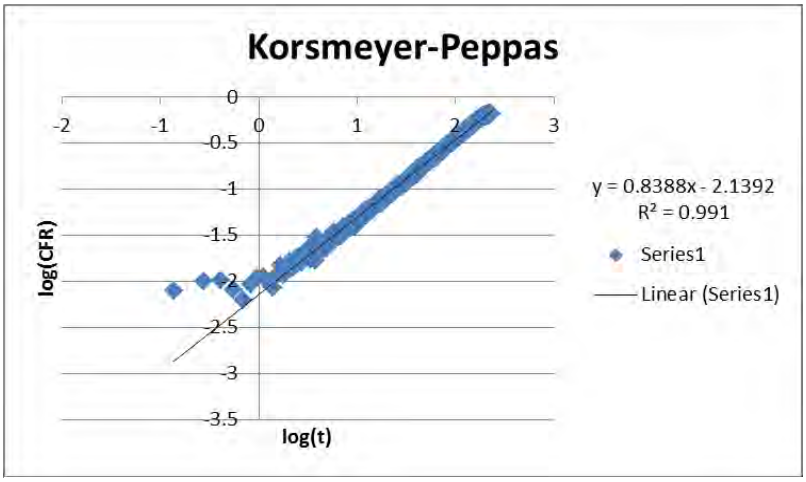

Figure 61: Korsmeyer-Peppas model plot for control liposomes, batch #2, at 7.46mW/cm^2

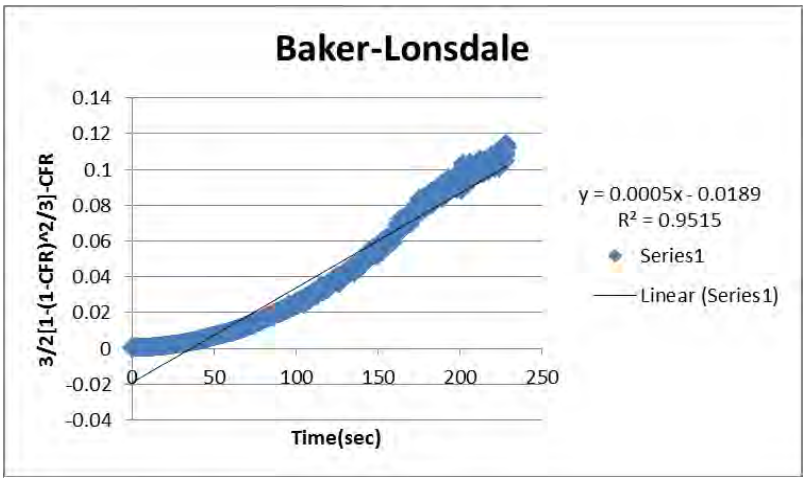

Figure 62: Baker-Lonsdale model plot for control liposomes, batch #2, at 7.46mW/cm^2

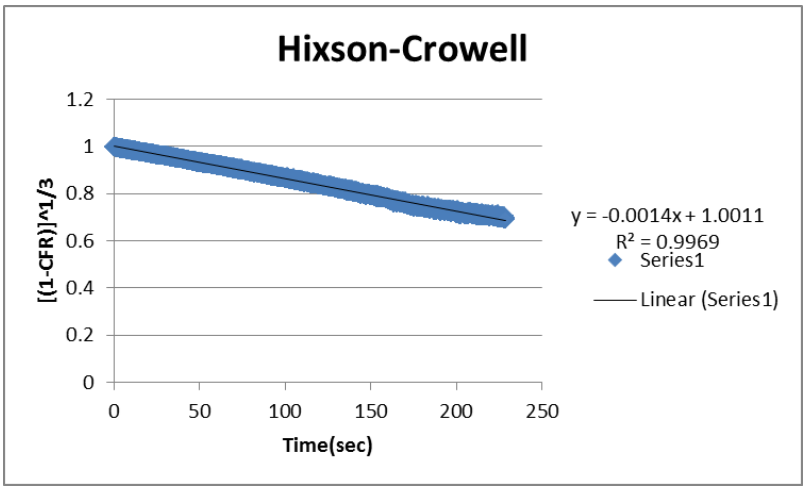

Figure 63: Hixson-Crowell model plot for control liposomes, batch #2, at 7.46mW/cm^2

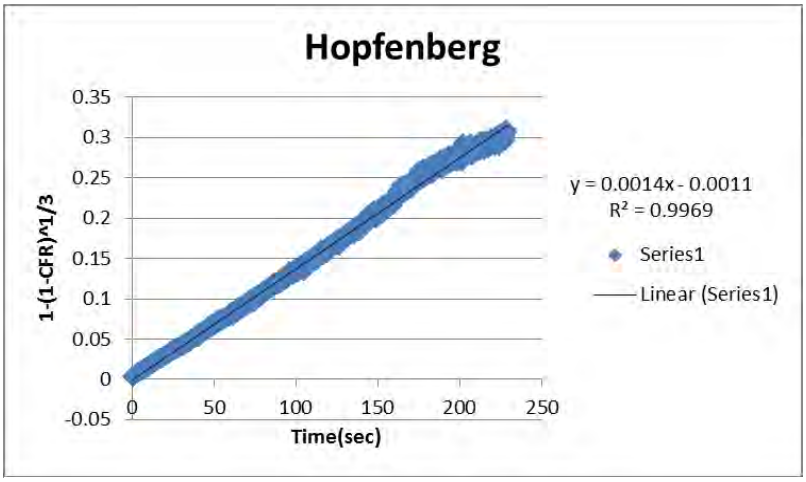

Figure 64: Hopfenberg model plot for control liposomes, batch #2, at 7.46mW/cm^2

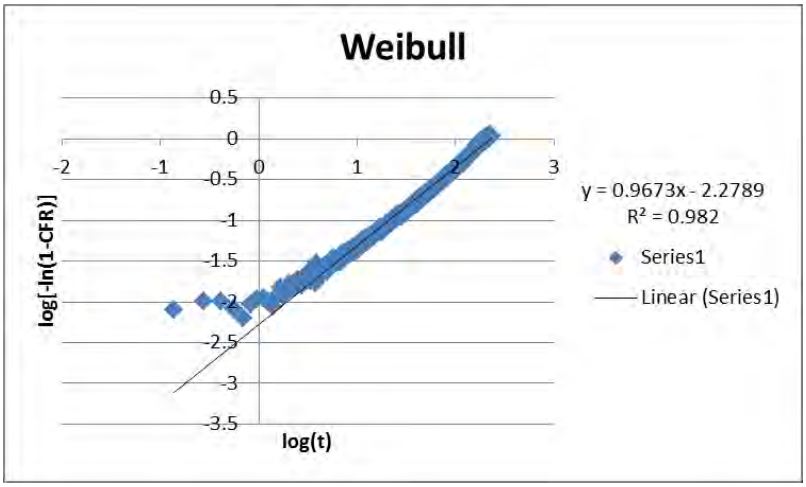

Figure 65: Weibull model plot for control liposomes, batch #2, at 7.46mW/cm^2

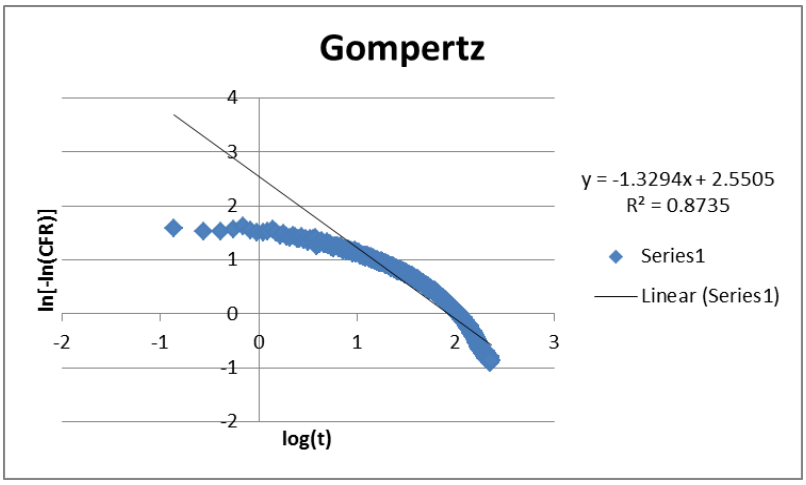

Figure 66: Gompertz model plot for control liposomes, batch #2, at 7.46mW/cm^2

Appendix B: Plots of Kinetic Models for 3rd Batch of NH_2 Liposomes at 7.46mW/cm^2

Figure 67: Zero-order model plot for control liposomes, batch #3, at 7.46mW/cm^2

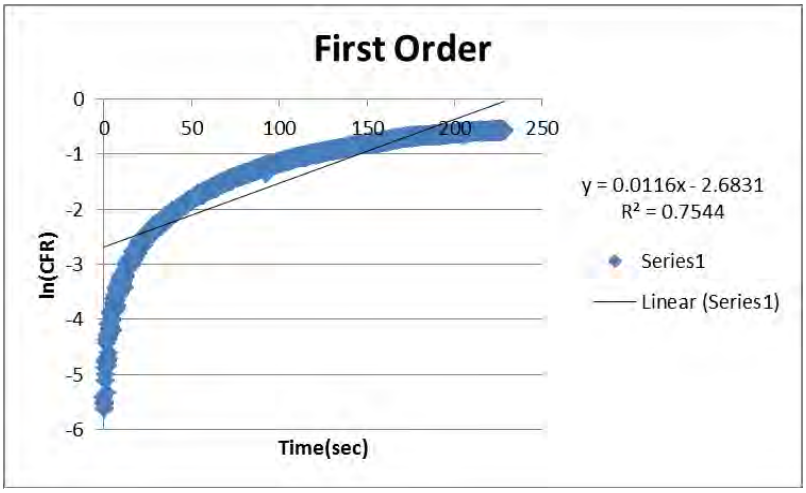

Figure 68: First-order model plot for control liposomes, batch #3, at 7.46mW/cm^2

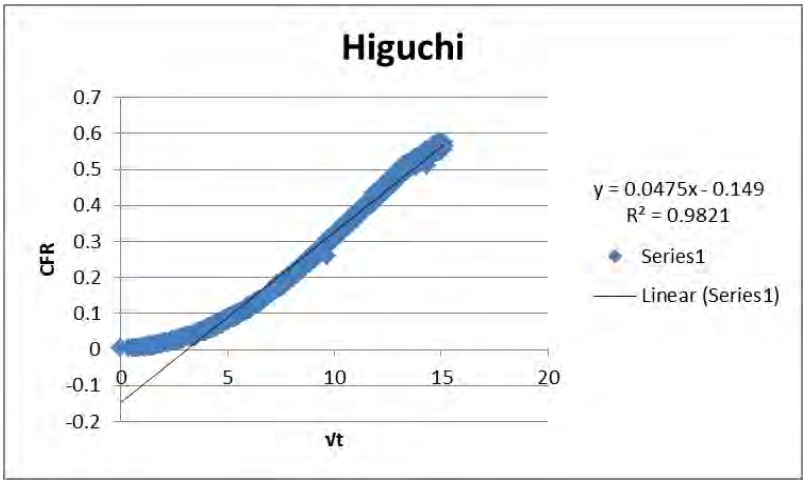

Figure 69: Higuchi model plot for control liposomes, batch #3, at 7.46mW/cm^2

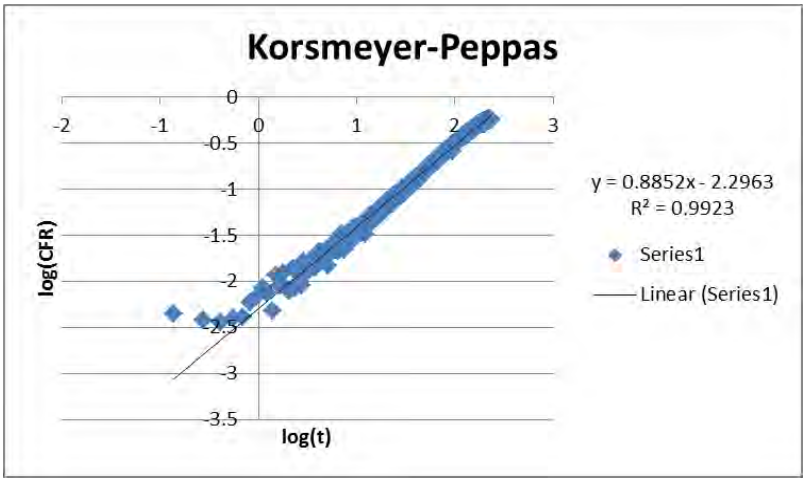

Figure 70: Korsmeyer-Peppas model plot for control liposomes, batch #3, at 7.46mW/cm^2

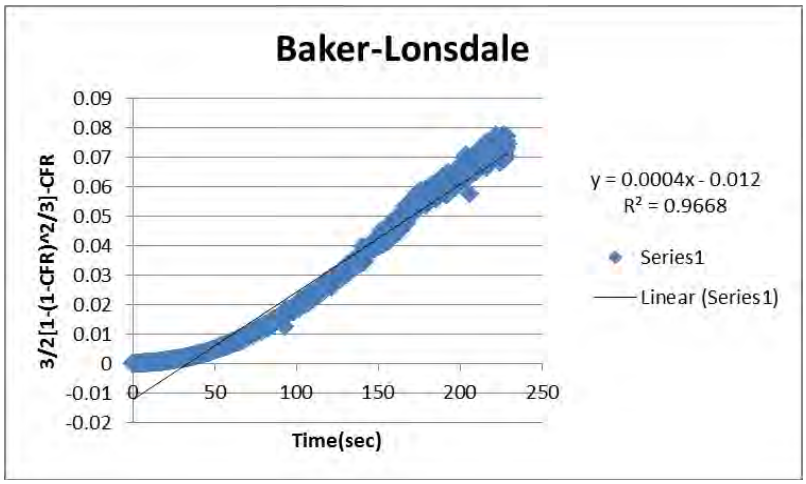

Figure 71: Baker-Lonsdale model plot for control liposomes, batch #3, at 7.46mW/cm^2

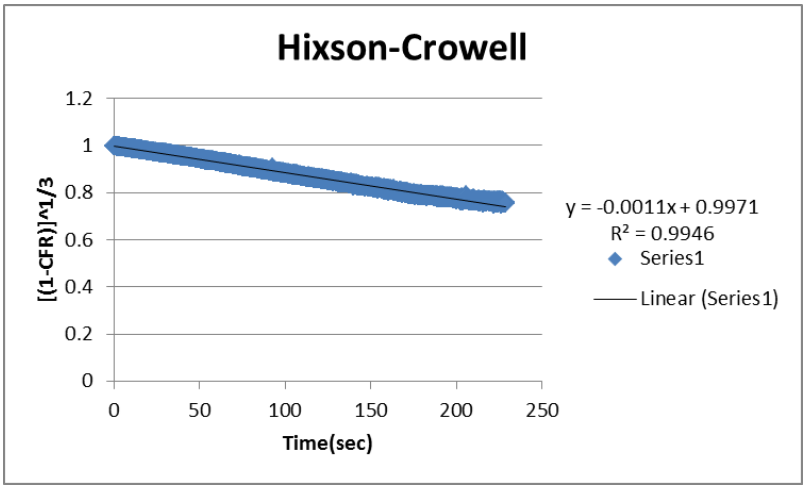

Figure 72: Hixson-Crowell model plot for control liposomes, batch #3, at 7.46mW/cm^2

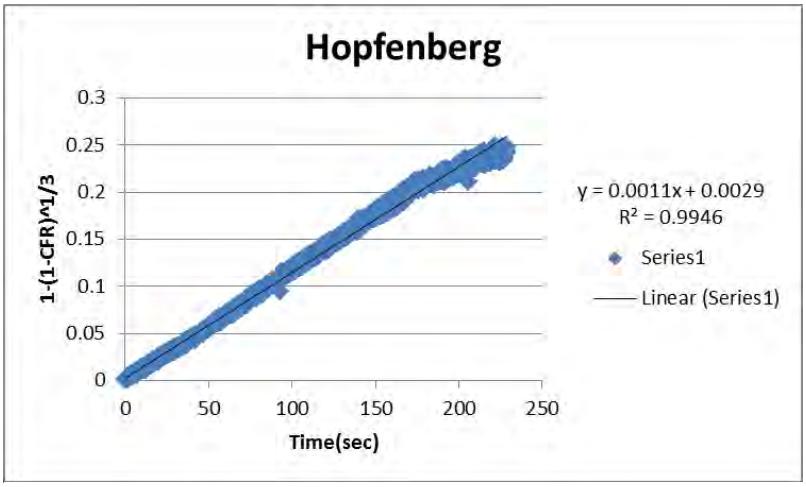

Figure 73: Hopfenberg model plot for control liposomes, batch #3, at 7.46mW/cm^2

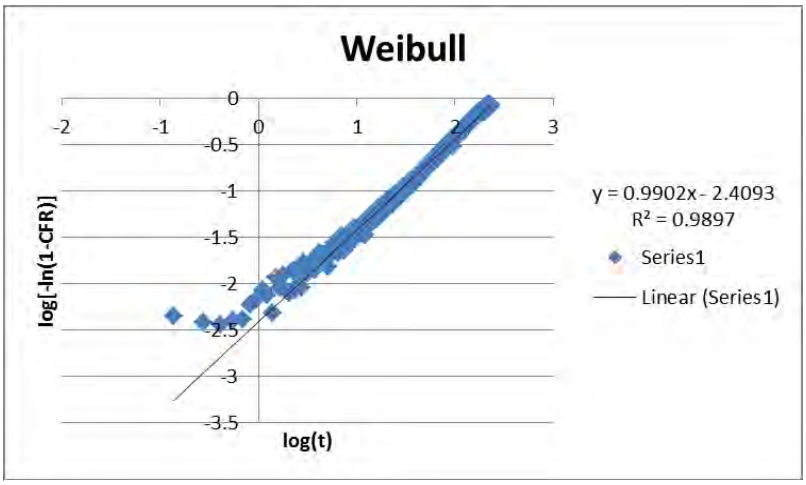

Figure 74: Weibull model plot for control liposomes, batch #3, at 7.46mW/cm^2

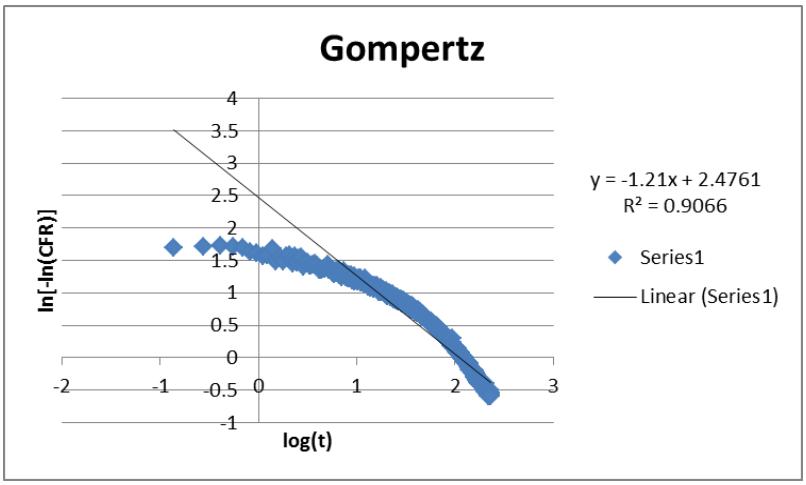

Figure 75: Gompertz model plot for control liposomes, batch #3, at 7.46mW/cm^2

Appendix C: Plots of Kinetic Models for All Batches of NH_2 Liposomes at 9.85 mW/cm^2

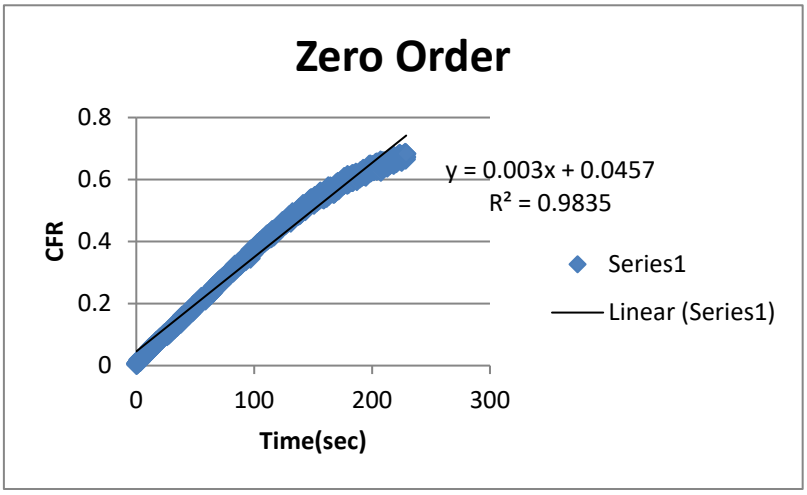

Figure 76: Zero-Order model plot for control liposomes, batch #1, at 9.85mW/cm^2

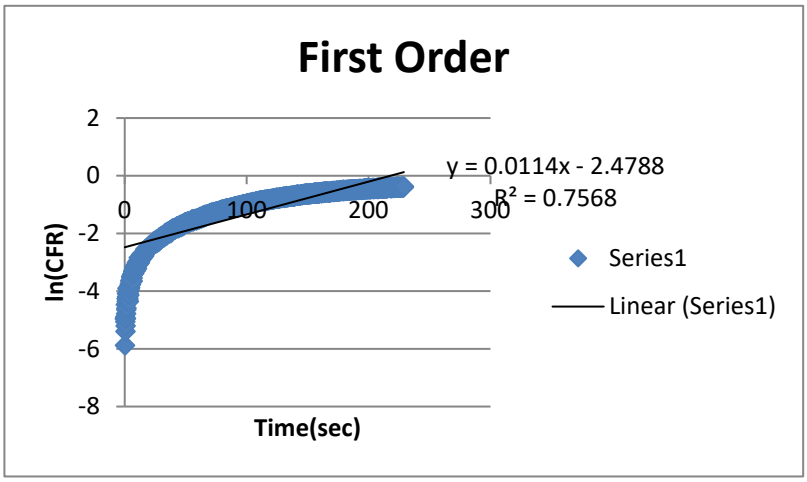

Figure 77: First-Order model plot for control liposomes, batch #1. at 9.85mW/cm^2

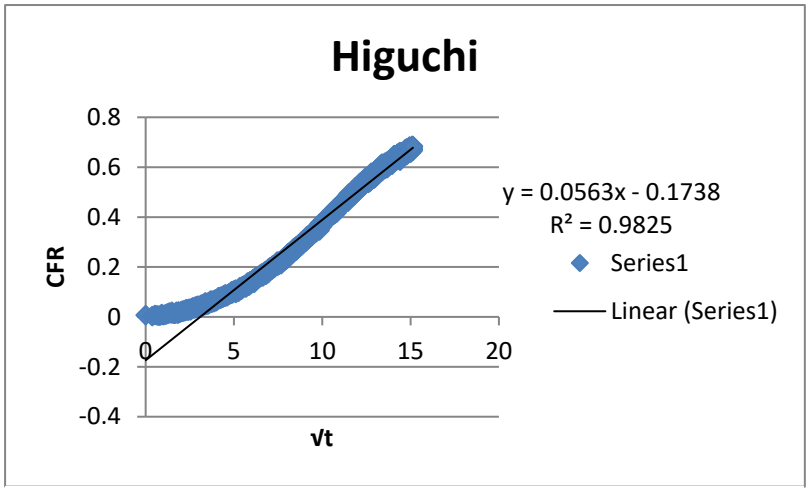

Figure 78: Higuchi model plot for control liposomes, batch #1, at 9.85mW/cm^2

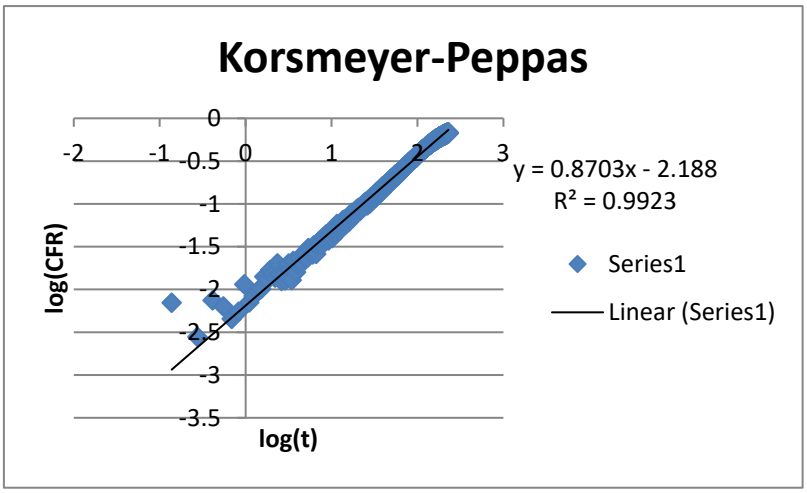

Figure 79: Korsmeyer-Peppas model plot for control liposomes, batch #1, at 9.85mW/cm^2

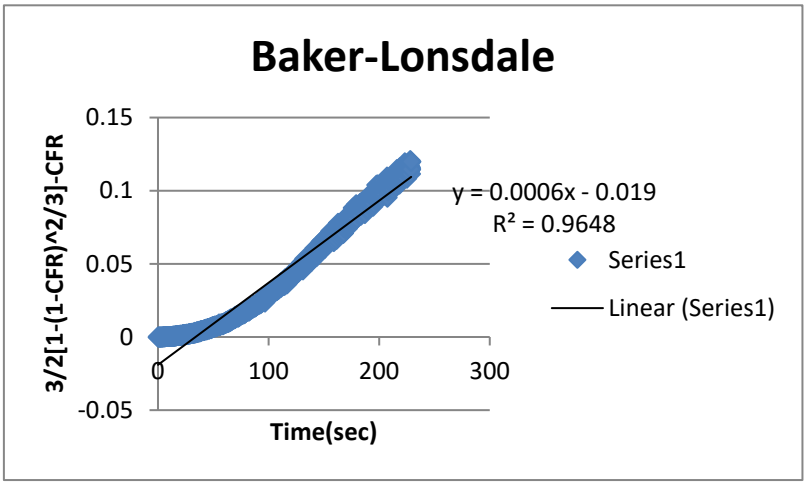

Figure 80: Baker-Lonsdale model plot for control liposomes, batch #1, at 9.85mW/cm^2

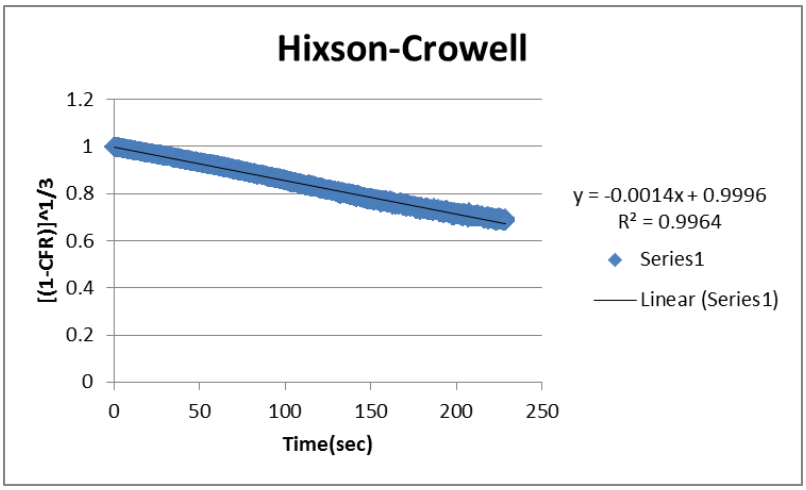

Figure 81: Hixson-Crowell model plot for control liposomes, batch #1, at 9.85mW/cm^2

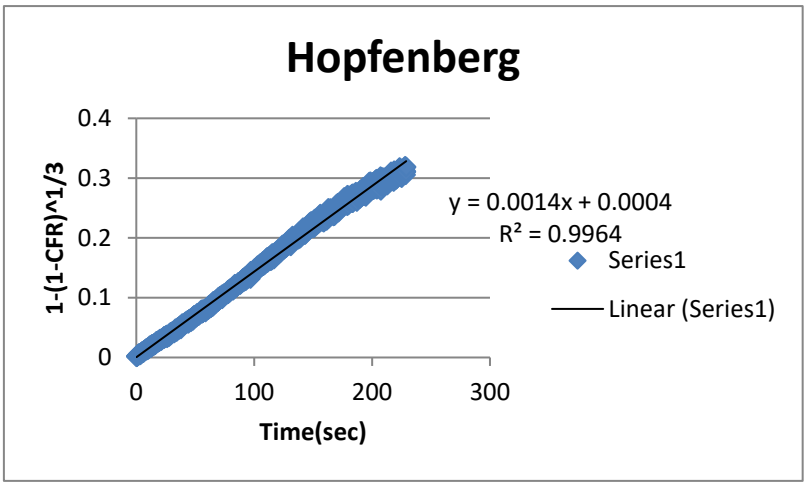

Figure 82: Hopfenberg model plot for control liposomes, batch #1, at 9.85mW/cm^2

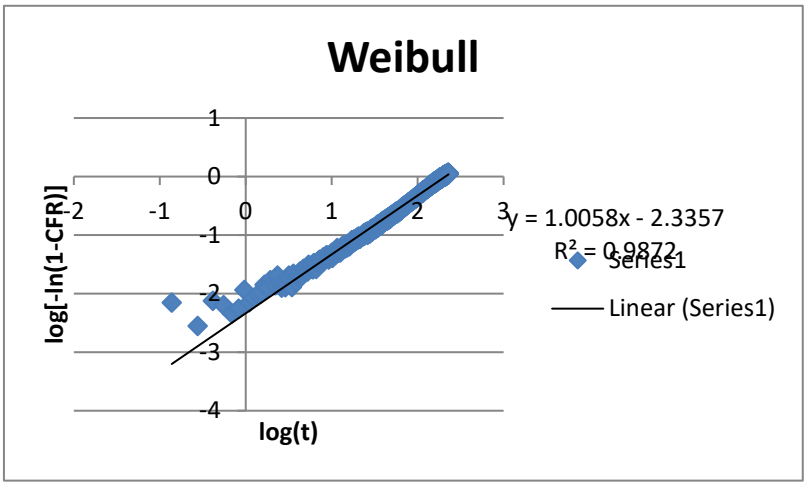

Figure 83: Weibull model plot for control liposomes, batch #1, at 9.85mW/cm^2

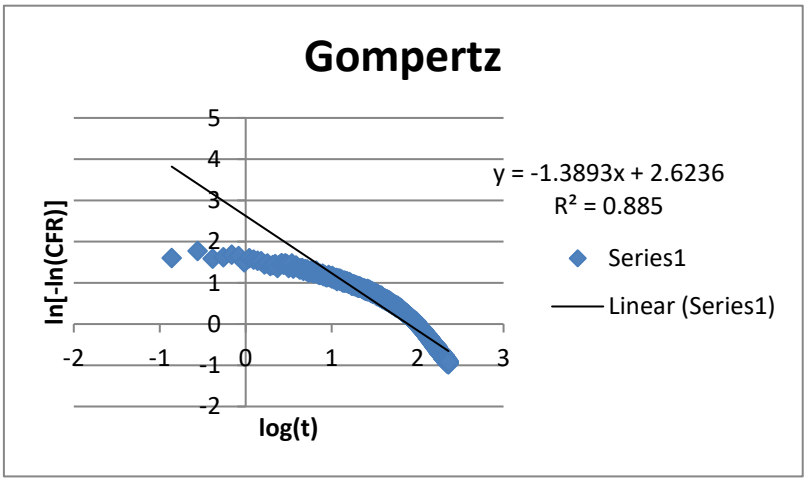

Figure 84: Gompertz model plot for control liposomes, batch #1, at 9.85mW/cm^2

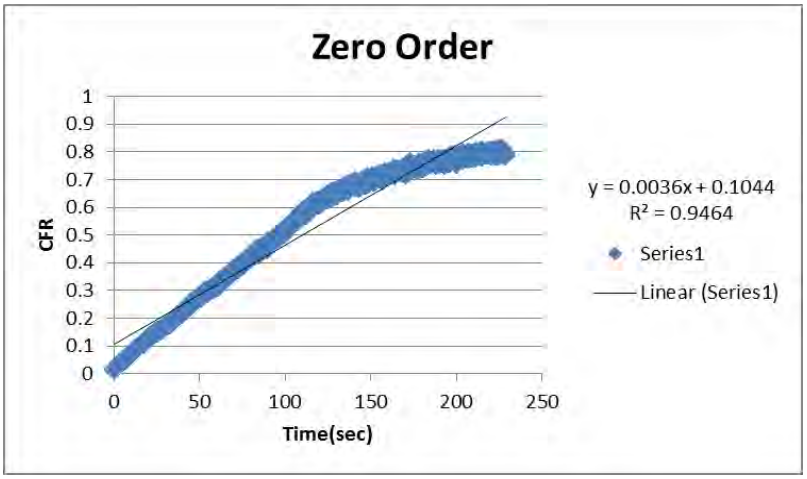

Figure 85: Zero-Order model plot for control liposomes, batch #2, at 9.85mW/cm^2

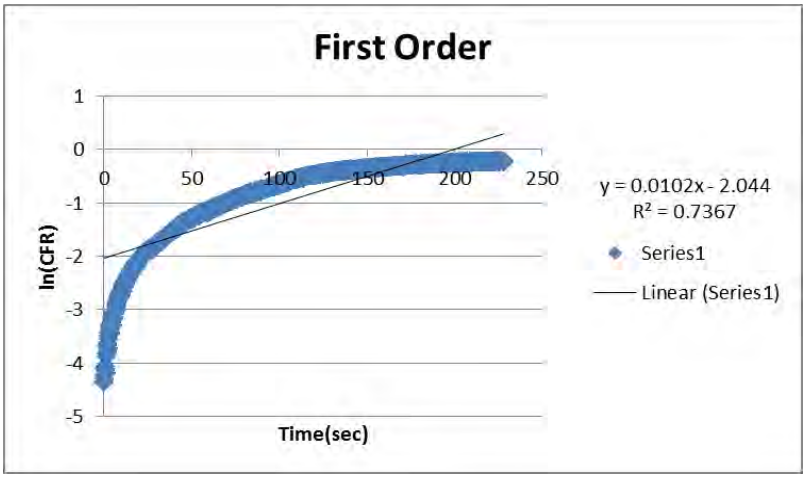

Figure 86: First-Order model plot for control liposomes, batch #2, at 9.85mW/cm^2

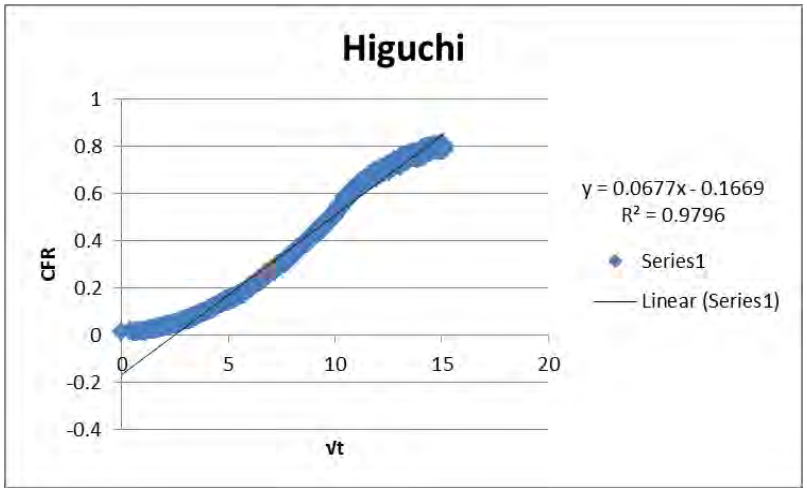

Figure 87: Higuchi model plot for control liposomes, batch #2, at 9.85mW/cm^2

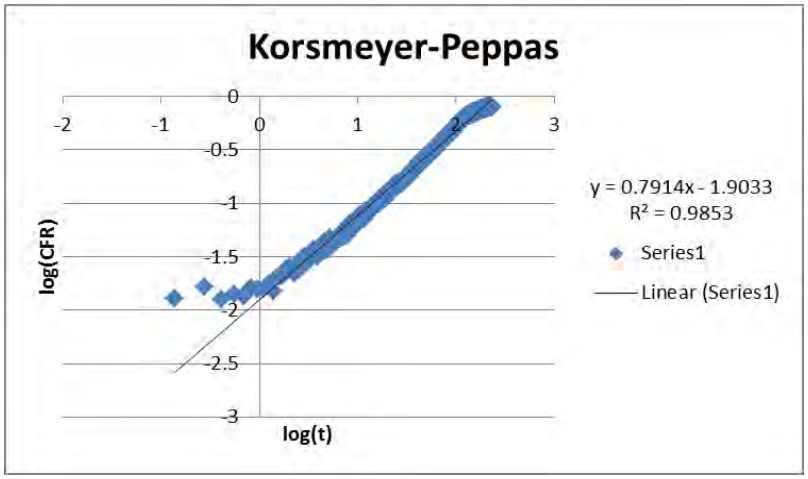

Figure 88: Korsmeyer-Peppas model plot for control liposomes, batch #2, at 9.85mW/cm^2

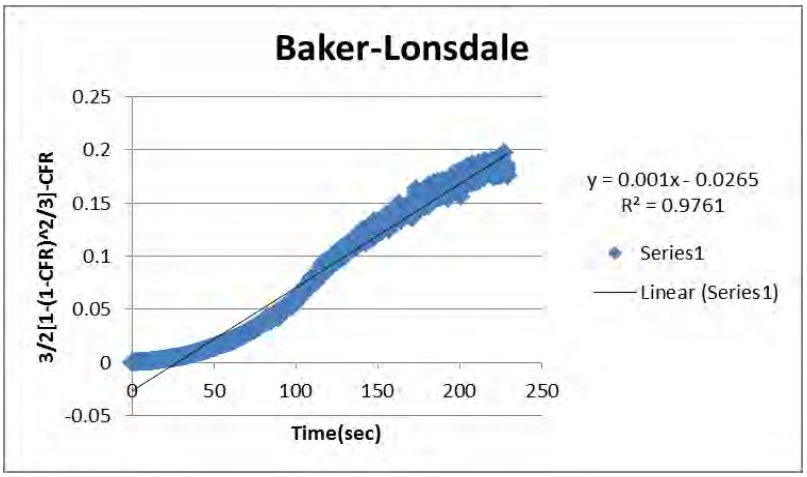

Figure 89: Baker-Lonsdale model plot for control liposomes, batch #2, at 9.85mW/cm^2

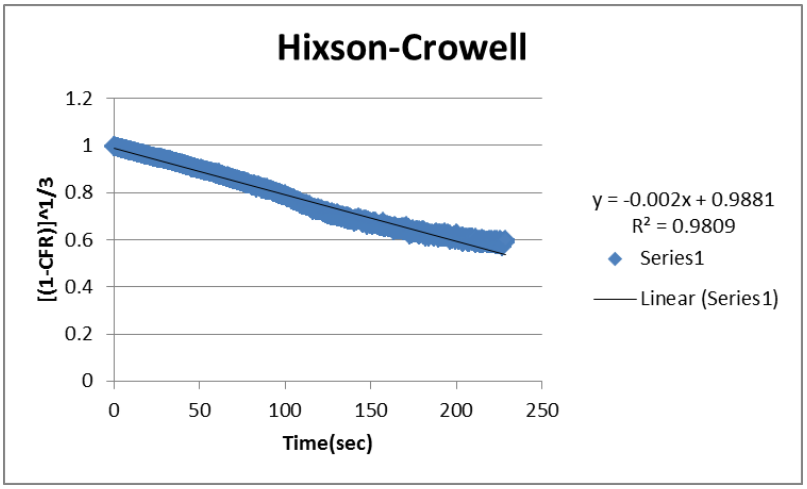

Figure 90: Hixson-Crowell model plot for control liposomes, batch #2, at 9.85mW/cm^2

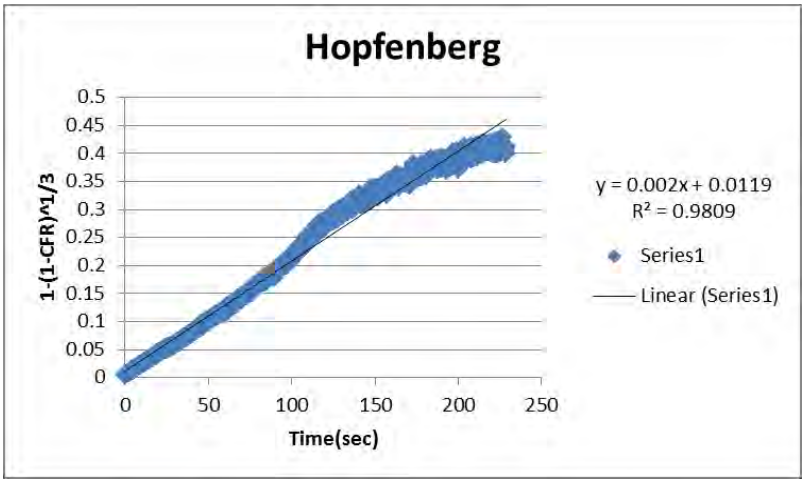

Figure 91: Hopfenberg model plot for control liposomes, batch #2, at 9.85mW/cm^2

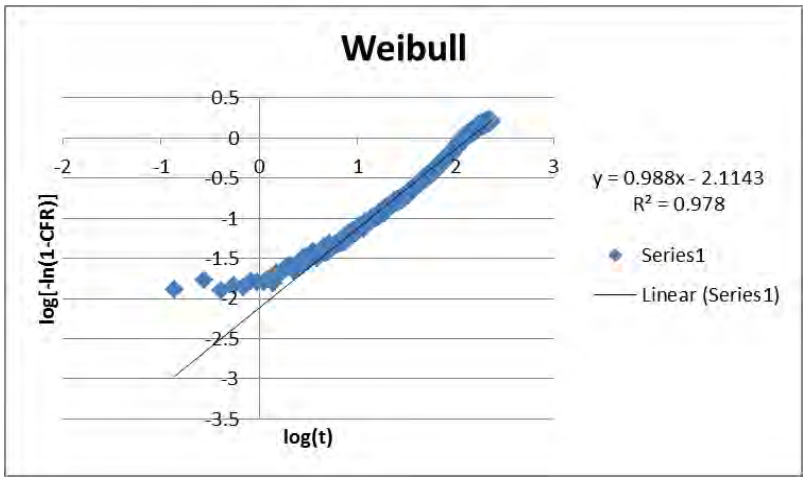

Figure 92: Weibull model plot for control liposomes, batch #2, at 9.85mW/cm^2

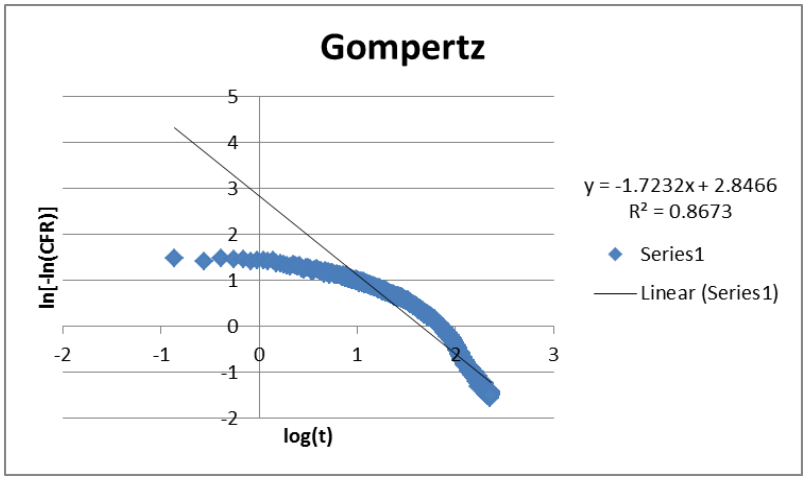

Figure 93: Gompertz model plot for control liposomes, batch #2, at 9.85mW/cm^2

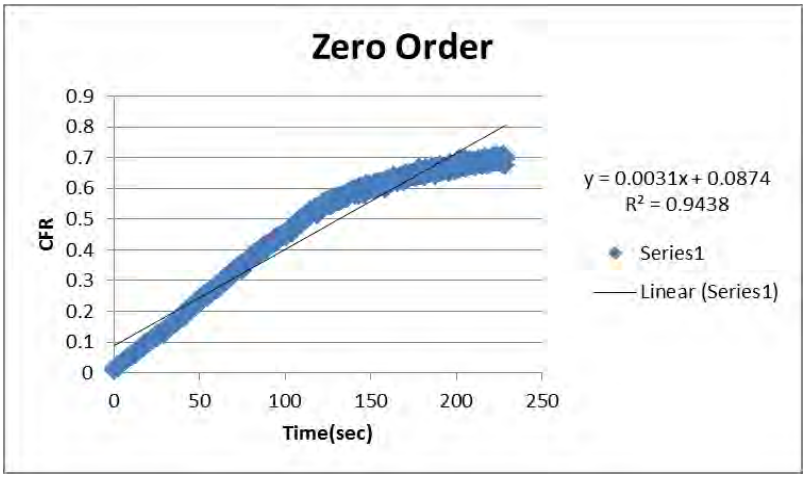

Figure 94: Zero-Order model plot for control liposomes, batch #3, at 9.85mW/cm^2

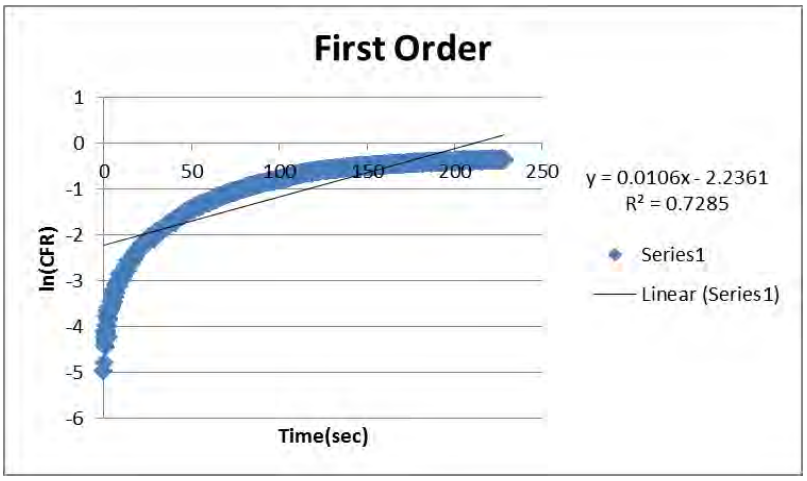

Figure 95: First-Order model plot for control liposomes, batch #3, at 9.85mW/cm^2

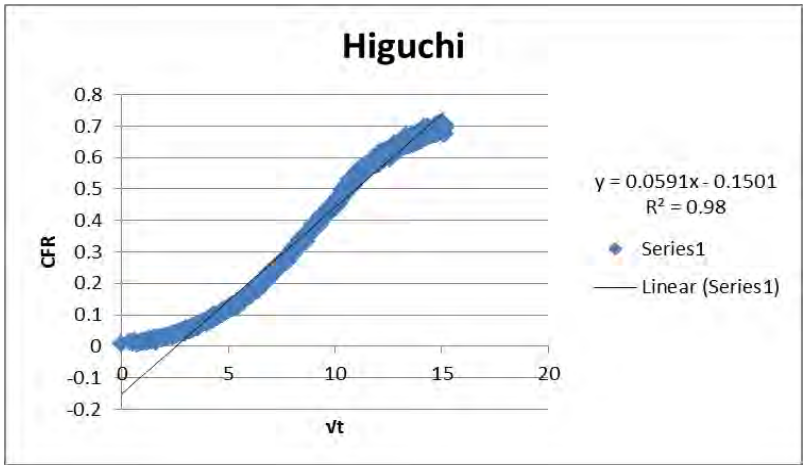

Figure 96: Higuchi model plot for control liposomes, batch #3, at 9.85mW/cm^2

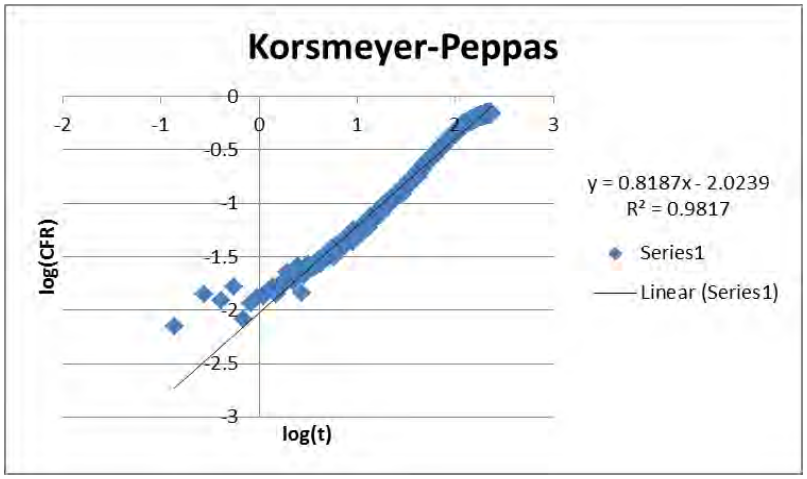

Figure 97: Korsmeyer-Peppas model plot for control liposomes, batch #3, at 9.85mW/cm^2

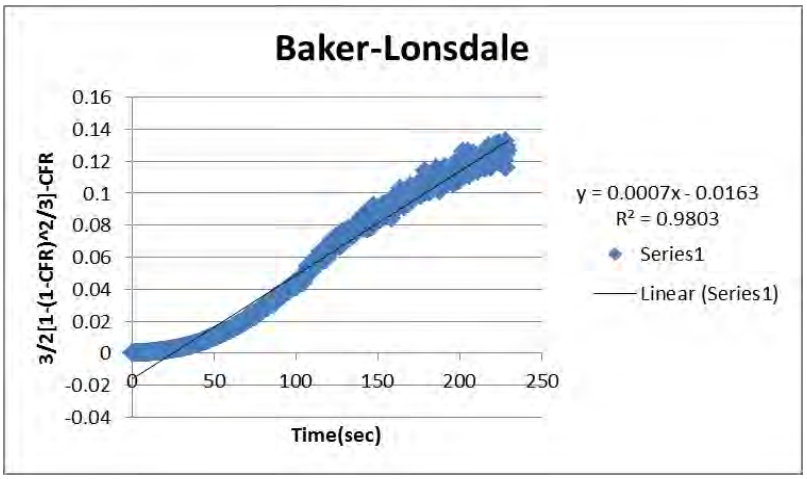

Figure 98: Baker-Lonsdale model plot for control liposomes, batch #3, at 9.85mW/cm^2

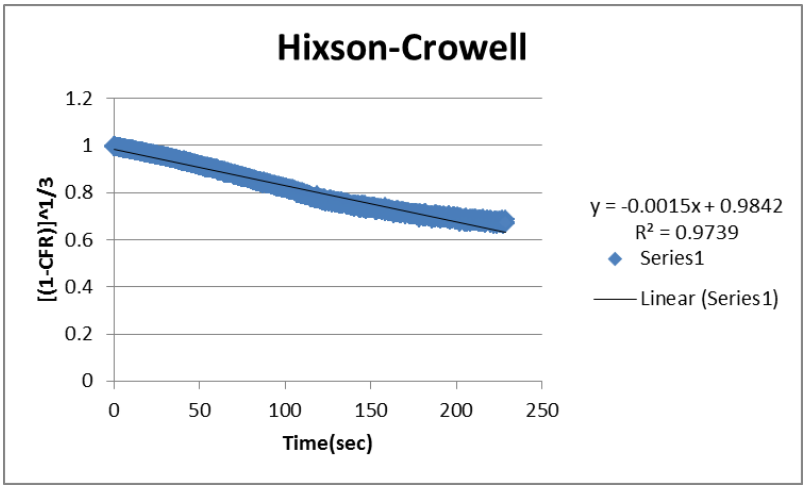

Figure 99: Hixson-Crowell model plot for control liposomes, batch #3, at 9.85mW/cm^2

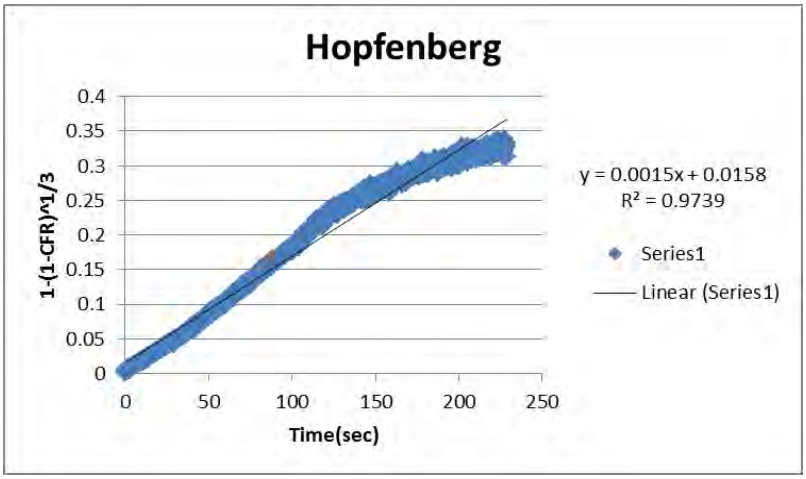

Figure 100: Hopfenberg model plot for control liposomes, batch #3, at 9.85mW/cm^2

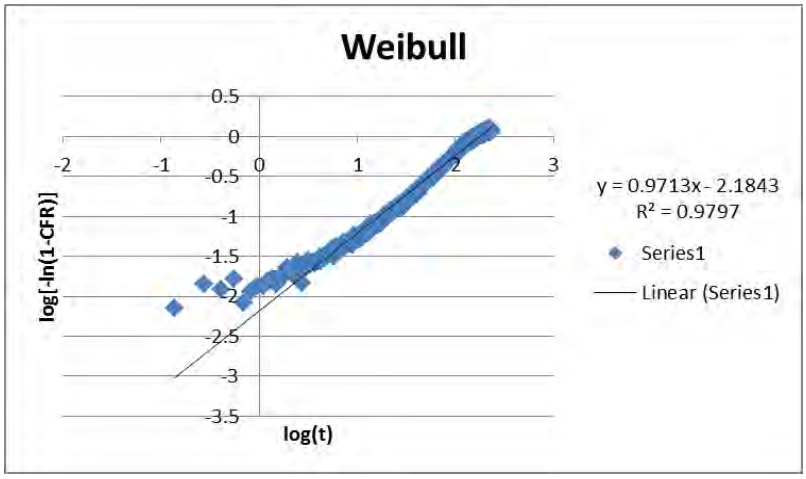

Figure 101: Weibull model plot for control liposomes, batch #3, at 9.85mW/cm^2

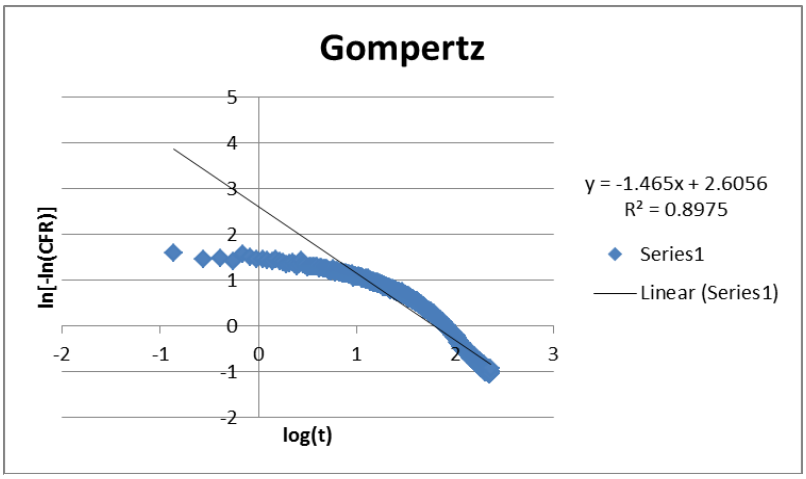

Figure 102: Gompertz model plot for control liposomes, batch #3, at 9.85mW/cm^2

Appendix D: Plots of Kinetic Models for All Batches of NH_2 Liposomes at 17.31 mW/cm^2

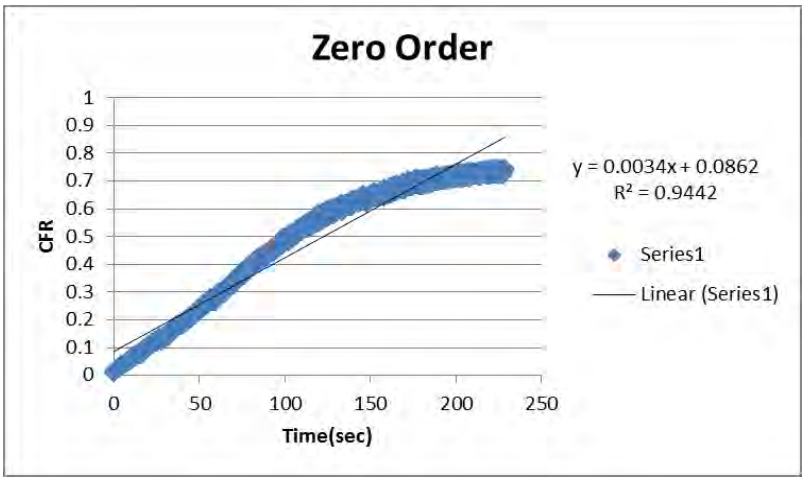

Figure 103: Zero-Order model plot for control liposomes, batch #1, at 17.31mW/cm^2

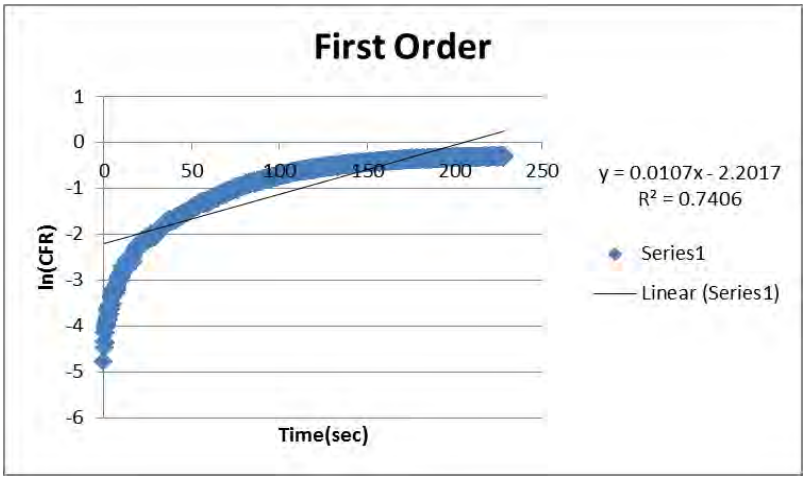

Figure 104: First-Order model plot for control liposomes, batch #1, at 17.31mW/cm^2

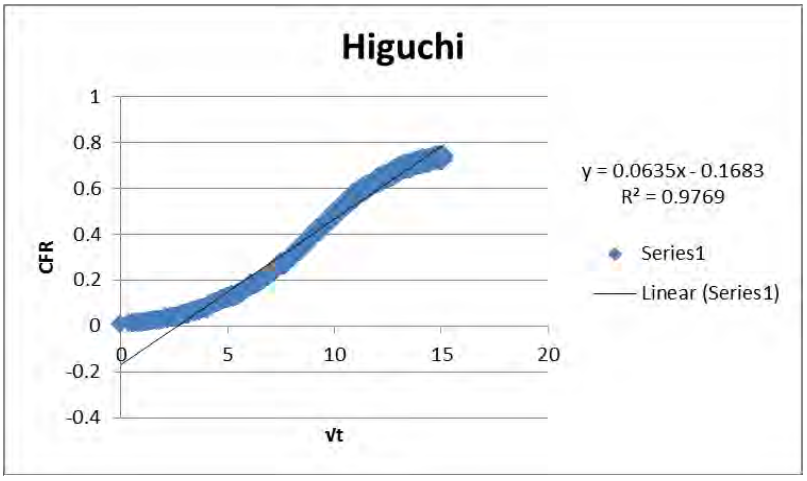

Figure 105: Higuchi model plot for control liposomes, batch #1, at 17.31mW/cm^2

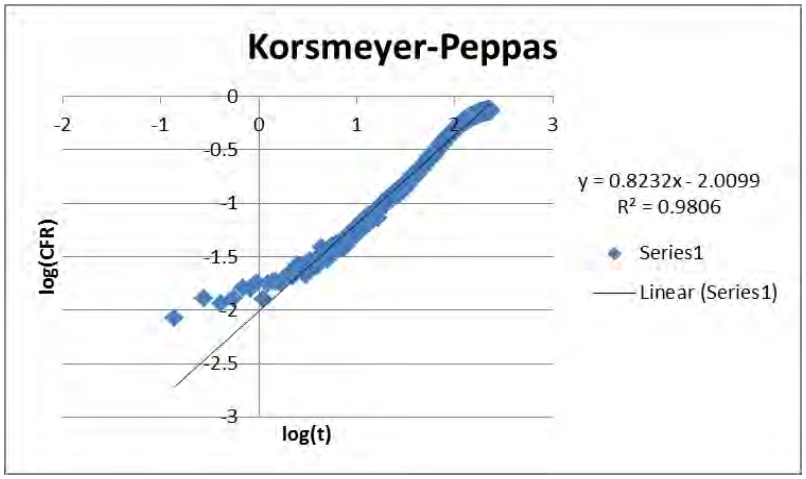

Figure 106: Korsmeyer-Peppas model plot for control liposomes, batch #1, at 17.31mW/cm^2

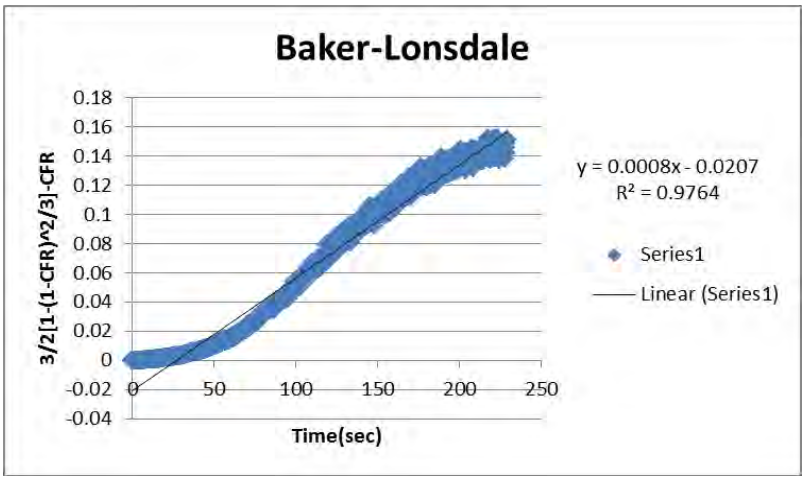

Figure 107: Baker-Lonsdale model plot for control liposomes, batch #1, at 17.31mW/cm^2

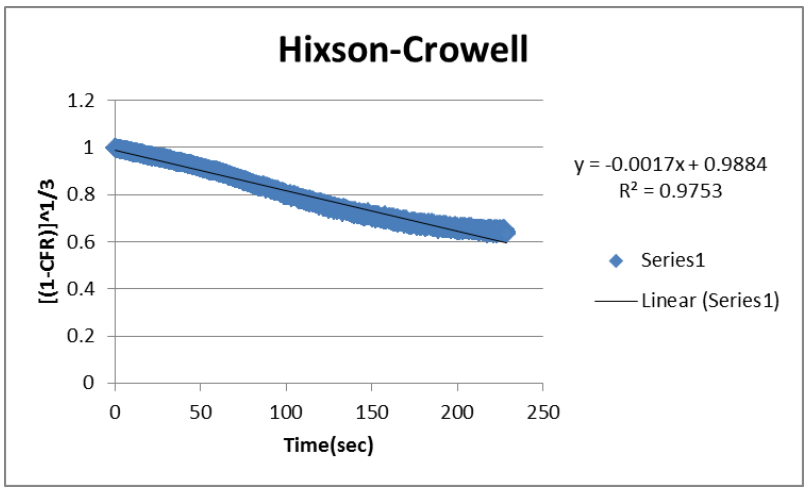

Figure 108: Hixson-Crowell model plot for control liposomes, batch #1, at 17.31mW/cm^2

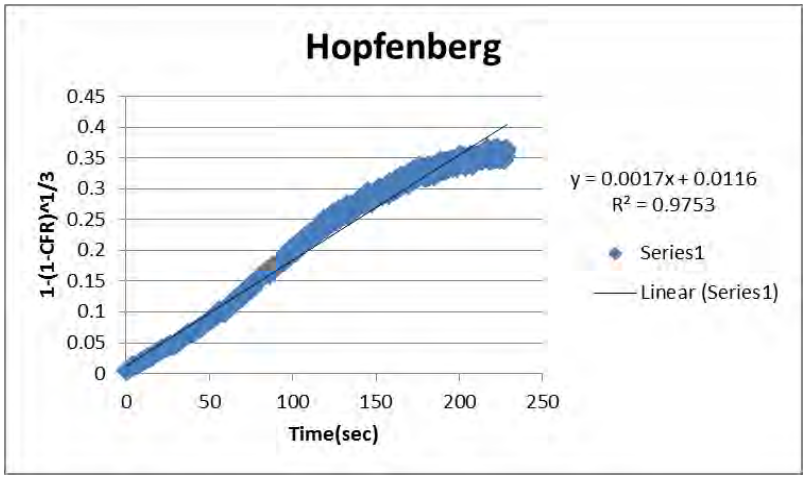

Figure 109: Hopfenberg model plot for control liposomes, batch #1, at 17.31mW/cm^2

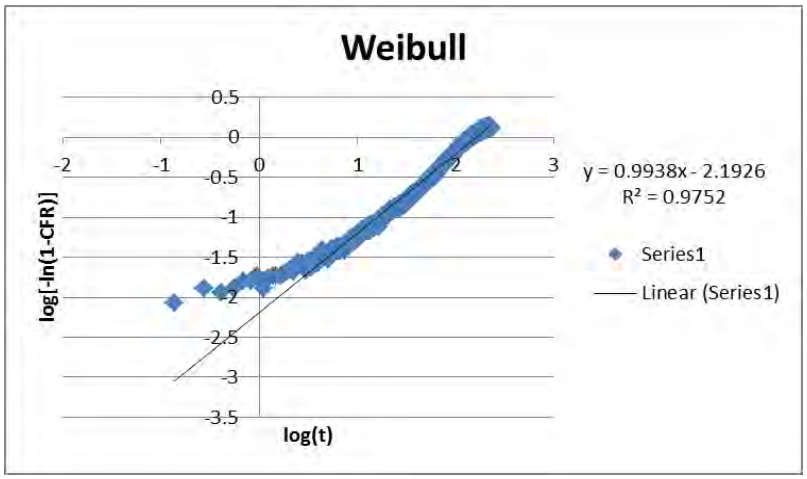

Figure 110: Weibull model plot for control liposomes, batch #1, at 17.31mW/cm^2

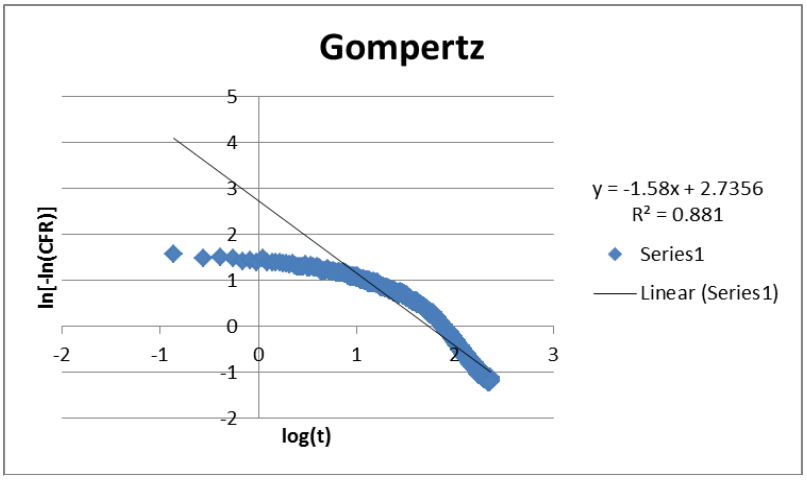

Figure 111: Gompertz model plot for control liposomes, batch #1, at 17.31mW/cm^2

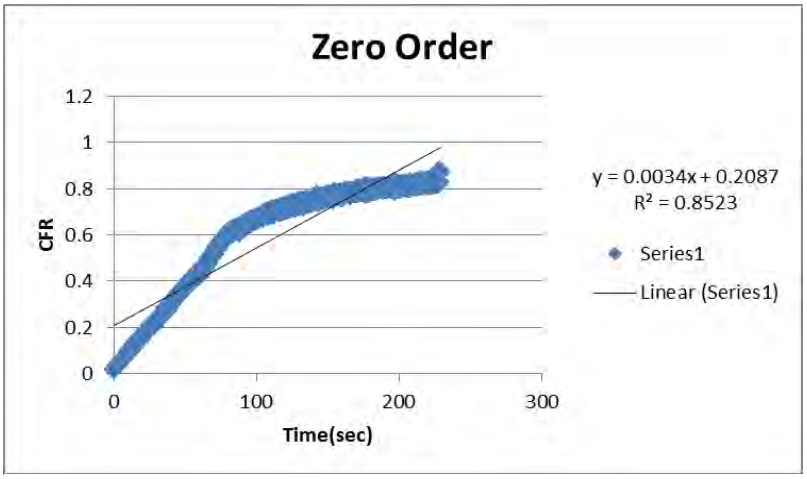

Figure 112: Zero-Order model plot for control liposomes, batch #2, at 17.31mW/cm^2

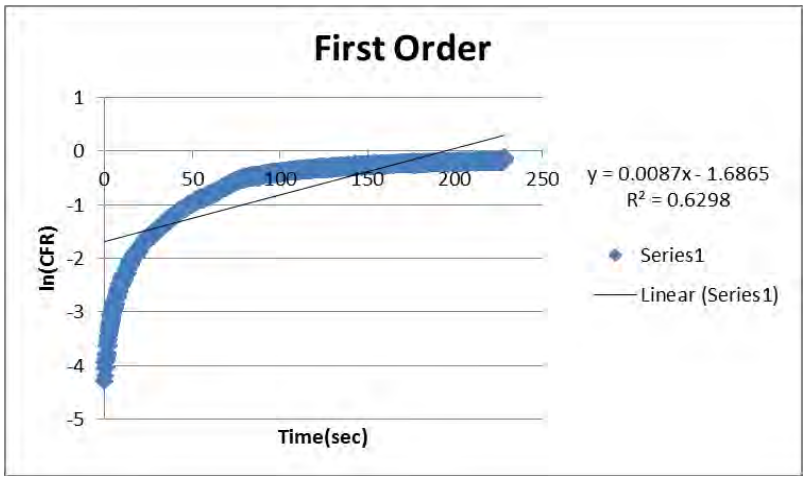

Figure 113: First-Order model plot for control liposomes, batch #2, at 17.31mW/cm^2

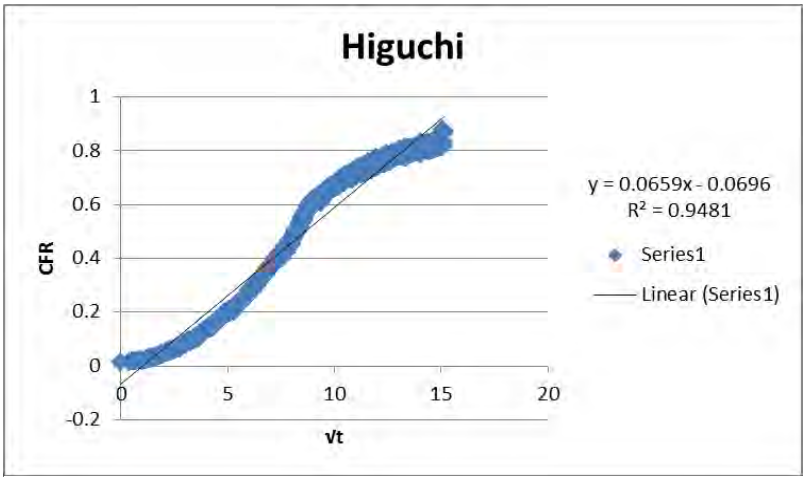

Figure 114: Higuchi model plot for control liposomes, batch #2, at 17.31mW/cm^2

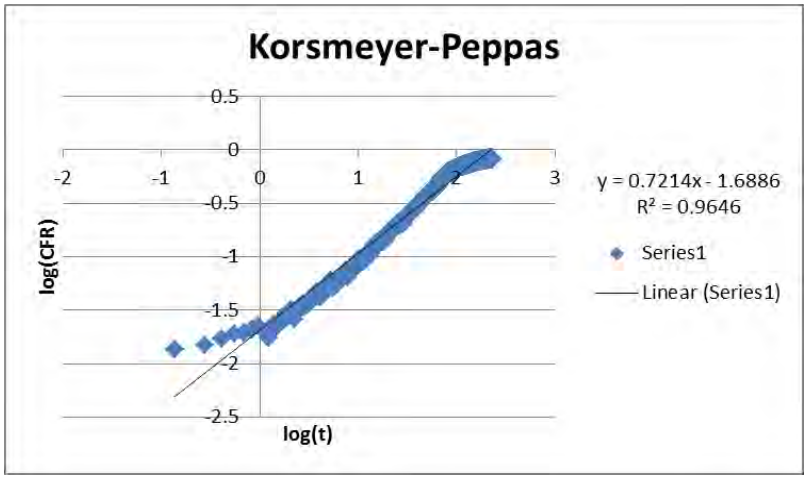

Figure 115: Korsmeyer-Peppas model plot for control liposomes, batch #2, at 17.31mW/cm^2

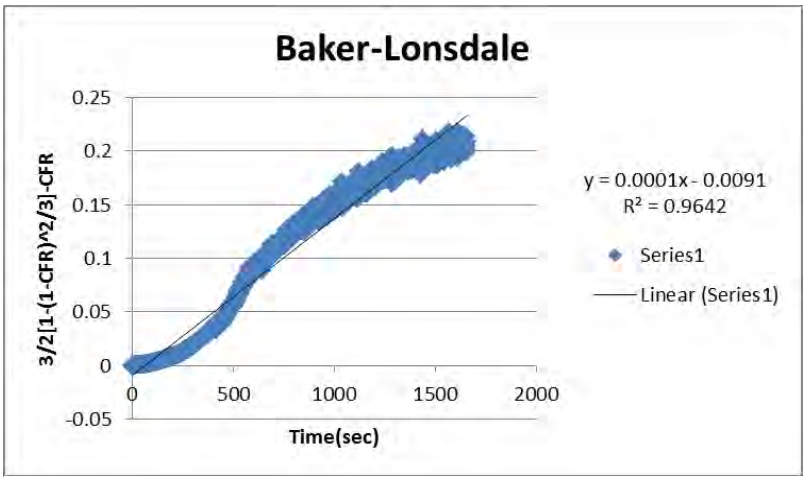

Figure 116: Baker-Lonsdale model plot for control liposomes, batch #2, at 17.31mW/cm^2

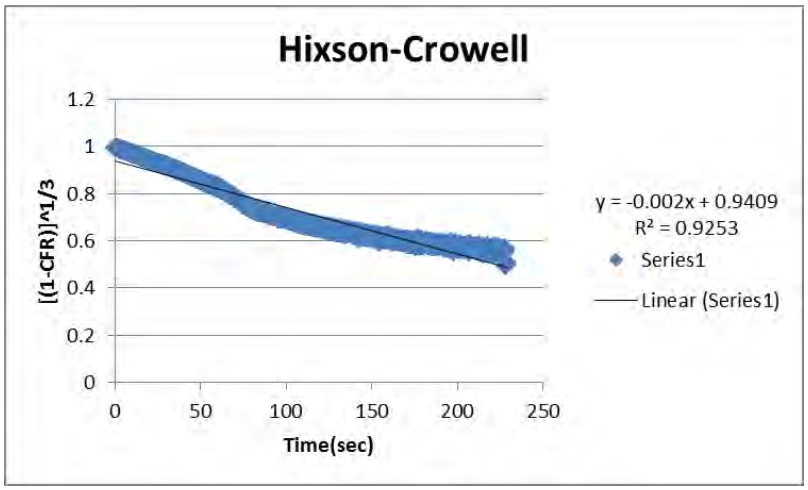

Figure 117: Hixson-Crowell model plot for control liposomes, batch #2, at 17.31mW/cm^2

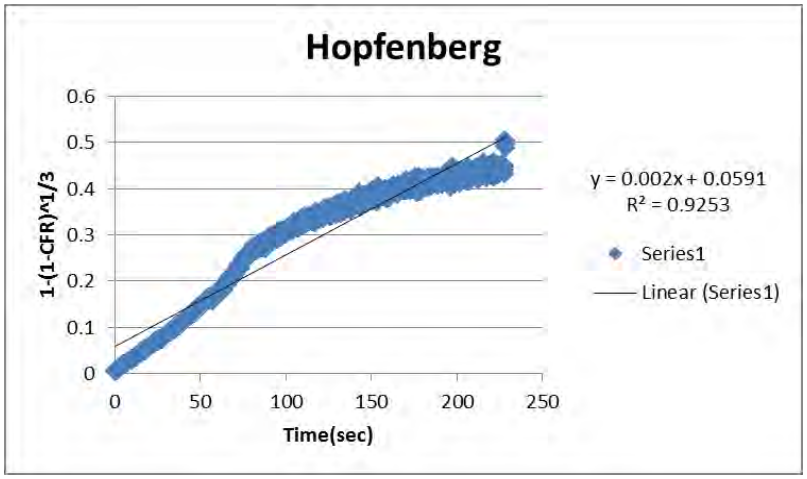

Figure 118: Hopfenberg model plot for control liposomes, batch #2, at 17.31mW/cm^2

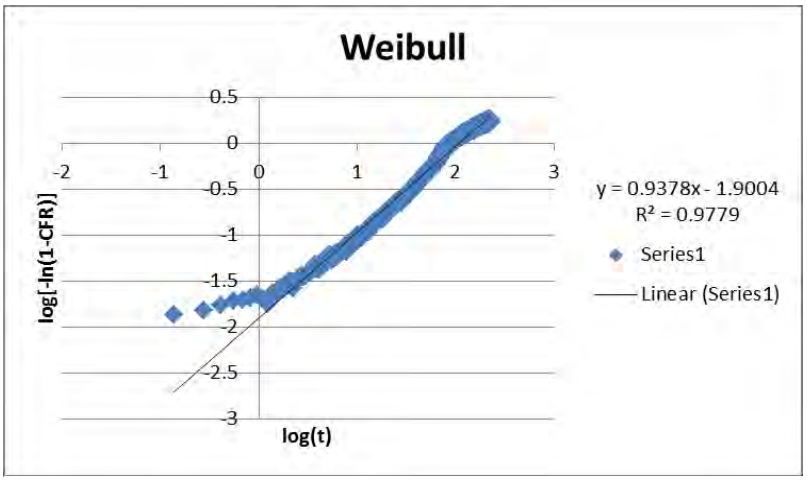

Figure 119: Weibull model plot for control liposomes, batch #2, at 17.31mW/cm^2

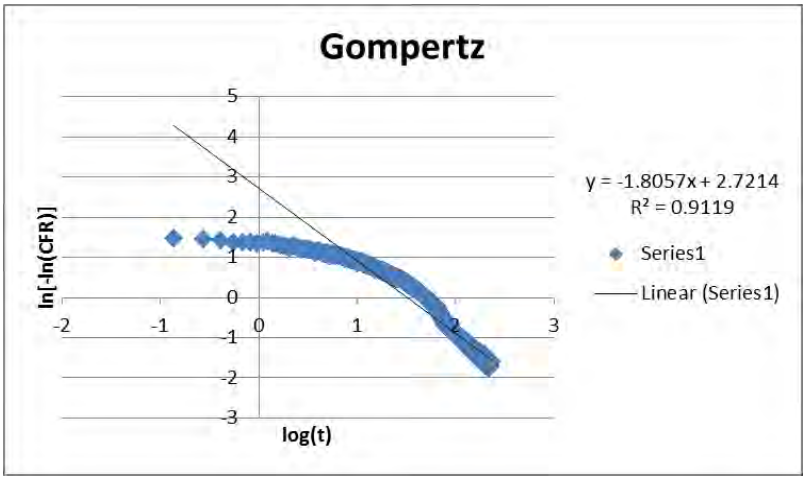

Figure 120: Gompertz model plot for control liposomes, batch #2, at 17.31mW/cm^2

Figure 121: Zero-Order model plot for control liposomes, batch #3, at 17.31mW/cm^2

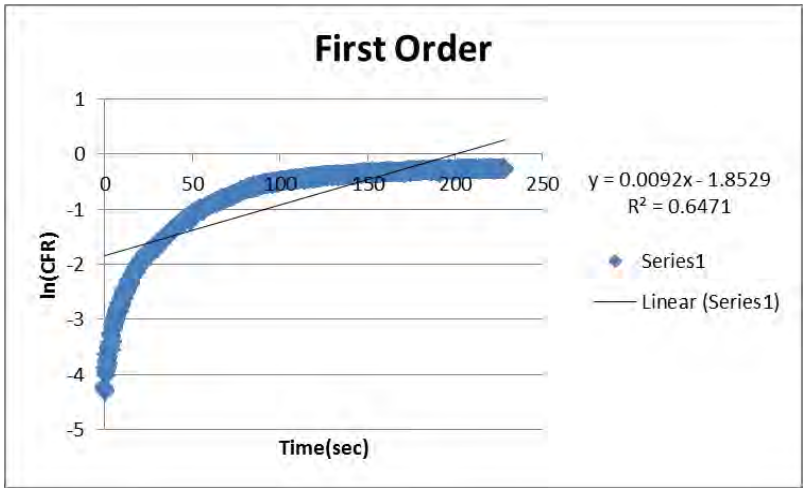

Figure 122: First-Order model plot for control liposomes, batch #3, at 17.31mW/cm^2

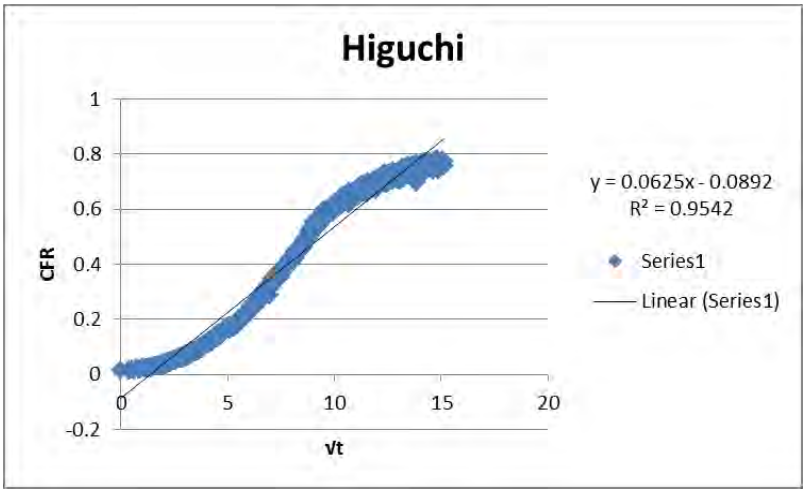

Figure 123: Higuchi model plot for control liposomes, batch #3, at 17.31mW/cm^2

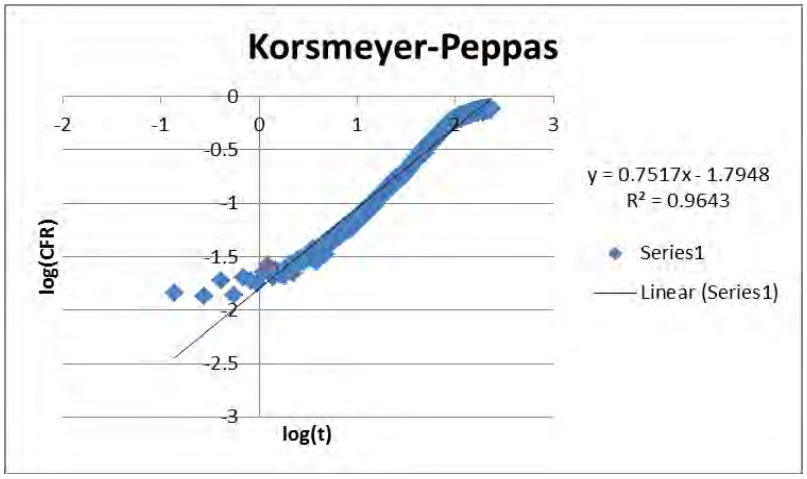

Figure 124: Korsmeyer-Peppas model plot for control liposomes, batch #3, at 17.31mW/cm^2

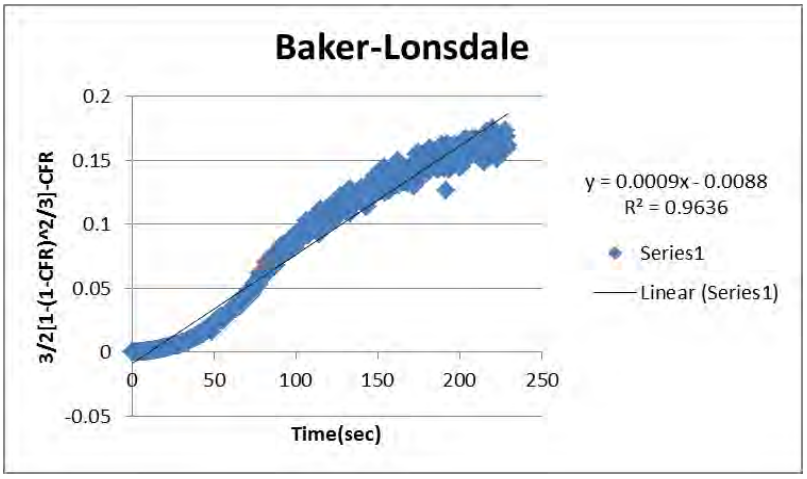

Figure 125: Baker-Lonsdale model plot for control liposomes, batch #3, at 17.31mW/cm^2

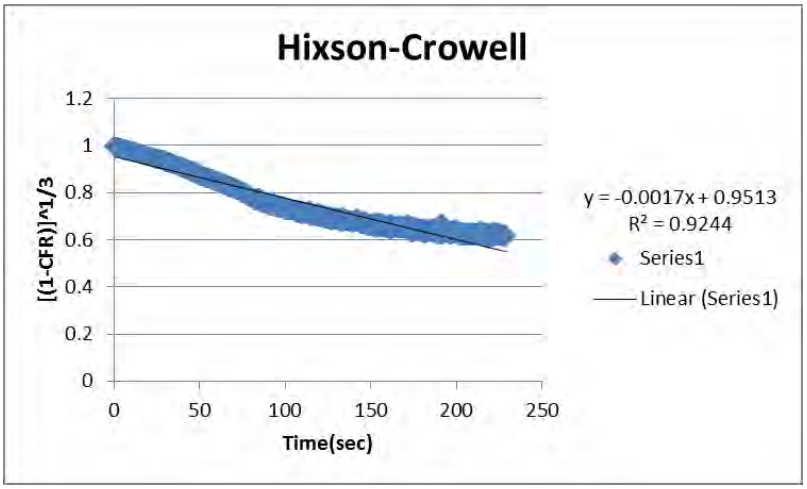

Figure 126: Hixson-Crowell model plot for control liposomes, batch #3, at 17.31mW/cm^2

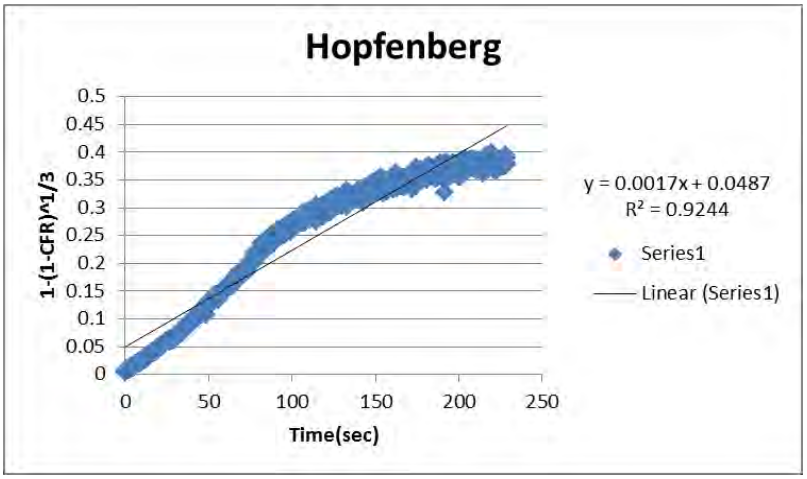

Figure 127: Hopfenberg model plot for control liposomes, batch #3, at 17.31mW/cm^2

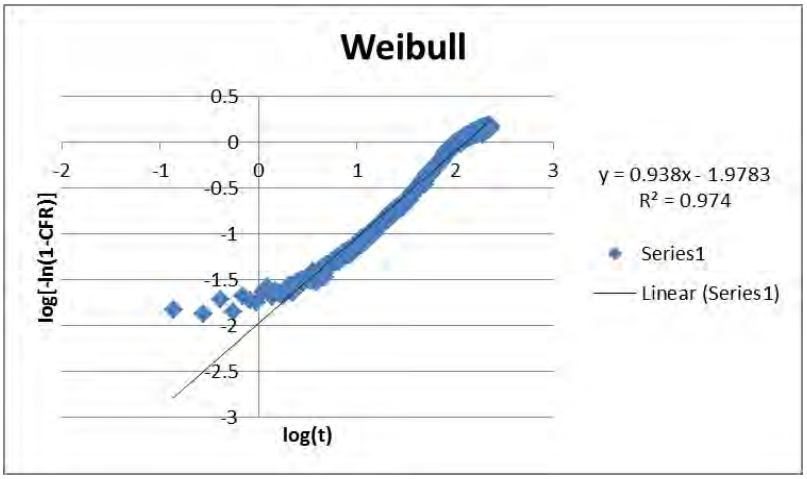

Figure 128: Weibull model plot for control liposomes, batch #3, at 17.31mW/cm^2

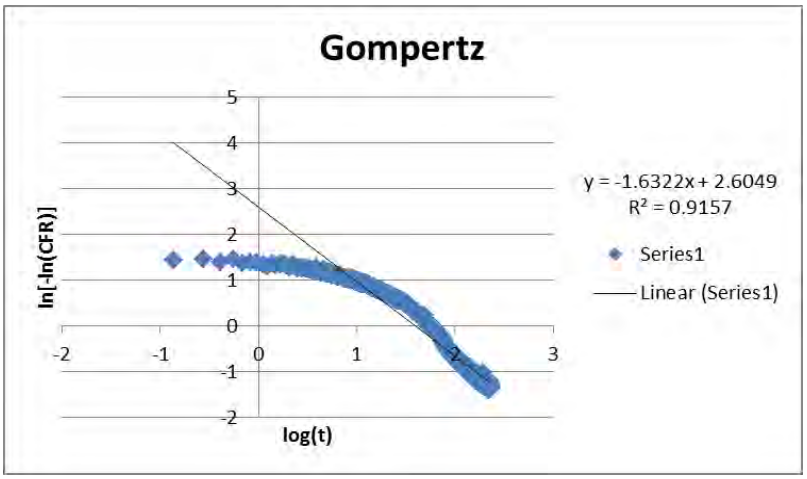

Figure 129: Gompertz model plot for control liposomes, batch #3, at 17.31mW/cm^2

Appendix E: Plots of Kinetic Models for 2nd Batch of Tf Liposomes at 7.46 mW/cm^2

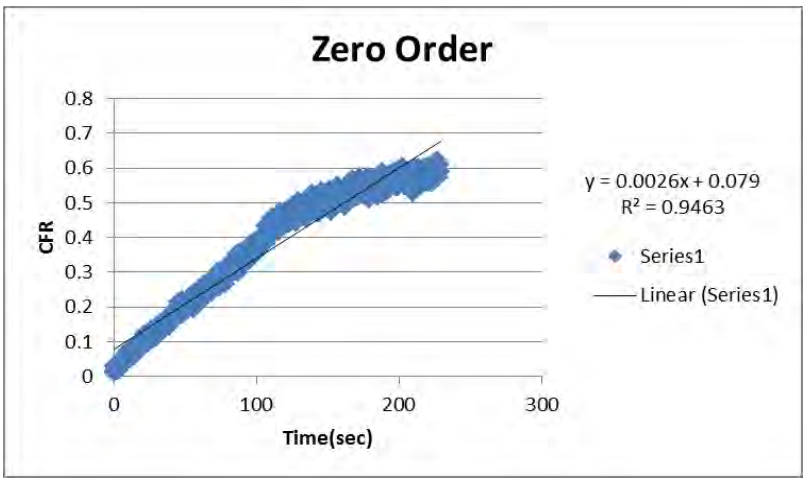

Figure 130: Zero-Order model plot for Tf liposomes, batch #2, at 7.46mW/cm^2

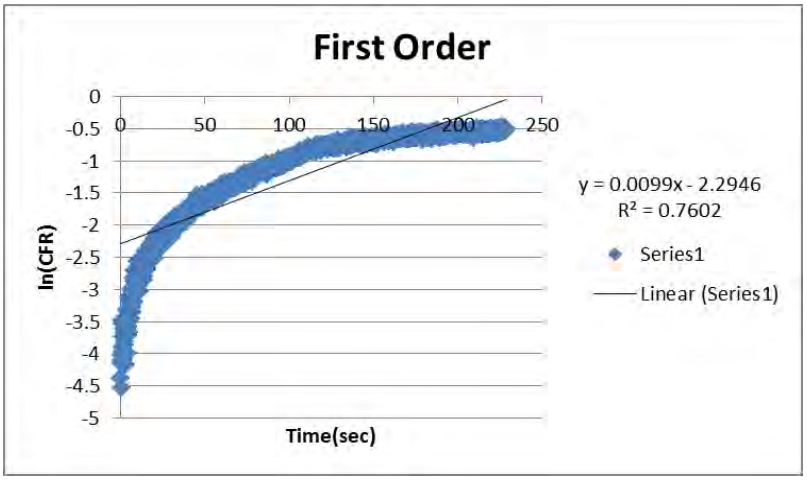

Figure 131: First-Order model plot for Tf liposomes, batch #2, at 7.46mW/cm^2

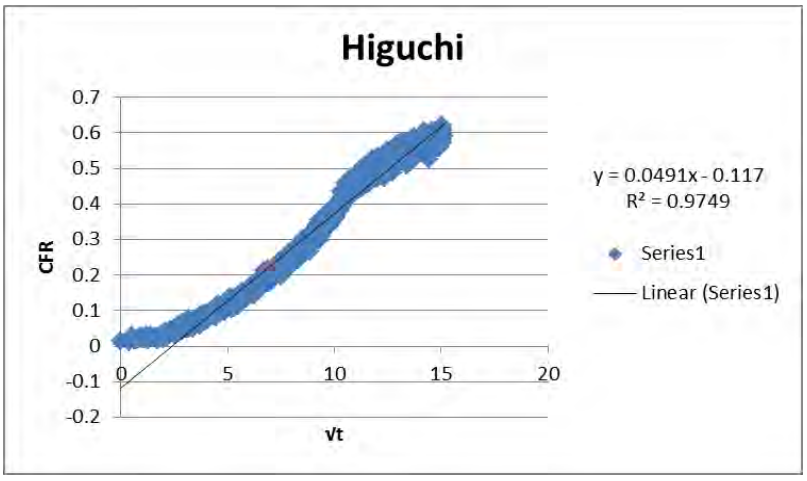

Figure 132: Higuchi model plot for Tf liposomes, batch #2, at 7.46mW/cm^2

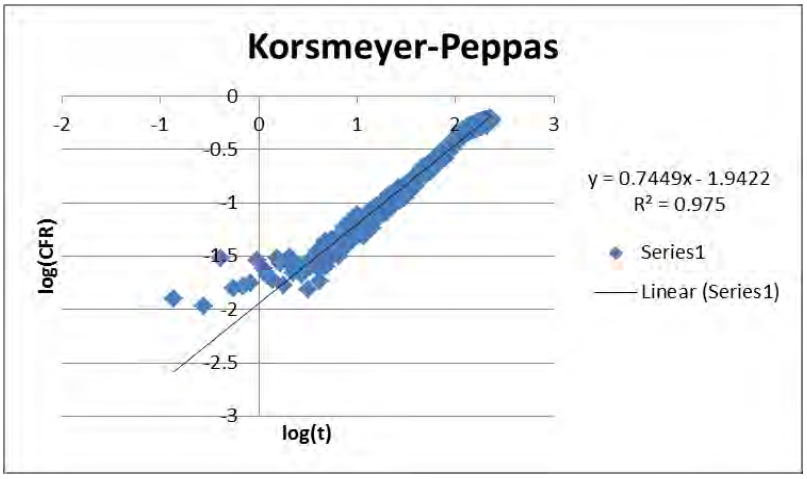

Figure 133: Korsmeyer-Peppas model plot for Tf liposomes, batch #2, at 7.46mW/cm^2

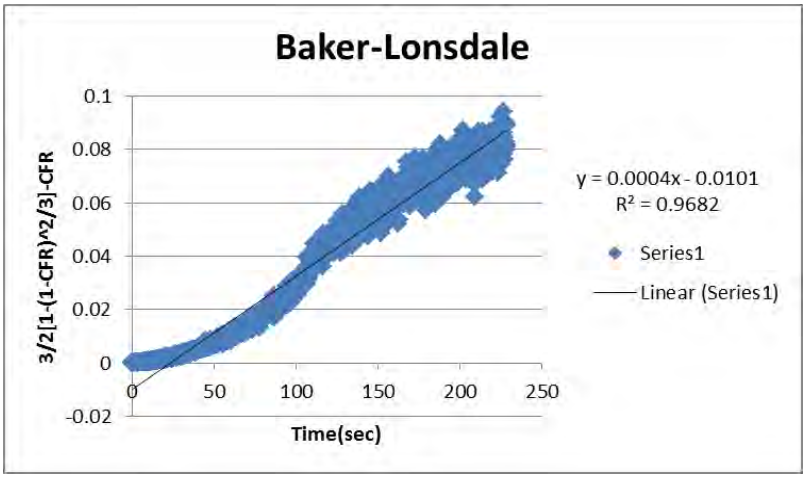

Figure 134: Baker-Lonsdale model plot for Tf liposomes, batch #2, at 7.46mW/cm^2

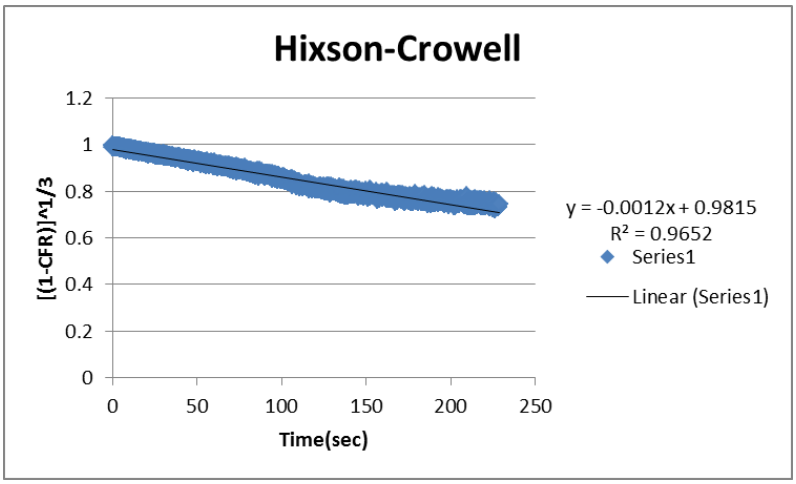

Figure 135: Hixson-Crowell model plot for Tf liposomes, batch #2, at 7.46mW/cm^2

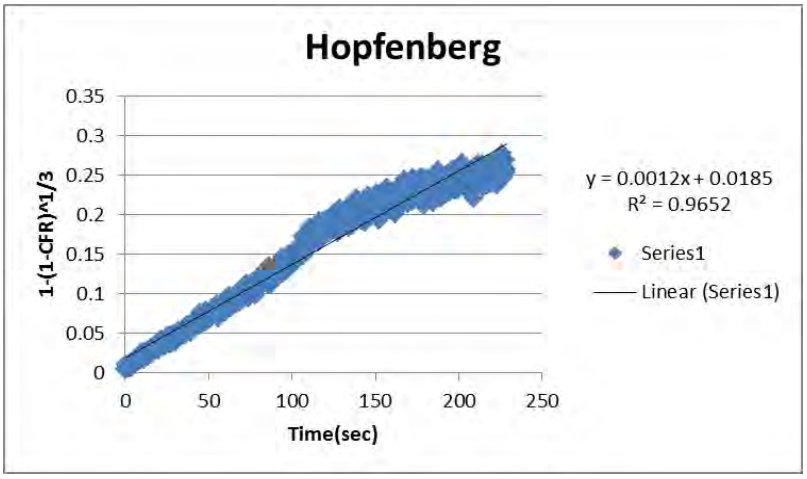

Figure 136: Hopfenberg model plot for Tf liposomes, batch #2, at 7.46mW/cm^2

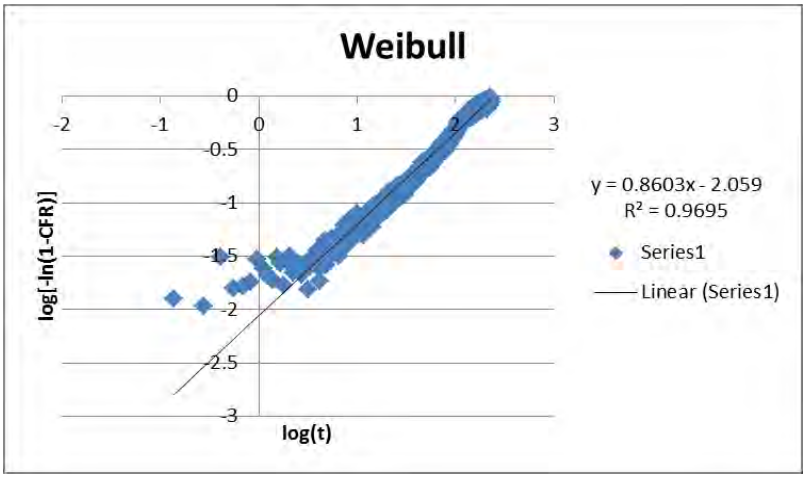

Figure 137: Weibull model plot for Tf liposomes, batch #2, at 7.46mW/cm^2

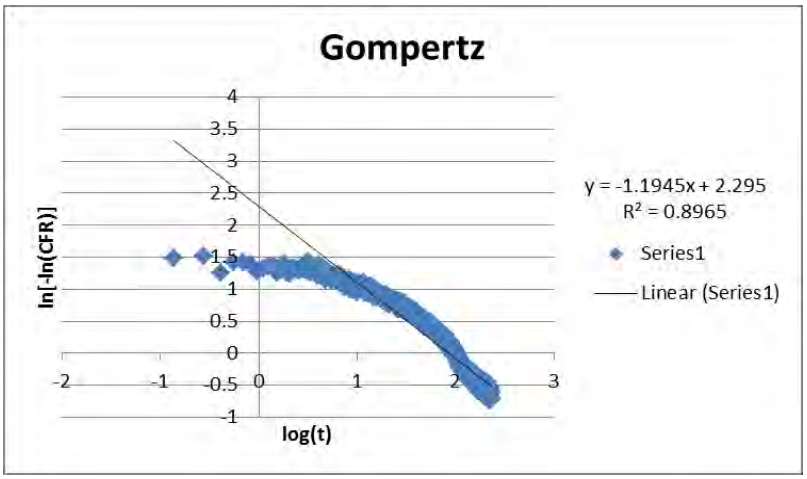

Figure 138: Gompertz model plot for Tf liposomes, batch #2, at 7.46mW/cm^2

Appendix F: Plots of Kinetic Models for 3rd Batch of Tf Liposomes at 7.46 mW/cm^2

Figure 139: Zero-Order model plot for Tf liposomes, batch #3, at 7.46mW/cm^2

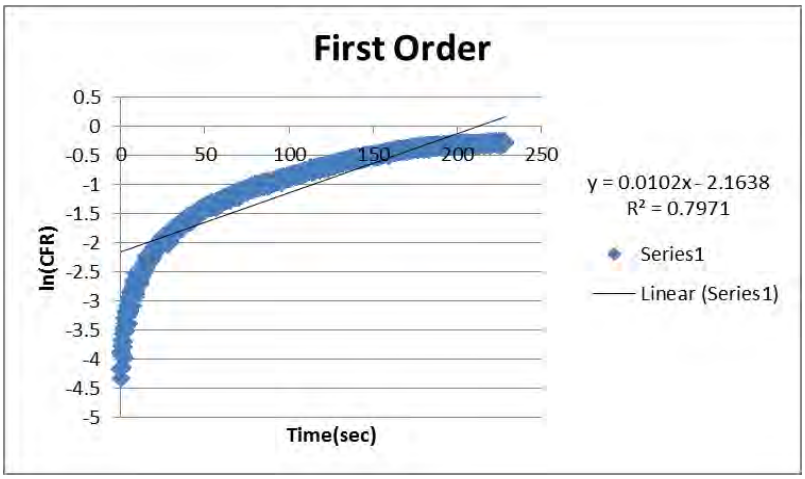

Figure 140: First-Order model plot for Tf liposomes, batch #3, at 7.46mW/cm^2

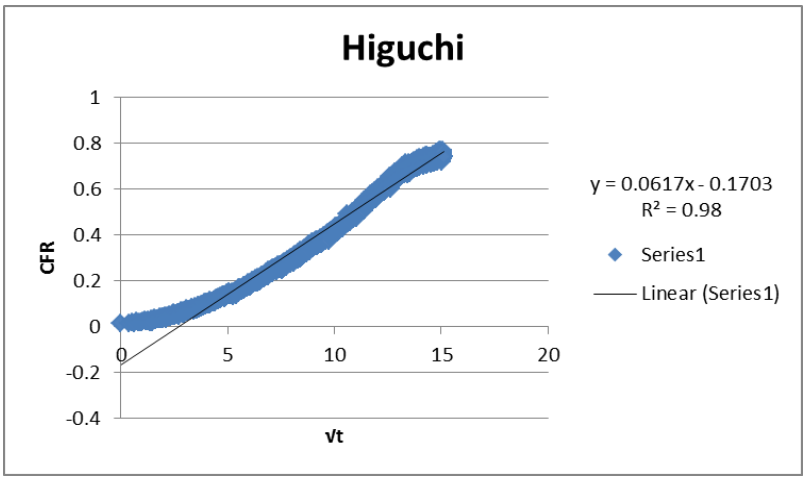

Figure 141: Higuchi model plot for Tf liposomes, batch #3, at 7.46mW/cm^2

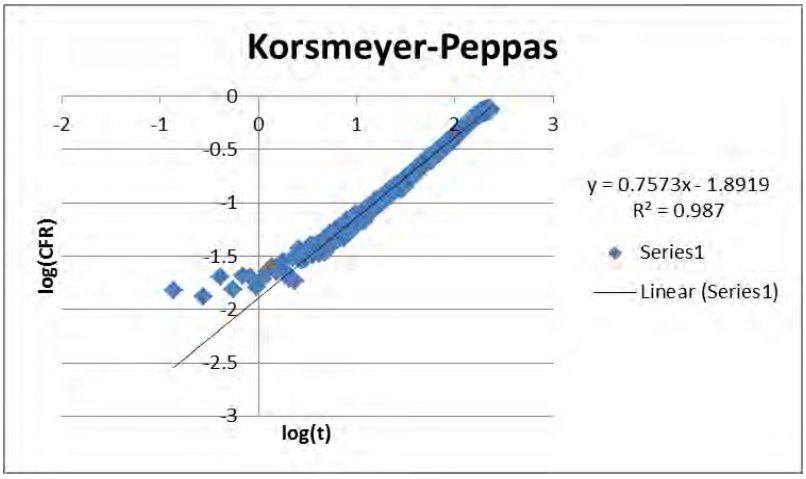

Figure 142: Korsmeyer-Peppas model plot for Tf liposomes, batch #3, at 7.46mW/cm^2

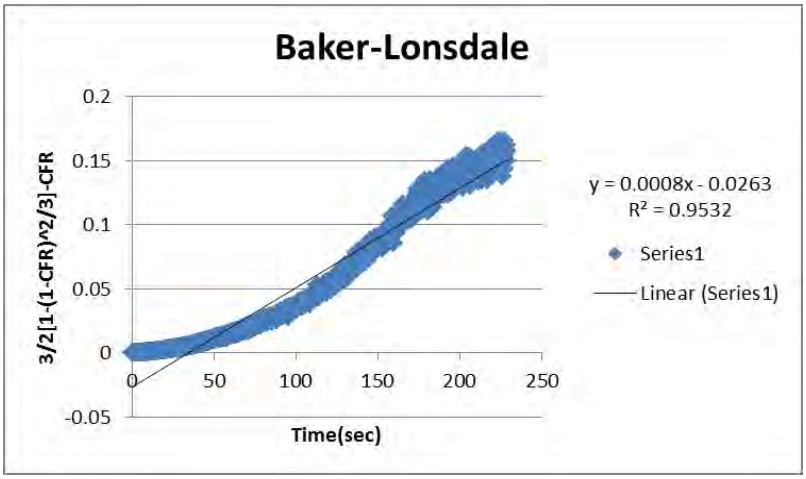

Figure 143: Baker-Lonsdale model plot for Tf liposomes, batch #3, at 7.46mW/cm^2

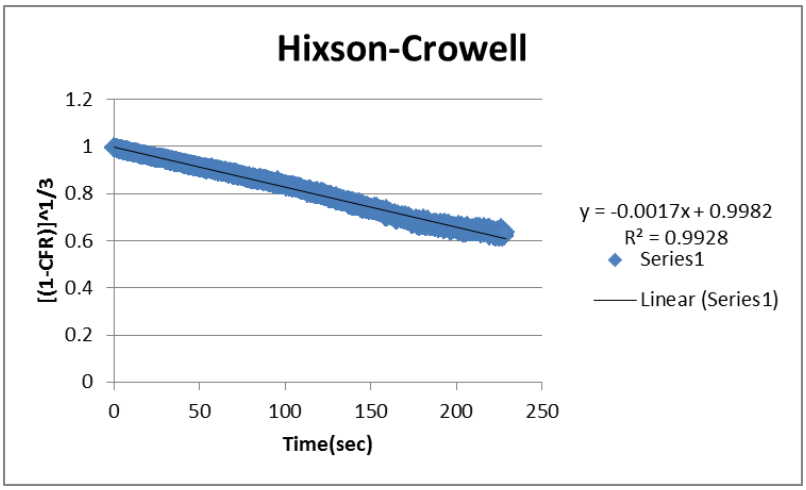

Figure 144: Hixson-Crowell model plot for Tf liposomes, batch #3, at 7.46mW/cm^2

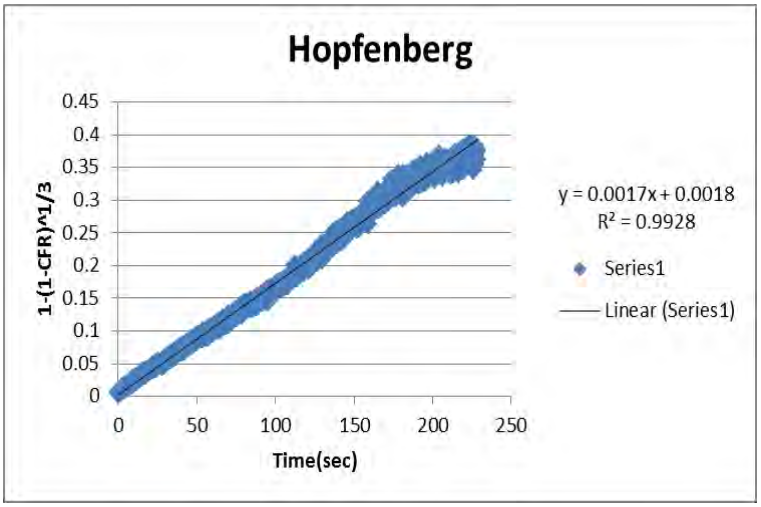

Figure 145: Hopfenberg model for Tf liposomes, batch #3, at 7.46mW/cm^2

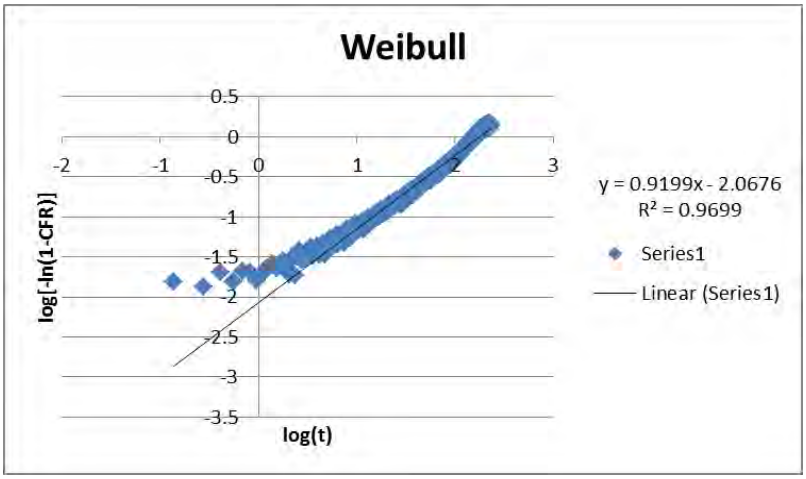

Figure 146: Weibull model plot for Tf liposomes, batch #3, at 7.46mW/cm^2

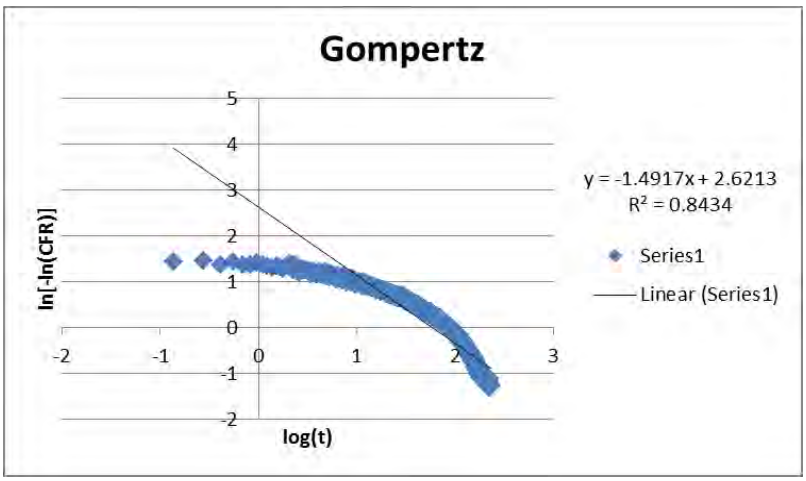

Figure 147: Gompertz model plot for Tf liposomes, batch #3, at 7.46mW/cm^2

Appendix G: Plots of Kinetic Models for All Batches of Tf Liposomes at 9.85 mW/cm^2

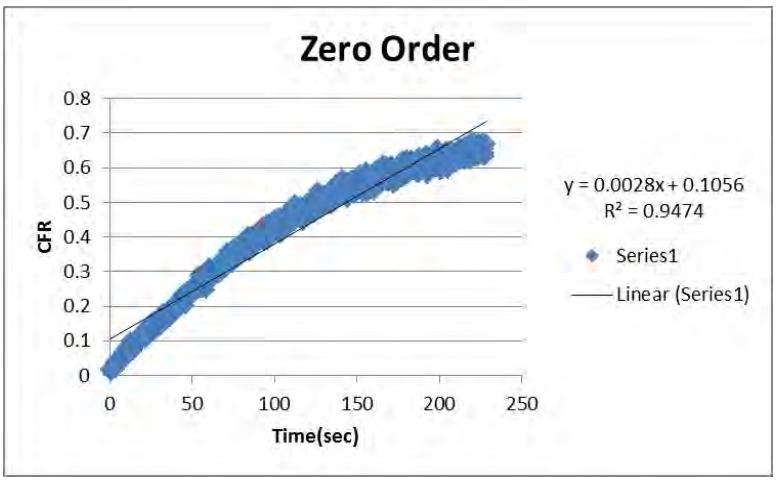

Figure 148: Zero-Order model plot for Tf liposomes, batch #1, at 9.85mW/cm^2

Figure 149: First-Order model plot for Tf liposomes, batch #1, at 9.85mW/cm^2

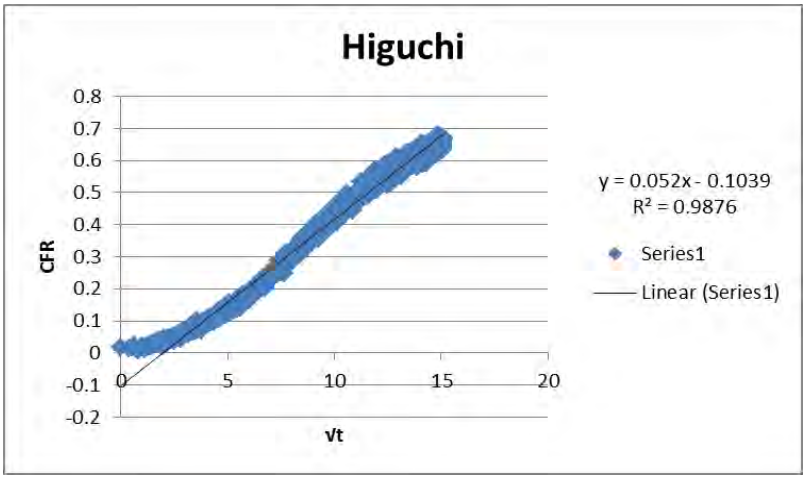

Figure 150: Higuchi model plot for Tf liposomes, batch #1, at 9.85mW/cm^2

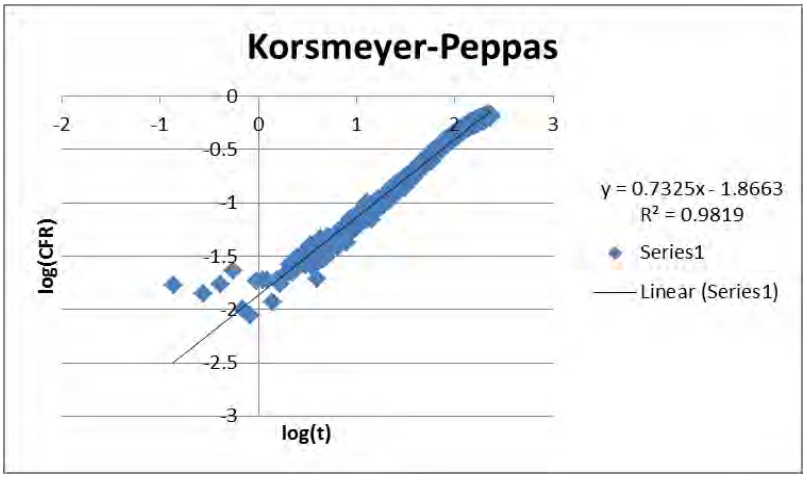

Figure 151: Korsmeyer-Peppas model plot for Tf liposomes, batch #1, at 9.85mW/cm^2

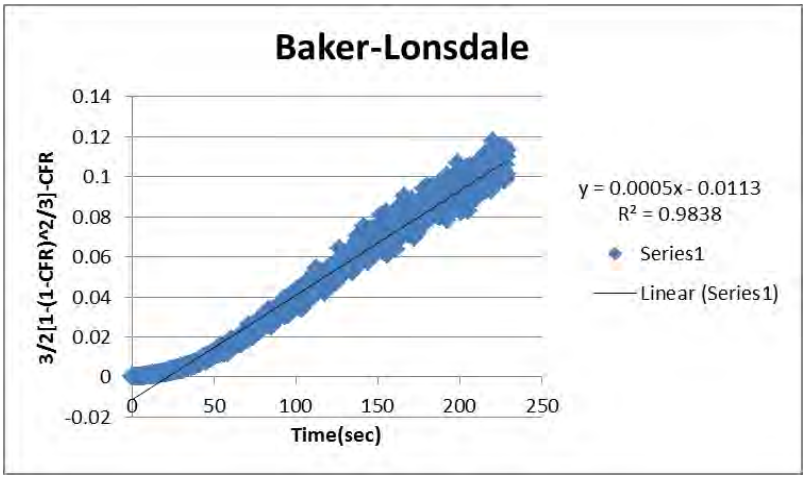

Figure 152: Baker-Lonsdale model plot for Tf liposomes, batch #1, at 9.85mW/cm^2

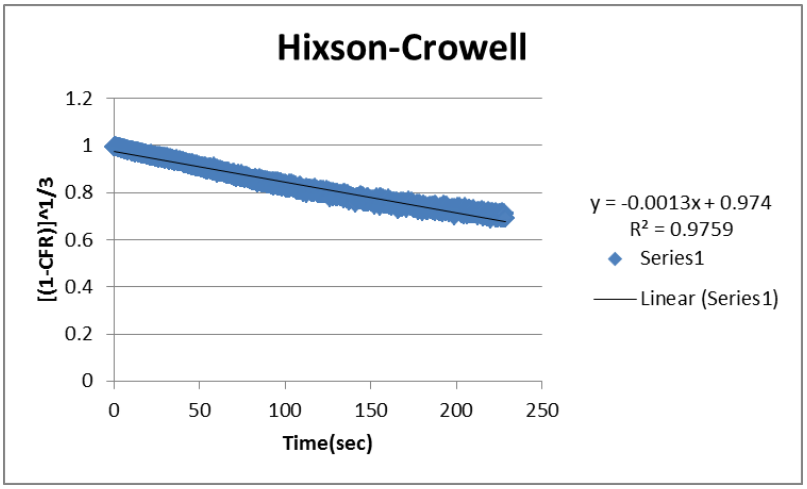

Figure 153: Hixson-Crowell model plot for Tf liposomes, batch #1, at 9.85mW/cm^2

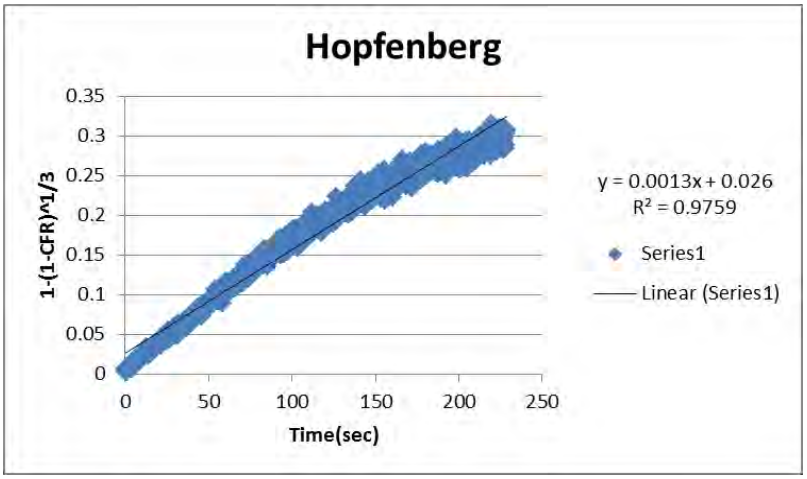

Figure 154: Hopfenberg model plot for Tf liposomes, batch #1, at 9.85mW/cm^2

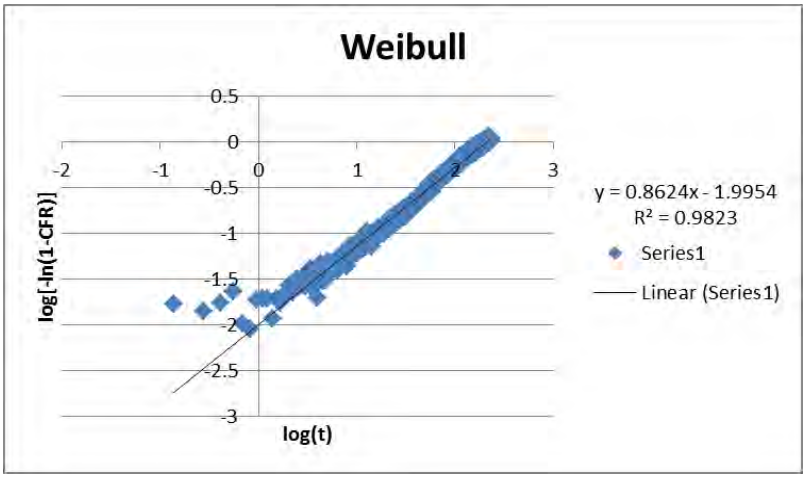

Figure 155: Weibull model plot for Tf liposomes, batch #1, at 9.85mW/cm^2

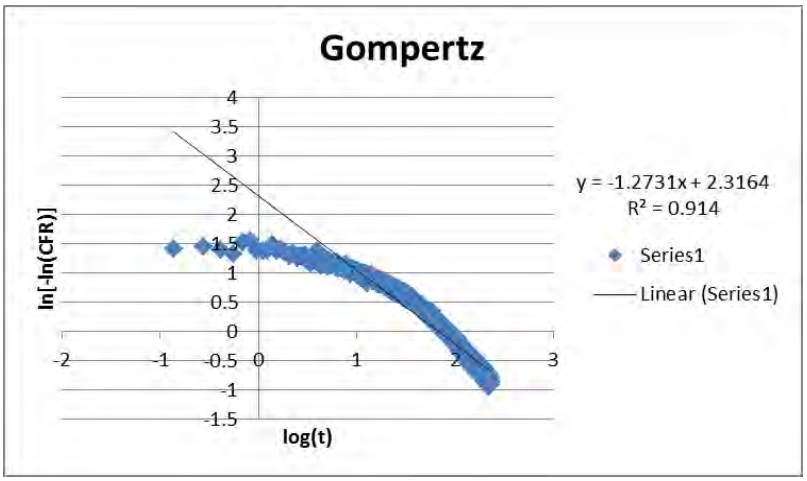

Figure 156: Gompertz model plot for Tf liposomes, batch #1, at 9.85mW/cm^2

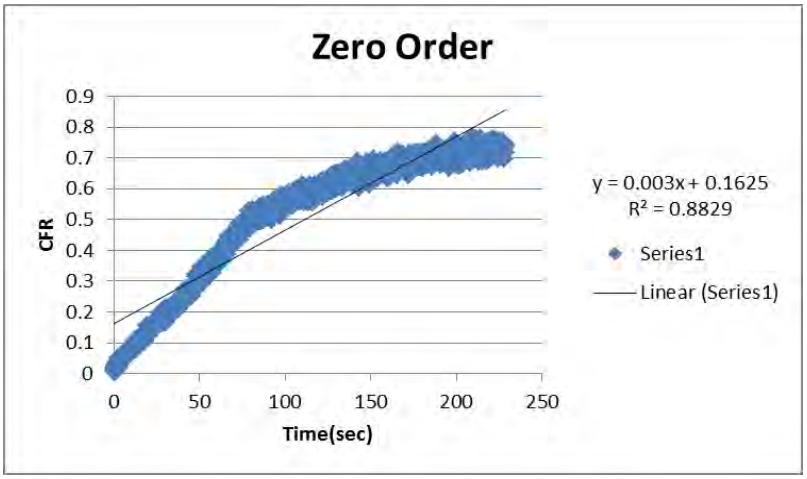

Figure 157: Zero-Order model plot for Tf liposomes, batch #2, at 9.85mW/cm^2

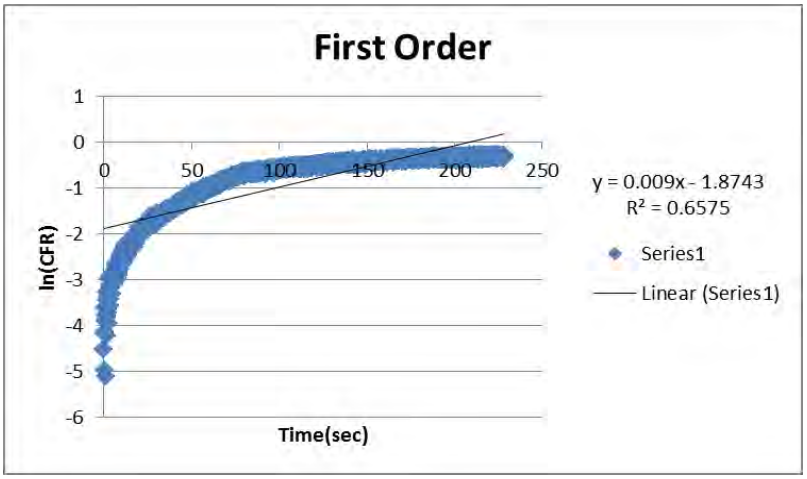

Figure 158: First-Order model plot for Tf liposomes, batch #2, at 9.85mW/cm^2

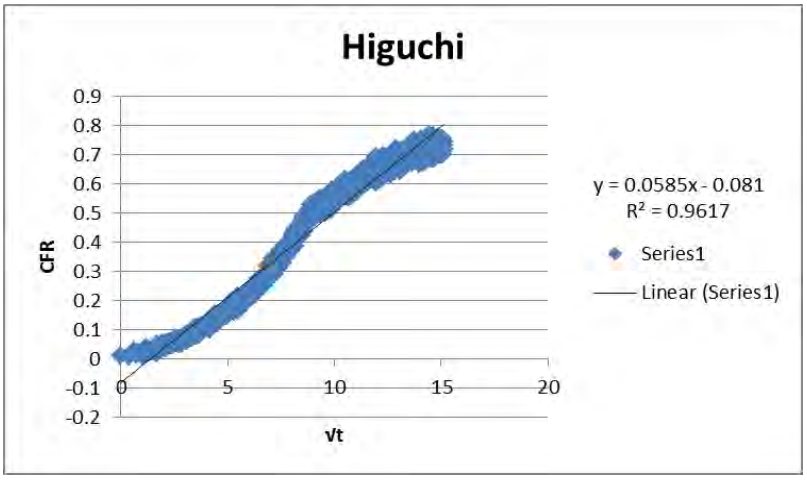

Figure 159: Higuchi model plot for Tf liposomes, batch #2, at 9.85mW/cm^2

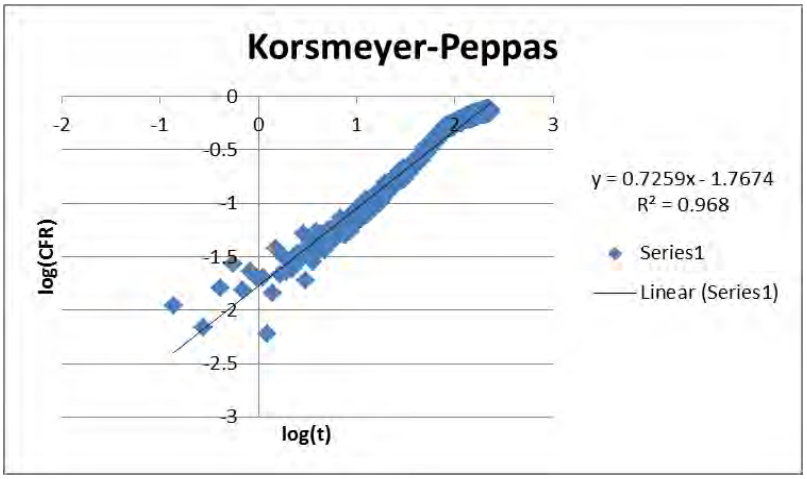

Figure 160: Korsmeyer-Peppas model plot for Tf liposomes, batch #2, at 9.85mW/cm^2

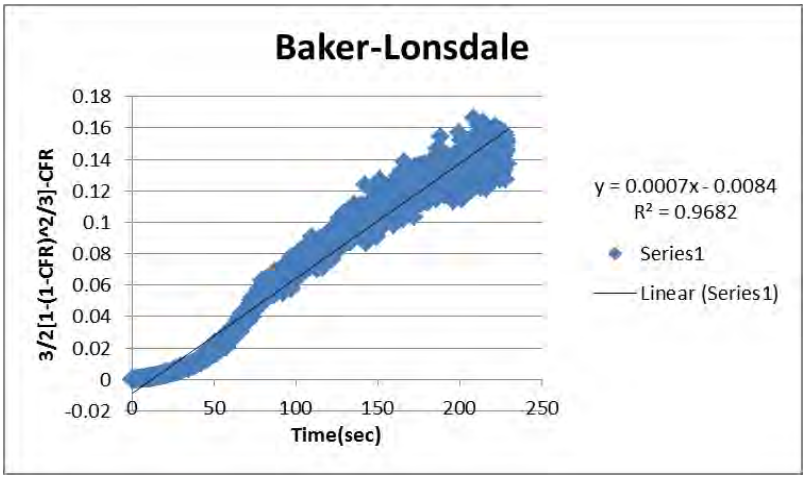

Figure 161: Baker-Lonsdale model plot for Tf liposomes, batch #2, at 9.85mW/cm^2

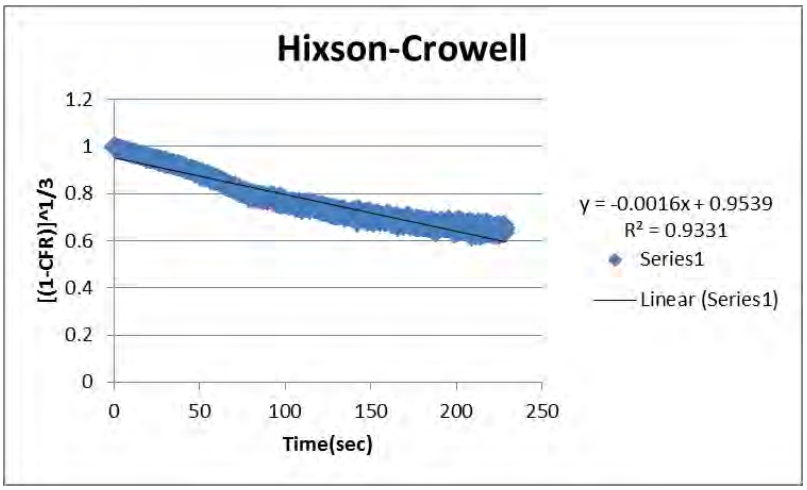

Figure 162: Hixson-Crowell model plot for Tf liposomes, batch #2, at 9.85mW/cm^2

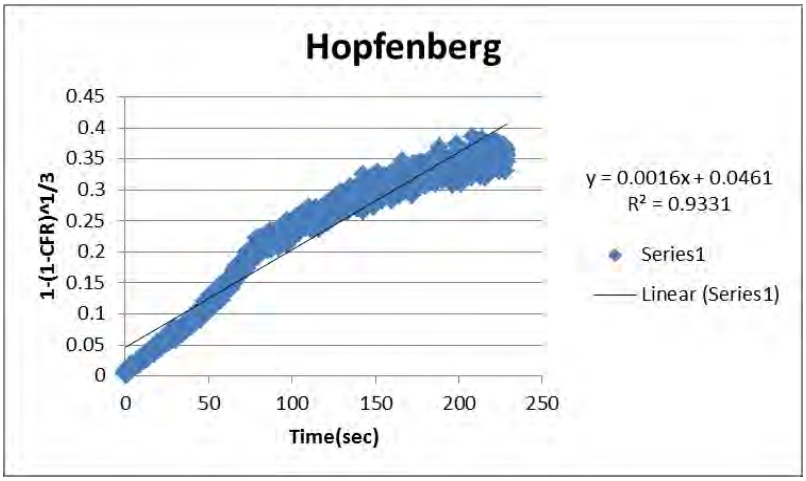

Figure 163: Hopfenberg model plot for Tf liposomes, batch #2, at 9.85mW/cm^2

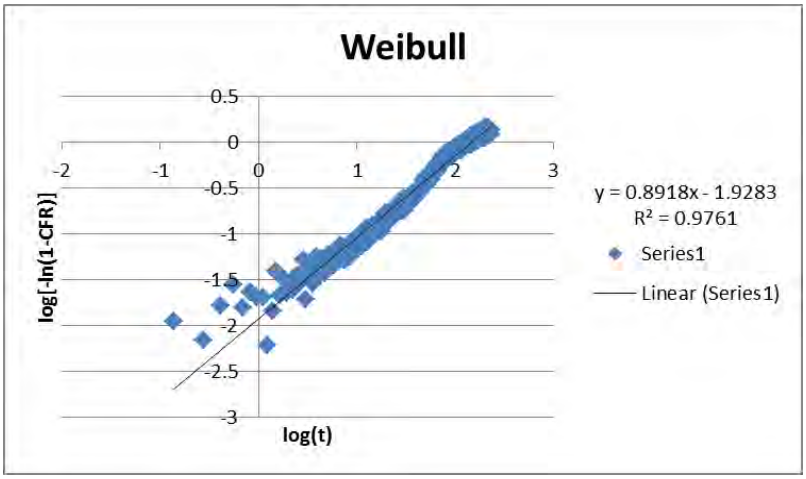

Figure 164: Weibull model plot for Tf liposomes, batch #2, at 9.85mW/cm^2

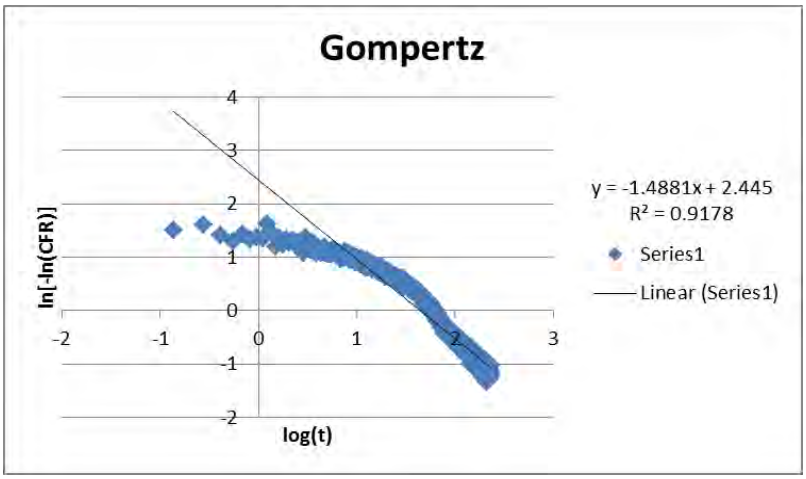

Figure 165: Gompertz model plot for Tf liposomes, batch #2, at 9.85mW/cm^2

Figure 166: Zero-Order model plot for Tf liposomes, batch #3, at 9.85mW/cm^2

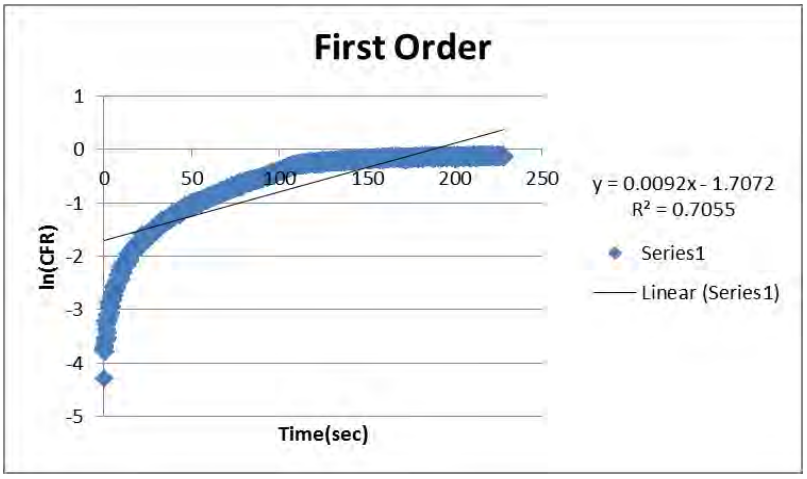

Figure 167: First-Order model plot for Tf liposomes, batch #3, at 9.85mW/cm^2

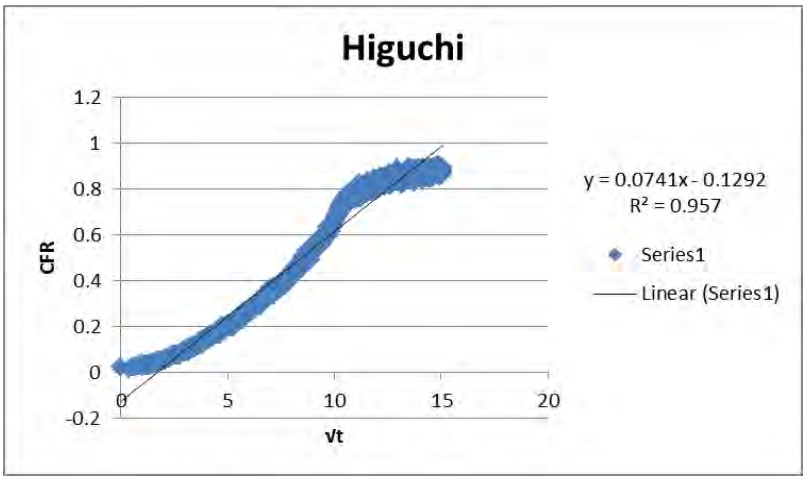

Figure 168: Higuchi model plot for Tf liposomes, batch #3, at 9.85mW/cm^2

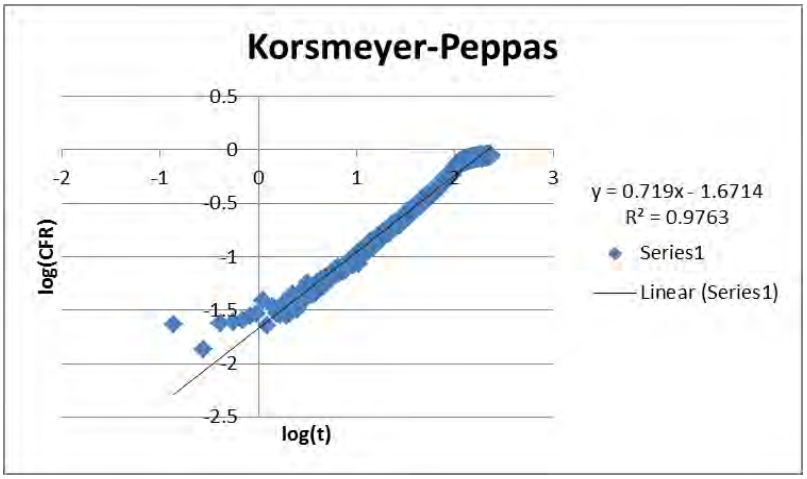

Figure 169: Korsmeyer-Peppas model plot for Tf liposomes, batch #3, at 9.85mW/cm^2

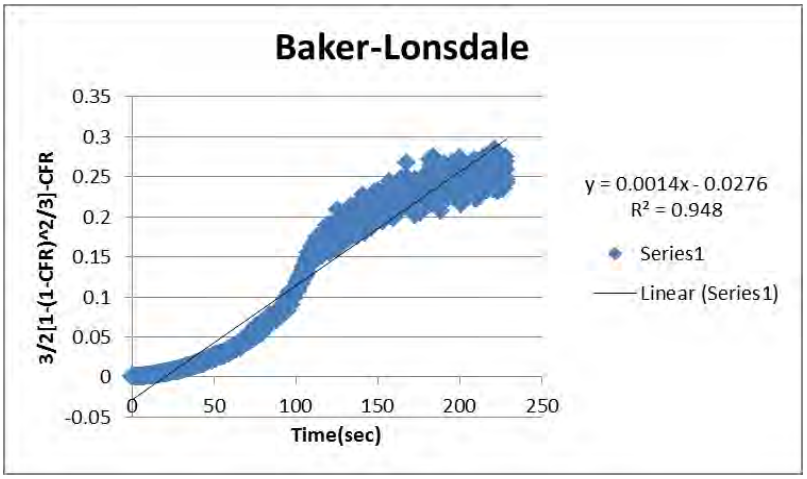

Figure 170: Baker-Lonsdale model plot for Tf liposomes, batch #3, at 9.85mW/cm^2

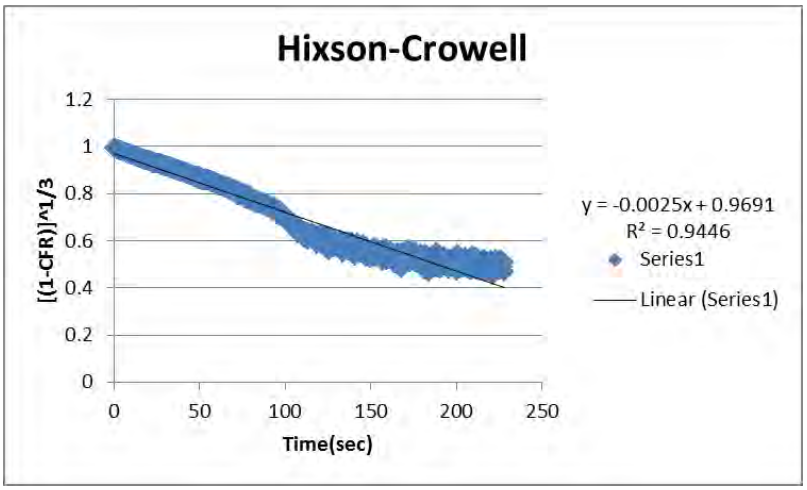

Figure 171: Hixson-Crowell model plot for Tf liposomes, batch #3, at 9.85mW/cm^2

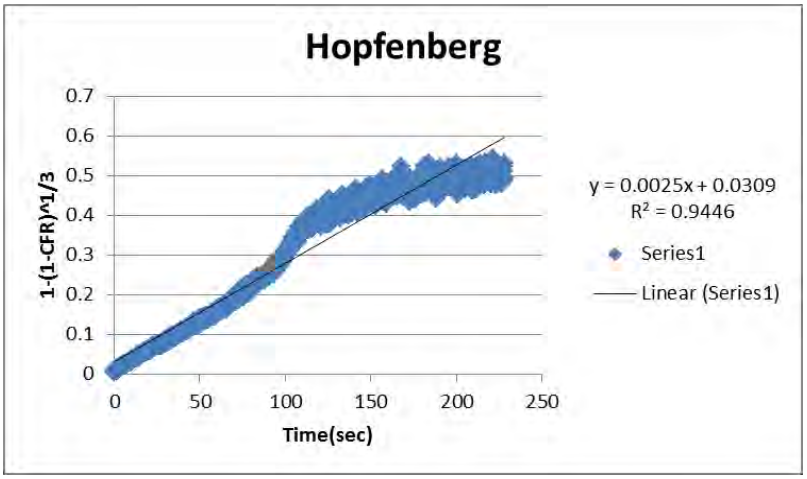

Figure 172: Hopfenberg model plot for Tf liposomes, batch #3, at 9.85mW/cm^2

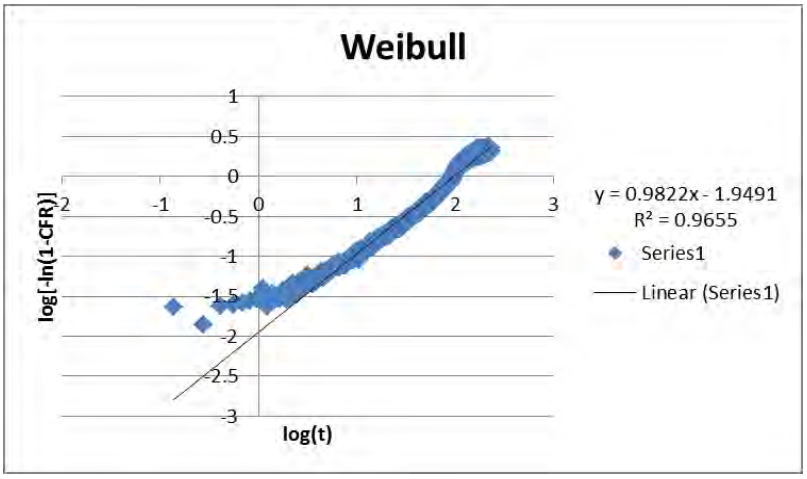

Figure 173: Weibull model plot for Tf liposomes, batch #3, at 9.85mW/cm^2

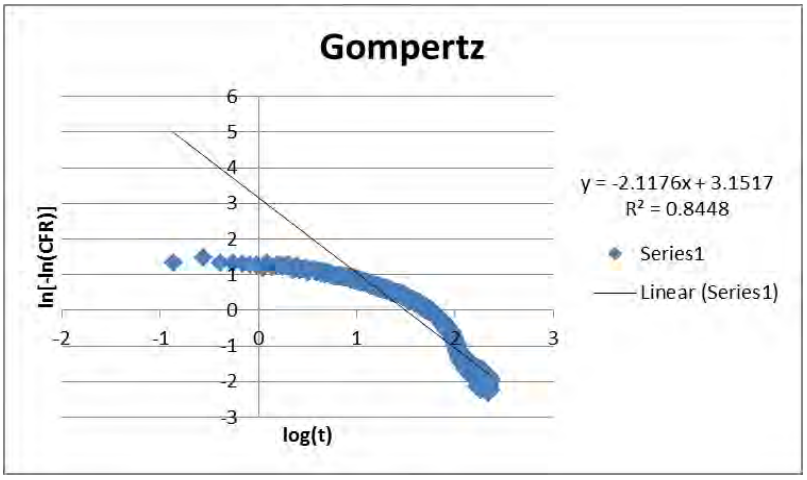

Figure 174: Gompertz model plot for Tf liposomes, batch #3, at 9.85mW/cm^2

Appendix G: Plots of Kinetic Models for All Batches of Tf Liposomes at 17.31 mW/cm^2

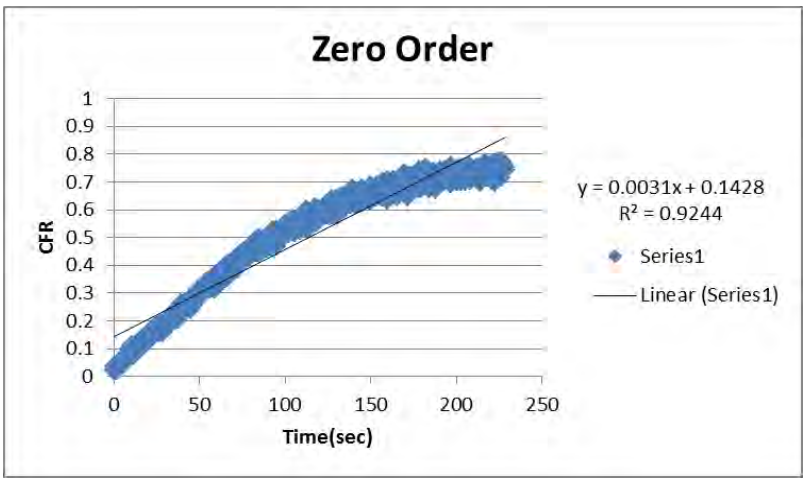

Figure 175: Zero-Order model plot for Tf liposomes, batch #1, at 17.31mW/cm^2

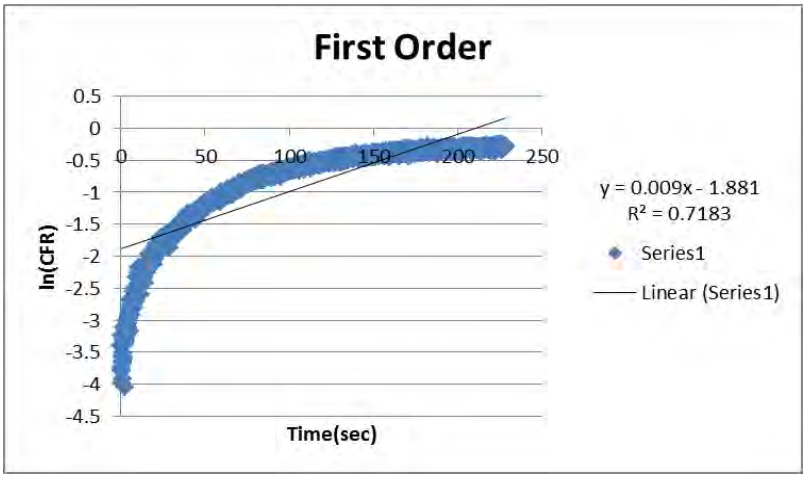

Figure 176: First-Order model plot for Tf liposomes, batch #1, at 17.31mW/cm^2

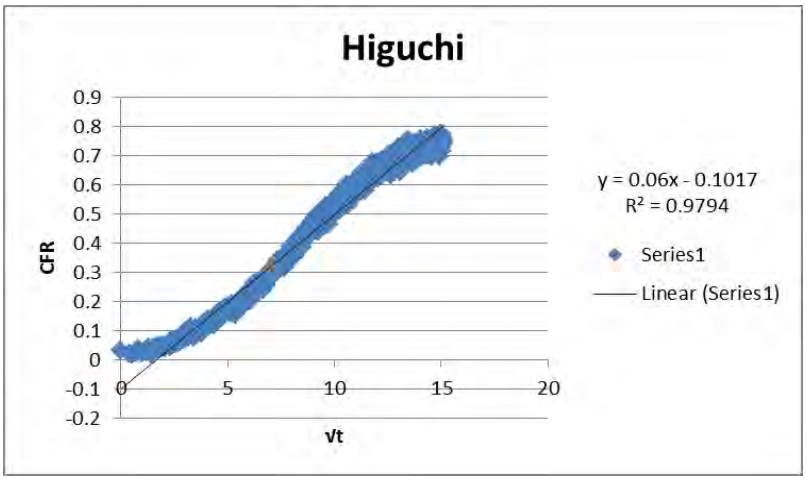

Figure 177: Higuchi model plot for Tf liposomes, batch #1, at 17.31mW/cm^2

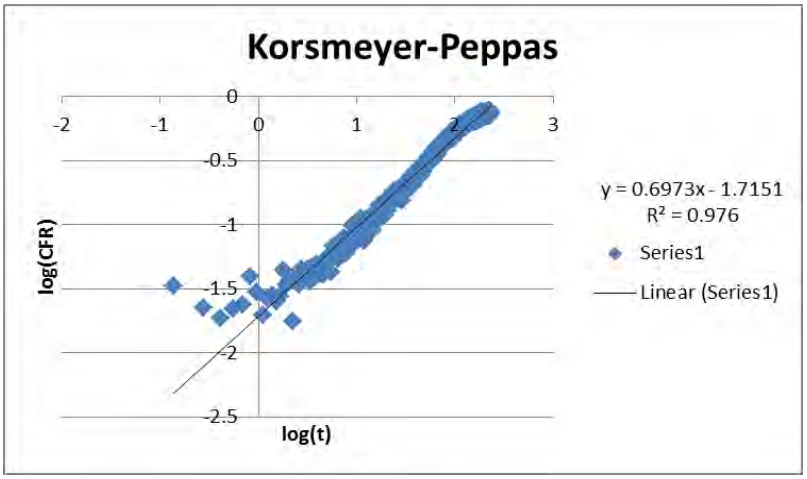

Figure 178: Korsmeyer-Peppas model plot for Tf liposomes, batch #1, at 17.31mW/cm^2

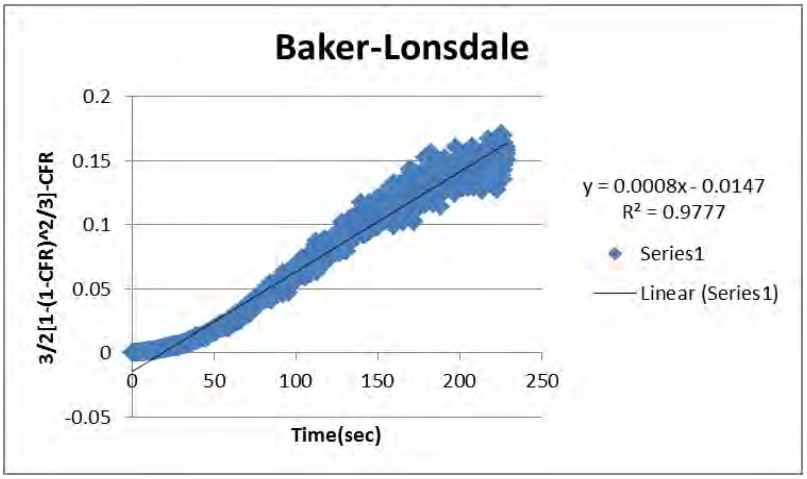

Figure 179: Baker-Lonsdale model plot for Tf liposomes, batch #1, at 17.31mW/cm^2

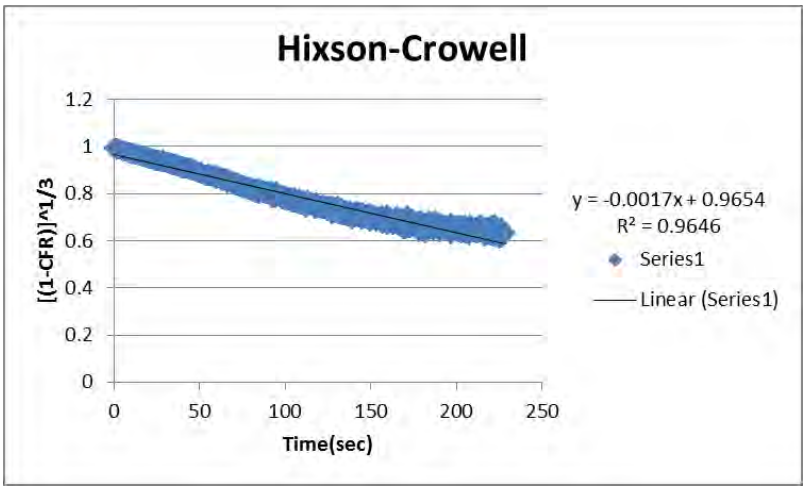

Figure 180: Hixson-Crowell model plot for Tf liposomes, batch #1, at 17.31mW/cm^2

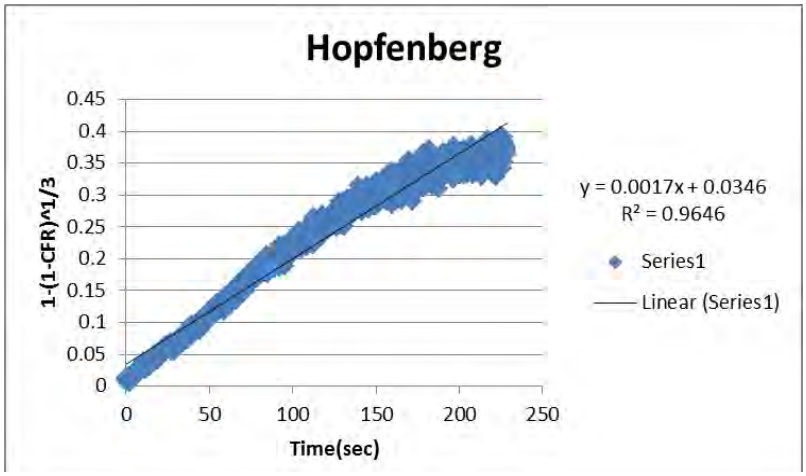

Figure 181: Hopfenberg model plot for Tf liposomes, batch #1, at 17.31mW/cm^2

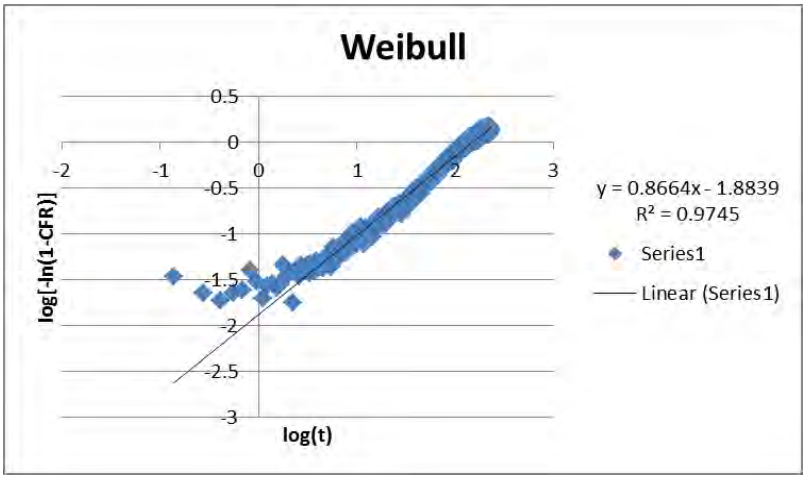

Figure 182: Weibull model plot for Tf liposomes, batch #1, at 17.31mW/cm^2

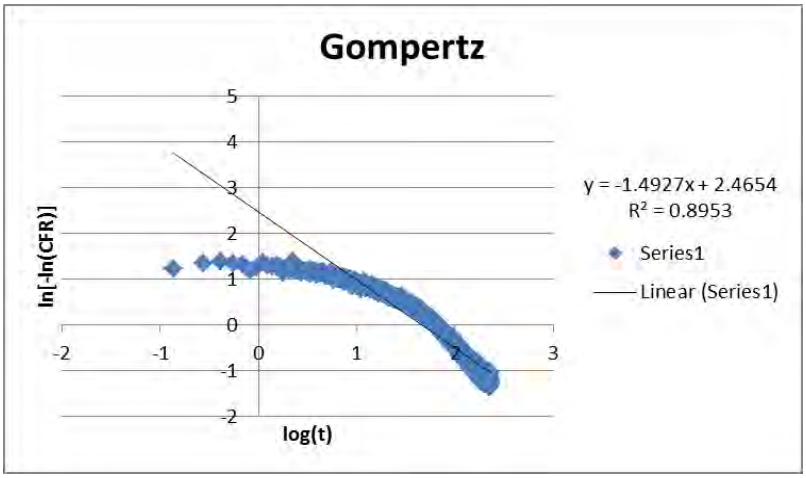

Figure 183: Gompertz model plot for Tf liposomes, batch #1, at 17.31mW/cm^2

Figure 184: Zero-Order model plot for Tf liposomes, batch #2, at 17.31mW/cm^2

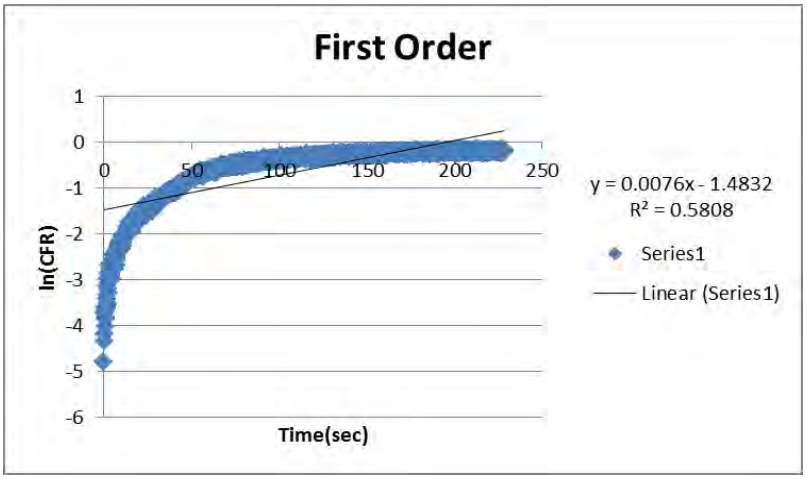

Figure 185: First-Order model plot for Tf liposomes, batch #2, at 17.31mW/cm^2

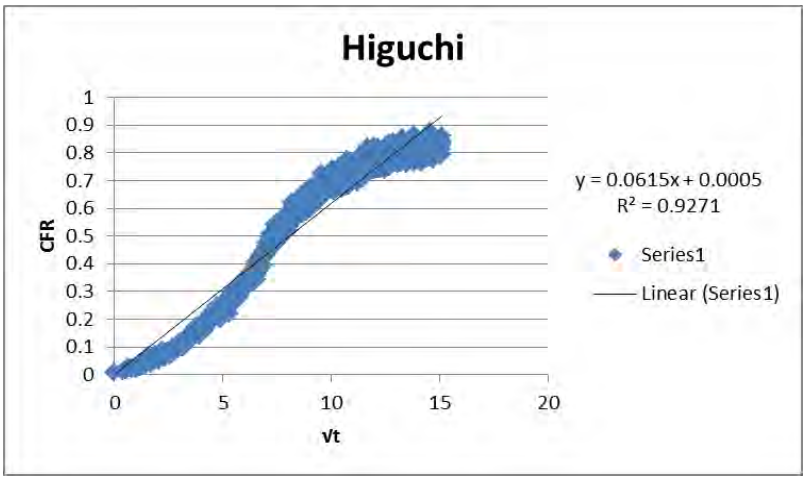

Figure 186: Higuchi model plot for Tf liposomes, batch #2, at 17.31mW/cm^2

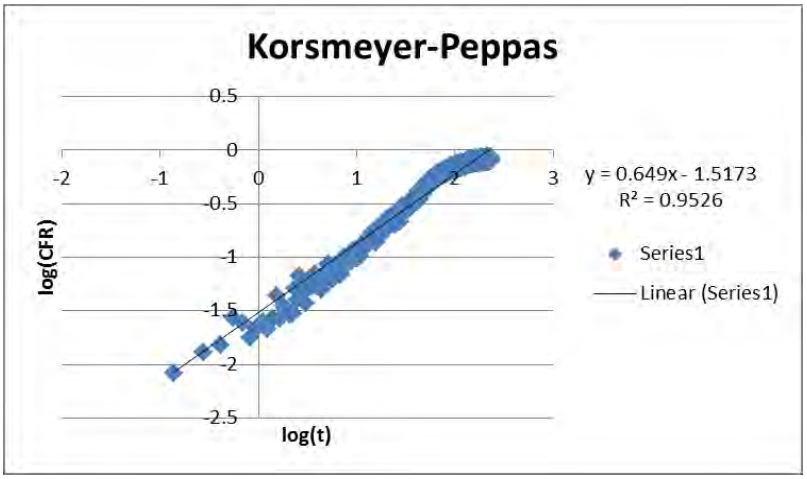

Figure 187: Korsmeyer-Peppas model plot for Tf liposomes, batch #2, at 17.31mW/cm^2

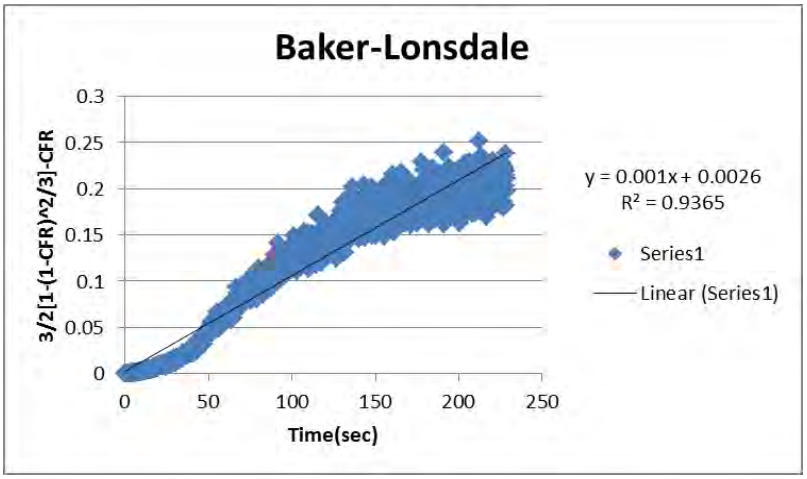

Figure 188: Baker-Lonsdale model plot for Tf liposomes, batch #2, at 17.31mW/cm^2

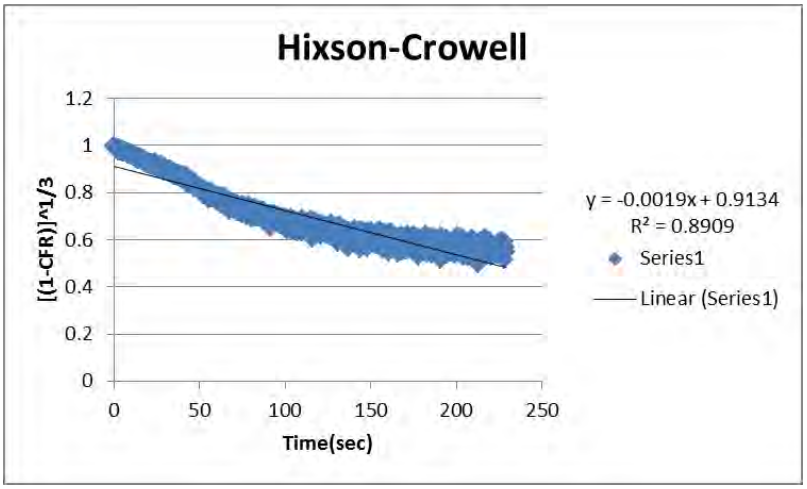

Figure 189: Hixson-Crowell model plot for Tf liposomes, batch #2, at 17.31mW/cm^2

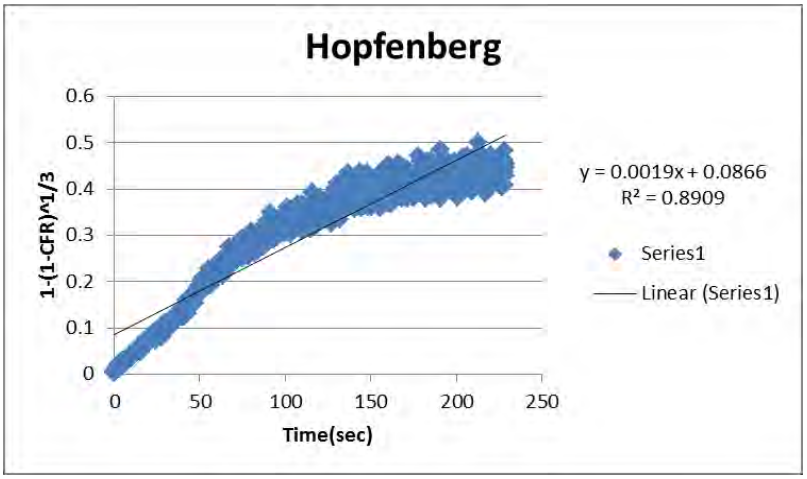

Figure 190: Hopfenberg model plot for Tf liposomes, batch #2, at 17.31mW/cm^2

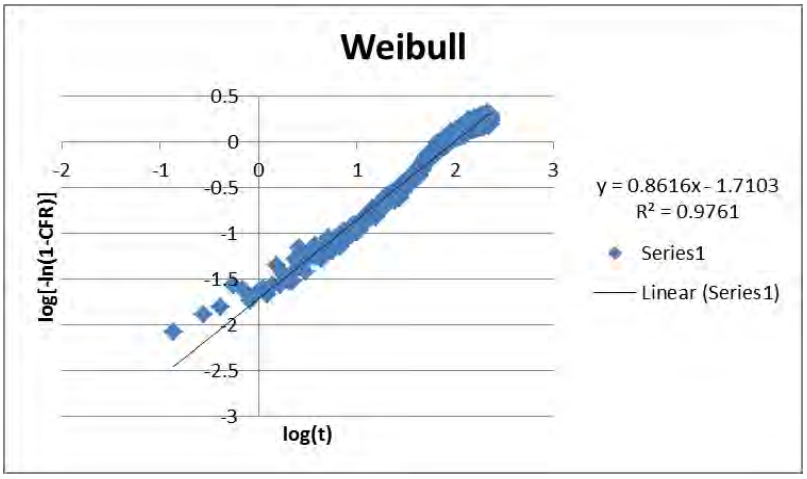

Figure 191: Weibull model plot for Tf liposomes, batch #2, at 17.31mW/cm^2

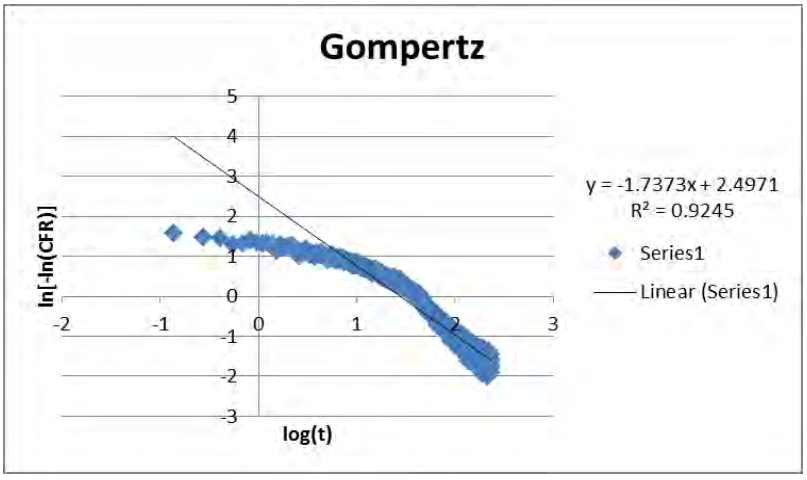

Figure 192: Gompertz model plot for Tf liposomes, batch #2, at 17.31mW/cm^2

Figure 193: Zero-Order model plot for Tf liposomes, batch #3, at 17.31mW/cm^2

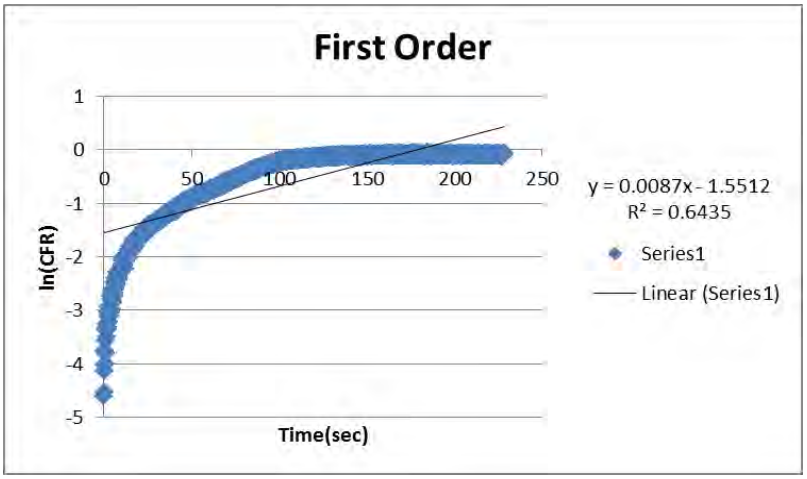

Figure 194: First-Order model plot for Tf liposomes, batch #3, at 17.31mW/cm^2

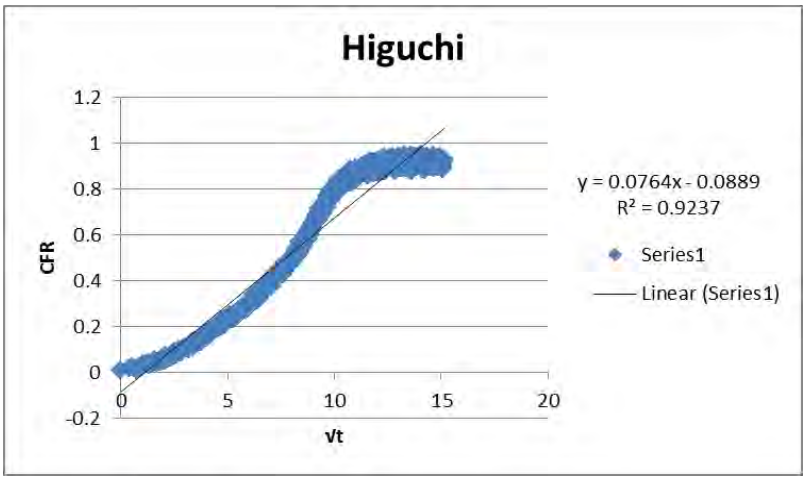

Figure 195: Higuchi model plot for Tf liposomes, batch #3, at 17.31mW/cm^2

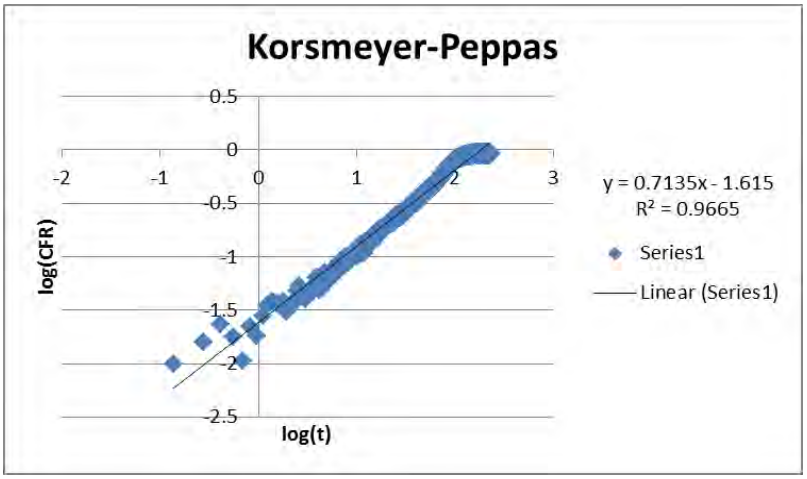

Figure 196: Korsmeyer-Peppas model plot for Tf liposomes, batch #3, at 17.31mW/cm^2

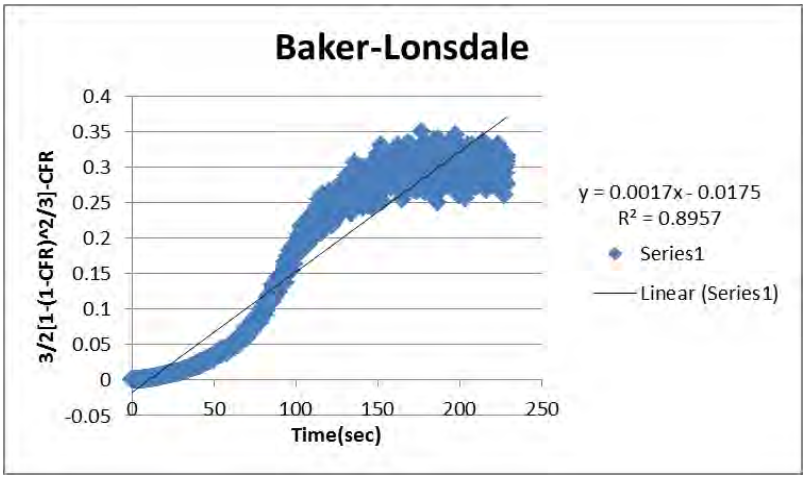

Figure 197: Baker-Lonsdale model plot for Tf liposomes, batch #3, at 17.31mW/cm^2

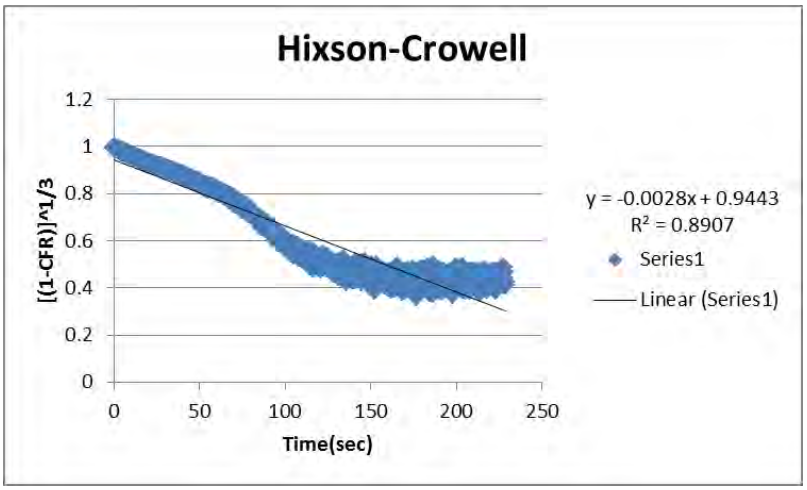

Figure 198: Hixson-Crowell model plot for Tf liposomes, batch #3, at 17.31mW/cm^2

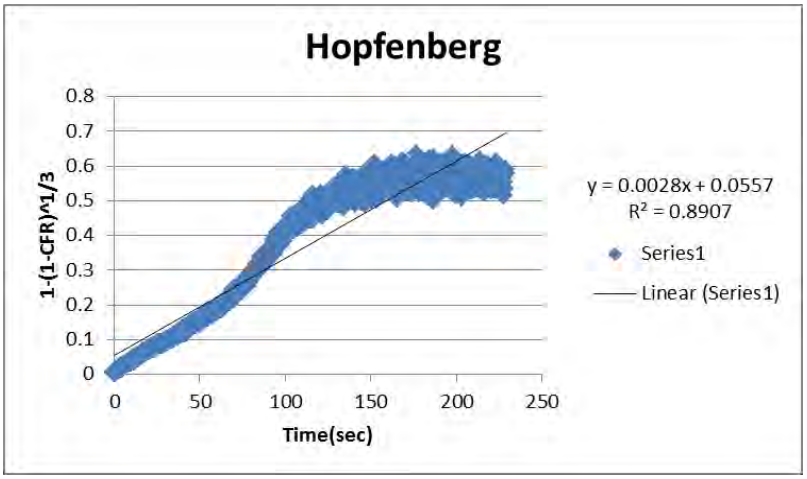

Figure 199: Hopfenberg model plot for Tf liposomes, batch #3, at 17.31mW/cm^2

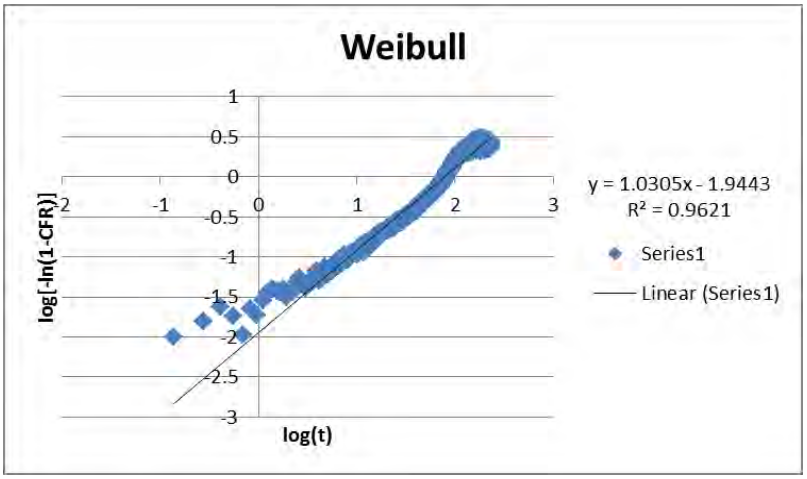

Figure 200: Weibull model plot for Tf liposomes, batch #3, at 17.31mW/cm^2

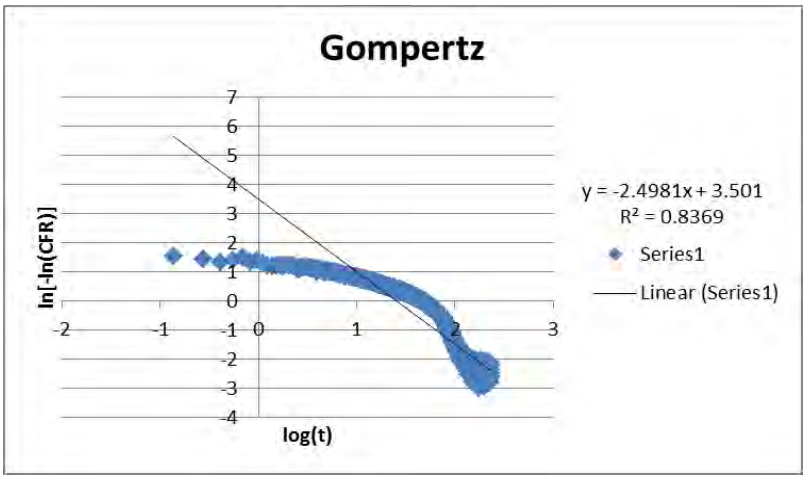

Figure 201: Gompertz model plot for Tf liposomes, batch #3, at 17.31mW/cm^2

Vita

Nour AlSawaftah was born in 1994, in Amman, Jordan. She received her elementary education from the Rosary Sisters School in Abu Dhabi, United Arab Emirates. She received her secondary education from Al Ma'arifa International Private School in Sharjah, UAE. She completed her internship at Moalajah FZC in Ajman, UAE. She received her B.Sc. degree in Chemical Engineering from the American University of Sharjah in 2016. In 2017, she joined the Biomedical Engineering master's program at the American University of Sharjah. She was awarded a graduate assistantship that allowed her to work as a graduate teaching and research assistant from 2017 till 2019. During her master's study, the results of this thesis were presented as an abstract and a poster titled "Ultrasound Enhanced Release of Transferrin Coupled Liposomes as Drug Delivery Carriers in Cancer Treatment" at the Society For Biomaterials (SFB) annual conference and exposition in 2018. In addition, she presented this thesis results as an abstract titled "Ultrasound Enhanced Release of Transferrin Coupled Liposomes as Drug Delivery Carriers in Cancer Treatment" in the UAE Graduate Students Research Conference 2018 (UAEGSRC-2018) and was awarded the best paper award.